

Diss. ETH No. 22901

Drone Based Experimental Investigation of Flow around Multi-MW Wind Farms in Flat and Complex Terrains

A dissertation submitted to
ETH ZURICH

for the degree of
DOCTOR OF SCIENCES

presented by

Balaji Subramanian

M.Tech. AE. Eng., Indian Institute of Technology, Kanpur, India
Born March 6th, 1982
Citizen of India

accepted on the recommendation of
Prof. Dr. Reza S. Abhari, examiner
Dr. Ndaona Chokani, co-examiner
Prof. Dr. Thomas Rösger, co-examiner

Zurich 2015

© 2015 Balaji Subramanian
All Rights Reserved

ACKNOWLEDGEMENTS

First and foremost my sincere thanks to Prof. Dr. Reza Abhari for giving me this opportunity to carry out my PhD research in the Laboratory for Energy Conversion, and for continuously motivating me to achieve my goals. I appreciate his contributions of time, ideas, and resources to make my PhD experience productive and stimulating. It was a great learning experience for me to work with him.

My sincere thanks to Dr. Ndaona Chokani for his invaluable guidance and support all these years, especially during my field experiments. I am very grateful for his comments on my presentations and papers that not only helped me to improve their quality but also taught me valuable skills of presenting my work effectively to different audience. I highly value his regular supervision and guidance.

I would like to express my sincere gratitude to Prof. Thomas Rösgen for accepting the role of co-examiner, and for his valuable comments and suggestions that helped me to improve this thesis.

My sincere thanks to Dr. Michel Mansour for enabling me to use Fast Response Aerodynamic Probe (FRAP) developed by him. He accompanied me on some of my field experiments and I learned a lot from him, especially on how to plan for a field measurement campaign. He was my mentor and always helped me whenever I needed his advice.

My sincere thanks to Mr. Flori Alickaj for helping me with instrumentation, and for supporting me with the electrical issues related to the measurement system. My sincere thanks to LEC workshop for supporting with the mechanical issues related to the measurement system.

Many thanks to Martin Muller for supporting me on various issues related to drone hardware, sensors and Paparazzi system. Also thanks to Christian Lindenberg and Leo Gruber for their support as safety pilot during my measurement campaigns.

My sincere thanks to all LEC members for their kind help and support all these years. Special thanks go to all members of the wind group. I always enjoyed working at LEC. Many thanks to Marlene Hegner for her kind help and support on administrative matters all these years.

Finally, I am deeply grateful to my family for their continuous love and emotional support during my PhD, without their continuous support, patience, understanding and encouragement throughout the years of my PhD life this thesis would have never been possible.

ABSTRACT

Wind energy continues to grow at double-digit rate annually, which puts increasing pressure on improving the wind turbine technology to maximize energy capture and to minimize the operational and maintenance cost of wind farms. The characteristics of wake downstream of a wind turbine has an important bearing on the optimized micro-siting of wind turbines in a given land area and on the loads seen by a wind turbine located downstream of an upstream turbine. In addition, it is known that the topography in complex terrain influences both the upstream wind and the downstream wake evolution resulting in increased uncertainties. Thus, a detailed knowledge of the flow field upstream of a wind turbine and in the wake are needed as it affects the energy production and the fatigue life of a wind turbine. These factors have a strong influence on the economic viability of a wind farm. In the past decades, only a few measurements in the wake of a full-scale wind turbine have been reported, and those that have been reported provided limited scope in terms of spatial resolution of a wind turbine wake structure.

Thus, the primary objectives of this work are, first to detail the turbulence structure of full-scale wind turbine's wake in flat and complex terrain with improved spatial coverage and resolution than prior works, and second to generate a data base to provide inputs and for validation of ETH Zürich's advanced wind simulation tools. To achieve these research objectives, an innovative measurement approach was developed at ETH Zurich that comprises of an uninhabited aerial vehicle instrumented with a Fast Response Aerodynamic Probe (FRAP). The key enabler for drone based wind measurements is the FRAP probe as it enables the direct measurement of 3D wind vector in drones frame of reference at high sampling rate. To transform the FRAP measured wind velocity vector into Earth's frame of reference, the drone is instrumented with a suite of sensors including an IMU, an absolute pressure sensor, a magnetometer, a GPS, and a temperature and humidity sensor. The drone based autonomous wake measurements are accomplished through the hardware and software of an open-source autopilot system called Paparazzi. Thus the FRAP-on-drone wind measurement system also includes a ground control station that monitors the drone during flight and logs the output of its on-board sensors. In parallel, an optical trigger system is used to track and log the position of wind turbine blades during drone based wake measurements.

The FRAP-on-drone wind measurement system was compared with a 3D scanning LIDAR and a good comparison was observed. The first-

ever measurements of the pressure field across a wind turbines rotor plane were reported. Additionally, the distinctive signatures of the blade tip vortices are measured in terms of the air speed and static pressure. It was shown by measurements that pitch between subsequent tip vortices that are shed from the wind turbines blades increases as the near-wake evolves. In the measured upstream wind speed profile in complex terrain, there is a jet-like structure with a maximum wind speed near hub height, a wind veer that differs by $\pm 12^\circ$ relative to the area-averaged wind direction, and the wind turbine had a yaw misalignment of 5° relative to the main wind direction. A Short Time Fourier Transform-based analysis method is used to derive time-localised turbulent kinetic energy along the drone's trajectory. In flat terrain, the region of the near wake is measured to extend up to 2.8 rotor diameters. In this region, tip vortices that can be distinguished from their elevated levels of turbulent kinetic energy, are clearly identifiable. The tip vortices evolve just below the shear layer that separates the high speed exterior flow from the relatively low speed flow within the near wake. Further downstream of $X/D = 2.8$, the wake flow is re-energised by the penetration of the relatively turbulent kinetic energy flow at the wake's boundary into the wake flow. By $X/D = 5-5.5$, the elevated turbulent kinetic energy flow has penetrated to the centre of the wake, and even though the upstream wind speed is recovered by $X/D = 10$, the turbulent kinetic energy is approximately two orders of magnitude larger than that upstream. Simultaneous measurements of the near wake (of one turbine) and the far wake (of a second turbine) confirm the distinctly different characteristics of the near wake and far wake. In complex terrain, the near-wake extends up to two rotor diameters. By $X/D = 2.7$, the elevated turbulent kinetic energy flow has penetrated to the centre of the wake, and the turbulent kinetic energy is more than three orders of magnitude larger than that upstream. The measurements in wake were made under neutral and unstable atmospheric conditions. Finally, Reynolds decomposition was used to reveal the structure of turbulence in freestream and in wake in the surface layer.

In summary, the instrumented drone allows high spatial and temporal resolution measurements of the highly three-dimensional structure and interactions in a wind turbine's wake, including its ability to capture tip vortices and nacelle wake evolution that were not possible earlier. With this innovative approach, the wake evolution downstream of a full scale wind turbine in flat and complex terrains were detailed for first time at high resolution. The drone based wind measurements were also used successfully to validate the ETH wake model and the IWTM model, which are under development at ETH Zurich.

ZUSAMMENFASSUNG

Die jährliche Wachstumsrate von Windenergie nimmt weiterhin zweistellig zu, wodurch der Druck erhöht wird, die Windturbinen-Technologie zu verbessern und die Betriebs- und Wartungskosten von Windparks zu minimieren. Die Eigenschaften eines Nachlaufgebiets stromabwärts einer Windturbine haben einen wichtigen Einfluss auf die optimierte lokale, relative Standortwahl von Windturbinen auf einer bestimmten Landfläche und ebenfalls auf die Lasten, denen eine Windturbine ausgesetzt ist, die stromab einer stromaufwärts positionierten Windturbine steht. Ausserdem ist bekannt, dass ungleichmässige Topographie sowohl den Wind stromauf-, als auch den Verlauf des Nachlaufs stromabwärts beeinflusst, woraus ein erhöhter Unsicherheitsfaktor resultiert. Die detaillierte Kenntnis des Strömungsfelds stromaufwärts einer Windturbine und im Nachlaufgebiet ist nötig, weil dies die Energieproduktion und die Lebensdauer einer Windturbine beeinflusst. Diese Faktoren haben einen starken Einfluss auf die Wirtschaftlichkeit eines Windparks. In den vergangenen Jahrzehnten ist nur über wenige Messungen im Nachlauf einer Windturbine berichtet worden und diejenigen Berichte, die darüber zu finden sind, bieten einen begrenzten Umfang bezüglich der räumlichen Struktur der Nachlaufströmung einer Windturbine.

Entsprechend sind die Hauptziele dieser Arbeit zweierlei: erstens, über diejenigen Turbulenzstrukturen ausführlich zu berichten, die in der Nachlaufströmung einer vollmassstäblichen Windturbine in flachem und in unregelmässigem Gelände mit verbesserter räumlicher Auflösung als in vergangenen Arbeiten erfasst werden; und zweitens, eine Datenbank zu erzeugen, die Referenzwerte für die Validierung des erweiterten Windsimulations-Tools der ETH Zürich bereitstellt. Um diese Forschungsziele zu erreichen, ist an der ETH eine innovative Messmethode entwickelt worden, die aus einer unbemannten Drohne mit einer schnellansprechenden aerodynamischen Sonde (FRAP) besteht. Diese FRAP-Sonde ist das Schlüsselement, das die drohnenbasierten Windmessungen ermöglicht, da mit ihr direkte Messungen des 3D-Windvektors im drohnenrelativen Bezugssystem mit hoher Abtastrate möglich sind. Um den mittels FRAP gemessenen Windgeschwindigkeitsvektor in das Erdbezugssystem zu transformieren, ist die Drohne mit Sensoren ausgestattet einschliesslich eines Inertialsensors, eines Drucksensors für den absoluten Druck, eines Magnetometers, eines GPS-Sensors und eines Temperatur- sowie Luftfeuchtigkeitssensors. Die autonomen, drohnenbasierten Messungen

der Nachlaufströmung werden über die Hardware und Software des frei zugänglichen Autopiloten-Systems „Paparazzi“ bewerkstelligt. Deshalb beinhaltet das FRAP-Drohnen-Windmesssystem ebenfalls eine Bodenkontrollstation, die die Drohne während des Fluges überwacht und die Daten der bordeigenen Sensoren aufzeichnet. Gleichzeitig wird ein optisches Trigger-System verwendet, um während der drohnenbasierten Messungen der Nachlaufströmungen die Position der Windturbinenschaufeln zu verfolgen und aufzuzeichnen.

Das FRAP-Drohnen-Windmesssystem wurde mit einem 3D LIDAR-Scanner verglichen und eine gute Übereinstimmung wurde ermittelt. Zum allerersten Mal wurde über Messungen des Druckfeldes quer durch die Ebene des Windturbinenrotors berichtet. Ausserdem wurden die charakteristischen Eigenschaften der Schaufelspitzenwirbel bezüglich der Luftgeschwindigkeit und des statischen Drucks gemessen. Es wurde durch Messungen gezeigt, dass sich die Teilung zwischen aufeinanderfolgenden Spitzenwirbeln, die von den Windturbinenschaufeln abgeworfen werden, vergrössert während sich das Nahfeld der Nachlaufströmung ausbildet. Im gemessenen Windgeschwindigkeitsprofil stromaufwärts in unregelmässigem Gelände gibt es eine strahlartige Struktur mit einer maximalen Windgeschwindigkeit in der Nähe der Nabenhöhe; eine Windabweichung von 12° relativ zur flächengemittelten Windrichtung. Ausserdem hatten die Windturbinen eine Fehlansrichtung des Gierwinkels von 5° relativ zur Hauptwindrichtung. Eine Analyseverfahren, die auf der schnellen Fourier Transformation beruht, wird verwendet, um die zeitlich festgelegte turbulente kinetische Energie entlang der Drohnentrajektorie abzuleiten. Im flachen Gelände erstreckt sich die Messung der Nahfeldnachlaufströmung über bis zu 2,8 Rotordurchmesser. In diesem Gebiet sind die Spitzenwirbel klar erkennbar, da sie sich anhand des erhöhten Niveaus an turbulenter kinetischer Energie identifizieren lassen. Die Spitzenwirbel entwickeln sich genau unterhalb der Scherschicht, die das äussere Gebiet höherer Geschwindigkeiten von dem Gebiet relativ niedriger Strömungsgeschwindigkeiten im Nahfeld des Nachlaufs begrenzt. Weiter als 2,8 Rotordurchmesser stromabwärts wird der Nachlaufströmung wieder Energie zugeführt durch das Eindringen derjenigen Strömung mit relativ turbulenter kinetischer Energie vom Rand ins Innere der Nachlaufströmung. Bis zu 5-5,5 Rotordurchmesser ist diejenige Strömung erhöhter turbulenter kinetischer Energie bis ins Zentrum der Nachlaufströmung eingedrungen und obwohl sich 10 Rotordurchmesser stromabwärts wieder die Windgeschwindigkeiten von stromaufwärts eingestellt hat, ist die turbulente kinetische Energie dort zwei Größenordnungen grösser als stromaufwärts der Windturbine. Simultane

Messungen des Nahfeldes der Nachlaufströmung (von einer Turbine) und des Fernfeldes der Nachlaufströmung (von einer zweiten Turbine) bestätigen die charakteristisch unterschiedlichen Eigenschaften des Nah- und Fernfeldes der Nachlaufströmung. In komplexem Gelände erstreckt sich das Nahfeld der Nachlaufströmung über bis zu zwei Rotordurchmesser. Bis zu 2,7 Rotordurchmesser stromabwärts ist die Strömung mit erhöhter turbulenter kinetischer Energie bis ins Zentrum der Nachlaufströmung eingedrungen und die turbulente kinetische Energie ist dort drei Grössenordnungen grösser als stromaufwärts der Windturbine. Die Messungen in der Nachlaufströmung wurden unter neutralen und instabilen atmosphärischen Bedingungen gemacht. Schliesslich wurde die Reynolds-Dekomposition verwendet, um die Struktur der Turbulenz in der Freistromung und in der Nachlaufströmung in der Oberflächenschicht zu zeigen.

Zusammenfassend erlaubt die instrumentierte Drohne räumlich sowie zeitlich hochaufgelöste Messungen der höchst dreidimensionalen Struktur und Wechselwirkungen in der Nachlaufströmung einer Windturbine. Dies bietet die Möglichkeit Spitzenwirbel und die Entwicklung des Nachlaufs der Maschinengondel zu erfassen, was früher nicht möglich war. Mit dieser innovativen Methode wurde zum ersten Mal die Entwicklung der Nachlaufströmung einer Windturbine in Originalgrösse in flachem sowie unregelmässigem Gelände in hoher Auflösung gemessen. Die drohnenbasierten Windmessungen wurden ebenfalls erfolgreich eingesetzt, um das ETH-Modell von Nachlaufströmungen und das IWTM-Modell zu validieren, die an der ETH Zürich entwickelt werden.

TABLE OF CONTENTS

ACKNOWLEDGMENT.....	I
ABSTRACT.....	V
ZUSAMMENFASSUNG.....	VIII
TABLE OF CONTENTS.....	X
NOMENCLATURE.....	XIV
1 INTRODUCTION	1
1.1 Motivation.....	1
1.2 State of the Art	7
1.3 Measurement Approach	15
1.4 Research Objectives	16
1.5 Thesis Outline.....	17
2 MEASUREMENT SYSTEM	19
2.1 Fast Response Aerodynamic Probe (FRAP).....	19
2.1.1 Sensor Packaging.....	19
2.1.2 Probe Design	20
2.1.3 Fast Response Data Acquisition Board (FRAQ).....	21
2.1.4 Static Calibration	24
2.1.5 Aero Calibration	26
2.1.6 Dynamic Calibration.....	30
2.2 Onboard Instrumentation	32
2.2.1 Inertial Measurement Unit (Attitude Sensor).....	33
2.2.2 Static pressure and temperature sensor.....	34
2.2.3 Magnetic Sensor (Drone Sideslip Angle).....	36
2.2.4 AttoPilot Current and Voltage Sensor.....	38
2.2.5 Optical Trigger System.....	38
2.3 Instrumented Drone.	41
2.3.1 1st Generation Drone: Funjet... ..	41
2.3.2 2nd Generation Drone: WindFlyer.....	41

2.4 WindFlyer Drone.....	43
2.4.1 Aerodynamic Analysis.....	43
2.4.2 Structural Analysis.....	49
2.4.3 Wind Tunnel Testing of WindFlyer.....	56
2.4.4 Assessment of FRAP System in Wind Tunnel.....	88
2.4.5 FRAP at Low Airspeeds.....	90
2.4.6 Propeller Selection.....	59
2.5 Other Accessories.....	68
2.5.1 Jig for IMU Initialization.....	68
2.5.2 Mechanical Frame.....	68
2.6 Paparazzi Autopilot System.....	70
3 MEASUREMENT METHODOLOGY.....	74
3.1 Wind Vector Calculation	74
3.2 Data Processing	76
3.2.1 Coordinate Axis Convention.....	79
3.2.2 Short-time Fourier Transform.....	79
3.2.3 Phase Locking.....	85
3.3 Uncertainty in Wind Measurement System.....	88
3.4 Flight Permissions.....	92
4 MEASUREMENTS IN FLAT TERRAIN.....	93
4.1 Measurement Site.....	93
4.2 Measurements in Freestream.....	95
4.3 Wake Evolution.....	96
4.3.1 Turbulent Kinetic Energy in Near-Wake.....	103
4.4 Freestream versus Far-Wake.....	106
4.5 Multiple Wakes.....	108
4.6 Comparison of Measurements to Predictions of Wake Flow.....	110
4.7 Summary.....	111
5 MEASUREMENTS IN COMPLEX TERRAIN.....	113
5.1 Measurement Site.....	113

5.2 Drone Measurements Versus LIDAR, SCADA and CFD.....	115
5.3 Flow Profile Around a Wind Turbine.....	119
5.4 Pressure Variations Across a Wind Turbine Rotor.....	121
5.5 Wind Speed and Turbulent Kinetic Energy in Wake.	122
5.6 Upstream and Wake Spectra.....	128
5.7 Tip Vortices.....	131
5.8 Wake Contour.....	137
4.8.1 Turbulent Kinetic Energy Contour in Vertical Plane.....	139
4.8.2 Double Wake.....	141
5.9 Summary.....	143
6 COMPLEX TERRAIN VERSUS FLAT TERRAIN.....	145
6.1 Measurement Sites.....	145
6.2 Wake evolution: Complex versus flat terrain.....	146
6.3 Comparison of turbulence structure in flat and complex terrains.....	149
6.4 Degree of Anisotropy.....	153
6.5 Friction Velocity.....	154
6.6 Integral Length and Time Scales.....	156
6.7 Summary.....	157
7 EFFECTS OF ATMOSPHERIC STABILITY.....	159
7.1 Measurement Site	159
7.2 Wake Evolution	160
7.3 Wake Profile	166
7.4 Dissipation Rate of Turbulent Kinetic Energy.....	170
7.5 Phase Locking.....	172
7.6 Wake profile: Measurements versus ETH Wake Model.....	174
7.7 Summary.....	175
8 SUMMARY AND CONCLUDING REMARKS.....	176
8.1 Future Suggestions	179
REFERENCE	181
APPENDIX.....	190

A: STFT, WT and MEM.....	190
B: Propeller Theory.....	203
C: FRAP Aero-Calibration.....	208
D: Field Operating Procedure.....	209

NOMENCLATURE

A	reference area
c	chord
C_L	lift coefficient
C_D	drag coefficient
C_{T0}	static thrust coefficient
C_θ	pitch angle coefficient
C_ψ	yaw angle coefficient
C_o	total pressure
C_q	dynamic pressure
$C_{L\alpha}, C_{m\alpha}, C_{n\beta},$ $C_{l\beta}, C_{lp}, C_{Lq}, C_{lr}$	longitudinal stability derivatives
D	diameter
$E_{battery}$	capacity of lipo battery
f, F	frequency
F_i	force (i=x-, y-, z-direction)
F_s	sampling frequency
H	propeller pitch
J	advance ratio
K	polynomial coefficient
L, L₀	length
Ma	Mach number
N	rotational speed
p_v	vortex pitch
p, P, P₀	pressure
$P_{average}$	power drawn from lipo battery
r	distance of a point from rotor axis
R	rotor radius
Re	Reynolds number
T	thrust
t, t', t₀, t₁	time
u, v, w	unfiltered velocity components, u along streamwise and w is in vertical direction
u', v', w'	resolved stochastic fluctuations
u_*	friction velocity
u_2, V	wind speed
V_a, V_f	FRAP airspeed
V_0	SCADA 10-minute average wind speed

V_z	vertical wind speed
$x(t)$	signal time series
X_{np}, X_{cg}	distance of neutral point and centre of gravity from leading edge
X	longitudinal axis (along rotor axis)
Y	lateral axis
Z	vertical axis
Z_{HH}	hub height
σ_x^2	variance of $x(t)$
σ	standard deviation
$\sigma_{u'}, \sigma_{v'}, \sigma_{w'}$	standard deviation of velocity fluctuations
β	blade angle
Δf	frequency resolution
Δt	temporal resolution
$\omega^*(t)$	window function
η	Klomogorov microscale
$\eta_{propeller}$	propeller efficiency
η_{motor}	motor efficiency
ν	kinematic viscosity
ρ	density
ε	dissipation rate of turbulent kinetic energy
ε_i	principal strains in direction ($i=1, 2$ and 3).
θ	pitch angle
θ_{el}	rotation angle
Ψ	yaw angle
λ	tip speed ratio
ν'	Poisson's ratio

ABBREVIATIONS

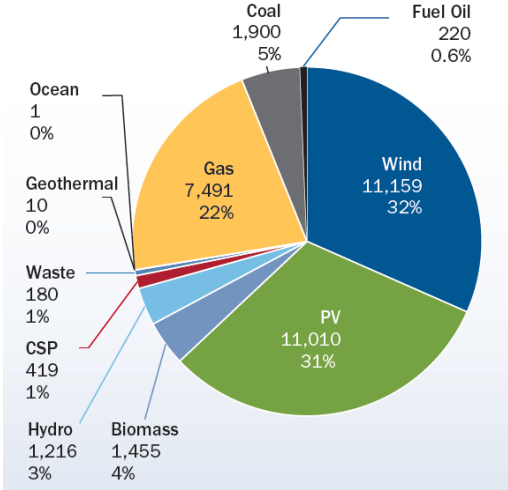
7S-FRAP	7-Sensor Fast Response Aerodynamic Probe
ADC	Analog to Digital Converter
AEY	Annual Energy Yield
AGL	Above Ground Level
AoA	Angle of Attack
AR	Aspect Ratio
AVL	Antenna Vortex Lattice
BPM	Blade Position Marker
CAD	Computer Aided Design
CAP	Composite Analysis Program
CFD	Computational Fluid Dynamics
CG	Center of Gravity
DA	Degree of Anisotropy
DAQ	Data Acquisition
ECN	Energy research Centre of the Netherlands
EGNOS	European Geostationary Navigation Overlay Service
EPP	Expanded Polypropylene
ETH	Eidgenössische Technische Hochschule
FFT	Fast Fourier Transform
FRAP	Fast Response Aerodynamic Probe
GCS	Ground Control Station
GNU	GNU's Not Unix
GPS	Global Positioning System
GUI	Graphical User Interface
GUM	Guide to Uncertainty in Measurements
HH	Hub Height
ICAO	International Civil Aviation Organization
IEA	International Energy Agency
IFD	Institute for Fluidynamics
IMU	Inertial Measurement Unit
LC	Load Cell
LDM	Laser Distance Meter
LEC	Laboratory for Energy Conversion
LIDAR	Light Detection and Ranging
MEM	Maximum Entropy Method
MEXICO	Model Rotor Experiments under Controlled Conditions
MW	Megawatt
NACA	National Advisory Committee of Aeronautics
NASA	National Aeronautics and Space Administration
NREL	National Renewable Energy Laboratory

PID	Proportional Integral Derivative
PIV	Particle Image Velocimetry
PSD	Power Spectral Density
pdf	Probability Density Function
RANS	Reynolds Averaged Navier Stokes
RC	Radio Controlled
RH	Relative Humidity
RPM	Revolution Per Minute
SCADA	Supervisory Control and Data Acquisition
SD	Secure Digital
SODAR	Sonic Detection and Ranging
SM	Static Margin
STFT	Short Time Fourier Transform
TKE	Turbulent Kinetic Energy
TSR	Tip Speed Ratio
UAV	Unmanned Aerial Vehicle
UTM	Universal Transverse Mercator
WAAS	Wide Area Augmentation System
WRF	Weather Research and Forecasting
WT	Wavelet Transform
WTG	Wind Turbine Group

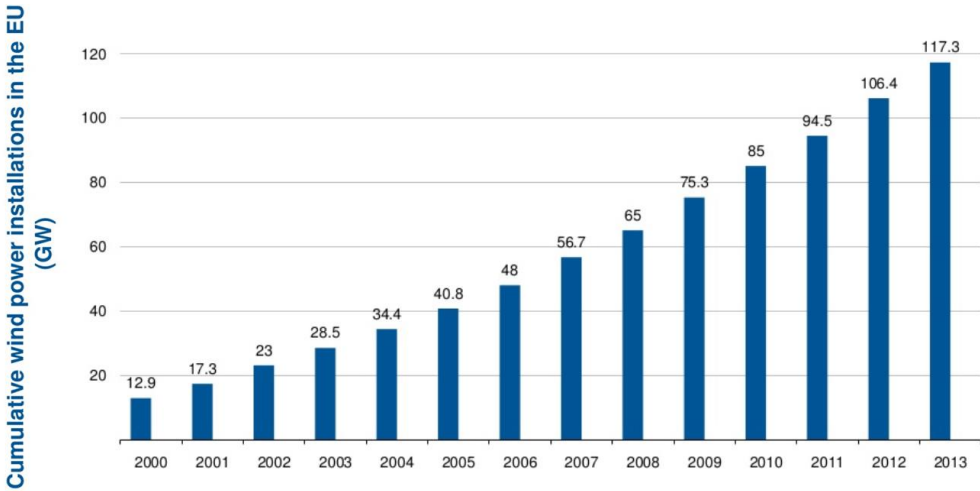
1 MEASUREMENT SYSTEM

1.1 Motivation

Renewable energy sources have attracted a lot of attention and investment in this recent decade. Globally, wind energy is growing at double-digit rate annually [1]. According to the statistics released by GWEC, wind capacity increased by 12.5% in 2013. In Europe, wind power installations are rising rapidly with wind contributing to 32% of the total new installations capacity, Figure 1. The power sector in Europe is also slowly moving away from fossil fuels, as this technology continues to decommission more than their installation. IEA projection shows that the wind energy has potential to reach a share of 18% of the world's electricity production by 2050 compared to the current 2.6% [2].



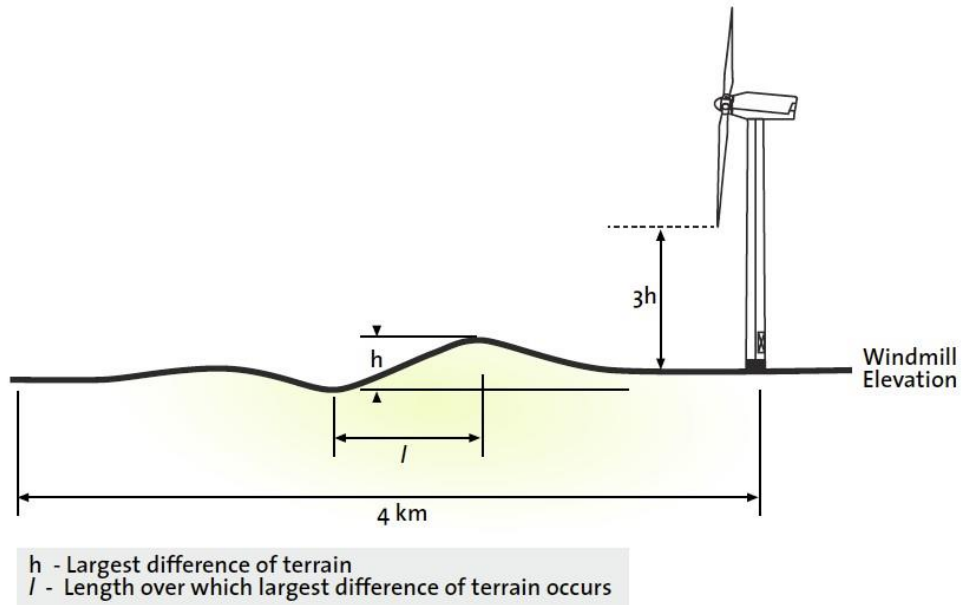
(a)



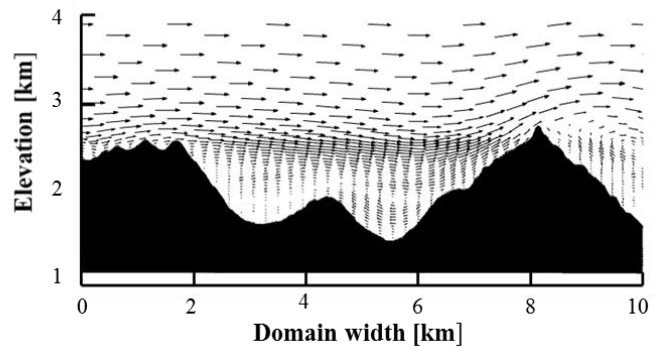
(b)

Figure 1. Share of new power capacity installations in EU in 2013 [1].

Public concern increased dramatically after the Fukushima nuclear disaster, which resulted in an increased pressure on governments to invest in alternative energy sources. In addition, concerns over the growing evidence linking global carbon emissions to permanent, irreversible climate change has accelerated this search for alternative energy sources. Wind energy proved to be one of the promising and reliable alternatives, mainly due to its cost competitiveness resulting from rapid technological development over the past decade and due to the fact that the fuel cost over the total lifetime of a wind turbine is zero. The rapid growth in wind power sector provides a strong motivation to improving wind energy technology to maximize annual energy yield and to minimize the operational and maintenance cost of wind farms. This can only be achieved through a proper understanding of the flow field around a wind farm. Presently there is a mismatch between the expected/predicted annual energy yield and the actual annual energy yield, suggesting the risk involved in development of large financially viable wind farm projects. The primary reason for this mismatch is the incomplete understanding of flow behaviour in two important areas - one is the behaviour of atmospheric boundary layer close to ground in complex terrain and the second is the wind turbine wake behavior in different terrains including its interactions with other downstream turbines. For full wake conditions, the power losses at downstream turbines can be as high as 30-40% and when averaged over different wind directions the losses are still 5-8% ([3]). Also, the wakes are known to increase the fatigue loads on wind turbines by up to 80% [3]. Thus a wind turbine's wake evolution and dissipation in different terrains, including its interaction with other wind turbines wakes in a wind farm is an important field of research. As the land area - with moderate or high wind characteristics - available for wind farm development is limited, so the developers want to optimize the placement of wind turbines in a wind farm to maximize the annual energy yield. This becomes particularly challenging if the wind farm is located in a complex terrain.



(a)



(b)

Figure 2. (a) Definition of complex terrain [4], (b) Wind flow field in a complex terrain simulated with LEC's advanced wind simulation tool [92].

The definition of complex terrain (from [4]) is, a terrain with elevation changes over the area within 4 km from the wind turbine that are greater than one third of the minimum height from the ground to the wind turbine's rotor. This definition is illustrated in Figure 2. As the wind energy market matures, flat sites with good winds are becoming increasingly scarce, thus sites in complex terrain with moderate winds are increasingly of interest. Such sites, which were previously considered suboptimal for investment, have gained prominence in recent years [5]. However, wind resource assessment in complex terrain is challenging, due to the lack of suitable measurement data and due to the difficulty involved

in accurate modelling of flow over complex terrains; thus there are higher uncertainties in wind resource estimates in complex terrain [5]. Furthermore the loads on wind turbines located in complex terrain are higher due to higher wind shear and increased levels of turbulence, thus resulting in a reduced lifetime of wind turbine components [6]. Micrositing of wind turbines in complex terrain is further complicated by the fact that the flow downstream of a wind turbine is highly unsteady and three-dimensional.

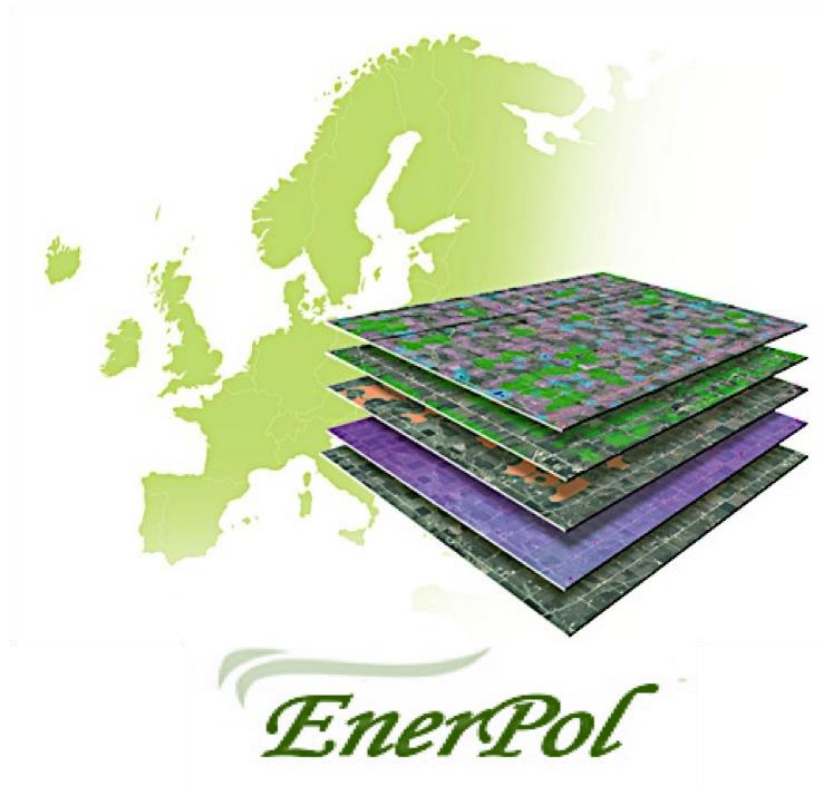
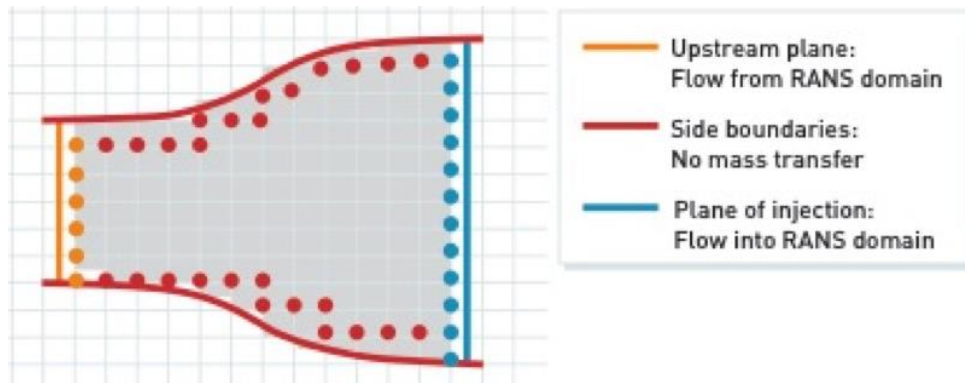


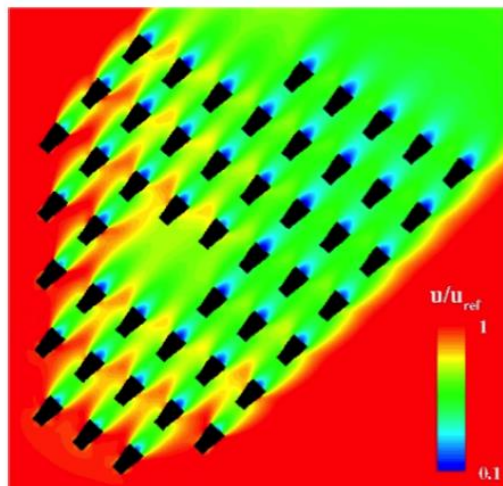
Figure 3. Enerpol - an integrated GIS based tool [7].

To deal with this challenge, an integrated GIS based tool called Enerpol (Figure 3) was developed at ETH Zurich for assessment of power systems and infrastructure, finance, and policy that enables multi-criteria decision making in those areas. One of its tasks is to identify and map the potential wind power sites based on profitability (eligible areas) across an entire country. Enerpol takes into account all the associated variables including anthropological, geographical, climatic, regulatory and financial, and contains models for power system infrastructure, weather, logistics, economics and risk. Geospatially referenced data within the framework of a Geographic Information System are used to identify all eligible areas, for these identified sites the best-suited wind turbines are determined from the

data base and based on the size of wind farms, the annual energy yield is then predicted; and the economic benefits and risks of developing the wind farms are then assessed in detail. Thus, this integrated approach takes into account all the geographical constraints on land like forests, urban areas, water bodies, transmission lines, transportation lines and even the environmental related constraints like noise and visibility, to simultaneously assess the economic benefits and risks involved in developing a wind farm. The first step for choosing potential areas involves use of a numerical weather prediction tool, Weather Research and Forecasting model (WRF) – a mesoscale numerical weather prediction model [111] - that is used for simulating the transient wind flow conditions for more than a year over an entire landmass. Then, an in-house micro-siting tool based on MULTI3 [8] is used for optimizing the locations of wind turbines at these potential sites and to analyze them in detail.



(a)



(b)

Figure 4. (a) Immersed Wind Turbine Model (IWTM) in ETH micro-siting tool [8], (b) Hub height wind velocity contour plot of multiple wind turbines wake interactions simulated using IWTM at

Lillgrund wind farm [8].

The present work is largely motivated by the need to provide measurement data for this micrositing tool and for a wake model that were under development at ETH Zurich. More details of the tools and wake models under development at ETH Zurich can be found elsewhere [8, 11], but a few salient features are provided here. In this micrositing tool, the wind turbines are modelled using an Immersed Wind Turbine Model (IWTM), Figure 4 a. The model is a streamtube, whose shape is based on the turbine's operating point. The inflow and outflow boundaries are one-diameter upstream and one-diameter downstream of the wind turbine's rotor plane (Figure 4 a). Thus, measurements at these boundary planes and along the side boundaries are of interest in the development of the immersed model. The IWTM is based on the in-house CFD code 'MULTI3', which is a second order Reynolds-Averaged Navier-Stokes (RANS) solver based on an explicit, finite-volume node-based Lax-Wendroff method and using the $k-\omega$ turbulence model [95]. The IWTM is a stream tube that models both the energy extraction and flow blockage of a wind turbine. The near-wake is modelled by the IWTM and the far-wake is resolved on the computational grid of the RANS solver. The immersed model allows for the simulation of multiple wake interactions and the effect of topography on the evolution of the far wake – for example Figure 4 b shows the hub height wind velocity contour plot of multiple wind turbines wake interactions simulated using IWTM at Lillgrund wind farm [8]. Thus, the immersed wind turbine model provides an alternative to the actuator disk model. The ETH wake model [11] is a semi-empirical, axisymmetric model that uses free shear flow theory to detail the evolution of the axial wind speed that is observed in sub-scale model experiments.

Thus, an innovative measurement system consisting of a drone instrumented with a fast response aerodynamic probe was developed to provide high resolution flow field measurements around full scale wind turbines. This is aimed at filling the gap in terms of lacking high resolution full-scale wind turbine measurements and to support the in-house development of advanced wind simulation tools and wake models.

1.2 State of The Art

Detailed upstream and wake measurements are needed to understand the flow behavior, as it helps in developing and validating simplified wake models [9-21] that can approximate the wake qualities. These wake models can model the velocity deficit, wake recovery and wake interactions downstream with certain assumptions, and can be used to quickly predict the annual energy yield of a wind farm. The wake models are useful in planning, design and operation of windfarms. The wake is typically divided into near- and far-wake [22]. The near wake is located immediately downstream of the rotor and the flow in this region is characterized by the signature of the wind turbine rotor. The far-wake is located downstream of the near-wake and is modelled in most cases with an axial symmetry assumption of the flow behaviour [22]. Ainslie [9] estimates that the maximum velocity deficit is attained after $1D-2D$ downstream, and Schepers [21] uses $2.25 D$ as the distance where the wake is fully expanded. Two of the most comprehensive sets of experiments undertaken to understand the flow physics and to enhance aerodynamics of subcomponent models were the NREL's Unsteady Aerodynamic Experiment [23] and the ECN's MEXICO project [24,25]. As there still remain several discrepancies between the predictions and observations, there is a need for full-scale experimental observations in order to validate and calibrate the prediction methods. While wind tunnel and water tunnel tests provide an environment to conduct detailed parametric studies under carefully controlled conditions, it is not possible to match all relevant non-dimensional parameters. As the Reynolds number based on turbine diameter is typically of the order 10^4-10^5 in wind and water tunnel experiments which is at least one order of magnitude smaller than in full scale conditions, this may be a concern regarding the widespread applicability of sub-scale experiments. Indeed the scale of the Reynolds number is relevant in physical process such as turbulent mixing, the entrainment of kinetic energy, the evolution and breakdown of tip vortices, etc, all of which are features of wakes in wind farms. In the past, only few measurements in the wake of a full-scale wind turbine have been reported.

Hogstrom et al. [26] attempted to map the wake behind a 2 MW wind turbine in flat terrain using three different measurement techniques - high resolution sodar, metrological mast and tala kite. While the field measured turbulence intensities in the wake were found to be twice larger than those measured in wind tunnels, the velocity deficits measured in wind tunnels were higher. Sodar was shown to be a powerful technique to get the wind profiles and turbulence spectra at several distances in the

range $2D$ – $3.6D$ from the turbine. Meteorological masts though at mercy of wind direction, were used to field calibrate the tala kites and a good wake structure was obtained from them. Finally, tala kites were used to obtain the centre line wake deficit and the longitudinal turbulence intensity at distances of up to $10.5D$, and they were found to be in good agreement with the wind tunnel data. Both sodar and mast measured spectra showed higher turbulence levels in the wake for frequencies above 0.004 Hz and decreased energy at lower frequencies. Simple analytical expressions for the estimation of turbulent kinetic energy and its dissipation rate in wind-turbine wakes were proposed by Crespo et al. [27].

In another study [28], a radiosonde suspended from a tethered balloon - calibrated using a met mast - was used to measure the hub height wind speed at four different downstream distances of $3D$, $5D$, $7D$ and $9D$ on a cluster of three 2.5 MW wind turbines. These measurements were designed to determine the rate of decay of the wake velocity deficit with down-wind distance under various meteorological conditions. At high wind speeds, a wake deficit of 50% was reported at $3D$ but nothing significant was observed at $5D/7D$. A short time period data set from tethered sonde showed poor spatial correlation with met mast tower and considerable scatter was observed even on 10 minute average values. Measurements were also made down-wind with the turbine off to determine the magnitude of terrain-induced variations in wind speed. In another study at MOD-2 [29], the authors used kite anemometry to measure and characterize the wind flow in the wake of a wind turbine at hub height. Wind measurements were taken upstream at $2D$ and downstream at $3D$, $5D$, $7D$ and $9D$ in WTGs 1 and 3 under operating and non-operating conditions. The authors reported wake deficits of 15 - 18 per cent at $9D$, and 30 - 40 per cent between $3D$ - $5D$ using single level measurements. With increase in ambient turbulence, the wake was observed to be dissipating more rapidly with the deficits recording 15 - 20 per cent at $7D$ and close to zero at $9D$. It was noted that most of the wake measurements were made under stable night-time flow. At this same site, Elliott et al. [30] collected wind data using nine meteorological towers and they were analyzed to characterize the wind flow over the site both in the absence and presence of wind turbine wakes. The arrangement of the towers with respect to the turbines permitted observations of the wake characteristics at various distances ranging from $2D$ - $10D$. At a height of 32 m above ground level, the impacts on lateral and longitudinal turbine spacing were investigated. The relationship between velocity deficit and downwind distance was surprisingly found to be linear with the average maximum deficits ranging from 34% at $2D$ to 7% at $10D$. Terrain and trees were found to have significant impact on the measured mean wind

speeds and turbulence intensities compared to grass lands. Terrain and tree induced effects were found to cause up to 30% reduction in mean wind speeds and 150% increase in turbulence intensities. In the near- and far-wake, the maximum velocity deficits were found to occur at or near the wake centerline, but the maximum turbulence intensities were measured at the outer periphery of a wake. Velocity deficits in the turbine wake were also examined as a function of the ambient wind speed and turbulence intensity at several downwind distances ranging from $1.9D$ - $8.4D$.

In yet another study [31], the energy yields of wind turbine clusters have been calculated to assess problems, costs and feasibility involved with constructing large offshore wind farm arrays. The author identifies the capabilities and limitations of the various predictive techniques for cluster performance and examines the role played by experimental studies in boosting the confidence of such estimates. According to the authors, with suitable choice of turbine spacing, the energy losses from cluster can be kept below 20-25%. The procedures are illustrated using the specific example of the Nibe cluster, where wake measurements are currently being made, and the annual energy loss for this cluster is estimated at 3%. It was concluded that existing modelling techniques, both mathematical and experimental, require improvement and the authors also highlight the need for a more detailed understanding of the mechanisms of wake generation and decay. The wake and its associated structural fatigue were experimentally investigated by Hassan [32], to understand the structural impacts on a turbine operating in the wake of another turbine. It was reported by the authors that the operation in a wake may increase the fatigue damage rate by over 170% and that extreme loads increase by 50%. Such a situation is inevitable inside large wind farms and it appears that important implications may result in terms of both reduction of fatigue life and increase in extreme loads. It should be noted here that deep within a wind farm cluster much higher turbulence intensities can be expected if close attention is not paid to array spacings.

The near-wake turbulent structure downstream of a medium-sized, horizontal axis wind turbine, located in a complex terrain, obtained under strong wind conditions using two met masts is presented in [33]. The turbulent energy increase in the interior of wake relative to the upstream values and the loss of energy at low frequencies and gain of energy at high frequencies obtained using spectral analysis were reported. For all wind speeds, increased turbulent levels were only observed near the blade tips and possibly around the hub height, no turbulent energy increase was measured in the remaining part of the wake. The authors noted that the turbulent field in wake strongly depends on the incident wind speed. Published results demonstrate a high frequency energy enhancement

linked to the degeneration of tip vortices and/or to shear generated turbulence at the wake boundaries. Another study [34] at the same complex terrain, using met mast and sodar, presented the terrain topographical effects on upstream wind and wake flow. Complex topography affects upstream wind flow and results in upstream profiles exhibiting a wind speed maximum below hub-height in response to the flow acceleration over the wind park's hill crest. A 30% mean wake centerline deficit was measured at 1.1D downstream, and was observed to vary inversely with wind speed. At 1D downstream, the wake centerline was above hub height and was attributed to the wind flow characteristics over the wind park. The obtained results reveal a nonlinear interaction of the near wake with the turbine tower shadowing, while cross-wind wake profiles indicate a potential core structure.

A set of experiments designed to investigate the performance and wake behaviour of a 17 m diameter horizontal-axis wind turbine in atmospheric conditions were reported in [35]. The spectral characteristic of the wind flow over this site was found to be that of a rural terrain. The velocity deficit measured in wake centre-line was 0.74 at 1D and 0.44 at 2.5D. The velocity deficit profile at 1D downstream was found to be Gaussian, indicating the rapid mixing promoted by the high ambient turbulence intensity. The response of the rotor to wind-speed fluctuations was reported to be consistent with theoretical estimates. In another study, acoustic sounder was used to measure in the wake of a 50 kW full-scale wind turbine [36]. It was reported from measurements that the wind velocity deficit, and turbulence intensity, take greater values at the centre of the wake than its boundaries. The wind speed and turbulence intensity profiles were noted to follow the expected theoretical behaviour at every single location in the wake. Also higher values of the temperature structure parameter were observed at the centre of the wake than at its edges. The u-component power spectra levels were observed to be higher at the high frequencies around the central parts of the wake while at its boundaries they are higher at the lower frequency portion of the spectrum. Comparison of wake model simulations with offshore wind turbine wake profiles measured using Sodar was reported by Barthelmie et al. [37] for predicting wind speed in a wake. The evaluation was based on six experiments - where free-stream and wake wind speed profiles were measured at varying distances between 1.7D and 7.4D - at a small offshore wind farm. Overall, it was concluded that it is not possible to establish any of the models as having individually superior performance with respect to the measurements.

A European Commission funded UpWind project to evaluate the performance of wind farm models and CFD models in terms of how

accurately they represent wake losses when compared with measurements from the Horns Rev offshore wind farm is presented by Barthelmie et al. [38]. The project aims to improve modelling of flow for large wind farms in order to optimize wind farm layouts to reduce power losses due to wakes and loads. Reducing wake losses, or even to reduce uncertainties in predicting power losses from wakes, contributes to cost reduction. The study indicates that wind farm models require modification to reduce under-prediction of wake losses while CFD models typically over-predict wake losses. These are for moderate wind speeds and narrow directional sectors focused along the rows of turbines, where power losses due to wakes are maximized. For the narrowest wind direction sectors ($\pm 1^\circ$) and the smallest turbine spacing ($7D$), the analysis focuses on the centre of the wake where the power at the second and subsequent turbines is about 60% of the freestream. Another research article from European Union funded UpWind project - which focuses on improving models of flow within and downwind of large wind farms - emphasizes special issues relating to the development of large wind farms both in complex terrain and in offshore [39]. The authors discuss modelling the behaviour of wind turbine wakes in order to improve power output predictions and present a preliminary comparison of different wake models in a number of different scenarios.

In addition to direct measurements, flow visualisation experiments are employed provide qualitative information of the flow field behind a wind turbine rotor [40, 41]. The tip vortex cores can be made visible with smoke and its path downstream can be traced to map the near-wake boundary [22]. The tip vortices after few revolutions are expected to catch up and merge into one. During the full scale experiment of NREL at the NASA-Ames wind tunnel [41], the only flow visualisation performed was with smoke injected from the blade tip but at low thrust coefficient. The visualisation of flow over a rotor blade mainly involves tufts. In this process, attempts have been made to correlate the flow pattern visualised using tufts with the near wake flow characteristics, to get a better understanding of how to interpret velocity signals. The root vortex is weaker than the tip vortex and thus hard to visualize with smoke. Also getting experimental data on the root vortex is difficult but important for yaw conditions. Lidars have been used in recent years for site assessment as they provide a general picture of the wind speed distribution across a given area. Measurements in the wake of a full scale wind turbine with Lidar [42-45] have been made, but they have limited spatial resolution and also provide limited details on the unsteady characteristics of the wake.

The unsteady three-dimensional structure of the wake has also been examined in wind tunnels with sub-scale models. A wind tunnel study of the flow downstream of a small horizontal axis, three constant-pitch

bladed wind turbine using particle image velocimetry (PIV) is discussed in [46]. The author employs a phase-locking technique to obtain the flow field in the rotating frame of reference. The post-processing of PIV images reveals the three dimensional velocity fields downstream of the rotor. In addition to PIV, hot wire measurements were also employed in the near-wake at different radial and axial distances. The results show that the tip vortices issued from the blade tips are not located on a cylindrical surface as it was assumed in linear propeller theory; rather they expand in radial direction and thus increase the diameter of flow tube. The analyses of the obtained results show the induced velocities due to tip vortices. It was reported that the individual presence of blades in near-wake flow disappears beyond a distance of one rotor; however the tip vortices stay present. In another wind tunnel study [47], a 1:300 scale model of a 5 MW wind turbine was tested in a uniform low turbulence flow (offshore conditions) to compare the model turbine performance with the theoretical design case which is based on blade-element theory for low Reynolds number blade aerodynamics. Velocity measurements in the wake suggest a transition from near to far wake at a downstream distance of 4D. A tip speed ratio (TSR) of 6 yielded a thrust coefficient of 0.52, which is within 5% of the predicted value of the theoretical design case. At 10D downstream, the turbulence intensities are still twice larger than in the undisturbed boundary layer. Time averaged flow fields and lateral profiles of the vertical velocity illustrate the characteristic swirl generated by the blade rotation, which persists until about a downstream distance of 7D. An experimental investigation into the properties of the vortex wake behind a model scale two bladed wind turbine operating at a tip speed ratio of 3-8 was carried out using Particle Image Velocimetry (PIV) [48]. Measurements of wake velocity and vorticity were reported up to 2.9D. The study focused on areas where current wake modelling requires attention; in particular, the strength and geometry of the trailing tip vortex spiral, vital for the prediction of fluid loading on the rotor blades. Good agreement was observed between experimental and numerical data on wake structures, especially the shape of the wake boundary, including features such as wake expansion and contraction, despite the difference in Reynolds number.

Due to the variability in wind direction a wind turbine is usually facing the wind at a yaw angle. Yawed inflow leads to a lower efficiency and to a periodic variation in the angle of attack on the blades and therefore to fatigue. The angle of the wake with the rotor axis is larger than the yaw angle and the resulting skewed wake is not symmetric with respect to the turbine axis. Skewed wakes have the downwind side of the rotor closer to the wake centerline than the upwind side of the rotor.

Medici [49] shows that a yawed turbine deflects the wake to the other side, showing the potential of controlling the wake position by yawing the turbine. This concept, Controlling Wind, is investigated at ECN to increase power output of a wind farm.

The use of manned aircraft and drones to measure flow properties in the Earth's boundary layer is well established in atmospheric sciences. This approach was used successfully to characterise atmospheric turbulence at different altitudes [50-53, 116, 117]. Rhyne et al. [50] measured the power spectra of atmospheric turbulence in severe storms and cumulus clouds. The low altitude power spectra of atmospheric turbulence measured on a Canberra aircraft in temperate and sub-tropical conditions was published by Burns [51]. In another study, the atmospheric boundary layer was probed with aircraft to reveal the mesoscale fluctuations in velocity (spectral composition) over land and sea [52]. Lovejoy et al. [53] used aircraft measurements to detail the anisotropic scaling of turbulence. Smedman et al. [116] employed airborne measurements in a near-neutral marine boundary layer to obtain the dissipation rate of turbulent kinetic energy from atmospheric turbulence spectra of wind measured in horizontal flight legs and at different heights. The measurements showed that large scale eddies were formed in a strong shear zone at the top of the boundary layer at about 1200 m and brought down to the region near the surface by the pressure transport term. Elston et al. [117] employed small unmanned aircraft to make in situ wind and thermodynamic measurements, and details the choice of sensors and algorithms for different platforms to obtain a desired measurement accuracy and resolution.

The fundamental basis of airborne measurements is Taylor's hypothesis that frozen turbulence is advected at wind speed. According to Taylor's hypothesis, turbulence is considered frozen as it advects downstream and thus the turbulent fluctuations at a point are caused by the advection of the frozen flow field past the point [88], Figure 5.

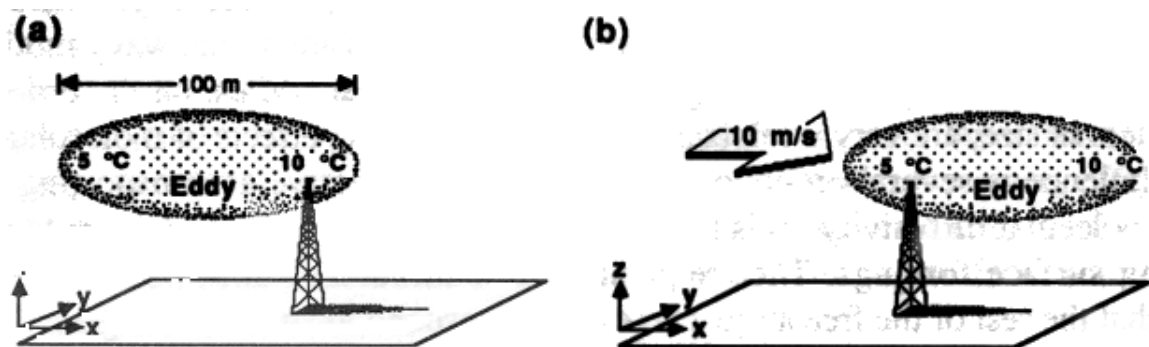


Figure 5. Taylors frozen flow hypothesis [88].

The present work extends the aircraft approach in atmospheric sciences to drones in wind energy. Reference [54] validates the use of Taylor's hypothesis in wind energy applications. While the present authors [55, 56] and others [57, 58] have reported the use of drones to make measurements in wind farms, the present work is the first to detail the turbulent characteristics of the wake and to present the detailed flow behavior downstream of a wind turbine rotor. Giebel et al. [57] provides an overview of currently available sensors, and details the preliminary study carried out by Risø National Laboratory using autonomous aerial vehicles for wind power meteorology. Wildmann et al. [58] argues the instrumented drone as a valuable tool in wind energy research. Comparisons of the turbulent kinetic energy measured in flight legs upstream and downstream of a wind turbine at different distances were also reported.

In the present work, an instrumented drone is used to detail the flow field around a multi-MW wind turbine located in both flat and complex terrains with high resolution. As mentioned earlier, a detailed knowledge of the flow field upstream of a wind turbine and in the wake is needed as it affects the energy production and the fatigue life of a wind turbine. Thus a drone based wind measurement system was developed at ETH Zurich to detail the flow field around a full scale wind turbine (Kocer et al. [55] and Mansour et al. [56]). This measurement approach provides insights into the impact of different terrains on the wake's turbulence evolution characteristics, and is aimed at filling the gap in terms of lacking high resolution full-scale wind turbine measurements and to support the in-house development of advanced wind simulation tools and wake models.

1.3 Measurement Approach

A novel measurement system consisting of a fast response aerodynamic probe and an autonomous, pusher propeller drone is introduced that is employed in wind farms to measure the flow field in upstream and in the wake of a full-scale wind turbine. The FRAP probe is custom built and is the result of years of fast response probe technology development at ETH Zurich. This FRAP probe directly measures the three-dimensional wind velocity vector in the drone's frame of reference and its data is logged in an onboard SD card. To transform this FRAP measured wind velocity vector into the Earth's frame of reference, the drone is instrumented with a suite of sensors including an IMU, an absolute pressure sensor, a magnetometer, a GPS receiver, and a temperature and humidity sensor. The drone's onboard sensors communicate in real-time with the Ground Control Station (a laptop equipped with paparazzi software) through a two-way modem to transmit data that are logged in a log file in GCS. In parallel, the drone's sensors data are also logged in the on-board SD card along with FRAP. An optical trigger system – that tracks and logs the position of the wind turbine blades during drone based wake measurements – was designed in-house for phase locking the FRAP measurement data. The optical trigger transmits blade position data to the Ground Control Station, and is also logged in the same log file. The schematic of measurement system is illustrated in Figure 6.

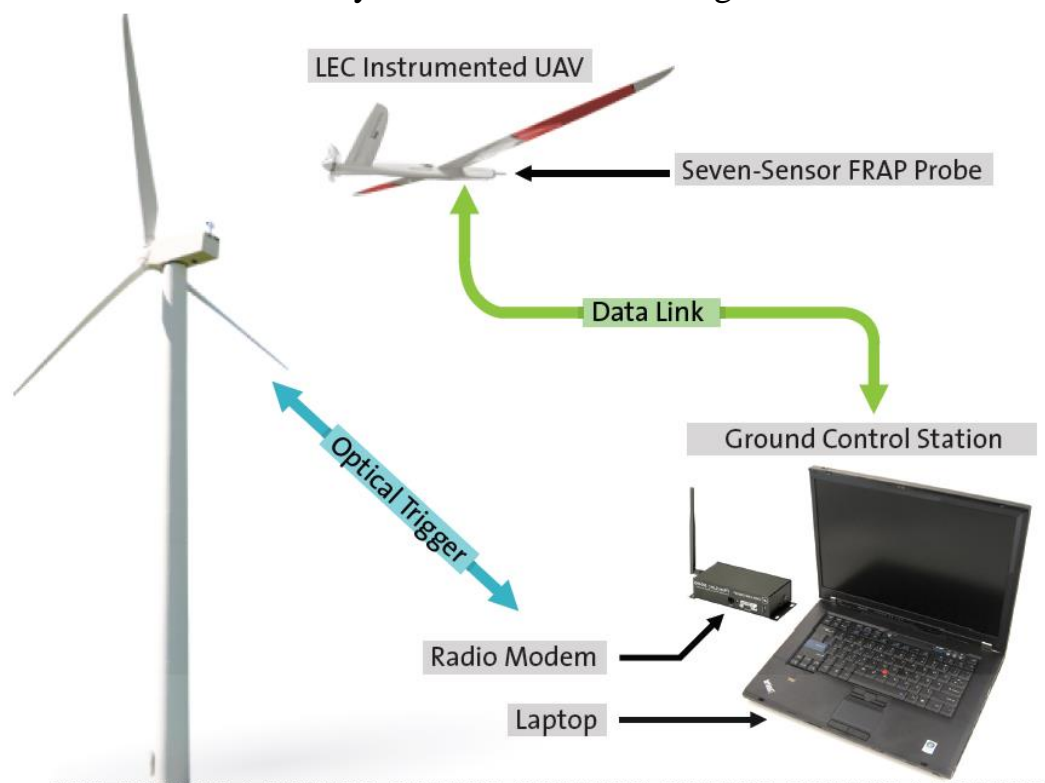


Figure 6. Measurement system schematics.

1.4 Research Objectives

The overall research objectives that encompass the scope of this thesis could be summarized as follows:

- Investigate the capabilities and limitations of a drone based wind measurement system.
- Generate a database for development, tuning and validation of improved wake models and advanced wind simulation tools at the Laboratory for Energy Conversion (LEC), ETH Zurich.
- Detail the flow structure of a full scale wind turbine with improved spatial coverage and resolution better than any previous works.
- Develop and demonstrate an approach to obtain turbulence quantities from FRAP measurements along a drone trajectory.
- Improve the understanding of the aerodynamic characteristics of wakes in flat and complex terrain.

1.5 Thesis Outline

Chapter 1

The necessities and challenges of full scale wind turbine measurements are described. It presents the background and also discusses the research objectives. This chapter introduces the drone based wind measurement approach.

Chapter 2

A detailed look into the measurement system is presented here. This chapter explains FRAP (including probe design, sensor packaging, calibration and data) and its data acquisition system, and the drone's on-board instrumentation. Details of the paparazzi autopilot system is also presented here.

Chapter 3

The steps involved in post-processing to obtain the final wind speed in the Earth's frame of reference are discussed here. The short-time Fourier Transform based approach to compute turbulent kinetic energy along the drone trajectory is explained in detail. Also presented are the approach to phase locking and turbulence spectra.

Chapter 4

The measurements in the wake, up to eleven rotor diameters downstream in a flat terrain, are presented as well as the evolution and breakdown of tip vortices that are characteristic of the near wake, and the turbulent mixing and entrainment of more energized flow that are distinctive in the far wake. The chapter also presents a comparison of measurements to wake models.

Chapter 5

The measurements in complex terrain are discussed in detail in this chapter. This includes the pressure variation across the wind turbine rotor, upstream and wake flow profiles, spectra, tip

vortices, wake contours and a comparison of drone measurements in freestream to LIDAR, CFD and SCADA.

Chapter 6

This chapter presents a comparison of the wake flow in flat and complex terrains. The Reynolds decomposition approach is used to reveal the nature of turbulent fluctuations in the surface layer - that includes the turbulence statistics, degree of anisotropy and friction velocity.

Chapter 7

A comparison of the wake evolution measured under neutral and unstable atmospheric condition in a flat terrain, including wake profiles at eleven different locations downstream, is presented here. The dissipation rate of turbulent kinetic energy measured at different atmospheric conditions is discussed and tabulated.

Chapter 8

This chapter presents the final concluding remarks and suggestions for future work.

2 MEASUREMENT SYSTEM

2.1 Fast Response Aerodynamic Probe: FRAP

The principle enabler for time-resolved wind measurements is the 7-sensor fast-response aerodynamic probe (7S-FRAP). The seven sensor Fast Response Aerodynamic Probe (7S-FRAP) was developed at ETH Zurich based on previous experience gained from other fast response probes developed for turbomachinery applications. More details on FRAP technology can be found at [59-62], however specific salient features of the probe developed for the current wind energy application are described below.

The main criteria in probe development were the capability to measure wind velocity in low dynamic head conditions (0-10mbar) with large bandwidth ($\leq 1\text{kHz}$) and at large flow angles ($\leq 70^\circ$), but without exceeding the maximum payload limitations of a drone. The probe needs to be robust to withstand in-flight forces and landing impacts. A drone was chosen as platform to carry the fast response probe for high resolution flow field measurements around a full scale wind turbine as it provides sufficient range – horizontal range of 1.5 km and vertical range of 1.5 times the vertical extent of rotor - to the measurement system.

2.1.1 Sensor Packaging

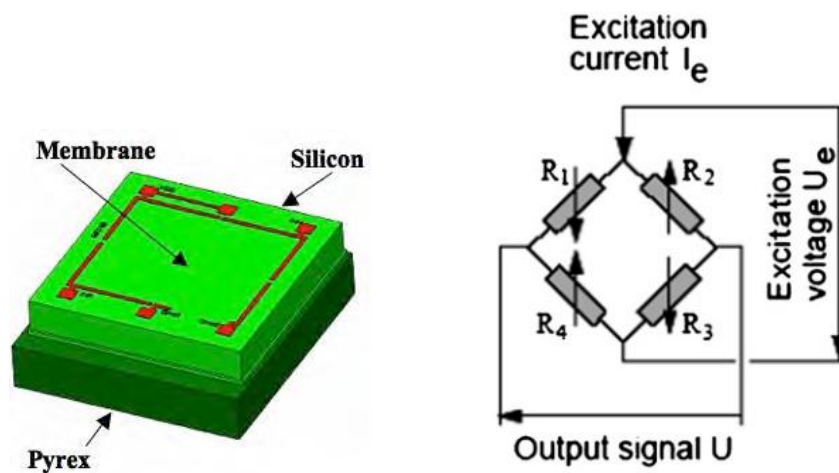


Figure 7. Miniature pressure sensor die, Intersema MS-7505-D (left) and the Wheatstone bridge circuit of the sensor (right).

A miniature pressure sensor die, shown in Figure 7 (left), is the sensing element of a FRAP pressure sensor. Also shown in Figure 7 (right) is the sensor's Wheatstone bridge circuit with output voltage U and excitation voltage U_e . This sensor is designed for low pressure applications

(≤ 50 mbar) that have stringent requirements on resolution and accuracy. Its sensor element consists of a silicon-micro-machined membrane bonded onto a Pyrex glass substrate. The pressure signal is proportional to the pressure difference between the front and the back side of the membrane, and is sensed by four implanted piezo-resistors.

The sensor packaging and bonding techniques are derived from MEMS technology. These packaging and bonding techniques ensure optimal spatial resolution, measurement bandwidth and protection of the sensors in harsh weather conditions. Moreover the gluing and bonding techniques employed in the present design provided a high degree of reliability and low disturbance to the sensors as the probe can experience large temperature and pressure fluctuations.

As shown in Figure 8, the miniature silicon piezo-resistive chip is glued onto a socket using silicon glue with very low E-modulus. The silicon glue is based on an inorganic ground structure, which offers a large temperature range of operation ($-90^{\circ}\text{C} - 200^{\circ}\text{C}$) and is highly resistant to corrosive media. Thus the thermomechanical stresses are minimized. The photopolymer socket is encapsulated into a threaded casing of 5.5 mm in diameter. The threaded casing enables a repeatable fixation of the sensor in the probe tip, as well as the quick replacement of a sensor in case of a failure.

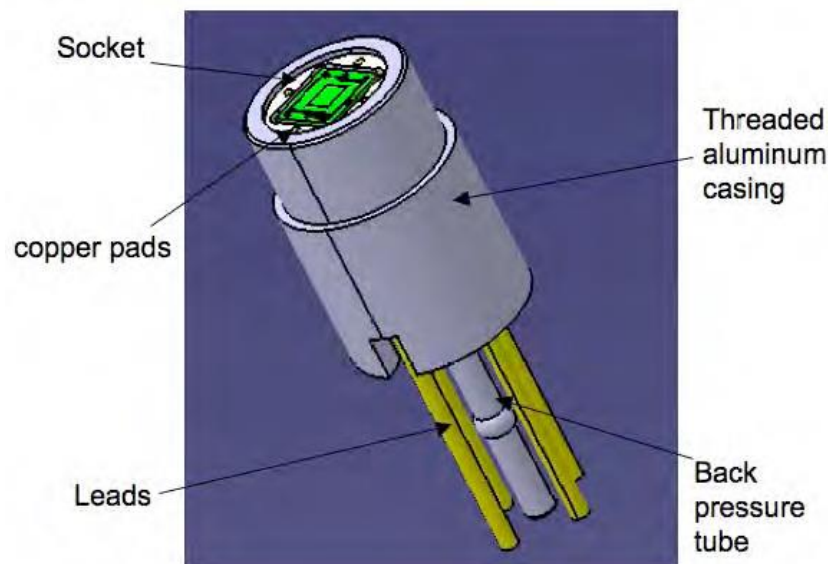


Figure 8. Encapsulated pressure sensor die.

2.1.2 Probe Design

A close up view of 7S-FRAP probe's head and one of its embedded differential pressure sensors are shown in Figure 9. The sensing elements of a 7S-FRAP probe are encapsulated into a hemispherical probe head of

diameter 20 mm , and are installed on a cylindrical shaft to give an overall probe length of 70 mm. This probe length of 70 mm is chosen as it minimizes the influence of potential field effects of the drone on the FRAP probe measurements. The probe shaft has a squared-end, which enables the repeatable installation of the probe on the drone. The sensing holes have a diameter of 1.3mm, which is less than one-twelfth of the probe diameter, ensuring negligible influence on the aero-calibration [63]. As the total and static pressures occur on the surface of a hemispherical probe at flow angles equal to 0° and about 45° respectively, the probe incorporates the surface pressure tapings at these positions with respect to the probe shaft axis. The volume and the length of the pressure taps of the probe tip body are minimized, as these dimensions have a significant impact on the probe aerodynamics and measurement bandwidth. The reduction of the pressure tap volume is a key parameter to yield a high frequency measurement bandwidth as the eigen frequency of the pneumatic cavity will affect the pressure sensor dynamic response. This issue is further discussed in the dynamic calibration section.

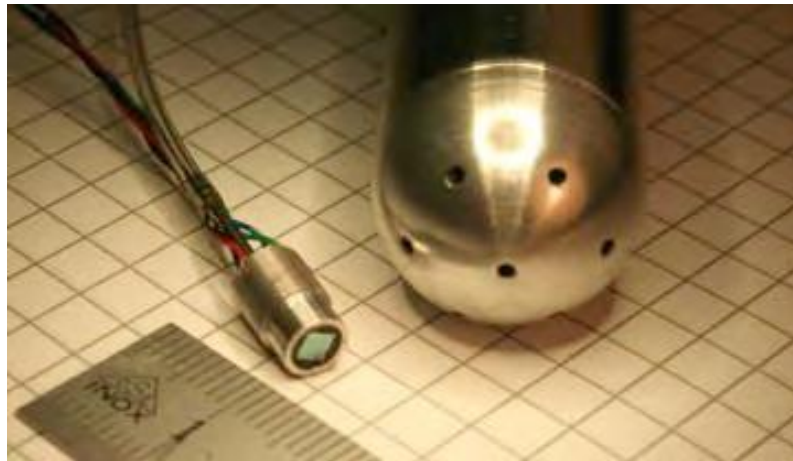
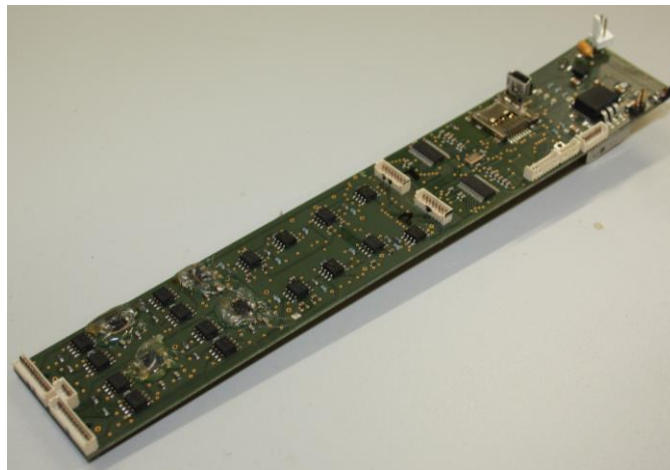


Figure 9. 7S-FRAP probe tip and an encapsulated pressure sensor.

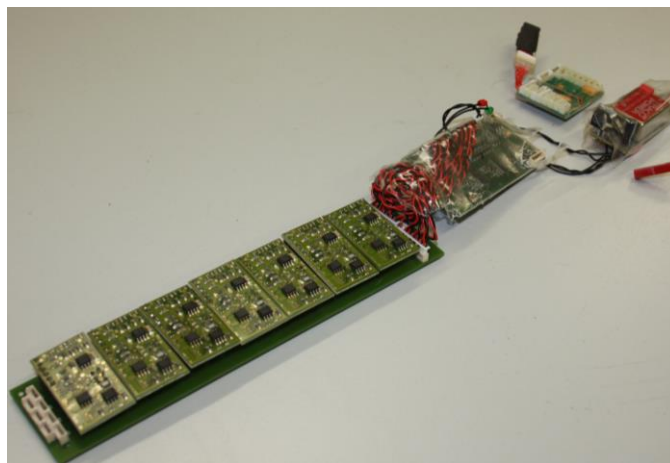
2.1.3 FRAP Data Acquisition System: FRAQ

The electronics accompanying the FRAP probe on-board of the drone is called FRAQ – Fast Response Data Acquisition, Figure 10 a. The FRAQ board is a double-sided, 6-layered PCB (three layers for signals, one layer for ground and the other two layers carry ± 15 V) that is designed in-house. This integrated FRAQ board performs the following four functions, namely amplification of the FRAP signals, analog-to-digital conversion, logging the digitized data in SD card, and providing the power supply (15 V and 5 V) to the above three units. It consists of seven amplifiers that amplify the seven FRAP sensor signals by a factor 100, seven Max11040 ADCs with 24 bit resolution that digitize the amplified voltage signals at

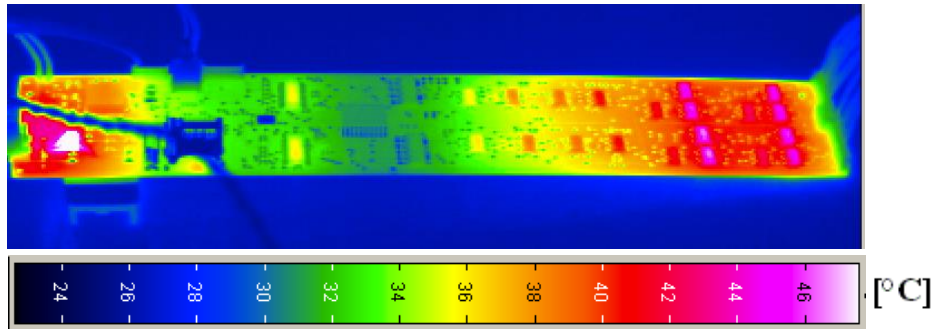
250/500 Hz, a LPC21xx based data logger with an on-board flash memory card (that runs on paparazzi software and stores the FRAP data in flash memory card at 250/500 Hz) and a DC-DC converter that generates a 5 V and a 15 V power supply from the on-board 12.1 V LiPO battery. Earlier version of the FRAP data acquisition system, shown in Figure 10 b, had four independent units to support the above mentioned four functions. But this old version of the system was heavy at 145 g and prone to frequent connector related malfunctions especially during drone landings. Thus, a new board – FRAQ - was built by integrating the four units into a single PCB that weighs only 75 g and is less noisy than its predecessor. The FRAQ board design also makes it possible to directly measure the analog voltage signals that are used for FRAP calibration and testing purposes. It was observed during initial tests (Figure 10 c) that the entire board heats up quickly after powering, thus raising the temperature from 25 °C (room temperature) to more than 65 °C, so the power supply route was later modified and an aluminum fin was added to reduce this maximum temperature to ~ 55 °C.



(a)



(b)



(c)

Figure 10. (a) Integrated FRAQ board, (b) Earlier version of the FRAP data acquisition system, (c) FRAQ surface temperature image with IR camera (Infratec VarioCam Head) with a pixel resolution of 386X288 pixels.

The new integrated FRAQ board was tested with the FRAP probe at zero wind speed to assess its performance. Figure 11 confirms that the output of all seven sensors of the FRAP probe measurement system (FRAP + FRAQ) shows no drift with time. The root mean square noise in the sensor signals is less than $0.18 \mu\text{V}$ at a sampling rate of 500 Hz.

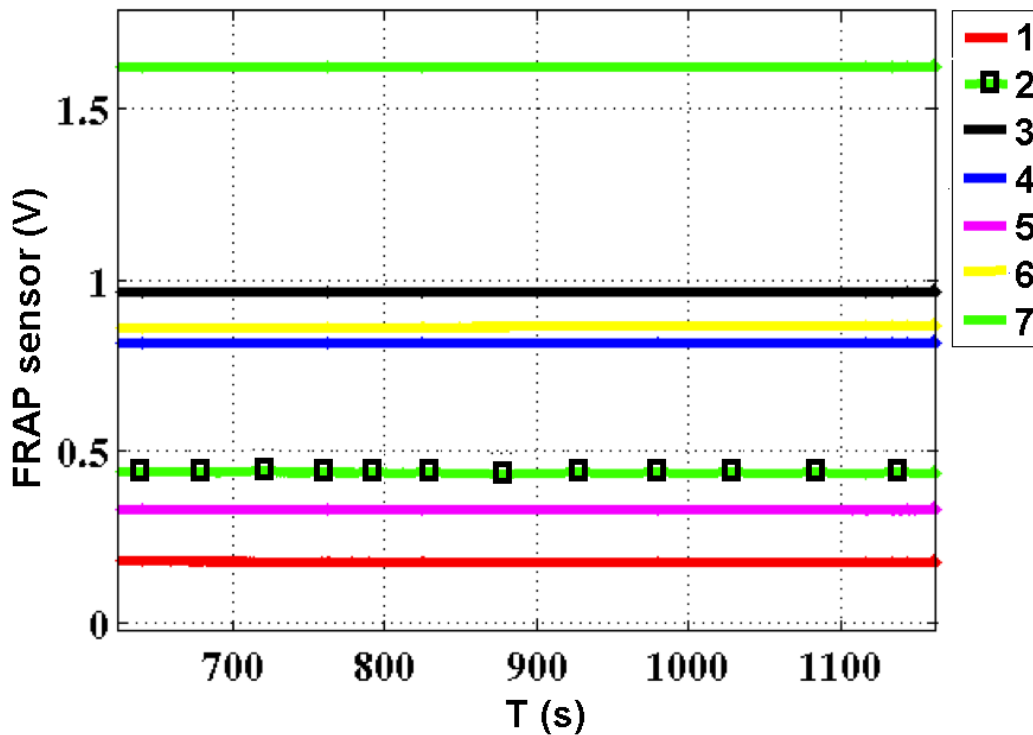


Figure 11. Output of all seven sensors of a probe measurement system (FRAP + FRAQ) at zero wind speed.

2.1.4 Static Calibration

A typical raw data calibration set from static calibration is shown in Figure 12. During static calibration, the FRAP probe mounted in an oven is subjected to a range of known differential pressures from 1-30 mbar and temperatures from 1-65°C. Each FRAP sensor produces two voltage outputs, one strongly dependent on pressure and the other strongly dependent on temperature. A fifth-order polynomial interpolation from static calibration, Equation 1, is employed to determine the pressure and temperature from the measured sensor signals.

For the sample sensor data shown in Figure 12, the measured sensitivities of the pressure sensor after amplification are 101 mV/mbar and 66 mV/°C for the pressure signal and the temperature signal, respectively. The noise on the pressure signal reduces the resolution of the analog-to-digital converter to 19-bit effective, which provides a differential pressure measurement resolution of $\pm 8.6 \cdot 10^{-3}$ Pa. The calibration model exhibits an average standard deviation compared to the measured data of ± 0.46 Pa and ± 0.14 °C, which corresponds to an error of less than 0.075% and 0.018% over the full calibration range of the probe.

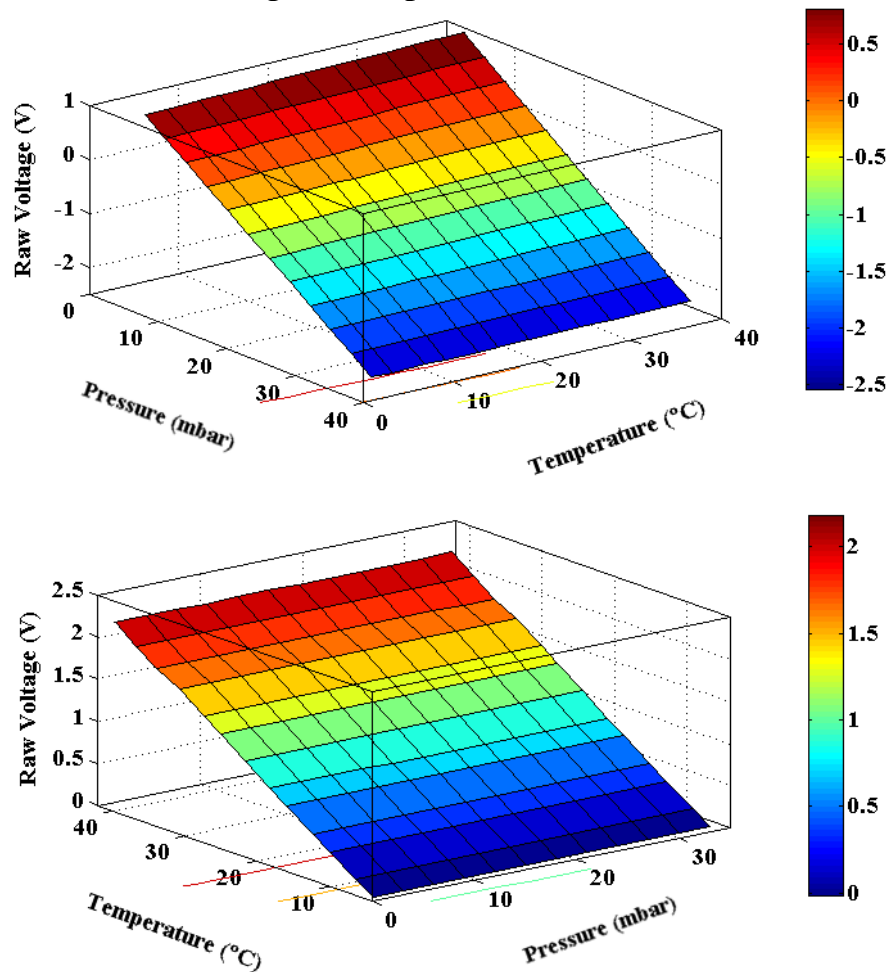


Figure 12. Sensor static calibration data.

$$p(U, U_e) = \sum_{i=0}^m \sum_{j=0}^n K_{p_{i,j}} U^i U_e^j$$

$$T(U, U_e) = \sum_{i=0}^m \sum_{j=0}^n K_{T_{i,j}} U^i U_e^j$$
(1)

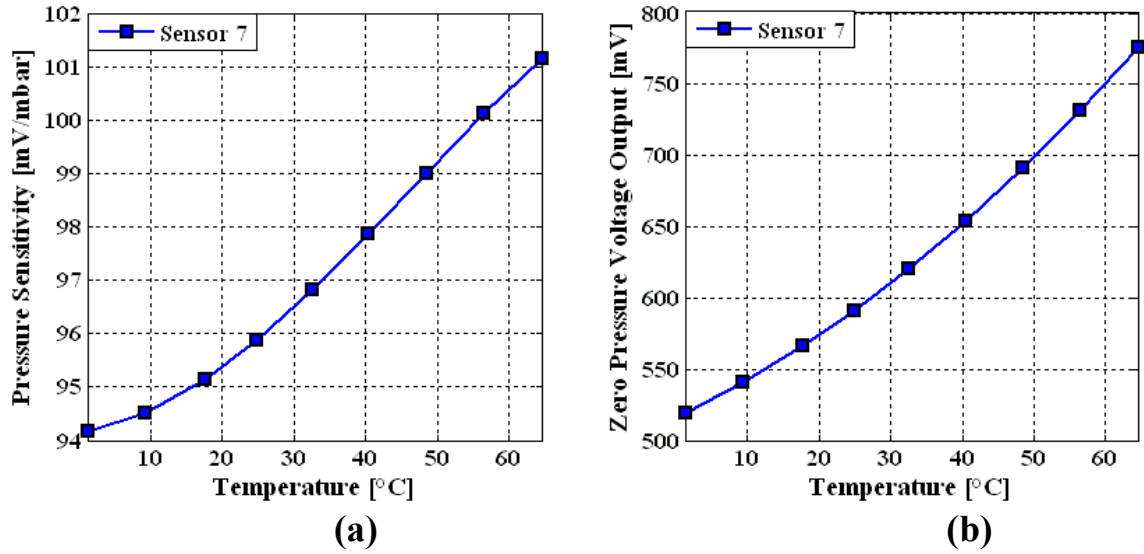


Figure 13. (a) pressure sensitivity versus applied temperature, (b) zero pressure offset versus temperature [56].

The output signal U is weakly temperature dependent, while the excitation signal U_e is decoupled from the pressure. However the effect of temperature on the pressure sensitivity (Figure 13 a) and on the zero pressure offset (Figure 13 b), which is the pressure signal output at zero applied pressure, is not negligible. The pressure signal output experiences 7.4% and 47% increase in pressure sensitivity and zero pressure output, respectively, when temperature varies from 1°C to 65°C. It can also be observed that the response to temperature variations is non-linear. Therefore the sensors must be calibrated over the full range of intended temperature use.

2.1.5 Aerodynamic Calibration

The FRAP probe is designed to be used in a non-nulling fashion to measure the wind velocity (in the drones frame of reference) in a turbulent atmospheric boundary layer. The definition of flow angles and the arrangement of pressure taps in a FRAP probe are shown in Figure 14. The pressure measured by the seven sensors of a FRAP probe are combined to compute four coefficients (Equation 2), that represents the local yaw angle ψ , pitch angle θ , total pressure P_o , and dynamic pressure q . This is then used to derive the local velocity vector \vec{v} relative to the FRAP probe.

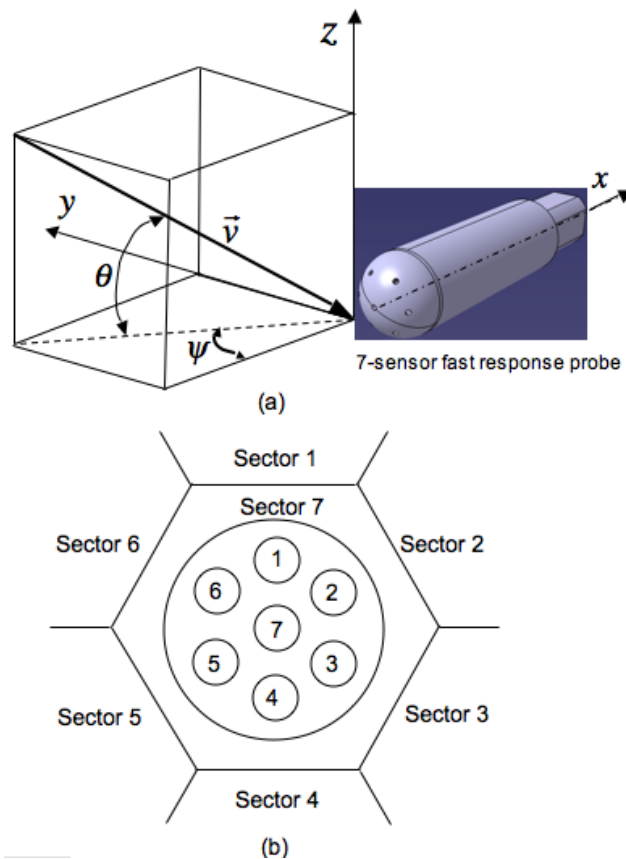


Figure 14. (a) Flow angles convention, (b) Pressure taps numbering and sectoring scheme.

At low flow angles, the flow remains attached over the entire surface of the probe and the central port (n=7) has the highest pressure. Therefore the pressure measured by all seven sensors is used to characterize the flow field. However at high flow angles, the flow separates on the leeward side of the probe, and an off-center pressure sensor (n=1-6) has the highest pressure. In this case only a subset of the seven pressure sensors is used to determine the flow conditions, based on the sensor reading the highest pressure and the sensors that are adjacent to it. The difference between high

and low flow angles leads to a sectoring scheme, which is employed in the current work as shown in Figure 14 b.

The aero-calibration of the probe was made in the fully automated freejet facility at ETH Zurich. A detailed description of the facility can be found in [59]. The probe is installed on a three axis traversing system (lateral motion, yaw angle and pitch angle motion) in order to rotate the probe relative to the fixed jet. The automatic calibration procedure follows pre-defined measurement grids for different probe yaw and pitch angles. For the low angle range the set of calibration data is taken on a homogenous grid that covers $\pm 30^\circ$ in yaw and pitch angles, for a Mach number of 0.07 that corresponds to a speed of 25 m /s.

Following an approach similar to that of Zilliac [64], a pitch angle coefficient C_θ is used to represent the local pitch angle θ , and a tangential pressure-difference coefficient C_ψ is used to represent local yaw angle ψ . Similar coefficients C_o and C_q are used to derive the total pressure and dynamic pressure, respectively. These coefficients are defined for low angles corresponding to sector 7 as in Equation 2.

$$\begin{aligned}
C_{\theta,7} &= \frac{2(P_4 - P_1) + (P_3 - P_6) - (P_2 - P_5)}{2(P_7 - \bar{P}_7)} \\
C_{\psi,7} &= \frac{(P_3 - P_6) + (P_2 - P_5)}{\sqrt{3}(P_7 - \bar{P}_7)} \\
C_{o,7} &= \frac{P_7 - P_o}{P_7 - \bar{P}_7} \\
C_{q,7} &= \frac{P_7 - \bar{P}_7}{q} \\
\bar{P}_7 &= \frac{1}{6} \sum_{n=1}^6 P_n
\end{aligned} \tag{2}$$

The polynomial curve-fit method of Gallington [65] is applied to the calibration data. Four sets of calibration coefficients are derived for the four flow properties (ψ , θ , C_o , C_q). The polynomial calibration coefficients $k_{ij\psi}$ and $k_{ij\theta}$, used to derive yaw and pitch flow angles, result from the solution of this set of linear equations using a least squares 10^{th} order polynomial approximation, as shown in Equation 3.

$$\begin{aligned}\psi &= \sum_{i=0}^n \sum_{j=0}^m k_{ij\psi} C_{\psi}^i C_{\theta}^j \\ \theta &= \sum_{i=0}^n \sum_{j=0}^m k_{ij\theta} C_{\psi}^i C_{\theta}^j\end{aligned}\tag{3}$$

A similar procedure as for the flow angles is applied to the pressure measurements in order to derive the polynomial calibration coefficients for the total pressure and dynamic pressure. The relations in Equation 4 are a function of the computed flow yaw angle. The polynomial interpolation order is 6 and 5 for total pressure and dynamic pressure, respectively.

$$\begin{aligned}C_o &= \sum_{i=0}^n \sum_{j=0}^m k_{ijt} \psi^i \theta^j \\ C_q &= \sum_{i=0}^n \sum_{j=0}^m k_{ijq} \psi^i \theta^j\end{aligned}\tag{4}$$

The calibration curves of the 7S-FRAP probe are shown in Figure 15 for $\pm 30^\circ$ in yaw and pitch, at a Mach number of $Ma = 0.074$ which corresponds to wind dynamic head and velocity of 4 mbar and 27 m/s, respectively. Table 1 tabulates the accuracy of calibration model of the 7S-FRAP probe. Thus at an airspeed of 20 m/s, the FRAP probe can resolve wind speed with a resolution of ~ 0.05 m/s and flow angles with a resolution of $\sim 0.1^\circ$.

Yaw Angle	Pitch Angle	Total Pressure	Dynamic Pressure
abs. [°]	abs. [°]	abs. [Pa]	abs. [Pa]
/ rel. [%]	/ rel. [%]	/ rel. [%]	/ rel. [%]
$1.44 \cdot 10^{-1}$	$1.37 \cdot 10^{-1}$	2.1	2.3
$/ 2.4 \cdot 10^{-1}$	$/ 2.3 \cdot 10^{-1}$	$/ 5.18 \cdot 10^{-1}$	$/ 5.68 \cdot 10^{-1}$

Table 1. Calibration model accuracy of the 7S-FRAP probe. Calibration range: $Ma = 0.074$, $\pm 30^\circ$ in yaw and pitch angles.

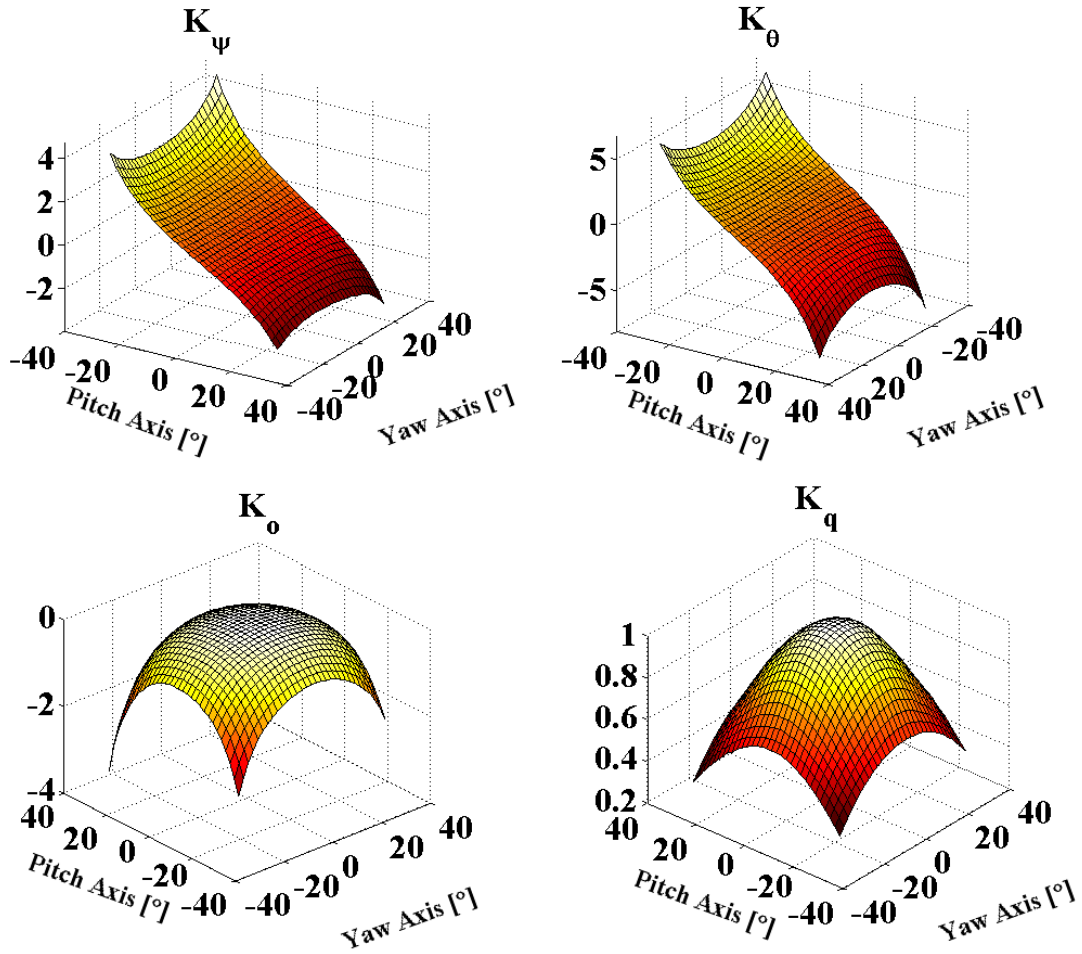


Figure 15. Aero-calibration coefficients, (a) yaw flow angle, (b) pitch flow angle, (c) total pressure, (d) dynamic pressure.

It is important to note that five sensors are sufficient to measure the wind velocity with FRAP probe. The seven sensor FRAP probe designed for drone based wind measurement applications carries two additional sensors as a measure of redundancy. Thus, the FRAP probe can also be used in 5-sensor mode to measure the flow field in drone's frame of reference. The three 5-sensor mode combinations possible with the FRAP probe are shown in Figure 16. This 5-sensor mode feature is used if one of the seven sensors is damaged in the field, say, during a drone crash landing. The procedure to extract the aero-calibration coefficients of a FRAP probe in 5-sensor mode is explained in [66].

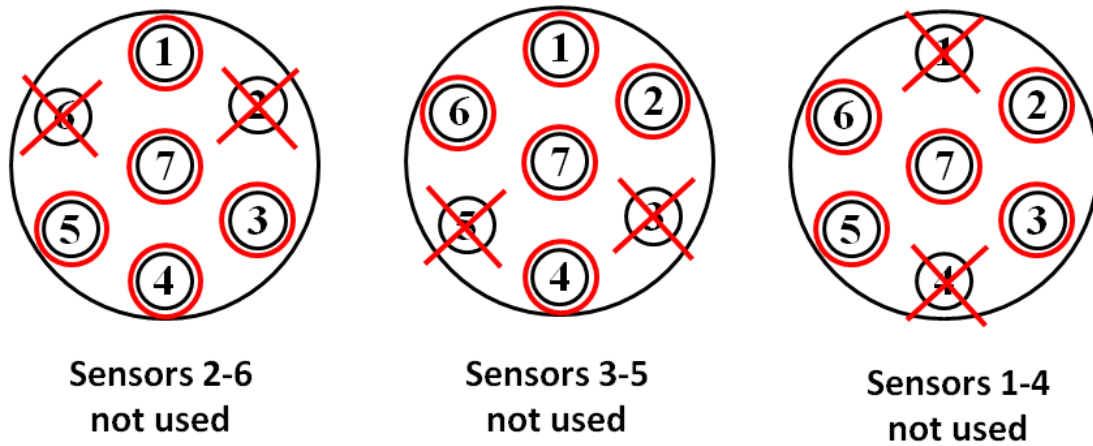


Figure 16. FRAP probe in 5-sensor mode.

2.1.6 Dynamic Calibration

The pneumatic cavity between the pressure tap and piezo-resistive sensor membrane can influence the unsteady pressure measurements. The acoustic resonance that is associated with the characteristic length of the pneumatic cavity implies that the measured signals around the eigenfrequency of the pneumatic cavity are strongly amplified and have a phase shift [67]. It is thus important to quantify the eigenfrequency of the newly designed shielded pressure tap. This eigenfrequency determines the frequency measurement bandwidth of 7S-FRAP probe.

The dynamic response of the pneumatic cavity was measured in the freejet facility, equipped with a fine mesh grid. The resulting flow turbulence has a constant amplitude over relatively low frequencies and then decays with a characteristic slope of $-5/3$ at higher frequencies. The amplitude response in terms of PSD/PSD_0 versus frequency is shown in Figure 17. The peak at 3.8 kHz corresponds to the eigenfrequency of the pneumatic cavity of the stagnation pressure sensor 7, which exhibits the largest pneumatic cavity of all seven sensors. The amplitude is flat up to a frequency of 3 kHz, above which the amplitudes are in excess of 3 dB. Thus the cutoff frequency of 3 kHz determines the bandwidth of the 7S-FRAP probe.

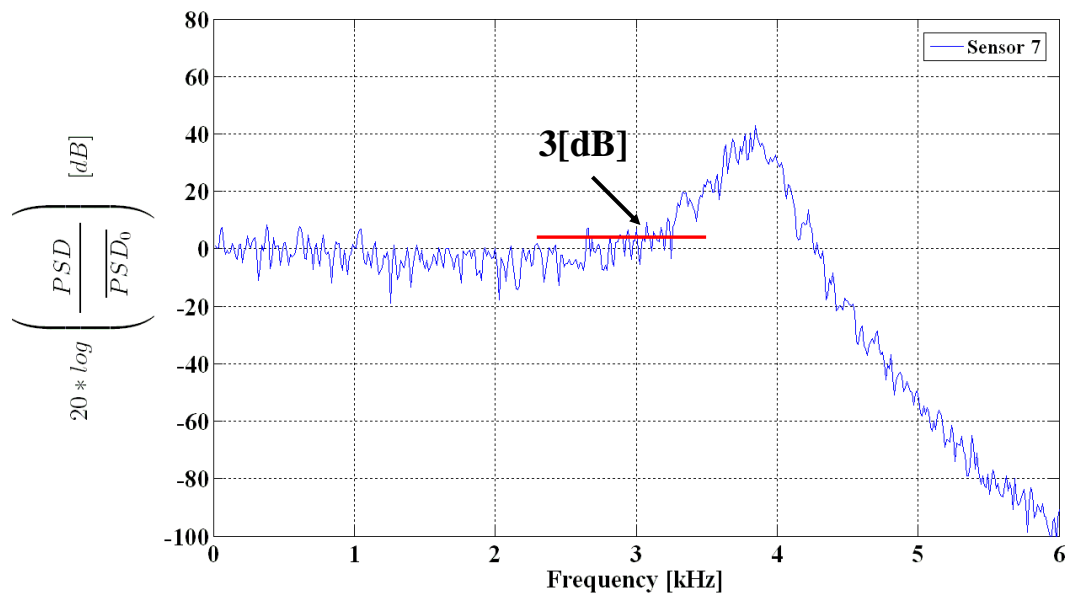


Figure 17. Amplitude response of stagnation pressure sensor 7. The measured response is from grid generated turbulence [56].

2.2 Onboard Instrumentation

The on-board sensors in WindFlyer and Funjet are summarized in Table 2. The GPS receiver installed on the Tiny v 2.11 autopilot board of the Funjet drone is a u-blox LEA-6H and the external GPS employed with the TWOG autopilot board in the windFlyer drone is u-blox NEO-6M. The GPS measures the position in UTM coordinates, height above sea level, ground speed and climb speed of the drone along its trajectory at a sampling rate of 4 Hz. GPS output accuracy depends on the signal strength that is affected by a number of factors like the measurement location, time of day, orientation of the GPS antenna, use of satellite based augmentation systems like EGNOS/WAAS etc, and its position accuracy measured is shown in Figure 18. More details on the u-blox GPS receivers can be found in [68].

On-board sensor	Variables measured	Sampling rate (Hz)	Autopilot Tiny v2.11/TWOG port connection
MS5611	Atmospheric pressure, temperature	10	I2C
SHT75	Relative humidity (RH), atmospheric temperature	2	ADC (12 bit)
ublox LEA-6H (Funjet)	Drone position, ground speed, climb speed and course	4	UART
ublox NEO-6M (WindFlyer)			
Arduimu (version 2, 3)	Attitude angles pitch and roll	4	I2C
PNI micromag 3-axis magnetometer	Magnetic heading	10	SPI
Attopilot	Current and voltage	1	ADC (12 bit)

Table 2. On-board sensors in WindFlyer and Funjet.

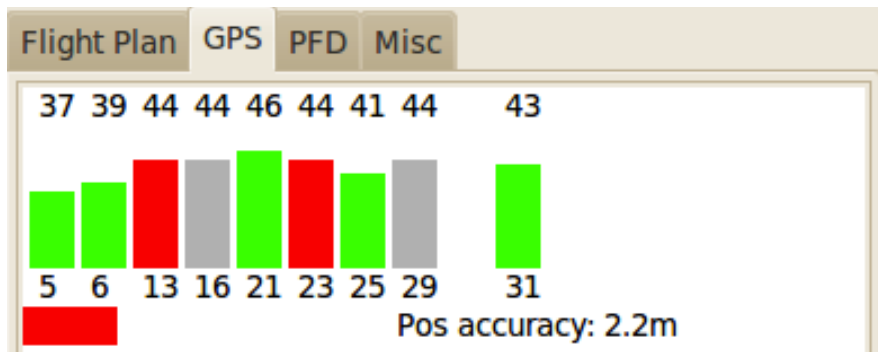


Figure 18. u-blox NEO-6M GPS module position accuracy.

2.2.1 Inertial Measurement Unit (IMU) Sensor

During measurements, the pitch and roll angles of the drone along its trajectory are continuously measured using an ArduIMU sensor. As the manufacturer did not specify the accuracy of angles measured by this Inertial measurement Unit (IMU) sensor, an attempt was made to evaluate ArduIMU's pitch angle accuracy against the pitching motion of the IFD wind tunnel traversing system. Figure 19 shows the deviation of the IMU pitch angle relative to the corresponding value of the wind tunnel traversing system. With a linear fit, it can be observed that the IMU pitch is over estimated on an average by 3% relative to the wind tunnel pitch system. As this error is negligible the IMU system is regarded as reliable. Also for reliable attitude angle measurements, the IMU needs to be mounted carefully at/close-to the CG of the drone.

At the beginning of each wind tunnel run, the drone is repositioned at the reference zero position of the traversing system in order to initialize the IMU. It turns out that the length of time period in which the initialization is performed has no influence on the quality of initialization. The average value of the IMU pitch angle for different initialization periods of 15, 30, 60 and 120 s remains within an interval of 0.01° . The standard deviation for each period remained below 0.025° . Furthermore, no deviation from the initial value was detected when the drone was reset to the reference zero position (of the traversing system) after each alpha-sweep run in the wind tunnel. The specific values of the average and standard deviation can be found in [69]. Therefore, it can be concluded that the accuracy of the IMU system is sufficient to measure the pitch angle of the drone in flight. The IMU system is not subject to any offset drifts. Furthermore, for all field measurements, an initialization period of 30 s after powering ON is considered sufficient.

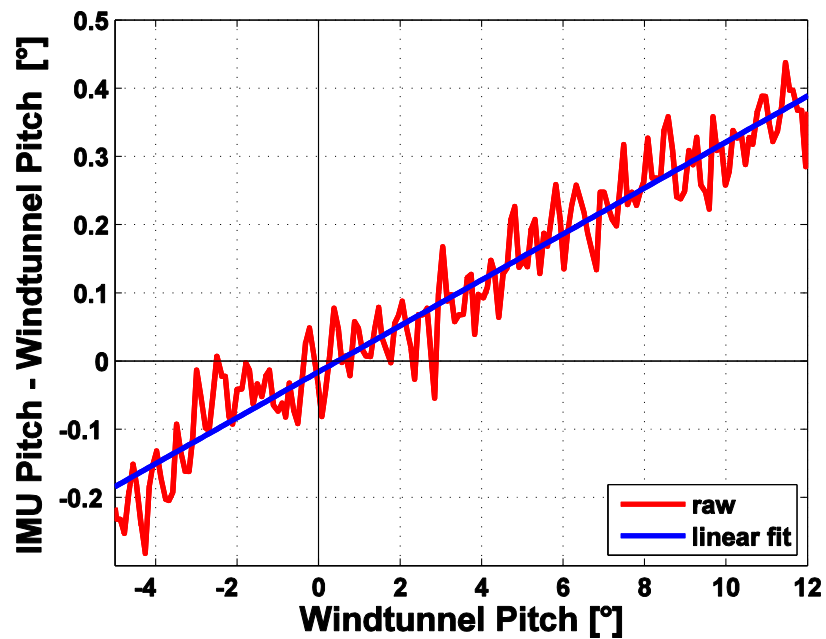
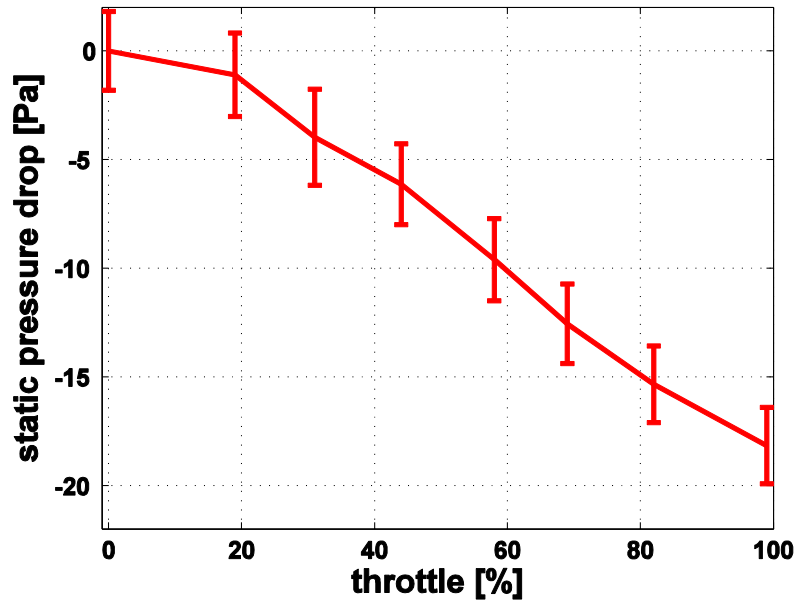


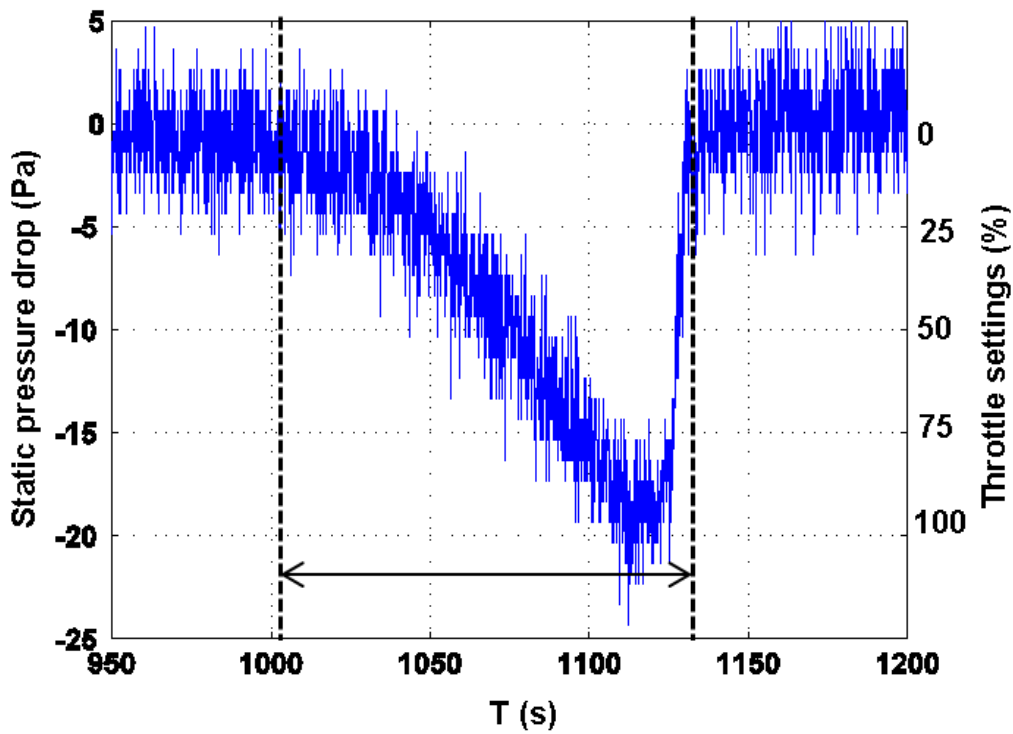
Figure 19. IMU pitch angle deviation

2.2.2 Static Pressure and Temperature Sensor

The barometric pressure along a drone trajectory is measured using a high resolution MS5611-01BA sensor on-board of the aircraft. MS5611 is a high-resolution altimeter sensor with an altitude resolution of 10 cm and is integrated into the drone's autopilot through an I2C bus interface [70]. The sensor measures both pressure and temperature signals with a high stability and with very low hysteresis losses. Thus, MS5611 sensor directly measures the FRAP back pressure and is also used in post-processing to compute the atmospheric density along a drone trajectory. As this sensor is located inside the drone fuselage, the pressure measured by this sensor is affected by propeller motion. The effect of different throttle settings on the static pressure drop inside the drone fuselage is measured and documented in Figure 20 a. The temporal variations in atmospheric pressure during this 125 s measurement period can be neglected as the pressure drop is seen to return to zero after the removing the throttle, Figure 20 b. The standard deviation of the pressure signal at different throttle settings is calculated with respect to the time period where the throttle was maintained at a constant level (approximately 10 seconds for each step). As the throttle set by autopilot in cruise mode is around 40-50%, a correction based on the pressure drop is applied to the final computed airspeed. This sensor is mounted inside the fuselage nose close to the FRAP probe.



(a)



(b)

Figure 20. (a) Static pressure drop caused by propeller at different throttle settings, (b) Raw signal from MS5611 during measurement at different throttle settings.

The temperature measured by the MS5611 sensor located inside the fuselage and the SHT75 sensor located outside the fuselage is depicted in

Figure 21. The SHT75 sensor (accuracy $\pm 0.1^\circ\text{C}$ [71]) is mounted outside the fuselage and it measures both the atmospheric temperature and relative humidity along a drone trajectory. The output of this sensor is used to compute the atmospheric air density along a drone trajectory. It can be seen from Figure 21 that the temperature outside fuselage is always lower than the temperature measured inside the fuselage for the whole measurement duration. Although the ambient conditions were maintained constant within the test facility during this measurement, a maximum temperature rise of 3.5°C was observed inside the fuselage due to the on-board heat generating sources like FRAQ.

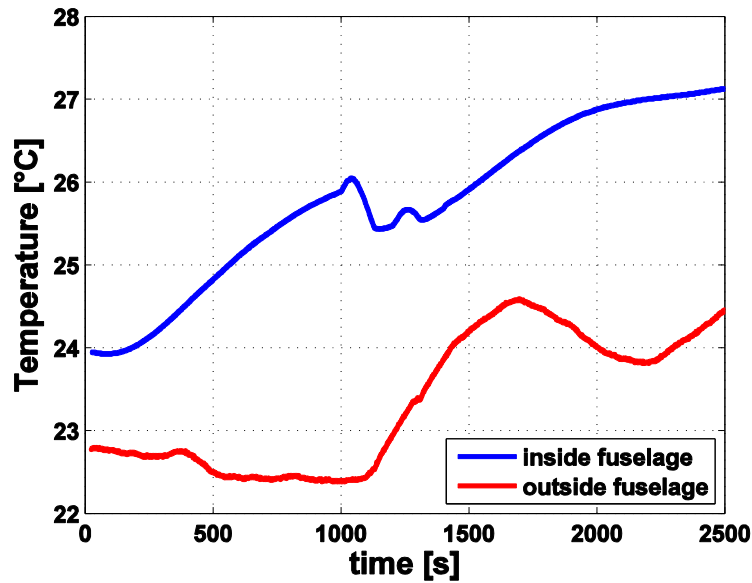


Figure 21. Temperature measured by the MS5611 sensor (inside fuselage) and the SHT75 sensor (outside fuselage).

2.2.3 Magnetic Sensor

The drone's heading is measured using Micromag 3, an on-board magnetic sensor mounted on the fuselage nose. This highly sensitive magnetic sensor (resolution 0.15 mGauss) on-board of the aircraft measures the Earth's magnetic field in all 3 axes of a rectangular coordinate system attached to the drone. To get the final wind speed in the Earth's frame of reference with reliable accuracy, the drone's sideslip and attitude angles are needed with reliable accuracy. GPS measures the aircraft-heading angle, but this assumes the drone as a point mass moving in space and thus does not provide the orientation of drone fuselage during flight. Depending on ambient wind speed and turbulence, the drone's fuselage orientation can change continuously during flight and this becomes especially significant when the drone is flying perpendicular to the main wind direction. Theoretically at zero ambient wind speed, both

parameters – GPS heading and magnetic heading - must match, but asymmetry in drone body, turbulence or wind can lead to sideslip. If no magnetic sensor data is available and if the drone trajectory is nearly parallel to the main wind direction, then GPS heading can be used as an approximation to the measured final wind velocity in the Earth frame of reference along this trajectory. But when the drone flies perpendicular to the ambient wind then the final wind velocity in the Earth frame of reference cannot be extracted if the magnetic sensor data is not available. However, it is important to note that the vertical wind speed in Earth’s frame of reference is independent of sideslip angle.

As the magnetic field from any on-board electronics or any on-board ferrous materials can affect the magnetic sensor output, a calibration approach is needed to take these effects into account [66]. Micromag 3 has an arrow printed on its PCB to indicate the “reference direction” for mounting the sensor horizontally on-board of the drone. The sensor modules are arranged in a South-West-Down (SWD) coordinate system. The reference direction is parallel to the x-axis of the magnetic sensor and this is also oriented parallel to the x-axis of the FRAP probe. The magnetic heading along drone trajectory is computed using using the X, Y and Z components of the magnetometer, the attitude angles (pitch and roll) of the IMU and the hard, soft iron correction coefficients. Figure 22 shows a comparison between GPS and magnetic heading measured during a test flight.

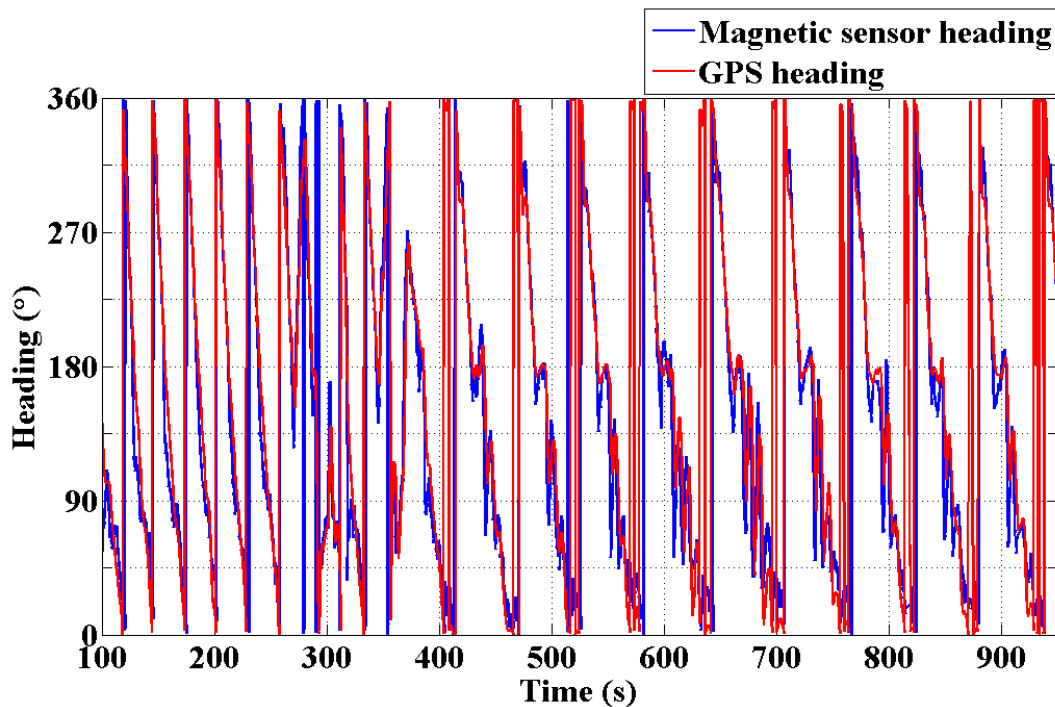


Figure 22. GPS heading vs magnetic heading during a test flight.

2.2.4 AttoPilot Current and Voltage Sensors

An attopilot sensor on-board is used to measure the battery voltage and the current drawn from the LiPo batteries during flight at a sampling rate of 1 Hz. The ampere values of the current sensor were double-checked with a multi-meter. The deviation of the measured values was found to be below 2%. However, the voltage sensor was found to be under-predicting the voltage compared to the value measured at the level of the battery between 4 and 5%. This means that the actual voltage of the battery is higher than displayed in the paparazzi interface, and that the batteries can be drained further during field tests.

2.2.5 Optical Trigger System

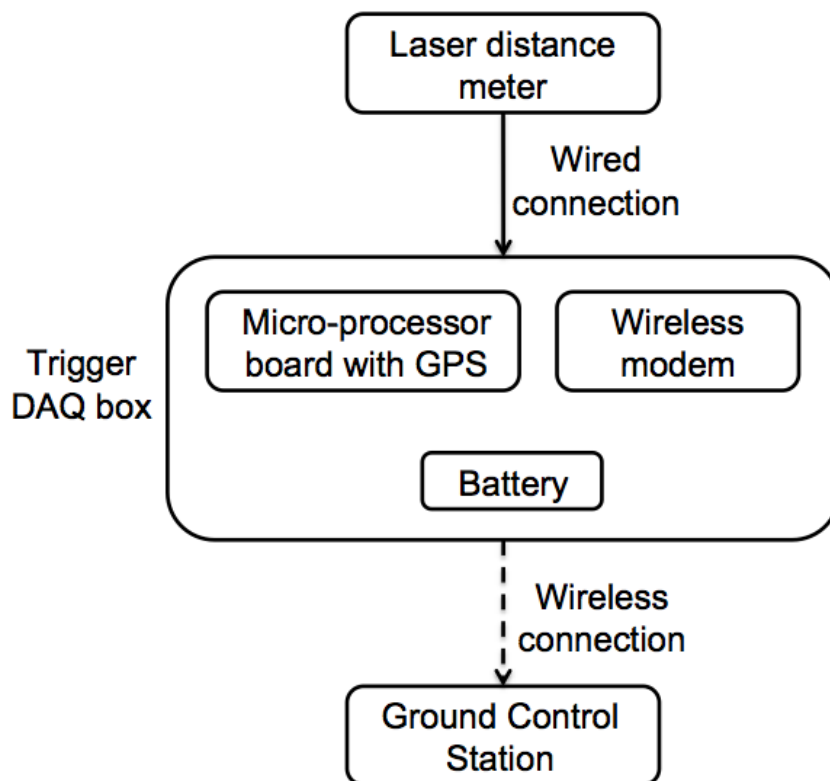


Figure 23. Schematic of optical trigger system [92].

An optical trigger system that tracks and logs the position of wind turbine blades in the telemetry log file during drone based wake measurements was designed in-house for phase locking the FRAP measurement data. This ground-based system consists of a Laser Distance Meter (LDM301) that is positioned upstream of the wind turbine (say at a distance of 50 m) during drone based wake measurements. A pilot laser on the LDM is focused on the wind turbine tower, with the pilot laser pointing

to a location on the tower that is (say) 10-15 m below hub height. As a blade passes close to the tower, it intercepts the beam and reduces the distance measured by LDM. When the LDM measured distance (briefly) reduces during blade passing, it sends a trigger signal to the GCS and is logged in the log file. The LDM has a range of more than 300 m and can measure distance with an accuracy of ± 6 cm at a sampling rate of 2 kHz. A schematic of the optical trigger system is shown in Figure 23. A serial interface connects the LDM to the trigger DAQ box. The trigger DAQ box consists of a paparazzi Tiny v2.11, a xbee modem and a 11.1 V LiPo battery. As the wind turbine blade passes by the tower, it changes the LDM output and generates a trigger at the blade passing frequency. This trigger signal is transmitted to the Ground Control Station (GCS) and logged in the telemetry log file. Thus, the measured trigger signal directly provides the position of wind turbine blades and the frequency of rotation (rpm) of the wind turbine rotor during wake measurements. The measured wind turbine rotor frequency (rpm) from the optical trigger system is compared to the 10-minute average SCADA values in Figure 24. The measured variations in rotor rotational speed with time are a manifestation of the variability in ambient wind speed. The mean rotor speed computed from the trigger system is compared to SCADA in Table 3, and it shows a difference of 3%.

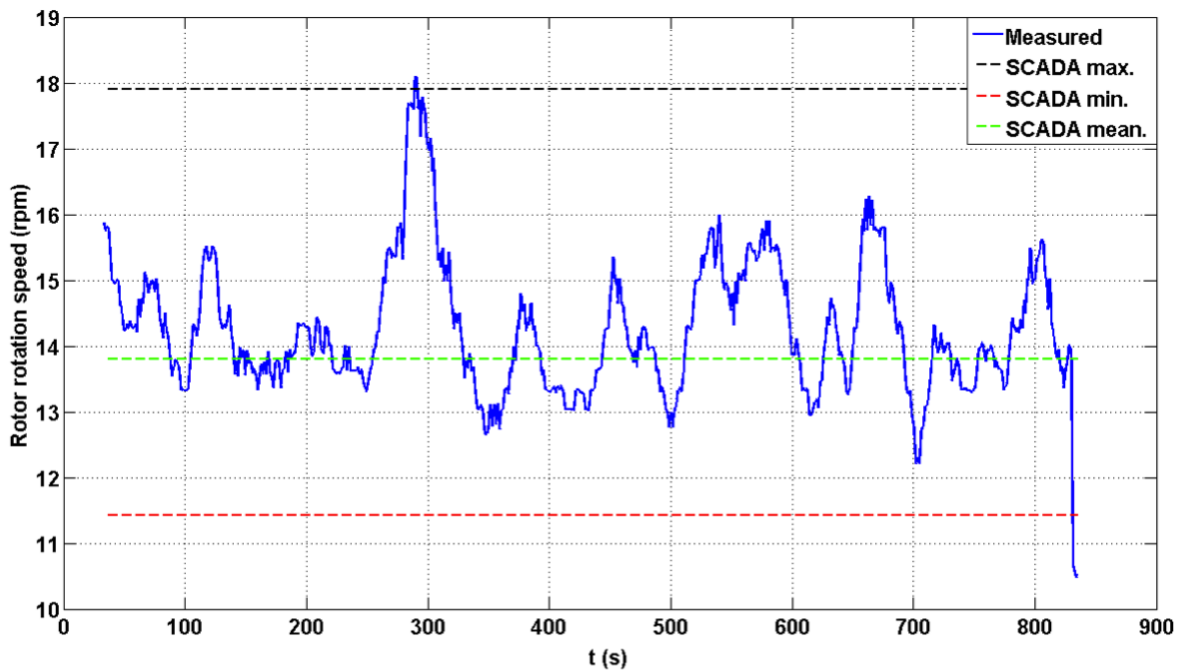


Figure 24. Rotor RPM measured with optical trigger system compared to SCADA.

Mean rotor speed (rpm)		Difference (%)
Measured with optical trigger system	SCADA	
14.3	13.9	3

Table 3. Rotor speed computed from optical trigger system vs SCADA.

As mentioned earlier, the trigger signal can be used for phase locking the wake measurement data. By assuming that all three blades of a wind turbine rotor are identical with rotational symmetry, the 120° sector of the area swept by rotor can be bucketed/collected into bins, say 12 identical bins of 10° each. Thus, the position of the drone along its trajectory can be tied to the rotor blade position – in different bins - measured using an optical trigger system. Figure 25 depicts a wake measurement trajectory of the drone collected into 12 identical bins based on rotor position. The position of the drone in one complete wake trajectory binned into three different rotor position bins, namely 10° - 20° , 50° - 60° and 90° - 100° , is shown in Figure 25.

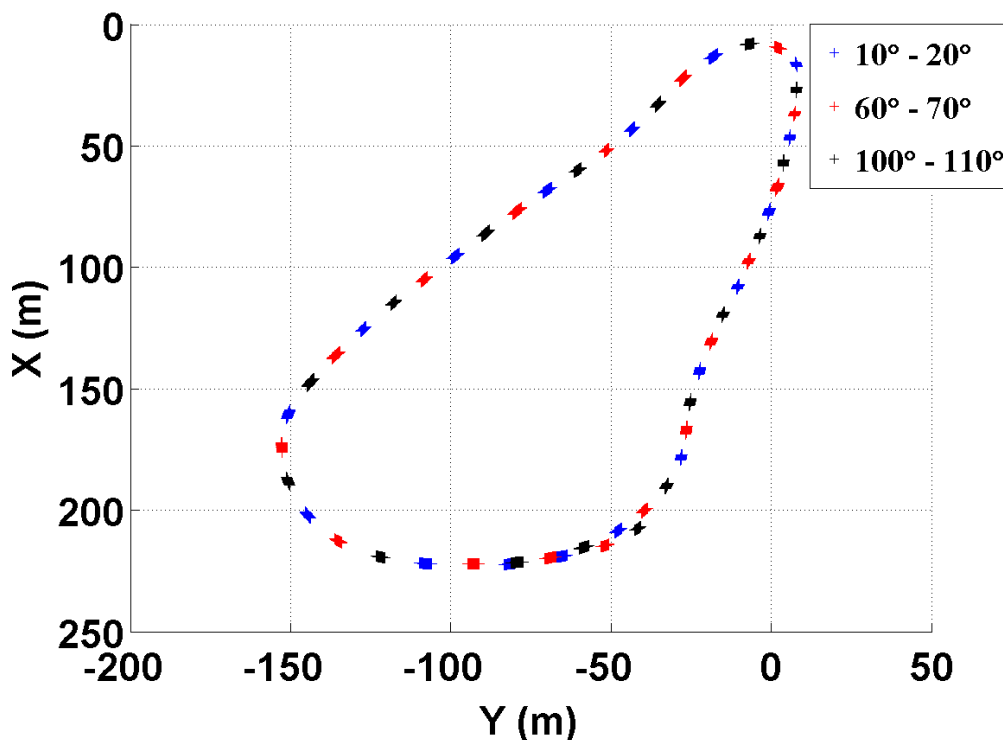


Figure 25. The measurements along the drone trajectory are binned based on rotor position into 12 identical bins of 10° each. Only one complete wake measurement trajectory (GPS positions) binned into 3 different rotor sector bins is shown here, namely 10° - 20° , 60° - 70° and 100° - 110° .

2.3 INSTRUMENTED DRONE

2.3.1 1st Generation Drone: Funjet

The 1st generation foam-based drone is called Funjet, Figure 26. The electric powered, pusher propeller drone has a wingspan of 795 mm, an overall length of 750 mm, and a take-off mass of 900 g respectively. The delta-wing airframe of the Funjet drone is manufactured by Multiplex GmbH and is made out of lightweight EPP foam material (expanded polypropylene). The drone's propulsion system consists of an electrical brushless engine (AXI 2212/26) with a 9"x 6" propeller that is powered by a 2500 mAh Lithium polymer (LiPo) battery pack to give it an endurance of 20-30 minutes. A landing gear and a landing foil protects the FRAP probe from damage during landing.

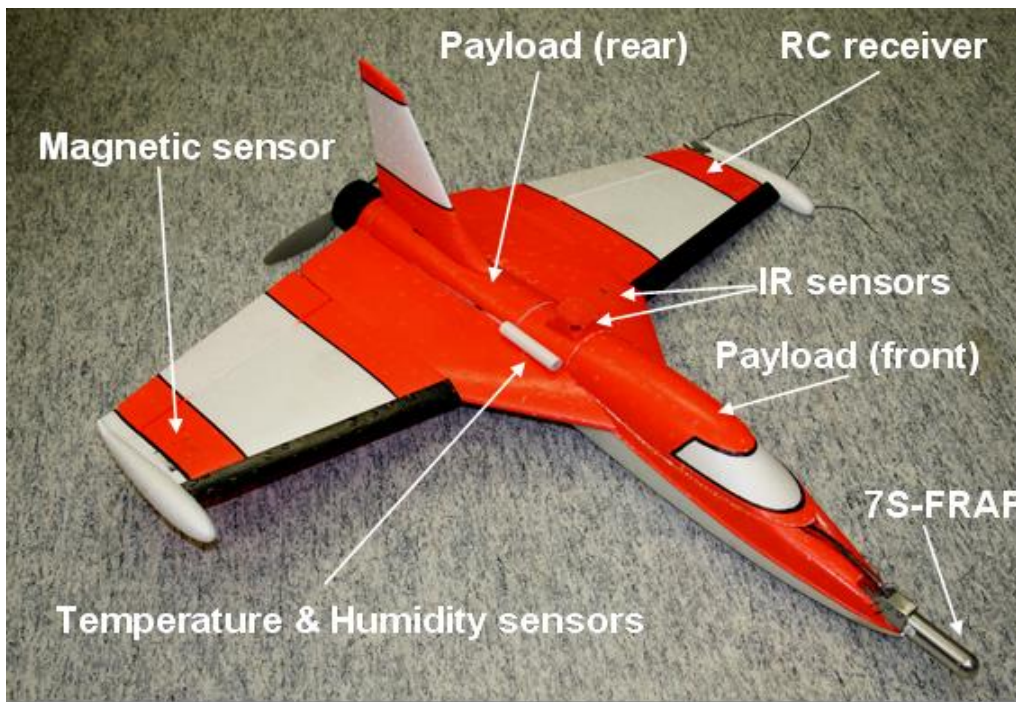


Figure 26. Funjet drone.

2.3.2 2nd Generation Drone: WindFlyer

The LEC's 2nd generation pusher propeller drone is called windFlyer, Figure 27. Unlike the 1st generation foam-based Funjet drones, windFlyer is an all composite airframe structure designed for heavier payloads and longer flight times. A fully instrumented windFlyer drone weighs 3 kg and has a maximum endurance of more than 2 hours (with an 8000 mAh LiPo battery pack). The drone is built with a vacuum bagging technique for superior flight performance and its aerodynamically efficient design results

in a low drag of ~ 2.4 N at a nominal cruise speed of 20 m/s. During wake measurements, this efficient aerodynamic design helps to minimize drone induced flow disturbances and thus improves the measurement accuracy. In addition, the high aspect ratio (AR) of 12 gives windFlyer a superior gliding performance and stability. A landing gear protects the FRAP probe from damage during landing, while a foldable propeller and flap ensure safe landing performance.

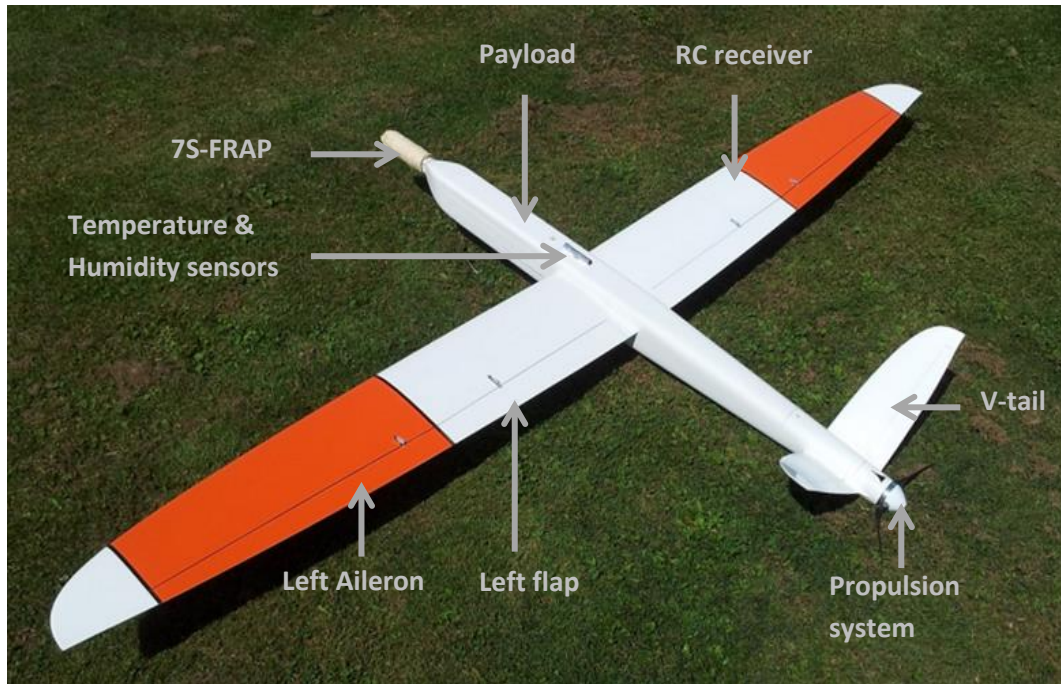


Figure 27. WindFlyer drone.

2.4 WindFlyer Drone

2.4.1 Aerodynamic Analysis

WindFlyer in steady level flight is subjected to aerodynamic loads (lift and drag) which are counterbalanced by weight and thrust respectively. Thus, the aerodynamic loading needs to be calculated to provide inputs to structural simulations. The panel code AVL was used to determine the aerodynamic forces and moments acting on windFlyer in mid-air. This panel code helps in quick but accurate computation of aerodynamic coefficients, without need for complex, three-dimensional Computational Fluid Dynamic (CFD) simulations.

Antenna Vortex Lattice (AVL)

The panel code AVL was chosen to evaluate the aerodynamic eigenfrequencies - to check if this can trigger a structural failure - of windFlyer over the complete flight envelope. Unlike XFOIL, it is possible to model the complete windFlyer drone in AVL and to analyze its aerodynamic characteristics. A windFlyer drone modelled in AVL is shown in Figure 28. This drone has 4 control surfaces, namely, the flaps (25 % of airfoil chord), the ailerons (25 % of airfoil chord) and the V-tail carrying the elevator and rudder (20 % of airfoil chord). All control surfaces were modeled and their effectiveness analyzed in detail with AVL. As seen in Figure 28, the drone fuselage was modelled as an axisymmetric body.

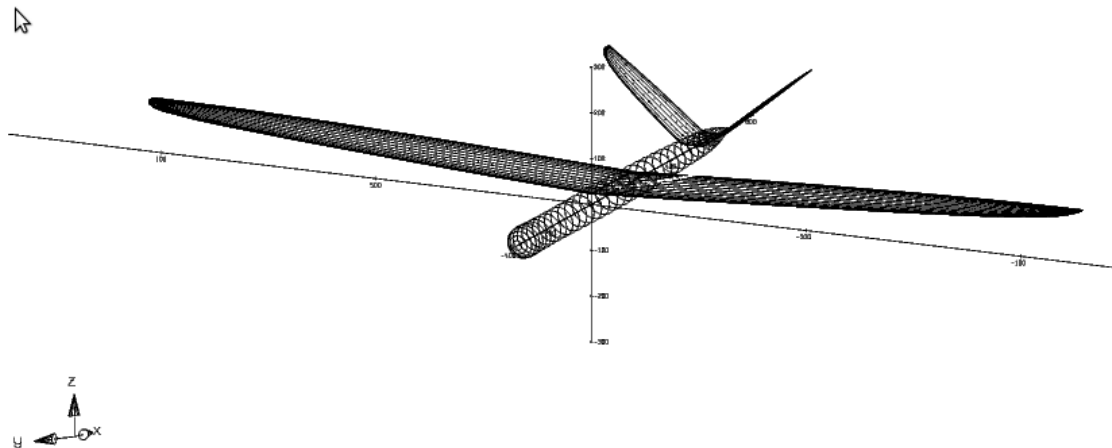


Figure 28. WindFlyer drone modelled in AVL.

Stability and Control

An eigenmode analysis was performed in AVL to assess the

aircraft's dynamic behavior. This process used inputs from both mass and geometry files - which also specified the aircraft's operational parameters including the component surface areas and moments of inertia, operating C_L , airspeed and density - to compute the eigenmodes of the system. Each of the conjugate pairs obtained from AVL (shown in Figure 29 and in Table 4) characterize a stability mode of the system. The dihedral provides excellent roll stability with high roll damping factor (i.e. 1), thus damping any motion within a second. The dutch roll mode is damped with a damping factor of 0.074, and takes about 25 seconds to return to steady state. The spiral mode is positive and undamped. The pitch behavior of the drone is characterized by a long and short period mode represented by the red and black circles in Figure 29. The phugoid mode results from a trade between kinetic and potential energy as the aircraft undergoes a series of subtle, yet lengthy, pitch oscillations. However, the frequency of the oscillation is sufficiently low at 0.07 Hz, and thus helps to maintain a stable altitude during flight. The high frequency short period mode is heavily damped, indicating strong pitch stability.

Modes	Eigenvalues		Mode description	Time period (s)
	Real	Imaginary		
1	-5.307	0.000	Roll Damping	
2	-0.162	2.187	Dutch Roll	2.87
3	-0.162	-2.187	Dutch Roll	2.87
4	-4.194	3.235	Short period	1.94
5	-4.194	-3.235	Short period	1.94
6	0.027	0.000	Spiral	
7	-0.225	0.438	Phugoid/Long period	14.35
8	-0.225	-0.438	Phugoid/Long period	14.35

Table 4. windFlyer eigenvalues and modes from AVL.

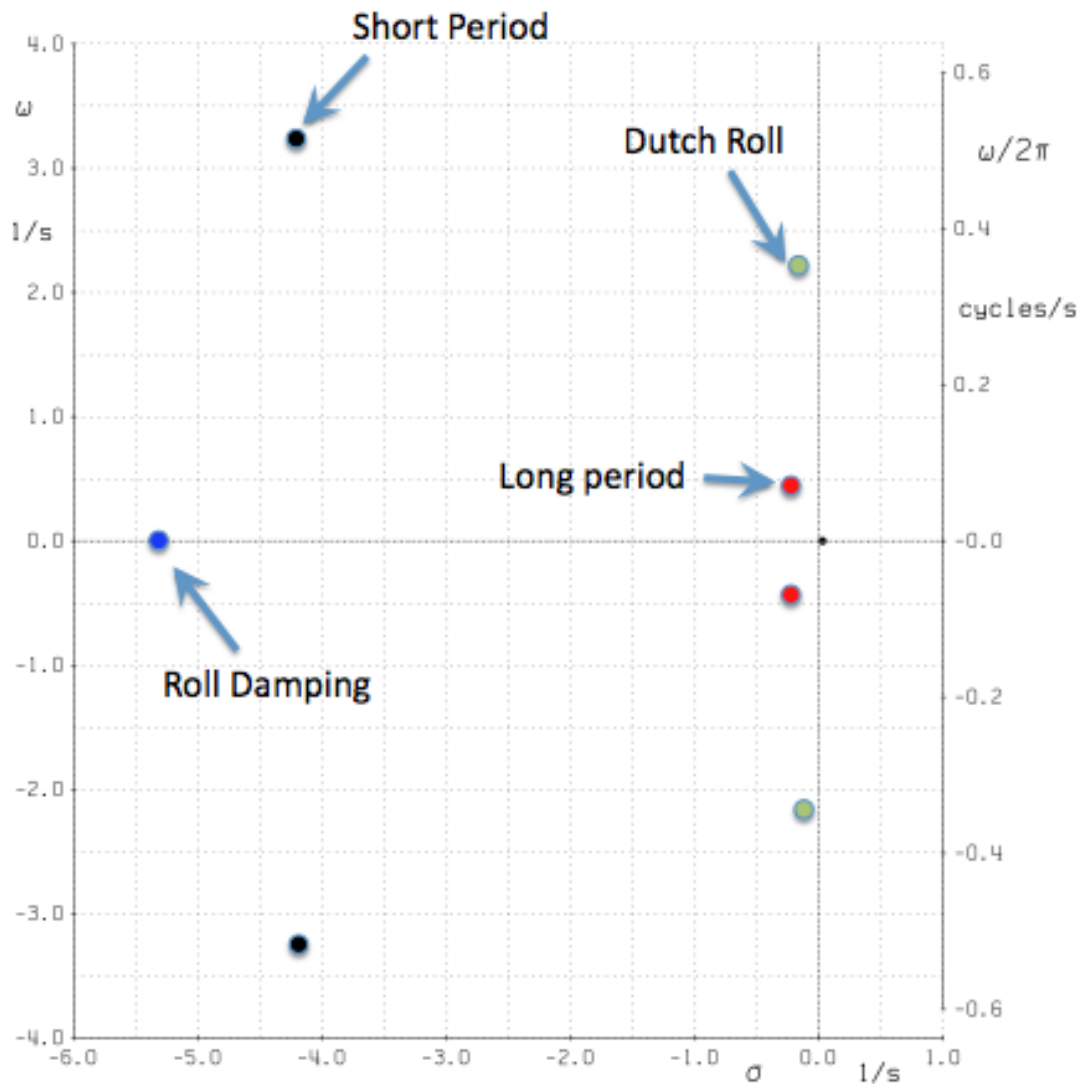


Figure 29. WindFlyer eigenmode analysis in AVL.

Center of Gravity

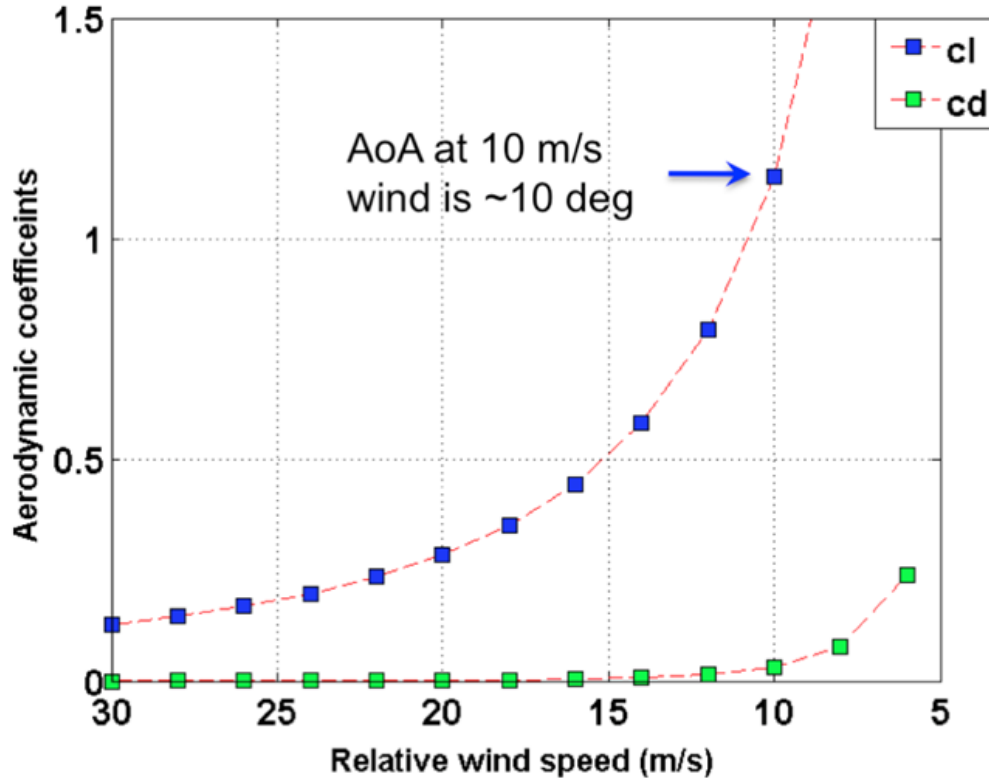
The location of the Center of Gravity (CG) heavily influences the pitch dynamics of the aircraft. Thus the static margin needs to be evaluated to check the positive pitch stability at different cruise speeds. From AVL, the drone's CG is found to be located at a distance of 68.75 mm behind the leading edge of the wing. So we can use Equation 16 to compute the Static Margin (SM). It must be emphasized here that the LiPo battery (payload) location in windFlyer could be varied to sufficiently adjust the CG of complete drone, and the present battery location is 110 mm ahead of the wing leading edge. The aircraft's neutral point varies, so test cases were run in AVL to assure that the possible CG locations produced acceptable SM throughout the flight envelope. The SM was found to vary from 6.1% at maximum flight speed (30 m/s) to 11.1% at takeoff (with flaps and speed

of 10 m/s), which are within acceptable bounds.

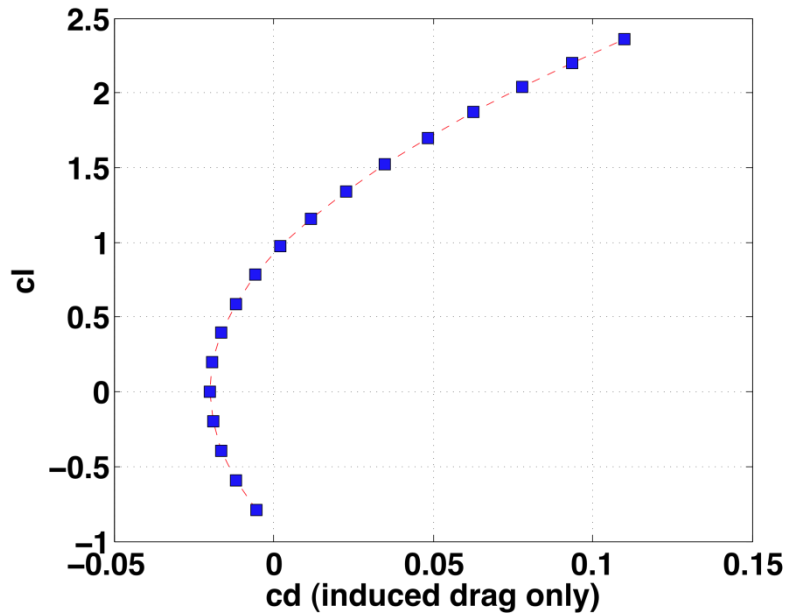
$$SM = \frac{(x_{np} - x_{cg})}{c} \quad (16)$$

Drag Polar

The variation of aerodynamic coefficients at different cruise speeds and the characteristic drag polar of windFlyer obtained from AVL are shown in Figure 30. These lift and drag coefficients define the aerodynamic performance of the drone. The aerodynamic characteristics at different cruise speeds and for different trim conditions are tabulated in Jacobi [73]. As AVL is an invicid solver, a profile drag of 0.02 is considered for all AVL drag calculations. The shape of the wing tip provides the windFlyer wing with a span efficiency factor of 99.8 % (negligible induced drag) during a cruise speed of 16 m/s, and this results in an L/D ratio of 25-30. The shape of the airfoil in the windFlyer wing and V-tail is ‘SM8016M’. Based on the stall angle computed for ‘SM8016M’ from XFOIL, the minimum safe cruise speed is 12 m/s without flaps and is 8 m/s with flaps deployed at 30°.



(a)



(b)

Figure 30. (a) Aerodynamic characteristics of windFlyer at different cruise speeds, (b) Drag polar of windFlyer obtained from AVL.

Treffz Plane

The Treffz plane is used to visualize the lift distribution along a wing span, Figure 31. Figure 31 shows that the lift distribution (dashed line) along the wing span is nearly uniform and falls sharply at wing tip. Thus, the windFlyer wing produces very low induced drag [73]. It also demonstrates that there is no local stalling in the wing at any section of the span and that the lift distribution is nearly elliptical. The fuselage wake is neglected here and both wings are assumed to be connected. The longitudinal stability derivatives at a cruise speed of 18 m/s obtained from AVL are tabulated in Table 5.

$\alpha = 1.9025$ $\phi b/2V = -0.0000$ $C_L = 0.3858$ $C_I = -0.0000$
 $\beta = 0.0000$ $q c/2V = 0.0000$ $C_Y = -0.0000$ $C_m = -0.0000$
 $M = 0.000$ $r b/2V = 0.0000$ $C_D = 0.02352$ $C_n = 0.0000$
 Flap = 0.0000 $C_{D1} = 0.00352$ $e = 0.9975$
 aileron $C_{Dp} = 0.02000$

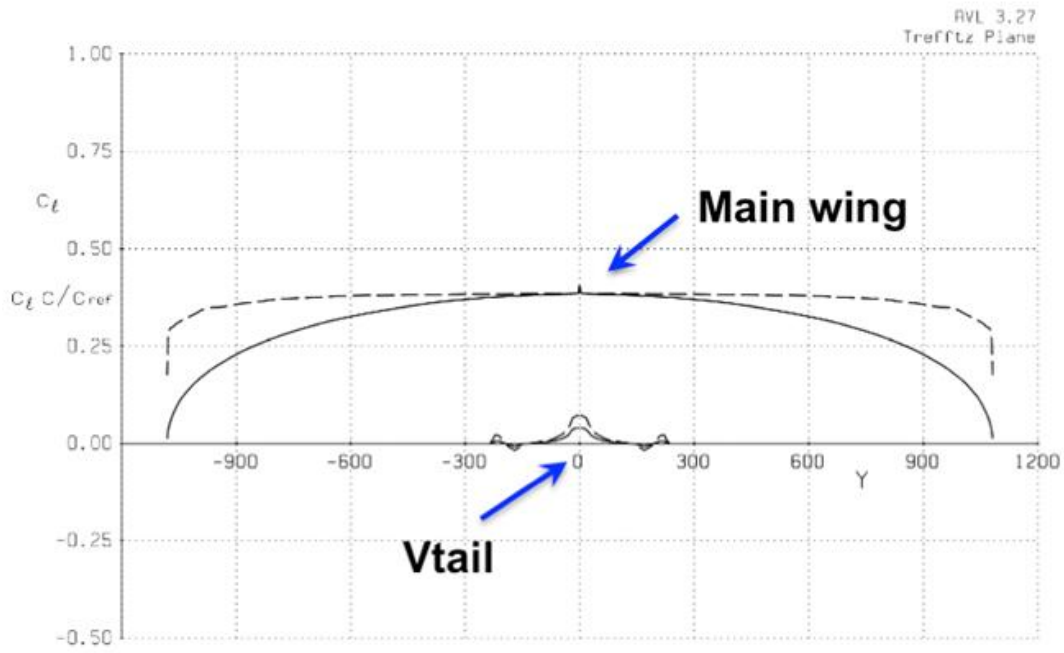


Figure 31. Lift distribution along wingspan: Solid Line represents the lift per unit span. Dashed Line represents local lift coefficient C_L .

Parameter	Stability derivative (1/rad.)
$C_{L\alpha}$	5.79
$C_{m\alpha}$	-0.44
$C_{n\beta}$	0.03
$C_{l\beta}$	-0.08
C_{lp}	-0.61
C_{Lq}	6.39
C_{lr}	0.10

Table 5. Longitudinal Stability Derivatives at a cruise speed of 18 m/s.

2.4.2 Structural Analysis

A circular load bearing beam connects the windFlyer fuselage with its wings. This beam is made from hard foam by weaving and wrapping carbon fibers around it to take the loads and to inhibit large deformations. To capture the effect of this beam in analysis, a surface is added in the DesignModeler of Ansys Workbench [69], Figure 32. This surface connects the suction side of the wing to its pressure side. In simulations, this beam is characterized by its thickness (0.26mm) and material properties (carbon fiber weaving). The hard foam was neglected for analysis. The beam is positioned at quarter-chord distance from the wing leading edge. The resulting geometry can be seen in Figure 32. In reality, the windFlyer has another beam – a much smaller one - within its main wing that is situated close to its trailing edge. It is assumed here that this second beam is a supporting element and thus omitted in simulations (conservative approach).

A structured shell mesh is a prerequisite to model orthotropic laminates. Since windFlyer is modeled solely by its outer surface, a wall thickness has to be applied to every surface within the Ansys Workbench. The advantage of using surfaces with a predefined thickness is that the mesh generator uses shell elements instead of the more costly solid elements. To generate a smooth mesh, the option for advanced sizing “fixed” was used. By specifying minimal and maximal size limits, a structured mesh with approximately 140'000 nodes and 46'000 elements was obtained. When using the volume model for meshing, the number of nodes easily exceeds 500'000.

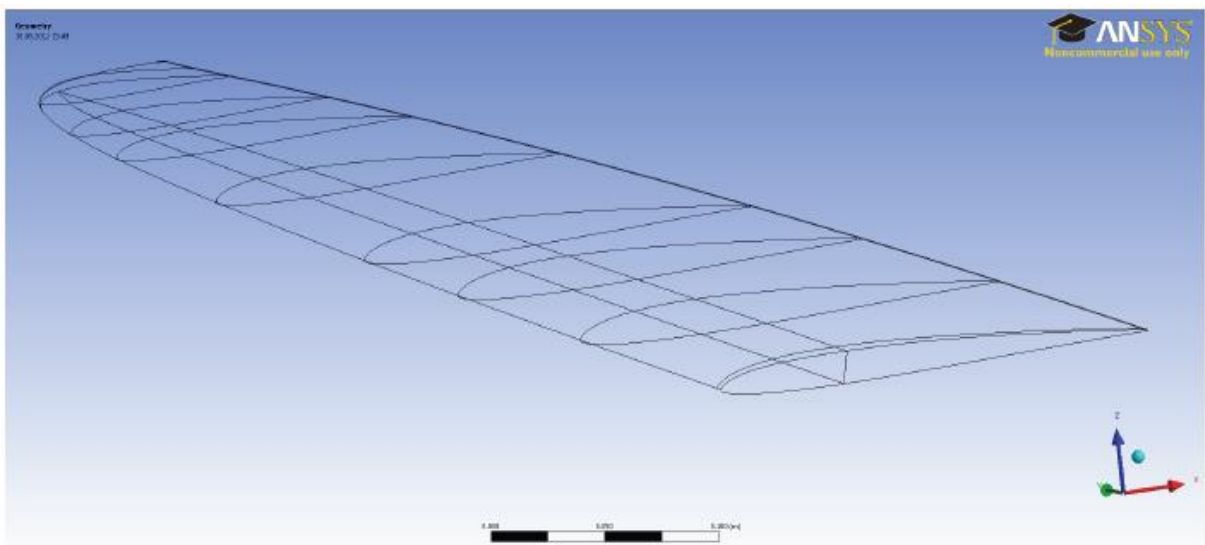


Figure 32. Ansys wing geometry with carbon spar beam.

Composite Modeling

The composite material of windFlyer does not have homogenous properties. It uses different layers in the fuselage and wings, consisting of hard foam, epoxy, glass and carbon fiber weavings. To account for the resulting anisotropic behavior and to avoid modeling each layer separately in a CAD-program, a new orthotropic material – whose behavior is similar to the actual laminate – was created. As the drone's wall thickness is small compared to the other geometrical dimensions, a two dimensional plate theory can be used and a three dimensional solid mechanics problem can be avoided. This implies that the material properties can be described by one E-modulus, one G-modulus and two Poisson ratios. One material was designed for the wings and a second one for the fuselage. The actual geometry of both laminates can be seen in Figure 33. The properties of the glass and carbon fiber plies are found in [73]. The epoxy used is Carboplast “L285” and the hard foam is Rohacell “51 IG/IG-F”. It should be noted that the actual fuselage laminate of windFlyer has a second 296 g/m² glass fiber layer in the vicinity of the connection to the main wings. This second layer is neglected in this analysis, which represents a conservative approach.

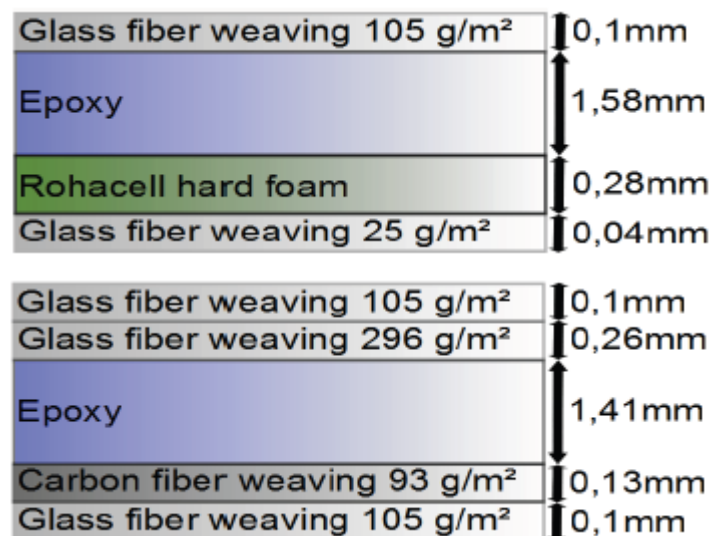


Figure 33. Laminate plies of wing (top) and fuselage (bottom).

A program called “ESAComp” was used to calculate the material properties of laminates made up of various plies (i.e. to obtain realistic laminate properties). ESAComp is a software for the analysis and design of composites [74] and its development was initiated by the European Space Agency (ESA).

- The glass fiber weaves of windFlyer are modeled by the ply “E;Epoxy;F-.130/169/50”. The area density (in g/m²), the fiber

volume content and the thickness are customized to account for the different glass fiber weaves.

- For the carbon fiber weave, the ply "T300;Epoxy;F-.220/193/50" is chosen with the area density, fiber volume content and thickness adapted in the same way as mentioned in glass fiber.
- The hard foam is modeled by "51 IG;FC-/52".
- The epoxy is modeled by "Hysol EA 934NA".

When the two laminates are composed of their individual plies, the material properties are calculated by ESAComp, Figure 34.

			Fuselage	Wings
Moduli (GPa)		E_x	11.49	4.33
	In-plane	E_y	11.49	4.33
		G_xy	1.78	1.04
	Out-of-plane shear (including shear distortion correction)	G_zx	0.96	0.12
		G_yz	0.96	0.12
Poisson's ratios		nu_xy	0.146	0.278
	In-plane			
		nu_yx	0.146	0.278

Figure 34. Equivalent material properties of fuselage and wings. Material properties of laminates calculated with ESAComp [69].

Boundary Conditions

The main wings are cut into 11 sections and the V-tail into 2 sections. On each of these sections a specific lift force computed from XFOIL (for a given true airspeed) is applied such that the sum of these forces balances the weight of the plane and its components. If the sum of the lift forces is too low, the AoA is increased and vice versa. For a given airfoil geometry at a particular wind speed, the AoA defines the moment and drag force on each surface. The sum of the drag forces is balanced by the thrust. Attention needs to be paid to the direction of the lift forces on the V-tails, which are rotated approximately 39° relative to the horizontal direction. The forces acting on the fuselage in Z direction (in Workbench convention) are windFlyer's weight and the weights of the various on-board

payloads. To compute the weights, a gravitational constant of 9.81 m/s^2 was used. Arrows in Figure 35 show the representative boundary conditions used for analysis.

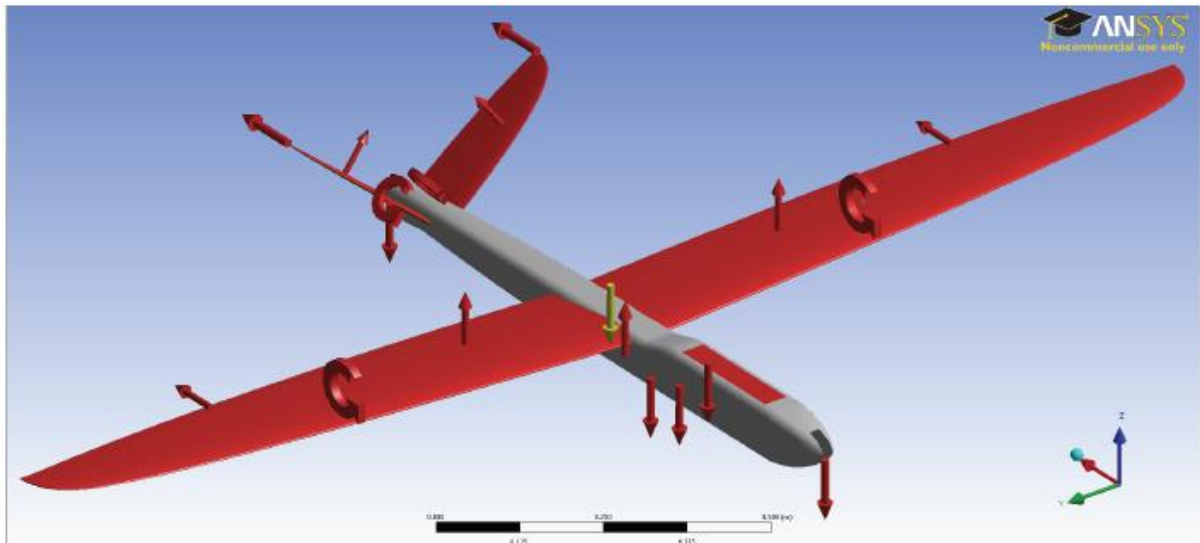


Figure 35. Boundary conditions.

The following five different scenarios were analyzed:

- Take-off and landing: During take-off and landing, a relative wind speed of 10 m/s was used. To be able to lift off the ground at such a low speed, the lift coefficients need to be as high as possible to overcompensate the total weight of windFlyer. Thus, the critical stall-angle is found by evaluating C_L for various AoAs and choosing the AoA with highest C_L . Flaps are on (30°) and the AoA was found to be 5° .
- Cruise: During cruise, the relative wind speed is assumed to be 15 m/s . The AoA was iterated until weight=lift. It was found to be 3° with flaps unemployed.
- High speed: In order to evaluate stress and strain at maximum flight speeds, a high speed case was evaluated. The relative wind speed is 25 m/s and flaps are off. The AoA was found to be 0° .
- Banking maneuver: To obtain values for a maximal stress scenario, a banking maneuver was analyzed. The bank angle is 40° , the relative wind speed is 25 m/s , the AoA is 0.8° , flaps are off, ailerons are at 2° , the turn radius is 76 m and a side slip of 15° is applied. This results in a load factor (= Lift/Weight) of 1.3 . The boundary conditions chosen are extreme and unlikely to occur in reality.
- Wind tunnel: windFlyer to be tested in the wind tunnel to obtain the aerodynamic coefficients required an "optimized flight plan" tool [81]. In the wind tunnel, a strut is fixed to the base plate inside the

fuselage. To check if this base plate can endure the aerodynamic loads, one scenario was evaluated with a wind speed of 25 m/s, an AoA of 0.8° (resulting from windFlyer's geometry) and flaps are off.

Composite Failure

Composites have complicated failure modes. For a single ply of a unidirectional fiber-reinforced matrix, the stress-strain curve is highly non-linear, Figure 36 [75]. In the first stage, matrix and fiber are deformed elastically. At a certain limit, microcracking occurs within the matrix (not visible and difficult to detect). The fibers have to withstand the additional stresses and stress concentrations occurring at the cracks. Once the fibers' maximal strength is exceeded, the laminate fractures. This process can be seen in Figure 36.

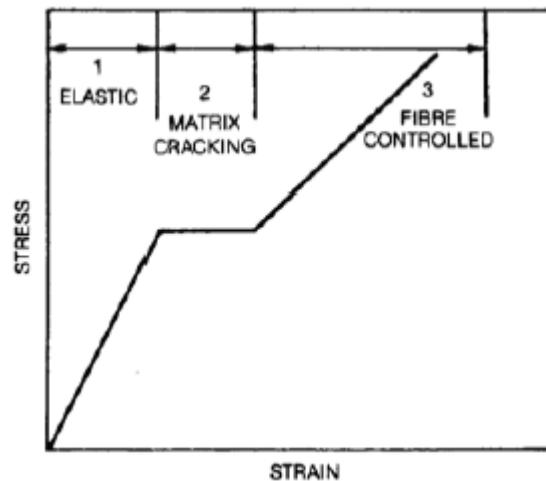


Figure 36. Idealized tensile stress-strain curve for a fiber reinforced cement [75].

In this project, the laminates are made up of various plies. Additionally, the plies do not have unidirectional fiber-reinforcement but have weavings, where interactions between the fibers have to be taken into account. This implies that no single value as a criterion for failure can be given without performing material tests. Instead, experiences and empirical values have to be used here. For materials with homogenous properties, fatigue values can be easily found from Wohlers curves. For laminates, this is not the case. Even for the same type of specimens and loads, life dispersions occur due to the heterogeneous nature of the laminates [76]. Thus, it will not be possible to make realistic estimations about fatigue failure or life-time expectations.

Strain Criterion

For composite materials, one important failure criterion is the maximal principal strain. In aviation, a widely used value is 0.4% for composites [77]. If all strains stay within this limit, matrix cracks are unlikely to occur and local damage can be avoided. This value includes a safety factor of 1.5. The fracture strains of the fibers are much higher and reach values of up to 2%. Thus, the laminate's maximal endurable strain will be limited by the matrix properties. Since in aviation people's lives are at stake and the planes are designed for a lifetime of over 20 years with intensive usage, it will be assumed that windFlyer will easily cope with any strains below this value. All cases will be evaluated by specifying the maximum principal strain. In order to obtain a grasp of all occurring strains (and not only the principal strains), the equivalent strain distributions will be shown as well. The maximum values of the equivalent strains will be above the maximum values of the principal strains. The equivalent strain is advantageous because it allows any three-dimensional strain to be expressed by a single strain value. Ansys 13.0 calculates the equivalent (von Mises) strain with Equation 17. The other relevant criterion connected to composites is the 'stress criterion'. This criterion can however only be used if each layer is modeled separately and hence the stress distribution can be evaluated in each ply. Since in this project the composite is modeled as a single equivalent laminate, this criterion will not return reasonable results.

$$\epsilon_e = \frac{1}{1+\nu'} \left(\frac{1}{2} [(\epsilon_1 - \epsilon_2)^2 + (\epsilon_2 - \epsilon_3)^2 + (\epsilon_3 - \epsilon_1)^2] \right)^{\frac{1}{2}} \quad (17)$$

where ν' is the effective Poisson's ratio and ϵ_i are the principal strains in direction (i=1, 2 and 3).

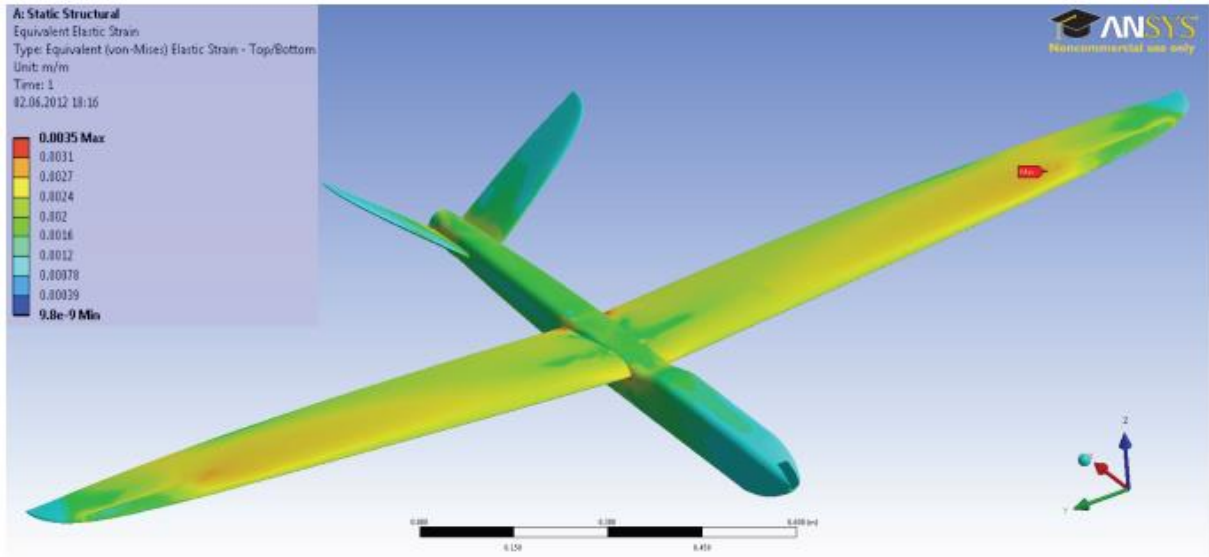


Figure 37. Equivalent strain distribution of windFlyer during take-off/landing.

A summary of results from the five different scenarios analyzed is as follows

- Take-off and landing is shown in Figure 37. Since the maximal principal strain is 0.21% and occurs in the carbon beam (and not the laminate), the structure is expected to withstand take-off and landing conditions without problems.
- For cruise conditions, the maximum principal strain of 0.26% is reached in the same carbon beam as before and there are also strains of 0.1% in the connection between wing and fuselage. The strains occurring in the cruise scenario are smaller and thus considered less important than the high-speed scenario.
- In the high-speed scenario, the highest strain of 0.26% occurs again in the carbon beam. Another strain concentration occurs at the interface of main wings and fuselage at the leading and trailing edge. The maximal principal strain is below 0.18% at these locations.
- The highest maximum principal strain in the banking maneuver occurs in the carbon beam and has a value of 0.36%. The highest maximum principal strain that occurs in the laminates is 0.23% and is located - as mentioned before in the high speed scenario - at the interface of main wings and fuselage at the trailing edge.
- In the wind tunnel case, the maximal principal strain is approximately equal to the high speed scenario. This makes sense as the same wind speed is applied. The maximal principal strain in the plate (on which the windFlyer is mounted in the wind tunnel with a strut) is 0.09% and occurs close to the empty square in the center of

the plate where the strut is attached. This value is far below the strain criterion used, so failure is improbable.

2.4.3 Wind Tunnel Testing of WindFlyer

The IFD wind tunnel (at ETH Zurich) is a closed loop wind tunnel with an octagonal test section, Figure 38.

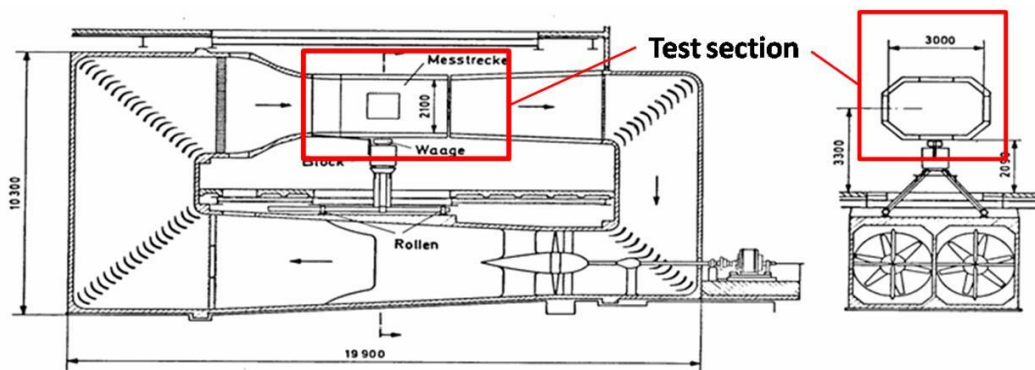


Figure 38. Overview of the IFD wind tunnel, ETH Zurich [79].

A fully instrumented windFlyer was tested in the IFD wind tunnel to completely characterize its aerodynamic performance and to assess the accuracy of its flow measurement system. The test section has a height of 2 m and a width of 3 m. At this point, it has to be mentioned that the dimensions of the IFD wind tunnel are not optimal to measure the aerodynamic properties of the windFlyer with high accuracy. The reason is the windFlyer's large wingspan of 2.25 m, which is why the sidewalls influence the 3-dimensional flow field near the wing tips. Figure 39 shows a fully instrumented windFlyer mounted inside the IFD wind tunnel test section. A symmetric NACA-profile shaped foam shroud was custom built for the wind tunnel tests to prevent turbulent flow underneath the windFlyer fuselage. This foam shroud guides the flow around the load cell and cable connections. The pitch and yaw motions of the drone are controlled through a traversing system located underneath the strut. With the data acquisition system of the wind tunnel, the parameters - pitch and yaw angle, temperature inside the test section, wind speed (calculated with a Venturi-system) - were recorded with a sampling rate of 10 Hz. The forces and moments were acquired with the analog output system of the load cell [69].

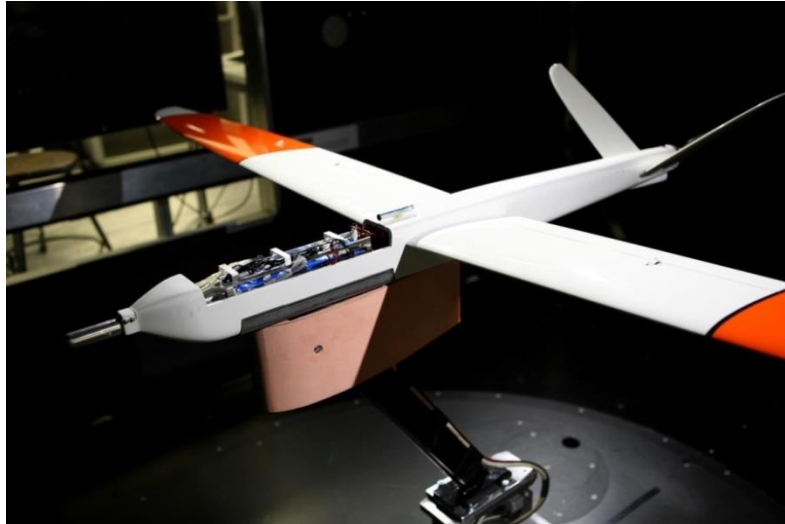


Figure 39. WindFlyer mounted in wind tunnel test section.

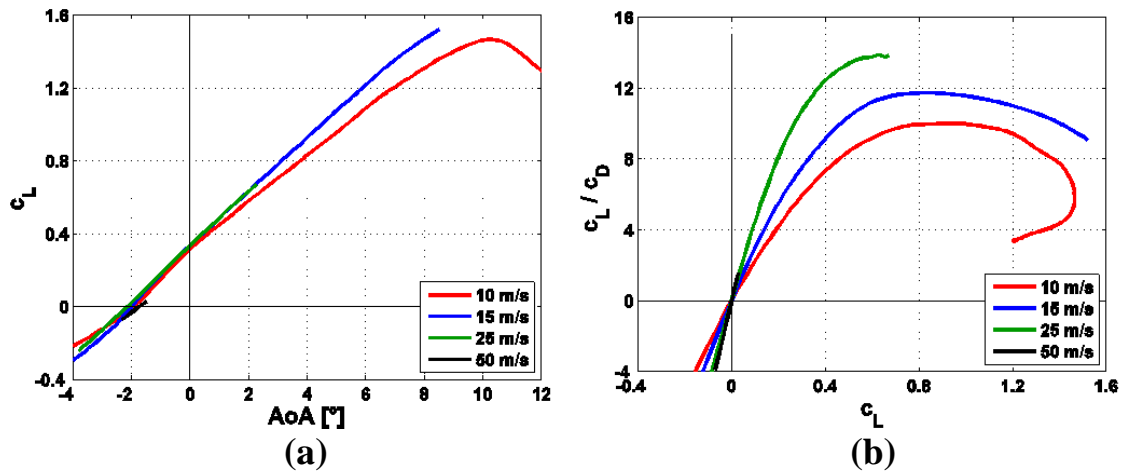


Figure 40. (a) Lift polars for four different airspeeds, namely 10, 15, 25 and 50 m/s. (b) Lift to drag ratio for four different airspeeds, namely 10, 15, 25 and 50 m/s.

The drone was tested in the wind tunnel at four different speeds in the range of 10-50 m/s, and the resulting lift polars and lift-to-drag ratio curves are plotted in Figure 40. The plots show the influence of Reynolds number on the aerodynamic characteristic curves, and the aerodynamic efficiency of windFlyer increases with airspeed. At 10 m/s, the maximum lift coefficient of 1.5 was observed at an AoA of 10° , and a further increase in AoA causes the wings to stall as the lift coefficient starts to drop. Figure 40 a suggests that the slope of the lift polar increases for higher wind speeds. This low speed tendency is typical for thin airfoils [78]. The lift-to-

drag ratio at different airspeeds shows clearly the influence of Reynolds number on the aerodynamic characteristic curves. According to the theory [69], a higher airspeed and hence a higher Reynolds number results in a lower c_D for the same c_L . This is clearly reflected in a variation of the maximum lift to drag ratio as a function of the airspeed, Figure 40 b. For 25 m/s the maximum lift to drag ratio is 13.9, which is 40% higher than the corresponding value for 10 m/s. Also at any c_L , it can be noted that the slope of the c_L/c_D curve increases with the airspeed from 10 m/s to 50 m/s.

Figure 41 shows the effect of flap deflection on the lift and drag polars of windFlyer. At 10 m/s, the maximum lift coefficient increases by 15 % with flaps extended from 1.5 to 1.72. The lift polar also shows that the angle of attack decreases by about 2° at c_{Lmax} , thus with flaps the wing stalls at a smaller angle of attack. This implies that - with flaps deployed - the stall speed for a fully-instrumented windFlyer weighing 3 kg is 9.1 m/s. However, this value is ideal and is only valid for horizontal level flights in undisturbed flow. Furthermore, the deflection of the flaps induces a dramatic shift in the drag polar as illustrated in Figure 41 b. At 10 m/s, the drag coefficient at c_{Lmax} increases by 24 % with flaps from 0.25 to 0.31. Thus, the flaps are effective in slowing down the windFlyer before landing. To ensure safety and the stability of any aircraft, a safety margin with respect to stall speed is necessary – thus a 30 % safety margin is assumed on all aerodynamic coefficients measured in wind tunnel.

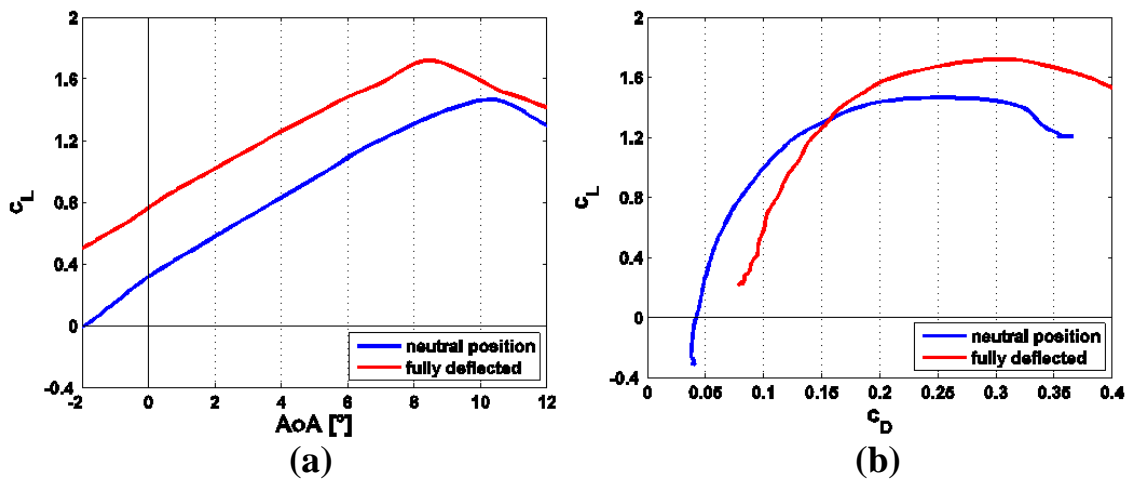


Figure 41. (a) Effect of flap deflection on the lift polar at 10 m/s. (b) Effect of flap deflection on the drag polar at 10 m/s.

One of the most prominent goals in windFlyer development - that directly helps in increasing the measurement duration per flight - was to maximize the drone's endurance. To maximize the useful measurement

duration, it is crucial to minimize the energy consumption at cruise speed and to optimize the flight plan. From the aerodynamic characteristics measured in the wind tunnel, the drag and propulsive power required for horizontal flight were calculated as function of the airspeed, Figure 42. In accordance with the theory [69], the drag curve clearly shows a minimum value of 2.14 N at an airspeed of 16.5 m/s. Figure 42 b shows the impact airspeed has on the required propulsive power. For horizontal flight, a cruise speed in the minimal drag region is desired in order to maximize the range of the aircraft and a cruise speed in the minimal propulsive power required region is desired in order to maximize the endurance of the aircraft. Based on field trials, a cruise speed of 19-20 m/s was chosen for all field measurements due to better flight stability in this region. Assuming that the efficiency of the propulsion system is not affected by the airspeed, the power consumption can only be minimized by maximizing the propulsive efficiency.

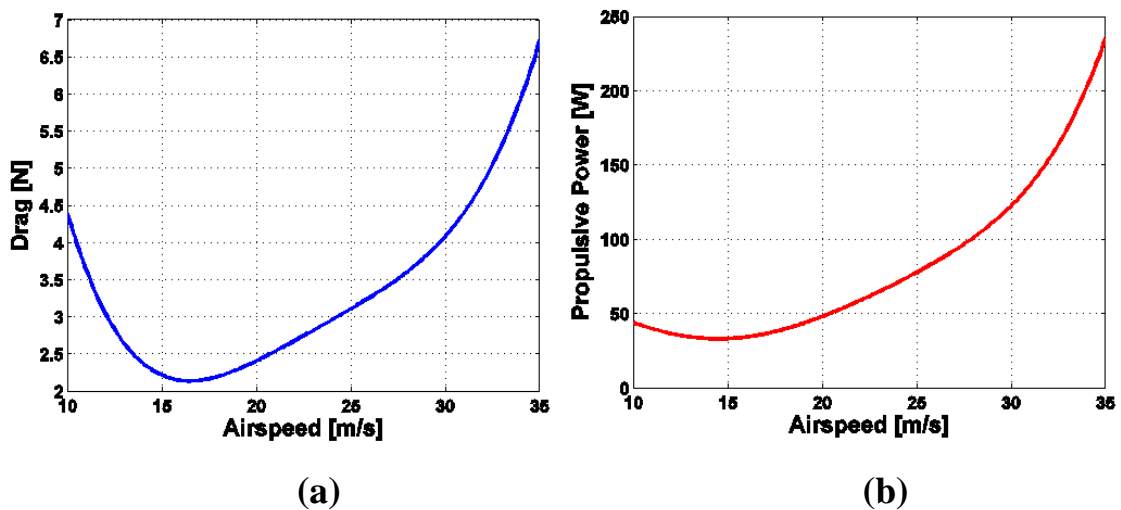


Figure 42. For horizontal flight, (a) drag as function of airspeed,(b) propulsive power as function of airspeed.

2.4.4 Propeller Selection

The windFlyer propulsion optimization tests were conducted at MG Erlenbach flight field, Switzerland, to assess the influence of flight dynamics parameters on the selection of the correct propeller-motor combination in a realistic environment. The propulsion optimization tests were planned with a series of flight tests. During this exercise, it was observed that the total flight time obtained with the existing propulsion system was more than 84 minutes, Figure 43. The battery voltage was seen to be stable during the run, but an abrupt drop was noticed after 10.5 V. As

the motor efficiency is a strong function of supply voltage and the voltage indicated by the paparazzi is conservative, the flight tests were carried out at voltages higher than 10.5 V. An oval trajectory (Figure 46) was chosen and flown with different propellers and motors, so that the energy consumed during flight allowed a direct comparison between different propellers.

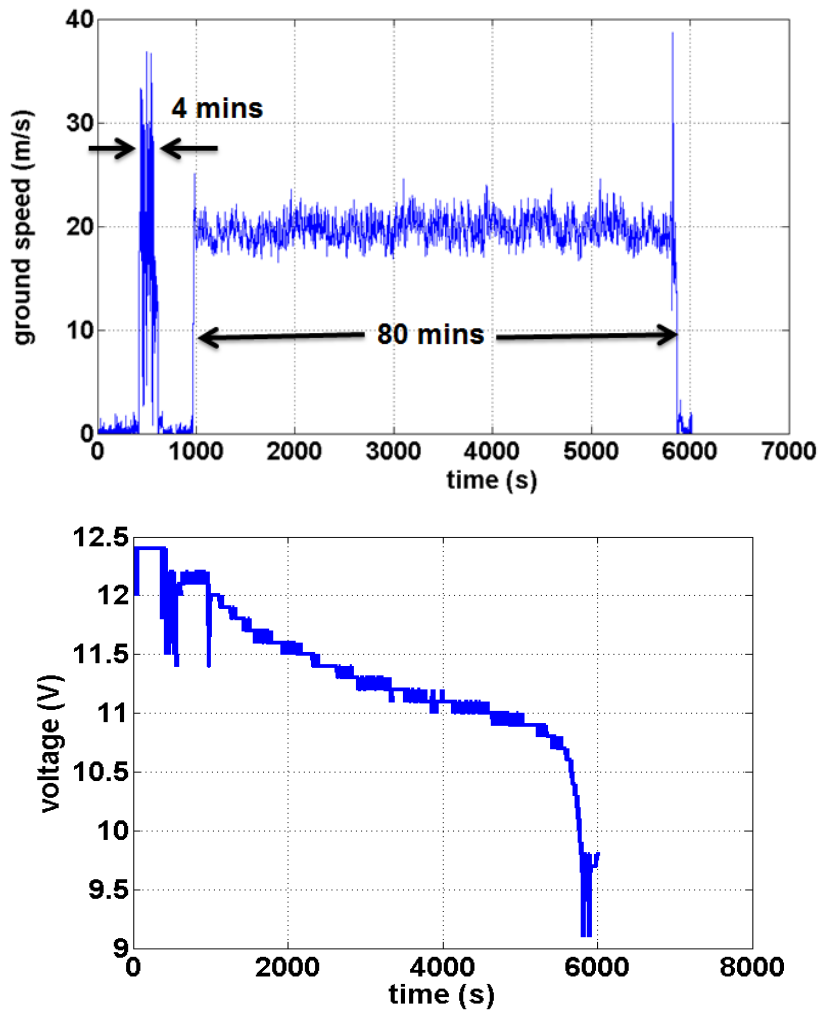


Figure 43. windFlyer reference flight, (above) ground speed variation with time, (below) LiPo battery voltage variation with time.

The weather forecast helped to choose the right days for flight testing with wind speeds less than 5 km/h. An RPM sensor (Figure 44) was added to measure the propeller revolution rate during flights at different air speed, in order to compute the advance ratio J . The measured RPM was transmitted through telemetry to the RC receiver and recorded manually at about 0.5 Hz. The airspeed measured with FRAP was then used to compute the advance ratio J .



Figure 44. Propeller rpm sensor.

Once the windFlyer was in air, the autopilot flew the standard oval trajectory for 3 loops at a cruise speed of 19 m/s with a throttle setting of 45%. Then the throttle setting in autopilot mode was varied from 25% to 85%, in steps of 10 %, to test each propeller at different flight speeds. The same oval trajectory was repeated (for 3 loops) at each different throttle settings. During the tests the actuator data and the energy consumption were logged at 2 Hz. Figure 45 shows windFlyer in the air and during landing.



(a)



(b)

Figure 45. windFlyer (a) in flight (b) during manual landing.

The initial flight tests were more focused on testing larger propeller diameters (diameter from 12" to 16") with a low rotational speed derivative (AXI 2814/32) of the original motor. During these tests, it was found that the larger propeller with the chosen motor does not produce enough thrust, thus affecting the takeoff and climb rate of windFlyer. The motor thrust scales with RPM. The same propellers were also tested with the original motor, but its higher rotational speed at full throttle overrated the current limitations of the motor thus forcing a change in the optimization approach. Furthermore, these initial flight tests yielded the observation that the tested propellers were operating at an advance ratio higher than the optimal value. To confirm this observation, measurements and verification with an RPM sensor were needed.

Implications of Cruise Speed on Trajectory Flown by Autopilot

In field tests, it was observed that the autopilot cruise speed setting affects the windFlyer trajectory accuracy. Figure 46 shows the windFlyer trajectory in the XY plane at three different cruise speeds with an 11x8 AN propeller and AXI 2814/16 motor. It can be clearly seen that if the cruise speed is chosen to high, the trajectory accuracy is compromised especially in the turns. For very low speeds, a deviation of the accuracy in the phases of horizontal speed was identified. A further decrease of the cruise speed setting yielded a very unstable behavior of the drone, which indicates that it

navigated close to the stall speed. The standard deviation of height however, was not compromised and stayed below 2m for all runs. This implies a trade-off between the maximization of flight time and the quality of the field measurements. A major deviation of the trajectory yields a penalty regarding the measurement efficiency [81]. To conclude, it is advisable to choose a cruise speed range between 17 m/s and 22 m/s in order to guarantee the quality of field measurements.

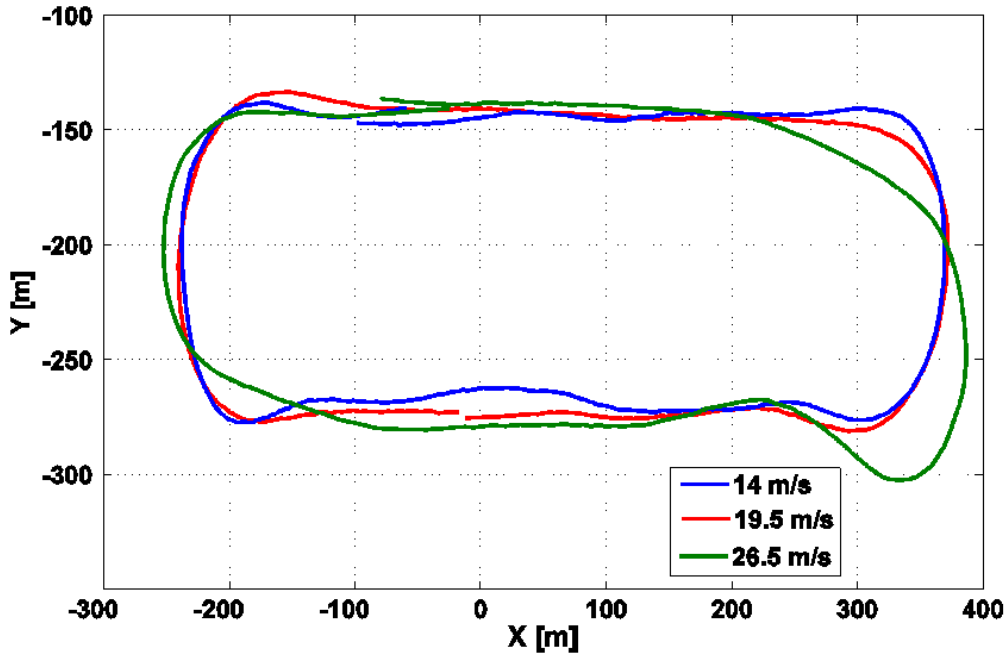


Figure 46. Impact of cruise speed of windFlyer trajectory accuracy.

The required electric power for straight horizontal flight can be written as

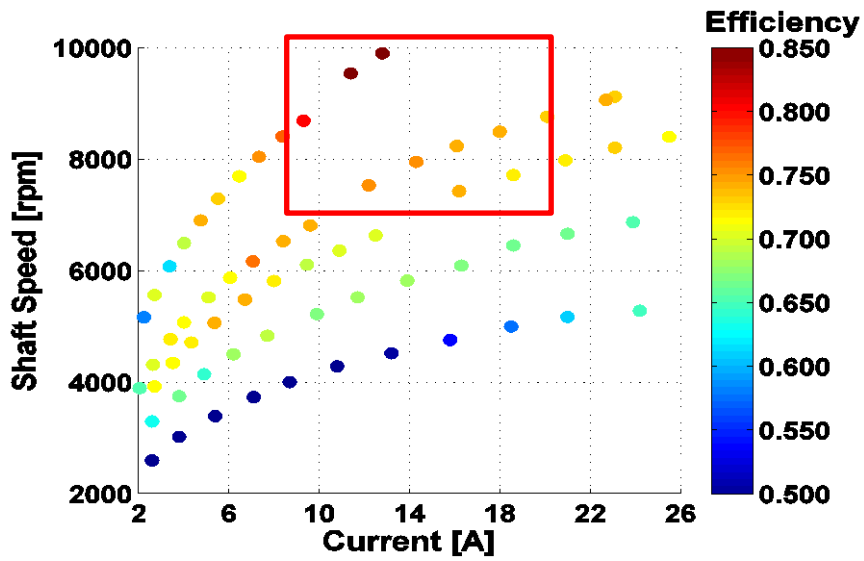
$$P_{elec} = \frac{D \cdot V}{\eta_{motor} \cdot \eta_{propeller}} \quad (18)$$

From flight tests, the efficiency of the different propellers was evaluated within the periods of straight level flight.

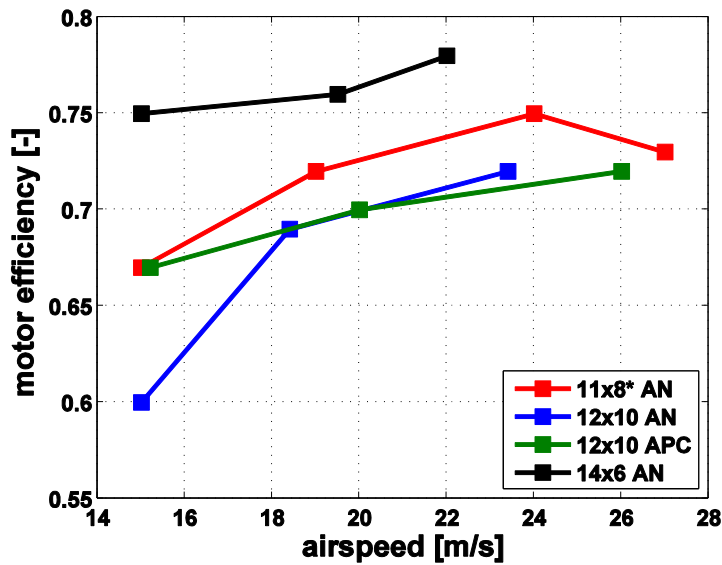
Motor Efficiency

As described in [82], the efficiency of motor was assessed in order to

quantify the associated losses during cruise flight. The evaluation of static tests indicates the influence of rotational speed and current on the motor efficiency. The efficiency for the measurement points is depicted in Figure 47 a. In accordance with the measurements carried out by [83], the efficiency is maximized for currents between 8-20 A and at high throttle settings (area highlighted in red). However, in cruise flight the motor operates at lower currents and rotational speeds, which are associated with higher losses. Figure 47 b shows the efficiency of the motor measured in straight level trajectories during flight tests.



(a)



(b)

Figure 47. (a) Motor efficiency of AXI 2814/16 at part load. The area highlighted by the red rectangle suggests the ideal operational regime of the on-board motor to maximize its operating efficiency at cruise speed, (b) Motor efficiency for different propellers at different airspeeds.

For a cruise speed above 20 m/s, the motor efficiency is above 70%. Since the maximal efficiency of the AXI 2814/16 is 82%, the losses associated with the motor are relatively low. Remarkably, the 14x6 AN propeller showed a motor efficiency of more than 75% for all airspeeds. However, the flight time with this propeller was consistently the lowest of all tested propellers (see Figure 49). This translates in a higher overall power consumption and hence a higher current, which explains the high values of the motor efficiency for this propeller. Therefore, it can be concluded that the efficiency losses occur mainly at the propeller itself for the 14x6 AN propeller.

Propeller Efficiency

The variation of advance ratio with airspeed for different propellers is shown in Figure 48. It can be seen that the advance ratio (Appendix B) is nearly independent of the airspeed. Thus, the propeller operates at approximately the same efficiency. However, based on the propeller database [82] created by the authors of [84], it was shown that all the tested propellers were operating at an advance ratio higher than J_{opt} , hence yielding a relatively low efficiency (between 30-40%). Since by the choice of a suitable propeller the propeller efficiency can be enhanced to 60%, it can be concluded that the highest potential to further increase the flight time is in choosing the right propeller.

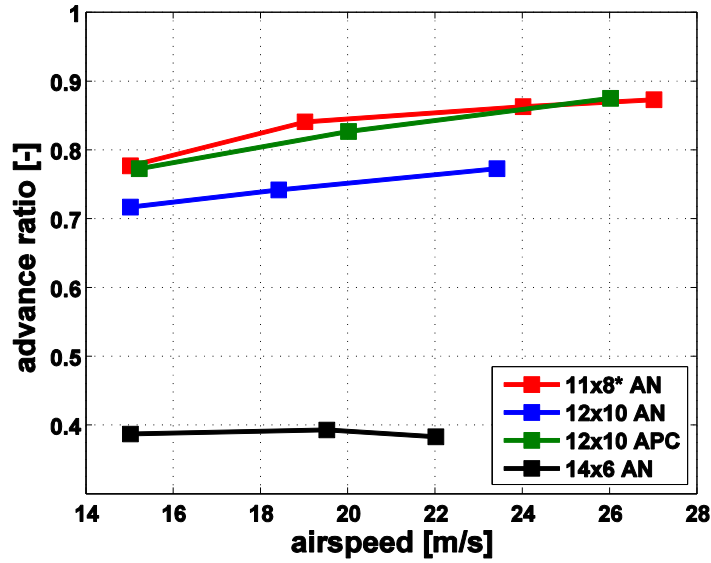


Figure 48. Advance ratio for different propellers at different airspeeds.

Adaptation of Cruise Speed

Based on the results from wind tunnel testing of windFlyer, it is evident that the airspeed has a tremendous impact on the power consumption, and hence on the flight time of the drone. The total flight time is the ratio between total energy stored in the battery and the average rate of power consumption from battery. The flight test results show the impact of ground speed on total flight time for different propellers, Figure 49. The total flight time decreases sharply with increase in ground speed and this trend is consistent for all tested propellers. The measurement point named “reference flight” refers to the endurance flight discussed in Figure 43.

$$t_{flight} = \frac{E_{battery}}{P_{average}} \quad (19)$$

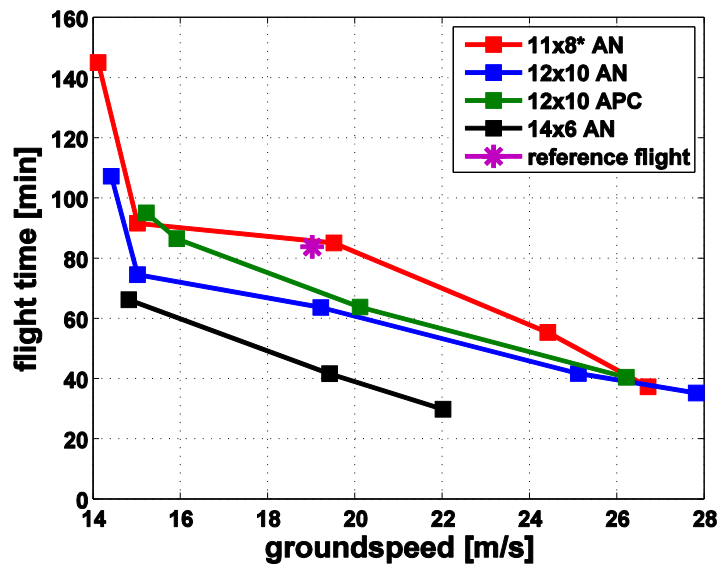


Figure 49. Effect of average ground speed on the flight time for different propeller

2.5 Other Accessories

2.5.1 Jig for IMU initialization

To initialize the IMU (roll and pitch) angles to a reference drone position before each flight in a repeatable way, a jig - that can support both Funjets and windFlyers in the field - was designed and manufactured in-house. The mechanical jig was build from aluminum and weighs 2 kg,

Figure 50 a. Before placing the drone, the jig was leveled in roll and pitch axis by independently adjusting the height of its four legs using a spirit level to make it horizontal. Before powering ON, a fully instrumented drone with a FRAP probe is then mounted on the mechanical jig. After placing the drone in the jig, the assembly is again adjusted in roll and pitch axis using a spirit level on the mechanical frame to ensure that it is horizontal. Thus at any measurement site the drone can be repeatably mounted on the same position before each flight. This ensures that the IMU is correctly referenced during initialization relative to the FRAP probe in a repeatable way. The jig also simplifies field assembly and helps in making the measurement less time consuming. Similarly after landing, the drone is mounted on the jig for offset gain measurements.



Figure 50. (a) Jig for IMU initialization.

2.5.2 Mechanical Frame

A mechanical frame was conceived for the generation I drones – Funjets – to support the FRAP probe and its associated electronics, and to provide stiffness/rigidity to its EPP foam fuselage. As EPP foam can deform during landing OR warp with time (Note: this can change the

orientation of a FRAP probe mounted on Funjet), a solution was needed to add stiffness/rigidity to the Funjet fuselage without adding significant weight. Thus, a mechanical frame with a box type design and weighing only 47 g (~ 5% of the total aircraft weight) was constructed from 1 mm thick aluminum sheets, Figure 51. This mechanical frame also prevents in-flight fuselage deformations, for example, the Funjet fuselage can bend in flight due to >150 g weight located ahead of its CG and due to aerodynamic forces. A deflection of just 3 mm at the aircraft fuselage nose can produce a 2° deflection in the FRAP probe axis that the IMU sensors will not be able detect. Both the FRAP probe and the FRAQ board are mounted on this frame, and the frame is leveled using a spirit level before each flight.

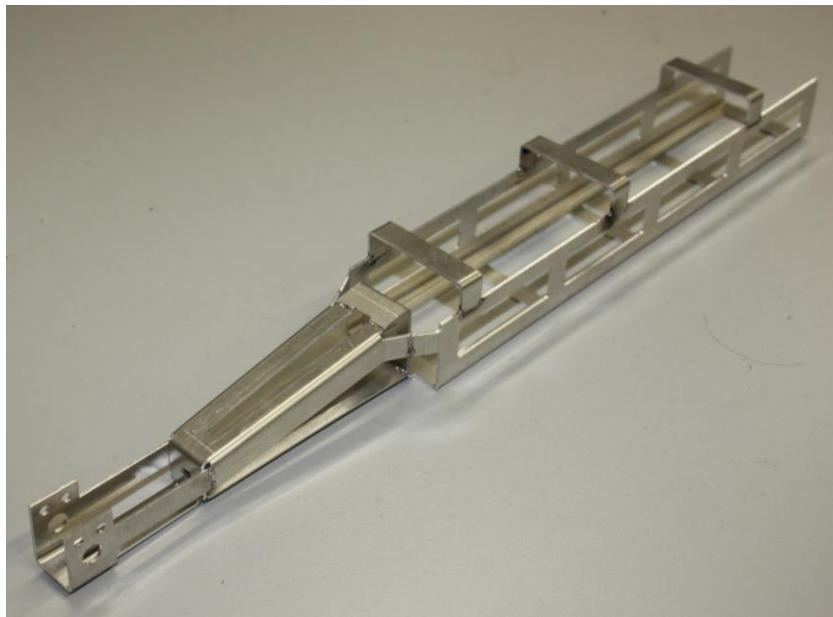


Figure 51. Mechanical frame to support the FRAP probe and its associated electronics on Funjet and windFlyer.

2.6 Paparazzi Autopilot System

Paparazzi is an autopilot system comprising of an open source hardware and software that enables autonomous flight [85]. The airframe hardware suite comprises an autopilot board – Tiny v2.11/TWOG, sensors – IMU, GPS, pressure, temperature etc, bi-directional data link radio modem, RC receiver, actuators, propulsion and battery. Both Tiny v2.11 and TWOG autopilot boards are designed around LPC2148 microcontrollers. In addition, a ground control laptop connected to a modem provides a platform for the operator to interact with the drone. The Linux based Paparazzi autopilot software contains at its heart an effective airborne stability and navigation code based on PID control, and an advanced ground control station application that allows an operator to visualize and control the unmanned aircraft during operation. The Ground Control Station (GCS) utilizes a bi-directional data-link for telemetry and control, and its purpose is real-time monitoring of the drone. An overview of Paparazzi system is shown in Figure 52.



Figure 52. Paparazzi system.

The bi-directional data link shown in Figure 52 is a wireless serial link established with an XBee modem and the safety link provides the manual control option for the drone. A safety pilot on the ground may use the R/C transmitter to control the aircraft in 'Manual' mode, control with augmented stability is achieved in 'Auto1' mode and full autonomous navigation is enabled with 'Auto2' mode. The complete flight mission is pre-planned and programmed into a flight plan. The flight trajectories described in a flight plan can be simulated and tested with 'Google or Bing' map tiles of the target location using a GCS display (a GUI). The graphical user interface of the Paparazzi software enables in-flight modification of flight trajectories and monitoring of all onboard sensor outputs (except FRAP) in real-time.

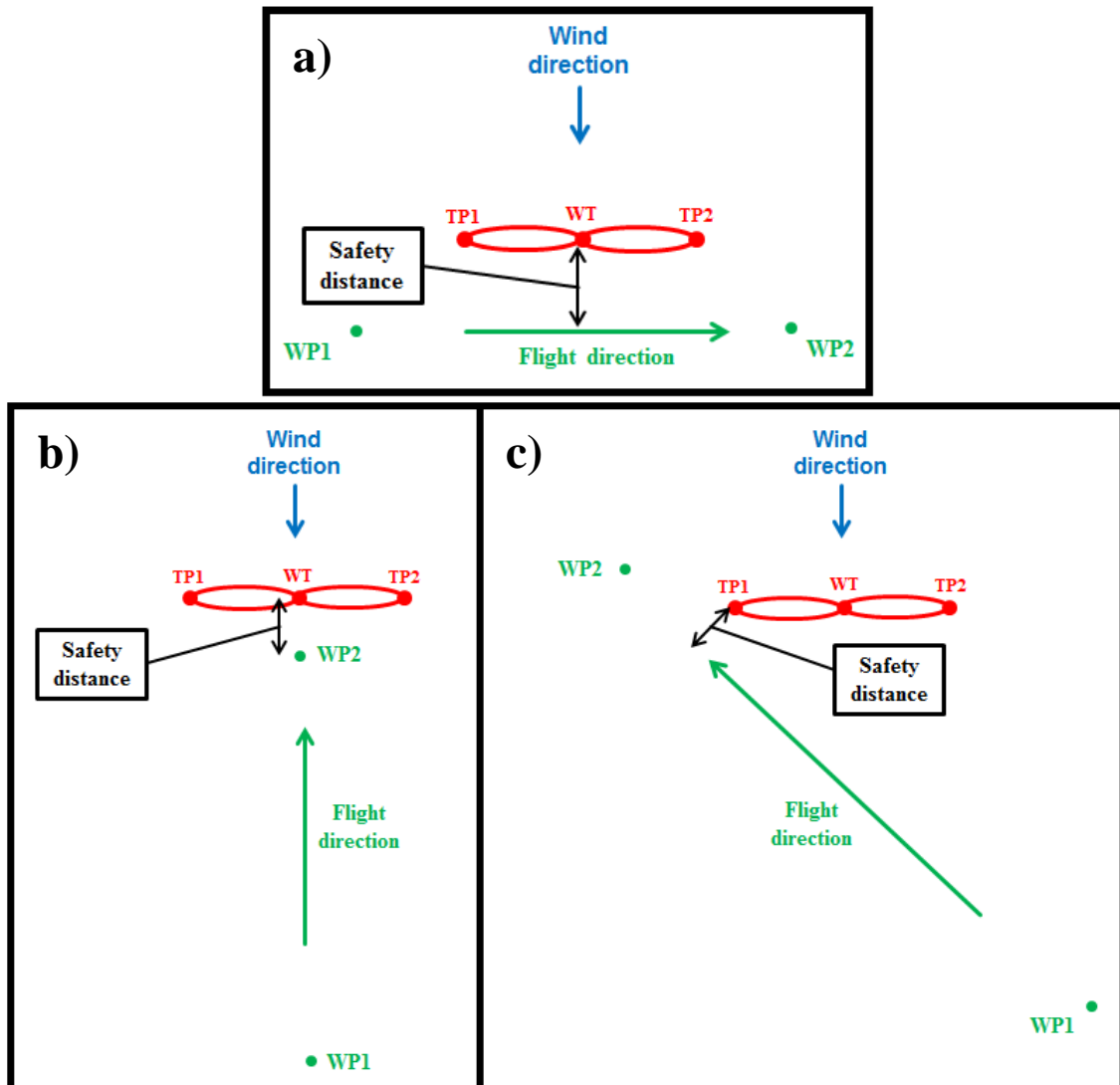


Figure 53. Orientation of drone trajectories - in a flight plan - relative to the main wind direction (or rotor plane orientation direction) (a) Parallel

to the rotor plane, (b) Perpendicular to the rotor plane, (c) Inclined at an angle to the rotor plane.

A flight plan describes the order and shape of trajectories flown by the drone's Paparazzi autopilot system. Before each flight, the measurement trajectories of interest are coded into a flight plan in GCS, and are loaded into the on-board autopilot with a USB cable. As flight trajectories need to be tuned based on wind direction (or based on wind turbine rotor orientation), the initial trajectories are planned based on the current wind direction obtained from instantaneous SCADA (inside the wind turbine tower). A set of Matlab routines are used to automatically generate the waypoints for measurements at any wind turbine based on its diameter, hub height, wind direction, the 'minimum' safety distance between the waypoints and the wind turbine rotor and the 'minimum' turn radius. Flight plans are customized based on the need to measure in freestream/near-wake/far-wake. The only 'safe' way to measure flow very close to a wind turbine rotor is by flying parallel to the rotor plane. The author successfully managed to autonomously fly and measure with the drone around a wind turbine at a distance as close as 20 m from the rotor plane.

The different types of flight plans used in the measurement campaigns can be broadly categorized into three types based on the orientation of drone trajectories relative to the main wind direction (or rotor plane orientation direction), Figure 53 a, b, c. The measurement trajectories can be oriented parallel/perpendicular/inclined at an angle to the main wind direction (or rotor plane orientation direction). In all flight plans, the wind turbine is marked with a waypoint 'WT' and the rotor blade tips are marked on both sides with waypoints 'TP1' and 'TP2'. As shown in Figure 53, the flight plan takes the drone from waypoint 'WP1' to waypoint 'WP2' along a level, straight line trajectory. Based on field experience, the 'safety distance' is chosen to be about 50-60 m from the rotor plane, but it mainly depends on the comfortability of safety pilot. The height of the drone trajectory relative to ground level is separately specified in the flight plan. As IMU accuracy is not evaluated at large bank angles, only measurements along straight line trajectories are considered useful. Also, as a safety precaution, the locations of all other neighbouring wind turbines were marked with waypoints in the flight plan. Figure 54 shows some sample flight trajectories generated with Paparazzi GCS. The measurements are accomplished using flight trajectories that are tailored to provide the level of detail that is required to advance the development of three-dimensional wake models that are embedded within computational fluid dynamics codes.

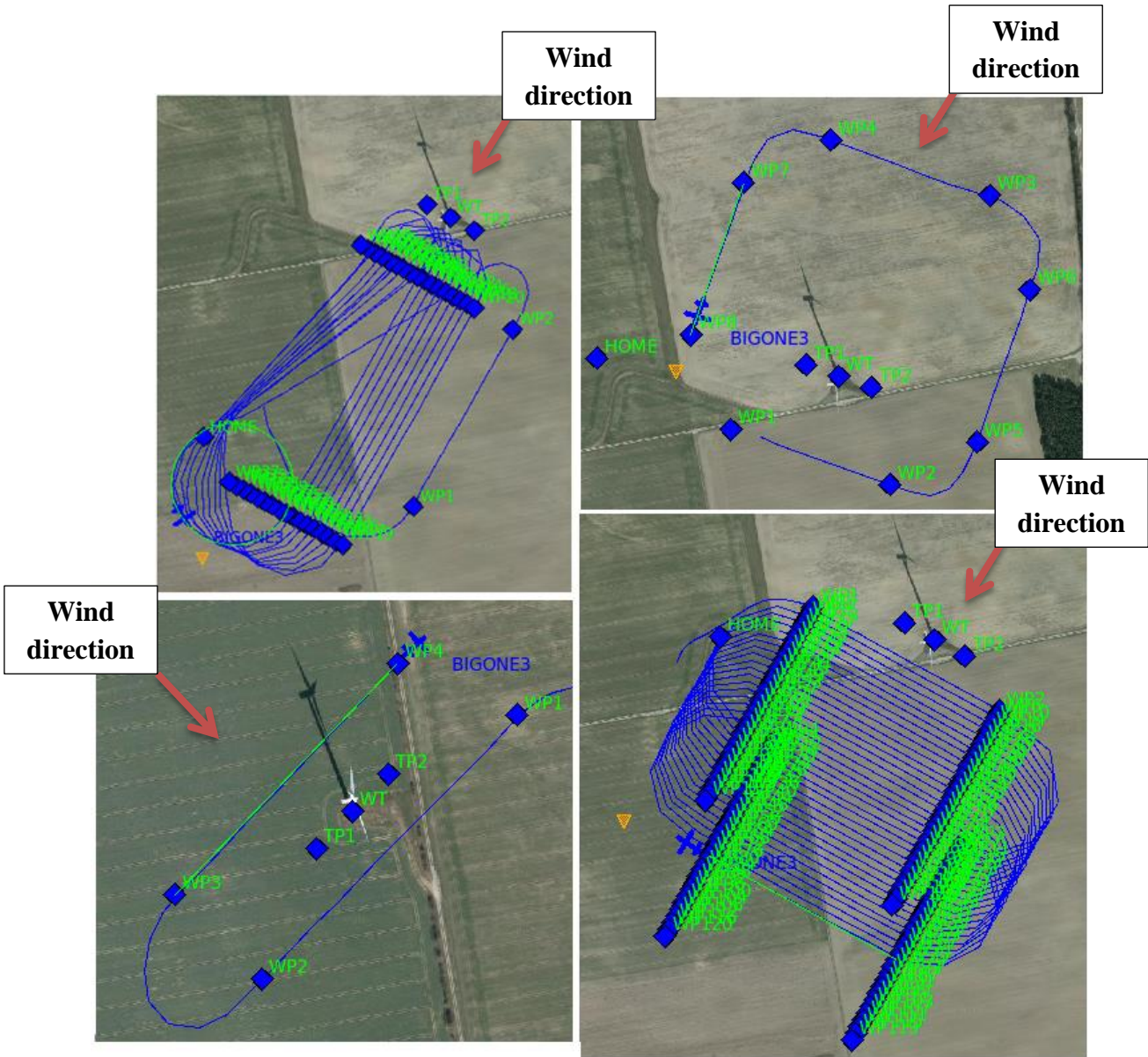


Figure 54. Sample flight trajectories generated with Paparazzi GCS.

3. MEASUREMENT METHODOLOGY

3.1 Wind Vector Calculation

The vector summation of air velocity (\mathbf{V}_a) in the drone's frame of reference and velocity of the aircraft in Earth's frame of reference (\mathbf{V}_p) gives the true wind velocity V of atmospheric air in Earth's frame of reference, Equation 20.

$$\mathbf{V} = \mathbf{V}_a + \mathbf{V}_p \quad (20)$$

The FRAP on the drone system measures the wind velocity (\mathbf{V}_a) in the flight frame of reference. Thus to evaluate the true wind velocity \mathbf{V} from Equation 20, \mathbf{V}_a must be mapped from the flight frame of reference to Earth's frame of reference through an axis transformation. The approach is illustrated in Figure 55 [86]. Prior to axis transformation, the FRAP air speed vector is decomposed into its components in the coordinate system attached to the drone using the flow angles, pitch (α) and yaw (β) measured with the FRAP probe. For the axis transformation, pitch (θ) and roll (ϕ) angles measured with IMU sensors and heading (ψ) measured by the magnetometer are used. The axis transformation matrix is given in Equation 21. The three rows of matrix M transform the longitudinal, lateral and vertical components of \mathbf{V}_a . The vector components of \mathbf{V}_a and \mathbf{V}_p can then be used in Equation 20 to compute the wind velocity vector in a North-East-Vertical coordinate system in Earth's frame of reference.

$$M = \begin{bmatrix} \cos \theta \sin \psi & -\sin \phi \sin \theta \sin \psi - \cos \phi \cos \psi & -\cos \phi \sin \theta \sin \psi + \sin \phi \cos \psi \\ \cos \theta \cos \psi & -\sin \phi \sin \theta \cos \psi + \cos \phi \sin \psi & -\cos \phi \sin \theta \cos \psi - \sin \phi \sin \psi \\ \sin \theta & \sin \phi \cos \theta & \cos \phi \cos \theta \end{bmatrix} \quad (21)$$

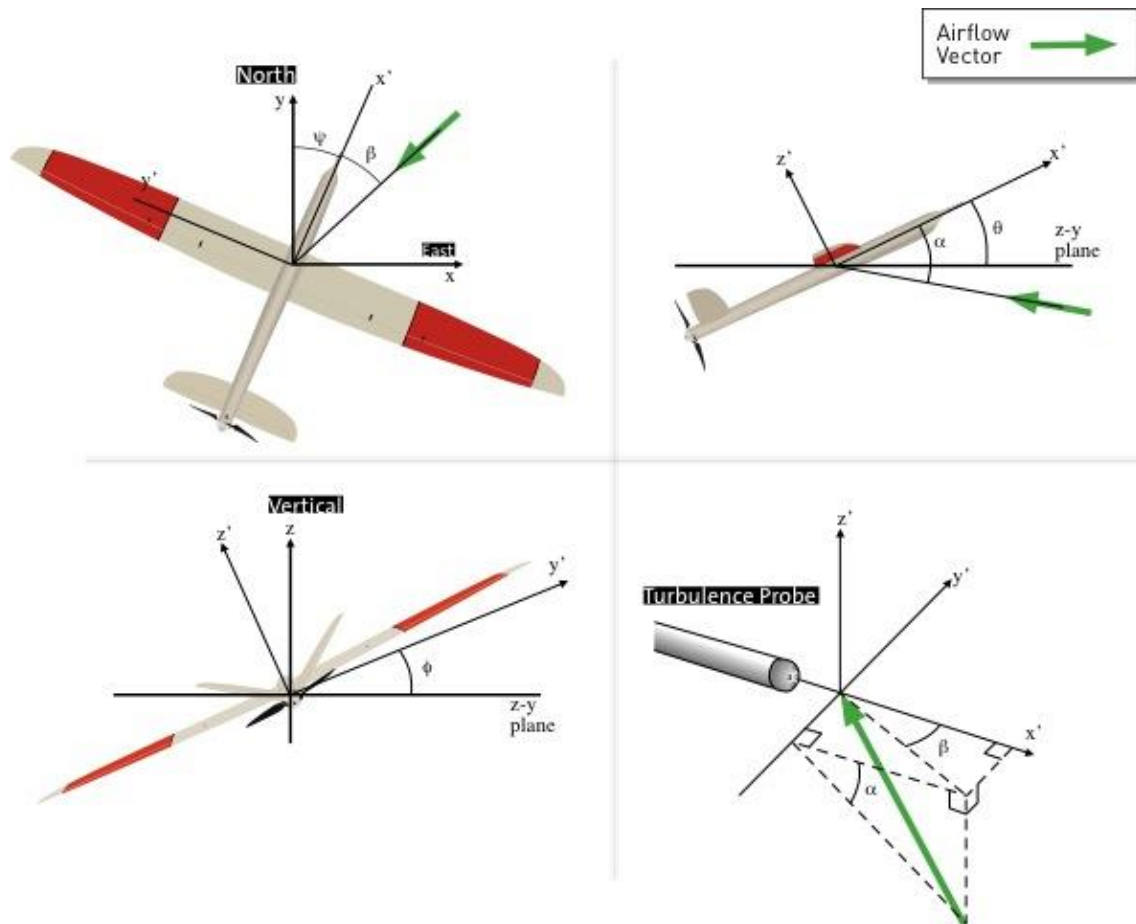


Figure 55. Relationship between the Earth and aircraft coordinates [86].

3.2 Data Processor

During measurements, the data from the onboard sensors – the absolute pressure sensor, the temperature and humidity sensor, the magnetic field sensor, the IMU and the GPS - are logged in an on-board SD card along with the pressure and temperature data from the seven sensors of the FRAP probe. These files created by an on-board data logger (in SD card) have a .t1m format [85]. This compressed data file is unpacked to the Paparazzi .data format using a command ‘sd2log’. In parallel, the onboard sensors data are also transmitted in real-time and logged at the Ground Control Station (GCS) in .data format. The synchronized logging of data from both the on-board sensors and FRAP simultaneously in the SD card with a single timestamp simplifies post-processing.

A data-processor software is developed to process 7S-FRAP and onboard sensor data to retrieve the wind flow field. There are two data files generated during the drone measurements. A telemetry log file that contains onboard sensor and optical trigger data, and a data file that contains the 7S-FRAP output. These two data files are fed into the pre-processor to be merged with the same sampling rate. An output file is generated after pre-processing that contains onboard sensors and 7S-FRAP data together at a unified frequency. This output file then sent to the post-processor together with the offset/gain file and two different files that contain sensor and aero calibration coefficients. In the post processor the voltage signal values from 7S-FRAP are converted into pressure using the sensor calibration coefficients. Flow angles and dynamic pressure are calculated using the aero calibration coefficients. The true airspeed of the drone is calculated from the dynamic pressure. The attitude angles, pitch and roll, and the heading are used to perform the axis transformation from the drone’s body axis to Earth’s frame of reference. The vector summation of the relative air velocity measured with the 7S-FRAP and the ground speed of the drone from GPS are used to calculate the wind vector in Earth’s frame of reference as detailed in Section 3.1.

The step-by-step tasks involved in post processing the log files are described in detail below.

1. Read all on-board sensors’ data (including LDM trigger) needed for post-processing from the telemetry log file.
2. Plot and visually check the raw data collected from all on-board sensors. Remove spurious data points.
3. The LDM trigger is used to track the position of all three wind turbine blades as a function of time during measurements. It is also used to compute the RPM of the rotor during measurements (Figure 23).

- a) Based on the trigger signal, a binary variable called Blade Position Marker (BPM) is created, whose value is assigned high (BPM = 1) only when the leading edge of wind turbine blade passes by the tower. At all other times, its value is assigned low (BPM = 0). Later this variable is used for phase locking the measurement data.
4. GPS UTM position coordinates and height above sea level of the drone along its trajectory are transformed into local coordinate system referenced to the center of base of wind turbine tower.
5. Read FRAP pressure and temperature sensor data, and other on-board sensors data from the SD log file.
6. Compute the time offset using the time stamps of the on-board sensors from the telemetry log file and the SD log file.
7. Shift the FRAP data timestamp using the time offset computed in the previous step to synchronize it with all other on-board sensor data in the telemetry log file.
8. Compute the magnetic heading along the drone trajectory using the X, Y and Z components of the magnetometer, the attitude angles (pitch and roll) of IMU and the hard, soft iron correction coefficients.

Note: Do a consistency check by plotting both GPS and magnetic heading on the same plot, Figure 22.

9. Up sample all on-board sensor data to the FRAP sampling rate (250 Hz/500 Hz) using linear interpolation. Pay particular attention to GPS and magnetic heading as they have a discontinuity at $0^\circ/360^\circ$.
10. Read the relevant static calibration and offset-gain files. The offset-gain file contains the zero differential pressure voltage of all seven FRAP sensors before and after the measurement. This provides a reference for all FRAP sensors and also ensures that the sensor drifts (if any) are corrected at this stage so that they do not affect the final measurement accuracy. The FRAP aero-calibration file is then chosen based on 5-sensor/7-sensor model.
11. Compute the FRAP air speed, yaw and pitch angles in the flight frame of reference (see Section 2.1).
12. Apply a transformation from the flight frame of reference to Earth's frame of reference (see Section 3.1).

Note: If magnetic heading is not available, then GPS heading can be used.

13. Finally, an axis transformation to the wind turbine frame of reference is accomplished based on the wind turbine SCADA yaw angle.

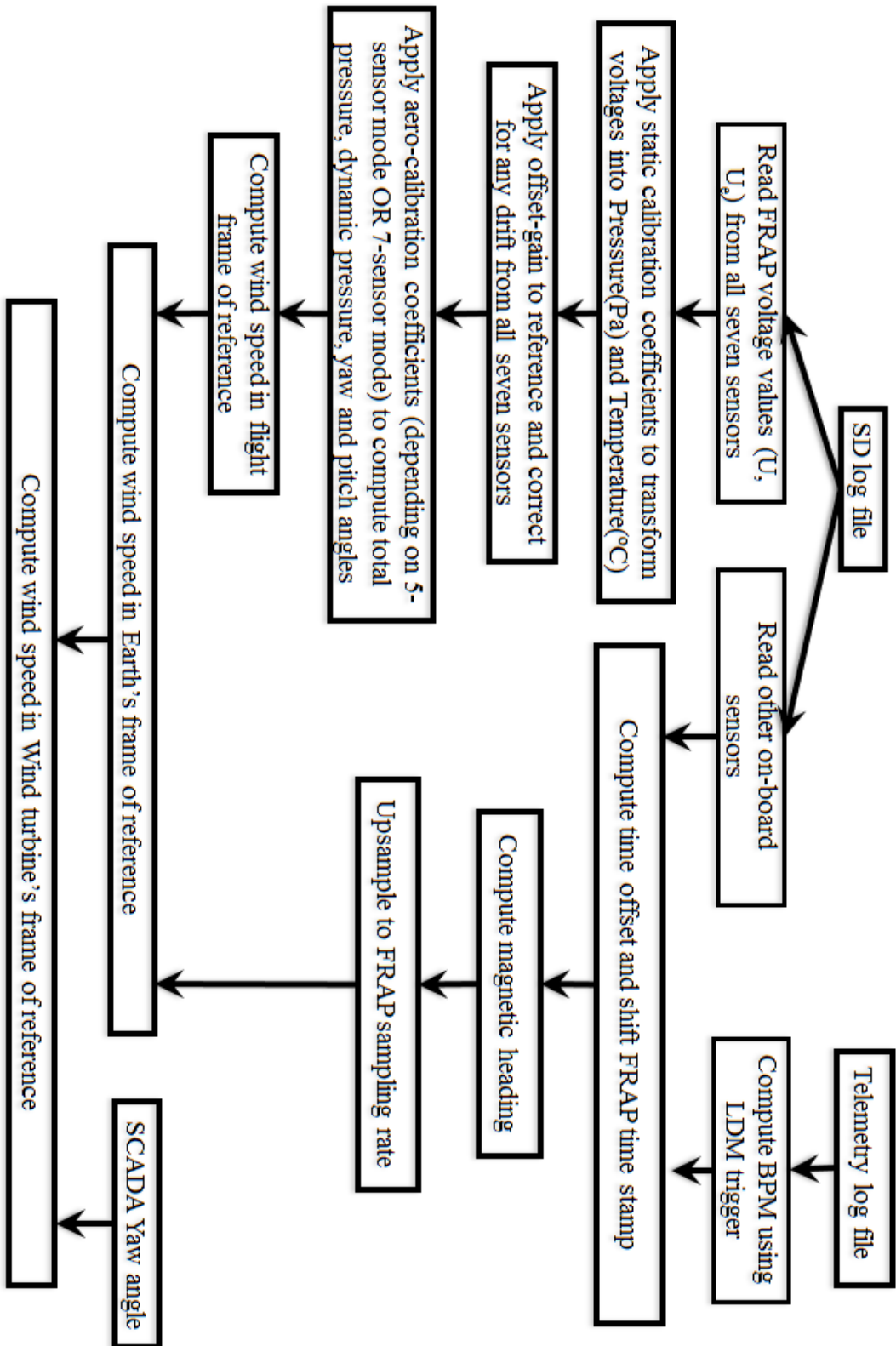


Figure 56. Post-processing schematics.

The schematic of the drone measurements data processing is shown in Figure 56.

3.2.1 Coordinate Axis Convention

A typical fully autonomous drone trajectory in a plane at hub height to measure in near-wake is shown in Figure 57. The wind turbine is located at the origin (0, 0) and faces the upstream wind that flows from the North towards the South. The wake evolves along the positive X/D axis and the Z-axis is used to represent the vertical height above ground level at the base of wind turbine tower. This coordinate system is employed throughout this thesis. The colours on the measurement trajectory indicate the height variations along the trajectory. The drone trajectory is pre-programmed into the on-board autopilot system, and during measurements the autopilot commands the drone to fly at an air-speed of 15 to 25 m/s. Thus, the upstream and near-wake field of a wind turbine at any predefined altitude can be scanned using an autonomous drone. During measurements, the flight plans are prepared based on the current ‘nacelle direction’ indicated by the real-time SCADA. These autonomous flight trajectories are then tuned (if necessary) during flights to accommodate for turbine yaw and to ensure that the resulting trajectories are always aligned parallel (or perpendicular) to the rotor plane.

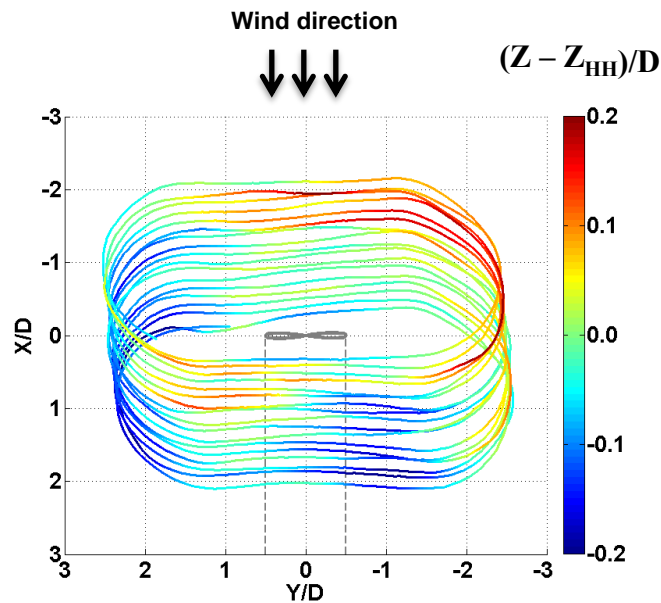


Figure 57. A typical autonomous drone trajectory for measurements in the near-wake.

3.2.2 Short-time Fourier Transform

All measured signals are in the time domain, and their frequency content can be analyzed using the Fourier Transform. In engineering

applications, the Fourier Transform serve's as a tool for analysis/processing of raw time domain signals to get additional information ie. the frequency spectrum of a signal that shows the components of a frequency present in it. As atmospheric turbulent flow signals in all cases contain more than one frequency component, the Fourier Transform describes how much of each frequency exists in the raw signal but it does not tell us when in time these frequency components exist. This information is not required when the signal is stationary, however it must be noted that signals from atmospheric flow measurements are non-stationary. Stationary signals are those whose frequency content does not change with time and a signal whose frequency content changes constantly with time is called a non-stationary signal. Thus, to get a time-frequency representation of a non-stationary signal i.e. to provide time and frequency information simultaneously, we need more sophisticated analysis tools like the Short-time Fourier Transform (STFT), Wavelet Transform (WT) or Maximum Entropy Method (MEM). The assumption here is that smaller intervals of a non-stationary signal can be considered as stationary.

As it is not possible to get frequency spectra of a signal at any given instant in time, our investigation focuses on obtaining spectral components at any given interval of time. This interval of time – set by the window function - defines the resolution in the time domain. Better time resolution (and poorer frequency resolution) are obtained with a narrower time interval (narrower window), and better frequency resolution (and poor time resolution) obtained with a wide window. The problem with wide windows is that they may violate the stationarity condition.

This time localization of a frequency component can be obtained by pre-windowing a signal using the Short-time Fourier Transform (STFT) as follows [87]

$$STFT_x^{(\omega)}(t, f) = \int_t [x(t) * \omega^*(t - t')] * e^{-j2\pi ft} dt \quad (22)$$

As noted earlier, in STFT, the signal is divided into small segments, which can be assumed to be stationary. The relatively short analysis window suppresses the signal outside a small neighbourhood of time t, and generates a local spectrum around time t. Thus, the time-frequency representation of a signal can be generated by time shifting the windowing function for the entire duration of the signal. In STFT, the time resolution and frequency resolution can be improved independently, but not simultaneously, by varying the length of windowing function. It is known that the joint time-frequency resolution of STFT is inherently limited. The

uncertainty principle prohibits the existence of windows with arbitrarily small duration, Δt , and arbitrarily small bandwidth, Δf .

$$\Delta f * \Delta t \geq \frac{1}{2} \quad (23)$$

Thus, there is a fundamental resolution trade-off that affects also the variance computed from STFT. The wind speed variance along a measurement trajectory can be computed from STFT spectra, around the neighbourhood of time t_1 , by

$$\sigma_x^2 = \int_0^{\frac{F_s}{2}} \Re \left[STFT_x^{(\omega)}(t = t_1, f) \right] * df \quad (24)$$

3.2.3 Methodology

The FRAP probe's static and aero-calibration models convert the voltage data measured by its seven sensors along a drone's trajectory into flow angles and dynamic pressure. This dynamic pressure, along with air density obtained from on-board temperature and pressure sensors, directly gives the wind velocity vector in the drone's (moving) frame of reference for the complete flight duration. In the drone's frame of reference, the variance (Equation 24) of the FRAP air speed is computed along the three orthogonal axes of a co-ordinate system oriented on the FRAP probe, Figure 14 a. As turbulent kinetic energy is a scalar quantity, the magnitude of the turbulent kinetic energy in the drone's frame of reference (over the short time period) is same as that in the Earth's frame of reference. The time interval chosen for the short-time Fourier transform is 0.2 s. Thus, the turbulent kinetic energy per unit mass can be computed along the drone's trajectory using the following relation.

$$TKE = \frac{1}{2} (\sigma_x^2 + \sigma_y^2 + \sigma_z^2) \quad (25)$$

The wind velocity vector in the flight frame of reference is then transformed into Earth's frame of reference using the data from drone's other on-board sensors. This tags and maps the measured wind velocity vectors in a spatial and temporal co-ordinate system i.e. (X, Y, Z, t) and the

data segments along trajectories of interest (level, straight line drone trajectories) are then extracted for more detailed analysis.

The power spectra in frequency space can then be obtained from the airspeed measured along these selected data segments extracted from the previous step. To convert from frequency space to wave number space, we invoke Taylor's frozen flow hypothesis. Wind speed measured by FRAP relative to the drone is used to transform the frequency spectra to the wave number spectra. Both spectra can be smoothed using the approach suggested by J.C. Kaimal et al [89]. The wave number/frequency weighted power spectra are obtained to give the integral length and time scales of turbulence for the specified measurement window.

The power spectra in wave number space are used to identify the boundary between the lower end of the inertial subrange and the upper end of the dissipation range; as this spectrum is characterised by a sharp drop in spectral amplitudes. The wave number (k) at which this drop starts is used to compute Kolmogorov microscale (η) following Dubovikov et al. [98]

$$k = 0.1 \times \eta^{-1} \quad (26)$$

The Kolmogorov microscale is then used to calculate the dissipation rate of turbulent kinetic energy (ε), using the following relation suggested by Kaimal et al. [99].

$$\eta = \left(\frac{\nu^3}{\varepsilon}\right)^{\frac{1}{4}} \quad (27)$$

where ν is the kinematic viscosity of air ($15.68 \times 10^{-6} \text{ m}^2/\text{s}$ at 300 K). Alternatively, the dissipation rate of turbulent kinetic energy can also be obtained from wave number spectra by curve fitting in the inertial subrange using following equation [108].

$$k.PSD = C \varepsilon^{\frac{2}{3}} k^{-\frac{2}{3}} \quad (28)$$

The unsteady measurements of wind velocity along the drone's trajectory are separated into mean and fluctuating parts using the Reynolds decomposition. In the three spatial directions the decompositions are

$$\begin{aligned} u &= \bar{u} + u' \\ v &= \bar{v} + v' \\ w &= \bar{w} + w' \end{aligned} \tag{29}$$

where the velocity components u , v and w are defined along the coordinate axes X, Y, and Z, with the X-axis oriented in the main wind direction. By definition, $\overline{u'} = \overline{v'} = \overline{w'} = 0$. As the wind velocity is non-stationary, an ensemble average is computed with an averaging time of $t_0 = 0.2$ s in all cases to separate the mean and fluctuating parts. The fluctuating parts are obtained directly from the wind velocity measured in the drone's frame of reference assuming that the drone's inertial response time is larger than $t_0 = 0.2$ s. In the wake of a wind turbine, the turbulent fluctuations contain both periodic (deterministic) and stochastic parts. The turbulent kinetic energy (TKE) along the drone's trajectory is then computed from the sum of square of the fluctuating parts,

$$TKE = \frac{1}{2}(u'^2 + v'^2 + w'^2) \tag{30}$$

Alternatively, the turbulent kinetic energy along the drone trajectory can also be computed from short time Fourier Transform (STFT) as seen in Equation 25; and it is important to mention here that both approaches yield the same turbulent kinetic energy values. In order to quantify the departure from isotropy, the degree of anisotropy (DA) is evaluated as [61]

$$DA = \frac{\overline{2u'^2}}{\overline{v'^2 + w'^2}} \tag{31}$$

The characteristic velocity scale of the friction velocity (u_*) is derived from freestream measurements made during the landings of the drones at the wind farms in flat and complex terrains. Even though the friction velocity decreases with height, the friction velocity is nearly constant in the surface-layer for a neutrally stratified atmospheric boundary layer as turbulence is mechanically generated by wind shear. From a local similarity hypothesis, the velocity scaling is given as [106]

$$u_* = (\overline{u'w'^2} + \overline{v'w'^2})^{\frac{1}{4}} \quad (32)$$

The normalised autocorrelation of the FRAP airspeed measured along any level, straight line drone trajectory yields the integral time scale (τ) - during the specified measurement window - using Equation 33. The the integral time scale (τ) is extracted as the value of time when $r = 1/e$ [99].

$$r = \frac{\overline{V_f(t)V_f(t+\tau)}}{\overline{V_f(t)^2}} \quad (33)$$

Thus using the measured airspeed (V_f) of the drone, the integral length scale (\mathcal{L}) can then be determined from $\mathcal{L} = V_f \tau$. As the turbulent flow field is convected at wind speed relative to the Earth, the calculated integral length and time scales are corrected using the wind speed measured relative to Earth's frame of reference.

Finally, the parameter used to examine the pitch of tip vortices is the vortex pitch, p_v , which is defined as the axial distance that a vortex is transported during one blade revolution. This is defined by Wood [100] as

$$p_v \approx \frac{1+u_2}{2\lambda} \quad (34)$$

where u_2 is the average velocity at the rotor plane.

3.2.4 Phase Locking

Phase locking would have been a straight forward approach if measurements were made by fixing the FRAP probe to a particular location in wake. Unfortunately, this is not the case with drone based wind measurements, where the probe continuously moves with the drone and makes measurements along its trajectory. Given the fact that the ambient wind speed and direction can also change during measurements, flight plans need to be designed carefully for phase locking. One approach is shown in Figure 1, where the drone is flown repeatedly along the same trajectory multiple times in the wake and the blade position is simultaneously measured using an optical trigger system. A circular trajectory was chosen as it has the minimum possible perimeter for a given area, but measurements along any set of repeated trajectories in the wake can in theory be used for phase locking. A general approach to phase locking is shown below.

1. Input for phase locking includes

- The data from wake measurements that includes the positions of measurement points along a drone trajectory (X, Y, Z), the wind velocity components (U, V, W) and the turbulent kinetic energy (TKE) measured at those drone positions in the wind turbine frame of reference.
- BPM: Blade position marker is a binary variable computed from the trigger signal whose value is assigned high ($BPM = 1$) only when the leading edge of wind turbine blade passes by the tower. At all other times, its value is assigned low ($BPM = 0$). Later this variable is used for phase locking the measurement data.
- Define the boundaries of the measurement volume in the wake ($X_{min}, X_{max}, Y_{min}, Y_{max}, Z_{min}, Z_{max}$) and chose the appropriate $\Delta X, \Delta Y, \Delta Z$ to bin this volume by dividing it into a number of equal parts. For this analysis,
 - $X_{min} = 0.5D, X_{max} = 3D, Y_{min} = -0.7D, Y_{max} = 0.7D, Z_{min} = -0.5D, Z_{max} = 0.5D$.
 - $\Delta X = 0.1D, \Delta Y = 0.05D, \Delta Z = 0.1D$.
- To bucket the 120° sector of the rotor swept area, we need to define the rotor bin size. For this analysis, the rotor bin size is taken as 10° (12 identical bins).

2. First use the 120° rotational symmetry (assuming that all three blades of a wind turbine rotor are identical) and divide the complete measurement data – all seven variables X, Y, Z, U, V, W and TKE – into multiple sections based on BPM. The boundary of each section is drawn at the location where BPM is high ($BPM = 1$).

3. Then, bucket the measurement data based on the pre-defined rotor bin size. In this thesis, 12 identical bins of 10° each are used as the standard bin size.
4. Now, the bucketed data from previous step are further spatially binned into different spatial bins of size ΔX , ΔY , ΔZ each. In this step, the spatial bins with data points lying outside the pre-defined wake volume boundary are filtered out.
5. Finally, find the spatial bins that contain data for all 12 rotor bins (OR the spatial bins that contain data for a maximum number of rotor bins), and plot the measured mean properties as a function of rotor position.

The process of extracting data from phase locking is explained in Figure 58 with aid of a flow chart.

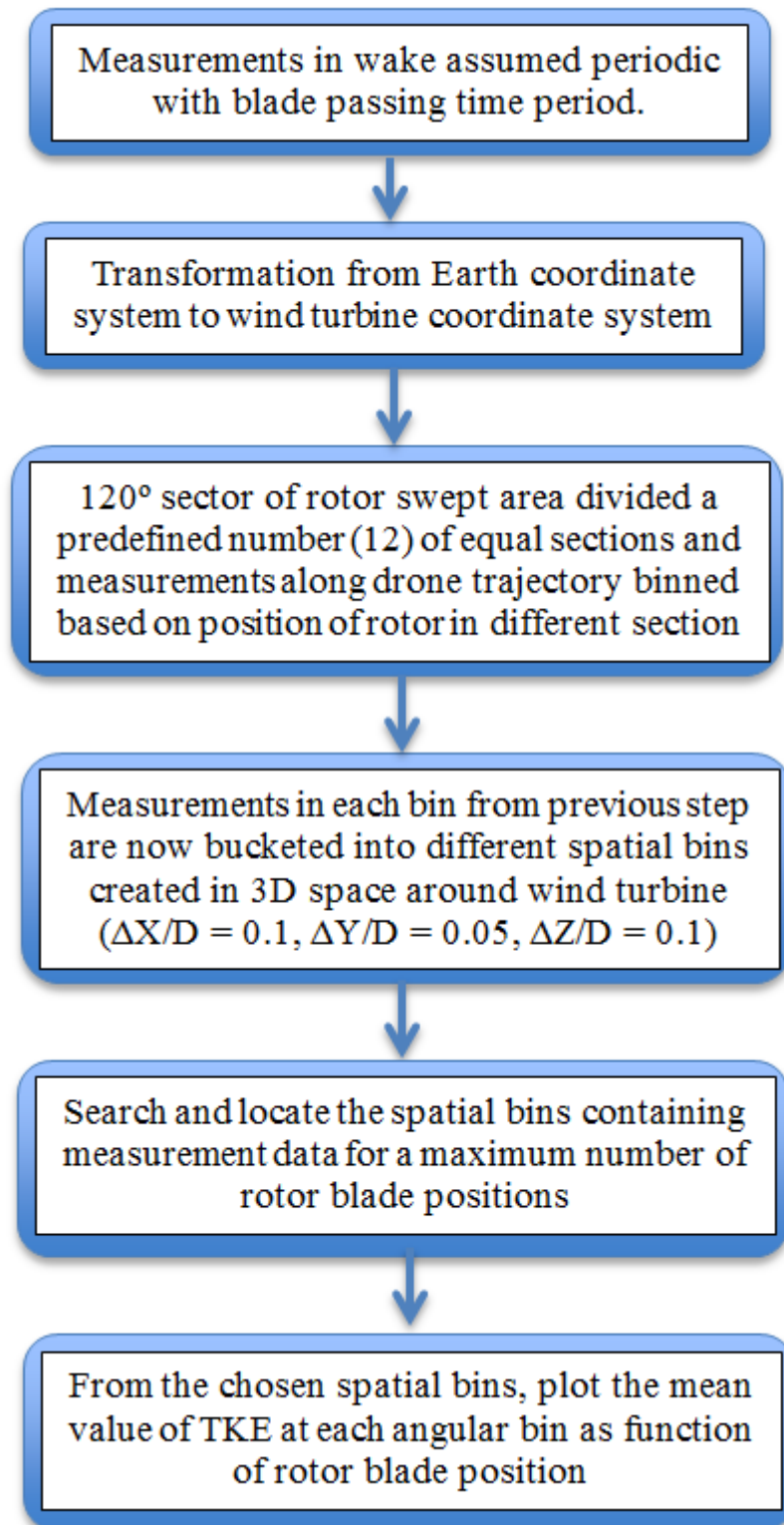


Figure 58. Flowchart for phase locking algorithm.

3.3 Uncertainty in Wind Measurement System

The wind velocity in the Earth's frame of reference is obtained by a vector sum of the drone's velocity in the Earth's frame of reference and the wind velocity measured by the 7S-FRAP probe in the drone's frame of reference. Thus, to determine the total uncertainty in the measurement, the uncertainties of all components in the overall measurement chain are systematically combined using the guide to extended uncertainty in measurements (GUM) detailed by Behr et al. [91]. In the GUM method, all uncertainty sources are modelled as probability distributions, and are combined with Gaussian uncertainty propagation to yield the final uncertainty in the measurement system. The GUM analysis yields a standard uncertainty of 0.7 m/s in the wind speed with a confidence level of 67% [92]. It is important to highlight here that 0.7 m/s is the uncertainty in wind speed measured in Earth's frame of reference, however the uncertainty in the wind velocity measured by the FRAP probe - at a cruise speed of 20 m/s - is less than 0.05 m/s. The term 'wind speed' is used to denote measurements in Earth's frame of reference and the term 'airspeed' is employed to describe measurements in the drone's frame of reference.

3.3.1 Assessment of FRAP System in Wind Tunnel

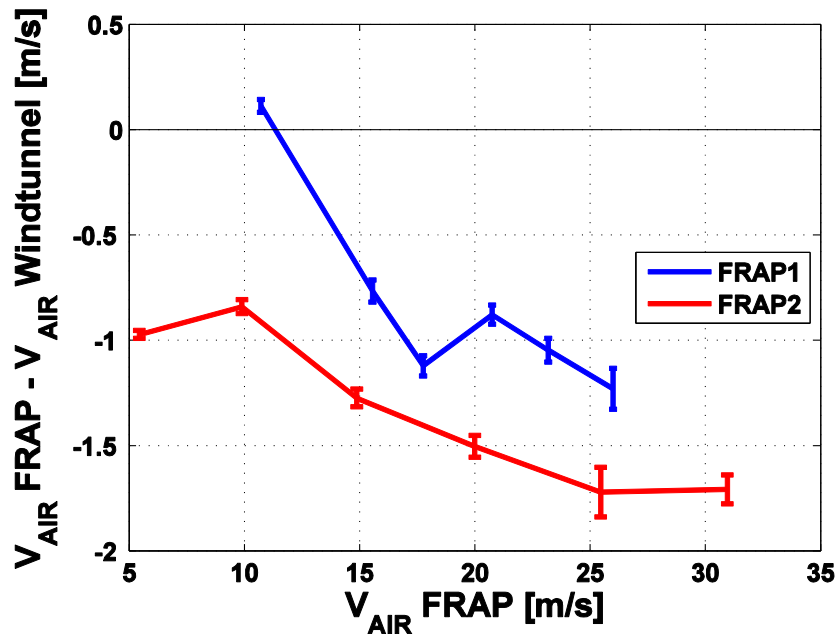


Figure 59. Comparison between FRAP and windtunnel airspeed.

The two FRAP measurement systems were assessed in detail in the wind tunnel, and their airspeed, pitch angle and yaw angle deviations were

documented for correcting the field measurements. The airspeeds and flow angles were measured with the two FRAP measurement systems, FRAP1 and FRAP2, during the wind tunnel testing of windFlyer and these values were later used in post-processing to correct the FRAP on-field measurements. The evaluation of the measurement runs at different constant airspeeds disclosed some discrepancies in the measured flow properties with respect to the ‘expected’ values. First, a deviation of the FRAP airspeed with respect to the value measured by the wind tunnel system was observed in each run, Figure 59. For airspeeds above 15 m/s, the relative airspeed measured with FRAP1 and FRAP 2 were consistently lower than the wind tunnel rated speed as seen in Figure 59. Unfortunately, no information was available on the accuracy of the wind tunnel venturi-system. A 5 hole FRAP probe tested in the same wind tunnel in 2012 also consistently measured wind speeds lower – by similar amount - than the wind tunnel rated speed [79]. Transient effects on the FRAP probe measurements can be excluded, as the airspeed setting of the wind tunnel was maintained constant for 60 s before each measurement.

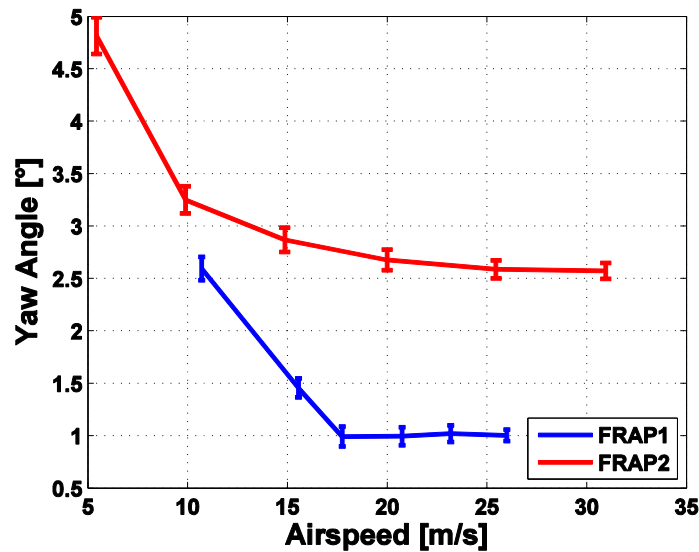


Figure 60. FRAP1 and FRAP2 yaw angle offsets at different wind tunnel airspeeds.

Second, a systematic offset of the yaw angle was identified during the velocity runs. The offset is dominant at low airspeeds. But even for airspeeds above 15 m/s it remains considerable, as depicted in Figure 60. At wind speeds above 15 m/s, the FRAP1 recorded a deviation of 1° and FRAP2 showed a 2.5° offset, when the windFlyer was aligned with the wind tunnel axis. Interestingly, the offset remains constant at wind speeds above 15 m/s and the differences between both probes indicate that this could be due to geometrical alignment errors in the freejet aero-calibration

or due to FRAP alignment in windFlyer. The latter issue was checked and discounted as the angular alignment error of FRAP in windFlyer was less than 0.4° .

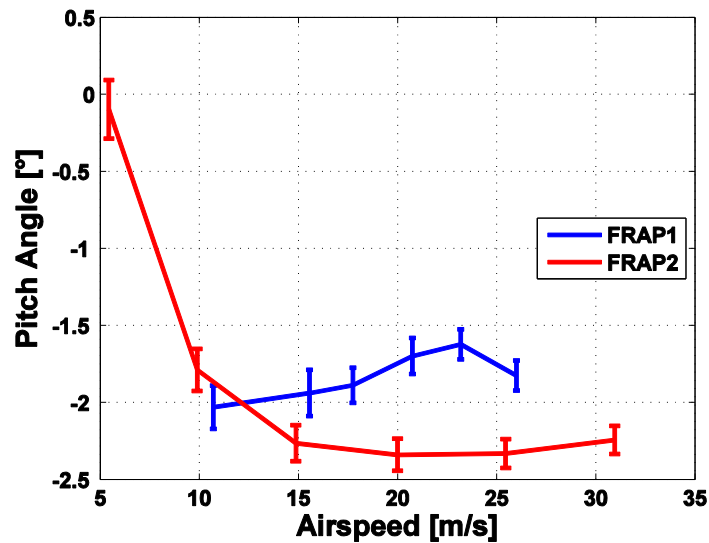


Figure 61. FRAP1 and FRAP2 pitch angle offsets at different wind tunnel airspeeds.

Third, a similar discrepancy was found in the average values of the pitch angle during velocity runs, Figure 61. The pitch angle showed a constant offset at airspeeds above 15 m/s for both probes. As for the yaw error, a misalignment with the fuselage can be excluded to explain this offset (less than 0.4°). The observed pitch and yaw angle offsets can be explained from aero calibration models (Appendix C), and they arise from the geometry of the metal arm used to support the FRAP probe in Freejet.

3.3.2 FRAP at Low Airspeeds

WindFlyer instrumented with the FRAP-2 probe was also tested at low airspeeds in the wind tunnel to assess its measurement capabilities. As seen from Figure 62, a considerable reaction time was observed for the pitch angle to stabilize at low airspeeds but the FRAP airspeed and yaw angle did not show any drift with time and they were measured with reasonable accuracy. For airspeeds of 5.5 m/s and 8 m/s, the pitch angle drifted with time by 2° over a period of 15 s. This pitch angle drift was only observed at airspeeds below 12 m/s. Therefore, it can be concluded that airspeeds above 12 m/s are necessary to prevent a lag in the reaction time of the FRAP system, when measuring in a dynamic flow field. This effect has to be taken into account for wind measurements during takeoff/landing and for kite based wind measurements with FRAP [80].

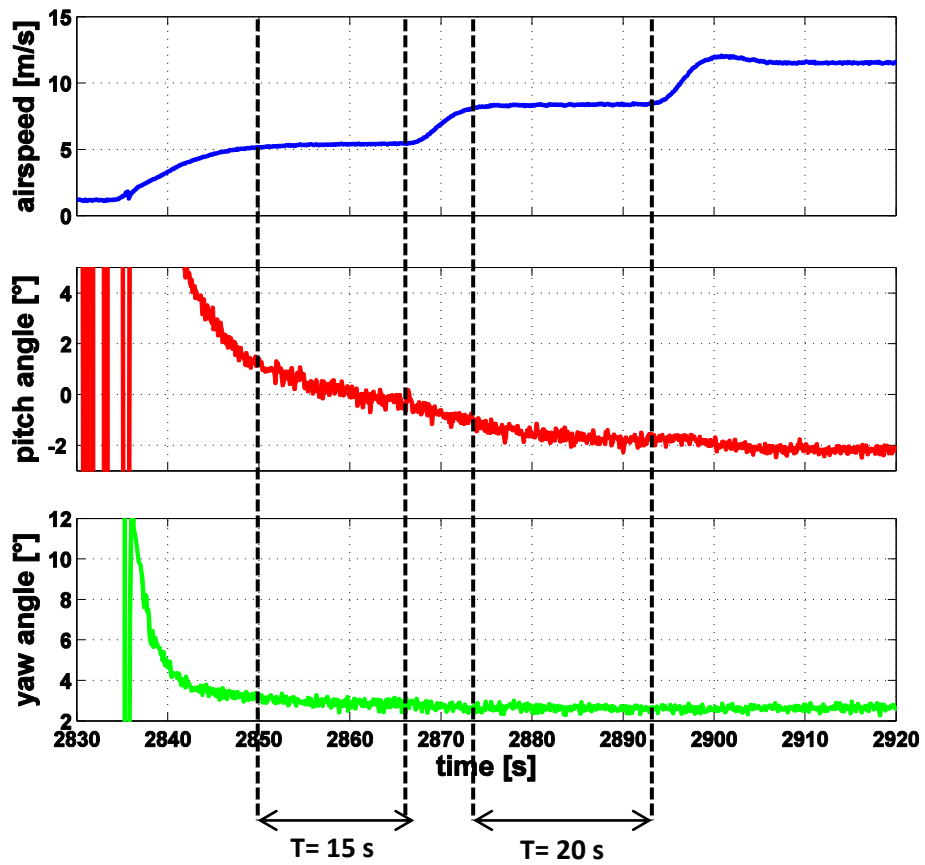


Figure 62. Lag in reaction time of FRAP 2 for low speeds.

3.4 Flight Permissions

In general, permissions are needed for doing measurements with drones but they depend on the measurement location (i.e. state/country) and also on the flight altitude and the drone's weight. Even for autonomous flights, direct visual contact must be maintained. For example, legislation in Switzerland is more flexible with drones weighing less than 30 kg do not require a licence. The person operating the drone, however, has to make sure the flying device is always visible to the eye [93]. In Germany, each state follows its own rules, so it is important to contact the responsible aviation office (Luftfahrtamt) at the respective regional council (Regierungspräsidium). If drone flights are within a control zone (see ICAO charts), then additional permissions are needed from the DFS and/or the local airport the zone belongs to. Also the public landowners should be contacted to obtain their permission.

The initiator of the measurements and the owner of the aircraft have to take full responsibility for the flights and its possible consequences, especially when operating in the vicinity of wind turbines. This includes all accidents that might occur even due to any hidden bug in Paparazzi. No warranty is issued with Paparazzi - especially not for downloaded software – due to the nature of Paparazzi as an open source project with many contributors. See the GNU General Public License for more details on liability [94]. Due to the experimental nature of small unmanned aircraft, the safety pilot has to exercise extreme caution during measurements and should never let the aircraft out of his/her sight.

4. MEASUREMENTS IN FLAT TERRAIN

The measurements of the near (less than three rotor diameter) and far wakes (up to eleven rotor diameters) in a utility scale wind farm in flat terrain are described in this chapter. These measurements detail at full-scale Reynolds number conditions the evolution and breakdown of tip vortices that are characteristic of the near wake and the turbulent mixing and entrainment of more energized flows that are distinctive in the far wake. Comparisons of these measurements to recently developed wake prediction models highlight how these measurements can support further model development. All measurements described in this chapter are made with the WindFlyer drone.

4.1 Measurement Site

	Turbine	
	WEA 5 (Siemens)	WEA6 (Vestas)
Rated power (MW)	3.6	3.0
Hub height (m)	93	105
Rotor diameter (m)	107	90
Cut-in wind speed (m/s)	3-5	3.5
Rated wind speed (m/s)	13-14	15

Table 6. Salient features of turbines WEA5 and WEA6.

The measurements are made at the 25.8 MW Altenbruch II wind farm in Cuxhaven, Germany. The wind farm is located in flat terrain at a distance of 5 km from the North Sea coast, Figure 63. The locations of the nine wind turbines are shown by the circle symbols in Figure 63; the turbines, WEA5 and WEA6, at which measurements are made are shown as filled white circles, whereas the other turbines are shown as filled black circles. Turbine WEA5 is a Siemens SWT3.6 with rated power of 3.6 MW and turbine WEA6 is a Vestas V90 with a rated power 3.0 MW. Other salient characteristics of the two turbines are summarised in Table 6. During the measurements, the predominant wind direction was from South-West, and the wind direction changed overall by no more than $\pm 8^\circ$. This change in wind direction is even smaller than the $\pm 15^\circ$ change that is used

in [101] in the binning of data. The wind speeds were in the range of 5 m/s to 11 m/s. The upstream fetch over land for the predominant wind direction is 15 km, and the land cover is flat, agricultural land. As the drone based wind measurement system can only measure band limited turbulence intensity, the overall turbulence intensity in the freestream at this site is obtained by a kite-borne aerodynamic probe system and is 12% [102]. The atmospheric stability condition is neutrally stable based on measurements of the atmospheric lapse rate using the drone's on-board suite of sensors.

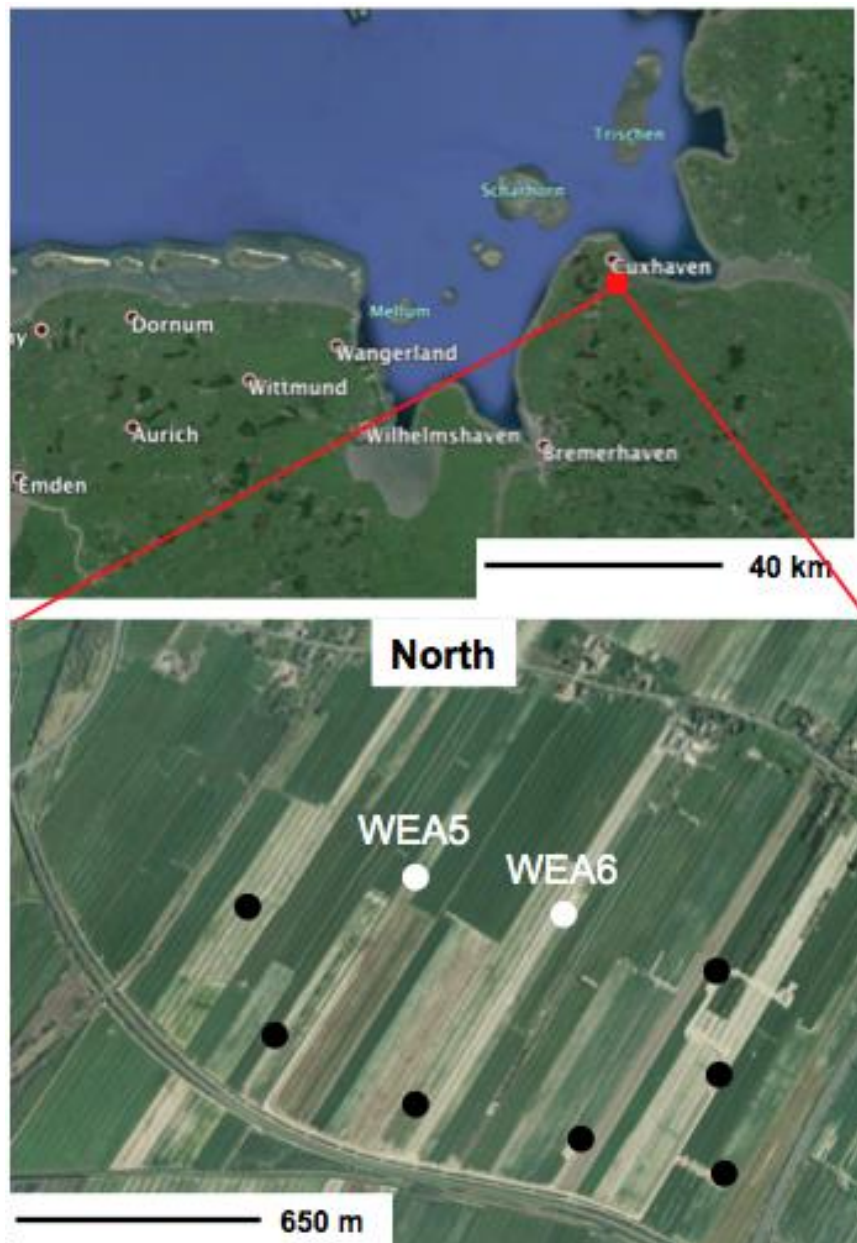


Figure 63. Above: Location of Altenbruch II wind farm (red square). Below: Layout of wind turbines in the wind farm. The circle symbols show the locations of wind turbines.

4.2 Measurements in Freestream

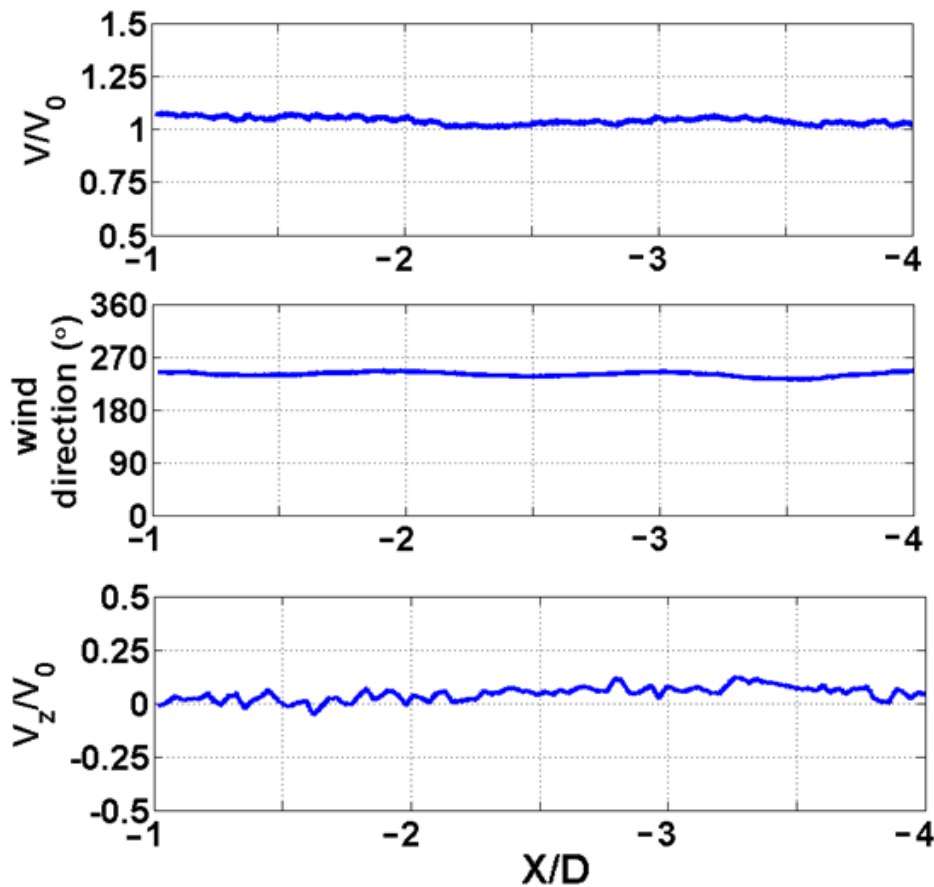


Figure 64. Wind speed, wind direction and vertical wind speed measured in freestream.

A freestream measurement in Altenbruch wind farm taken at 100 m AGL is shown in Figure 64. During this measurement, the SCADA wind speed (V_0) and direction logged at a turbine located 220 m laterally from this windFlyer drone trajectory is 8.1 m/s and 240° . Altenbruch wind farm's close proximity to the sea means that the nature of wind in freestream should reveal the onshore behaviour of this site. Figure 64 shows the spatial variation of wind speed, wind direction and vertical wind speed in freestream from $X/D = -1$ to $X/D = -4$. As seen from the plots, the wind speed is nearly constant with a mean value of $V/V_0 = 1.04$, the wind direction variation is less than $\pm 8^\circ$ about a mean value of 242° , the vertical wind speed range is between $-0.1 < V_z/V_0 < 0.1$ with a mean of 0.4 m/s and a uniformly low turbulent kinetic energy of $2 \times 10^{-3} \text{ m}^2/\text{s}^2$ was measured along this trajectory indicating the near absence of terrain features with short time turbulence length scales. As noted, the wind speed measured in the freestream at hub height is 3.5% higher than the SCADA wind speed, capturing the impact of the wind turbine on the upstream flow.

4.3 Wake Evolution

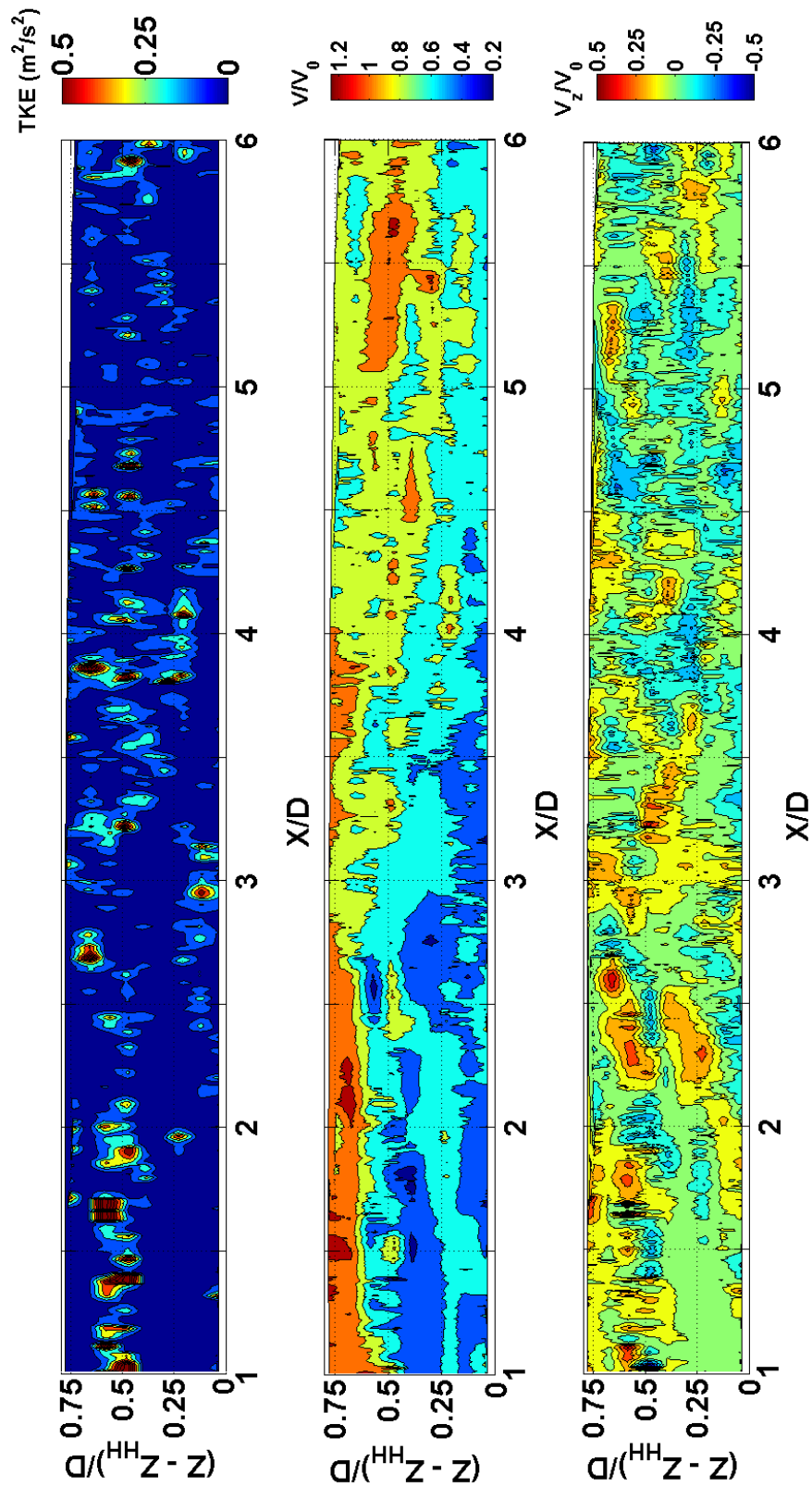


Figure 65. Measurements of turbulent kinetic energy, wind speed and the vertical wind speed in a vertical plane downstream of turbine WEA6.

The evolution of the wake up to six diameters downstream is shown in Figure 65 in terms of the turbulent kinetic energy, wind speed and vertical wind speed. The measurements are made in a vertical plane downstream of turbine WEA6 in a wind that is from the south-west. The turbulent kinetic energy in the near-wake, $X/D < 2$, shows the evolution of the tip vortices, which are identified as the high turbulent kinetic energy regions that are shed from the blade tips. The tip vortices are convected downstream close to a span of $(Z - Z_{HH})/D = 0.5$. The wind speeds show the presence of a thin shear layer at $(Z - Z_{HH})/D = 0.65$, which separates the relatively low speed flow ($V/V_0 < 0.5$) within the wake from the relatively high speed flow ($V/V_0 > 1$) outside the wake. The near-wake region extends up to $X/D = 2.8$. Downstream of $X/D = 2.8$, mixing starts within the wake and is manifested by the penetration of relatively high turbulent kinetic energy flow from the wake boundary into the relatively low energy flow within the wake. This mixing is also seen in the measured wind speeds, as relatively high speed flow from outside the wake starts to penetrate into the low wind speed wake downstream of $X/D = 3$, and subsequently re-energises the wake flow. The above process continues up to $X/D = 5.5$, as seen both in the measured wind speeds and also as a zone of negative vertical wind speed, $V_z/V_0 < 0$, in the vertical wind speeds. This re-energised flow penetrates further into the wake and reaches the centre of the wake at $X/D = 5$. Turbulent kinetic energy shows that the flow mixing starts evolving from the wake boundary at $X/D = 3$ and reaches the centre of the wake at $X/D = 4.5$; further downstream of $X/D = 4.5$ elevated turbulent kinetic energy penetrates into the entire wake. There is an intense mixing of flow between $X/D = 3$ and $X/D = 5$, and the tip vortices are no longer distinctly visible.

The streamwise evolution of the wake is quantified in terms of the spatially-averaged wind speed, the spatially-averaged turbulent kinetic energy and maximum turbulent kinetic energy that are shown in Figure 66. The spatially-averaged flow property is derived from the area-averaged flow property in the plane that is shown in Figure 65. In the near-wake, $X/D < 2.8$, the spatially-averaged wind speed is 55% of the reference wind speed, and then the wind speed starts to recover at a rate of 10% per diameter distance downstream between $X/D = 2.8$ and $X/D = 5.5$. The spatially-averaged wind speed at $X/D = 6$ is 80% of the reference wind speed. The spatially-averaged turbulent kinetic energy also drops downstream with distance; this starts with a sharp decrease in the near-wake to $0.075 \text{ m}^2/\text{s}^2$ at $2.8D$, followed by a rise to $0.12 \text{ m}^2/\text{s}^2$ at $X/D = 3.7$. The region between $X/D = 2.8$ and $X/D = 5.5$ is where enhanced flow

mixing occurs and this is the reason for the increase in wind speed, and the increase/decrease that is observed in the spatially-averaged turbulent kinetic energy. Further downstream at $X/D = 6$, the spatially-averaged turbulent kinetic energy again reaches $0.075 \text{ m}^2/\text{s}^2$. For $X/D < 2$, the maximum turbulent kinetic energy is more than six times the values seen after $X/D = 3$. The presence of tip vortices is the reason for high levels of maximum turbulent kinetic energy in near-wake and it decreases downstream due to mixing and dissipation. It is also important to note that the maximum turbulent kinetic energy in the near wake represents the strength of tip vortices.

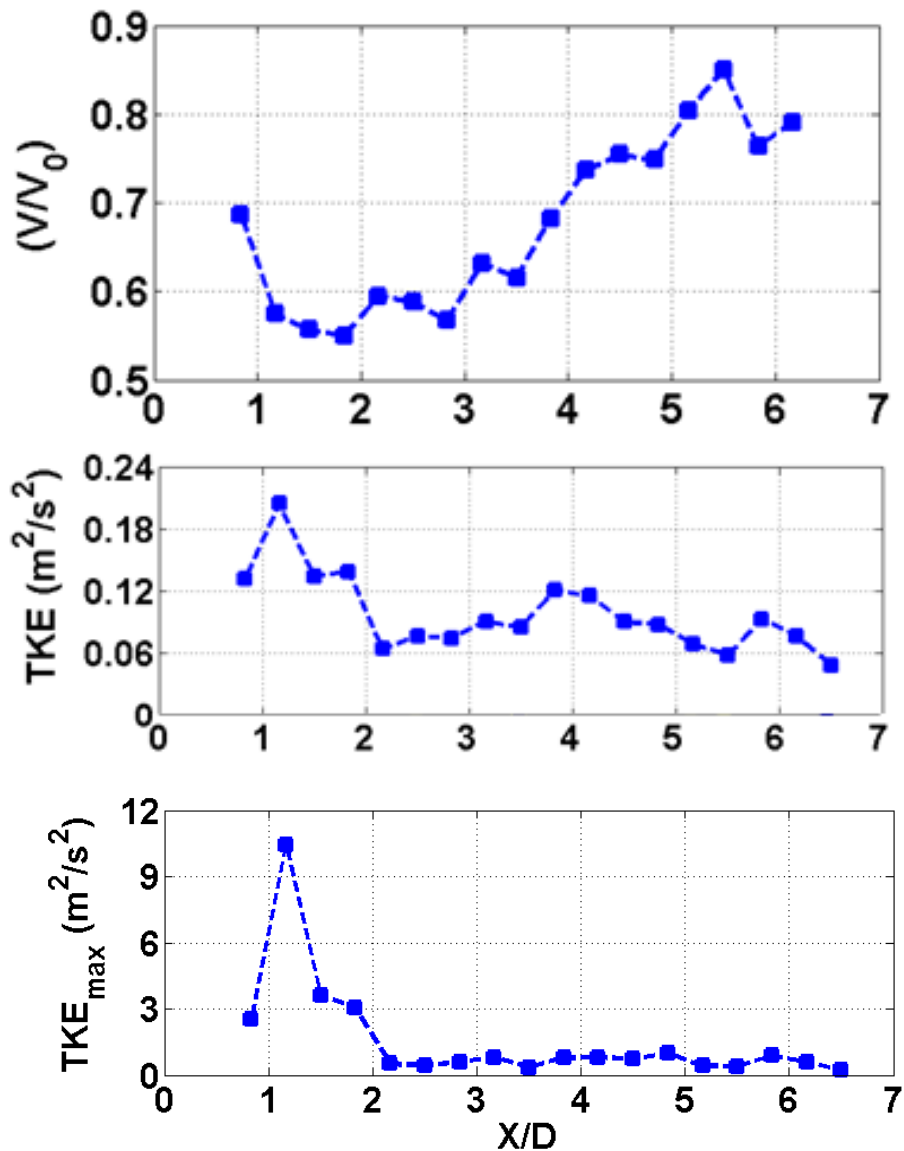
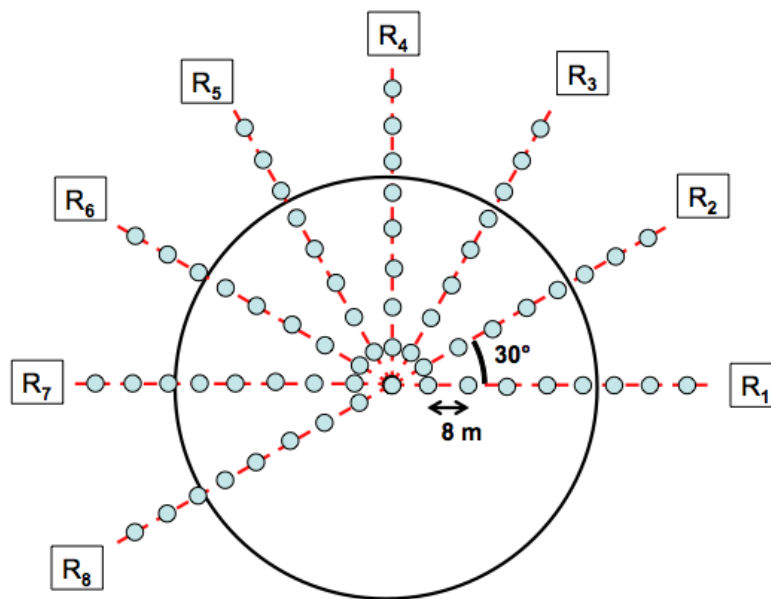


Figure 66. Streamwise evolution of spatially-averaged wind speed, spatially-averaged turbulent kinetic energy and maximum turbulent kinetic energy measured in wake of turbine WEA6.

The three-dimensional structure of the wake is next examined from a series of measurements made in a cylindrical coordinate system. A plan view of the measurement trajectories is shown in Figure 67 a, and is comprised of eight azimuthal measurement planes, R_1 , R_2 , R_3 , R_4 , R_5 , R_6 , R_7 , R_8 , each with nine radially spaced points that are $0.09D$ apart. It takes 12 minutes to scan one azimuthal measurement plane. At each point, the measurement extends from $X/D = 0.8$ to $X/D=6.5$ in a direction parallel to the turbine's axis. The measurements above, shown in Figure 65 and Figure 66, correspond to measurements in the azimuthal plane R_4 . The streamwise evolution of the spatially-averaged wind speed, the spatially-averaged turbulent kinetic energy and the maximum turbulent kinetic energy in the azimuthal planes R_1 - R_3 and R_5 - R_8 are shown in Figure 68, Figure 69 and Figure 70. The recovery of the spatially-averaged wind speed is seen in all azimuthal planes, with the mixing and recovery occurring predominantly between $X/D = 2.8$ and $X/D = 5.5$. In all measurement planes, the spatially-averaged wind speed in the near-wake, $X/D < 2.8$, ranges between 0.5-0.7 and then shows a recovery to reach spatially-averaged wind speeds between 0.7-0.8 at $X/D = 6$. Along the azimuthal plane R_8 , the wind speeds are lower as this measurement plane is located below hub height. The spatially-averaged turbulent kinetic energy in the near-wake, $X/D < 2.8$, varies little. Further downstream $X/D > 2.8$, the turbulent kinetic energy then starts to drop at a rate of $0.02 \text{ m}^2/\text{s}^2$ per diameter. Downstream of $X/D = 5.5$ the turbulent kinetic energy again varies little. The maximum turbulent kinetic energy drops downstream in all cases, due to mixing, to reach a value between $0.4 - 0.8 \text{ m}^2/\text{s}^2$ at $X/D = 6$.



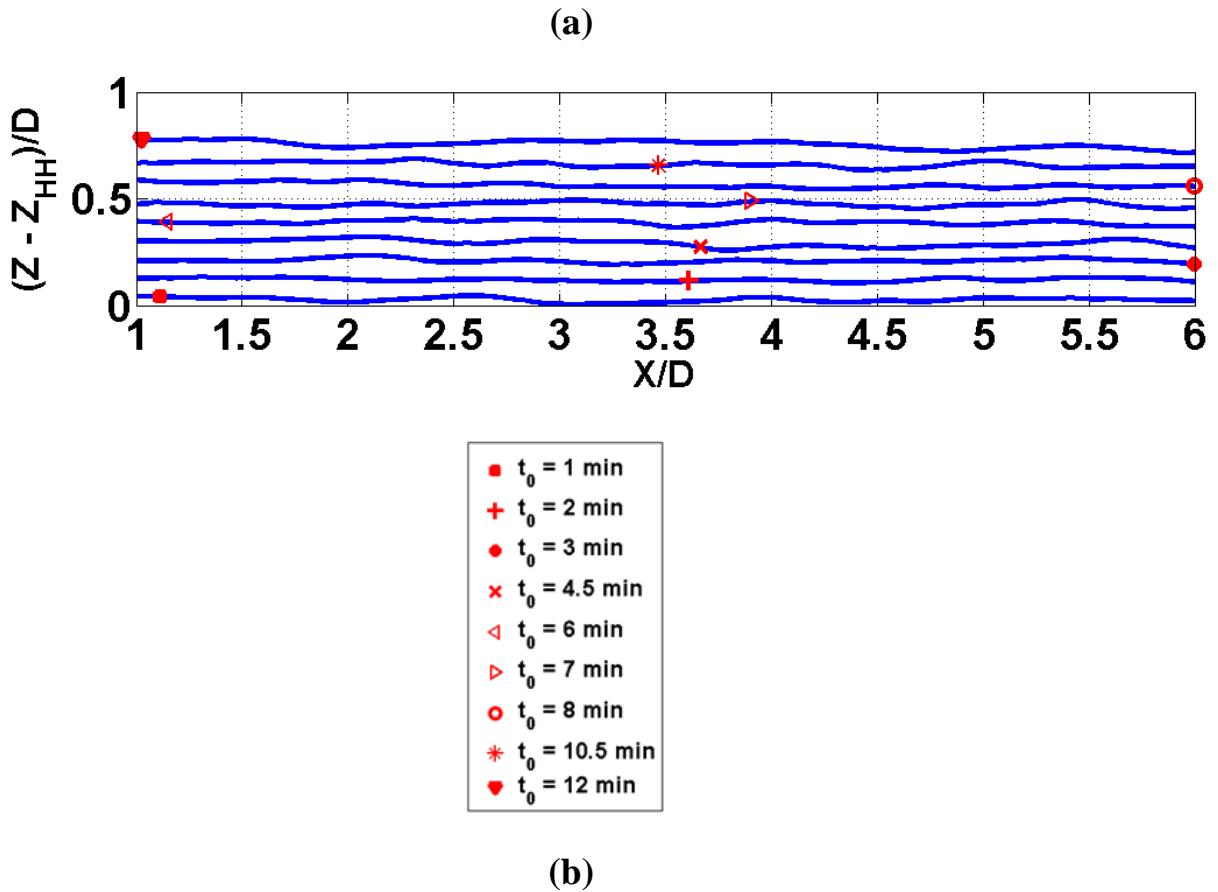


Figure 67. (a) Frontal view of azimuthal measurement planes, R_1 - R_8 . The nine radially spaced points in each plane show a flight trajectory of the drone that extends from $X/D = 0.8$ to $X/D = 6.5$ parallel to the turbine axis. (b) Measurement trajectory in wake along azimuthal plane R_4 with markings indicating the position of drone at different instant in time.

It is evident from the above that the minimum turbine spacing in a wind farm that is located in flat terrain should be greater than five and a half rotor diameters to ensure that the wake flow is mixed out in order to reduce the unsteady loads on downstream turbines and to ensure that more energy can be extracted. This observation from measurements in flat terrain at the Altenbruch II wind farm may also be relevant for offshore wind farms. Thus, for example at the Lillgrund site the turbine spacings are $3.3D$ and $4.3D$ [103]. For this offshore wind farm, measurements [103] and simulations [8] show pronounced wake losses depending on the wind direction.

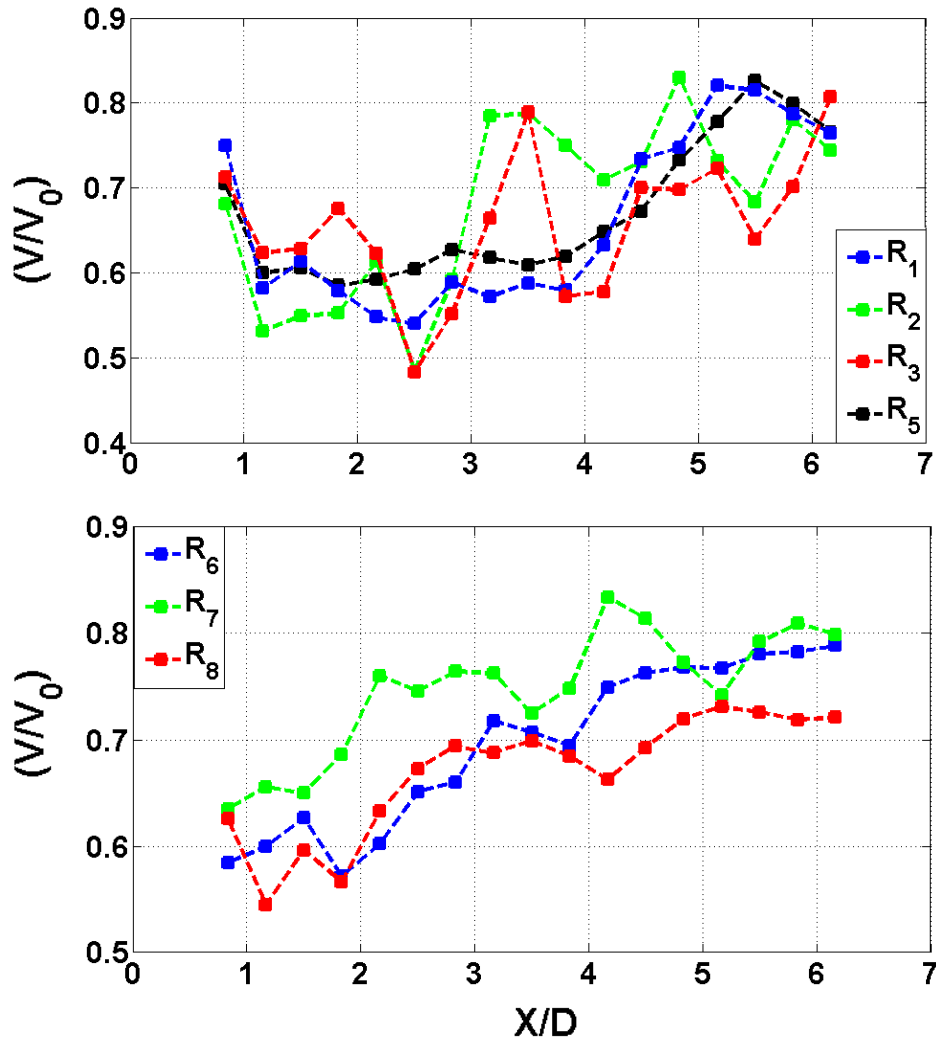
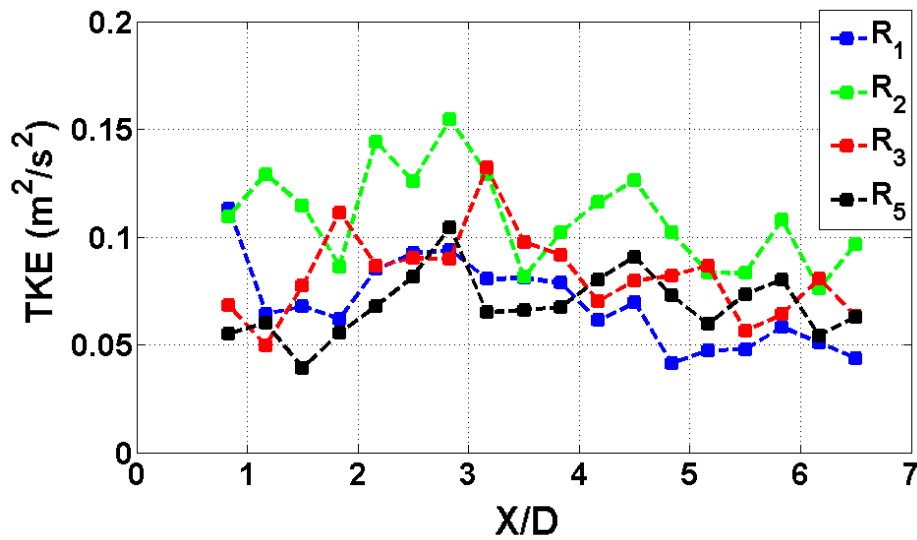


Figure 68. Streamwise evolution of spatially-averaged wind speed in azimuthal measurement planes R_1 - R_3 and R_5 - R_8 .



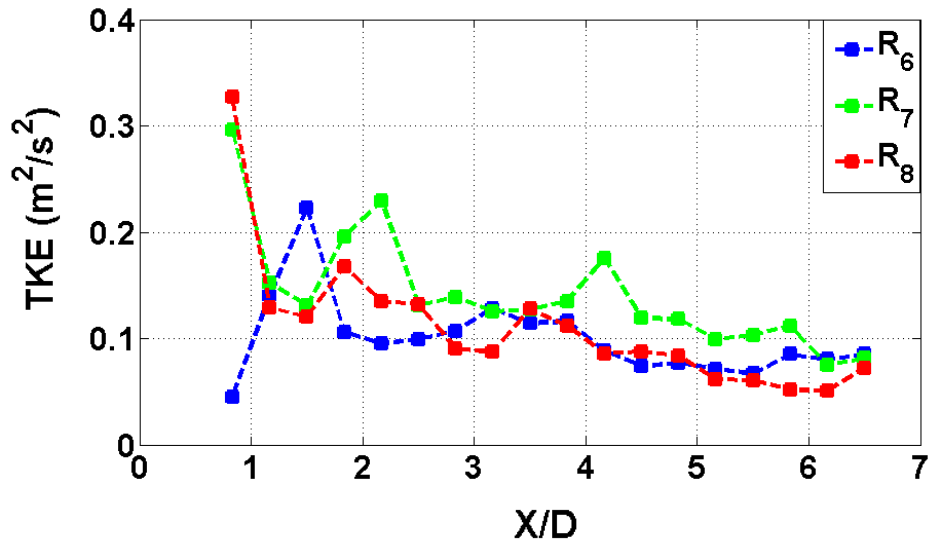


Figure 69. Streamwise evolution of spatially-averaged turbulent kinetic energy in azimuthal measurement planes R_1 - R_3 and R_5 - R_8 .

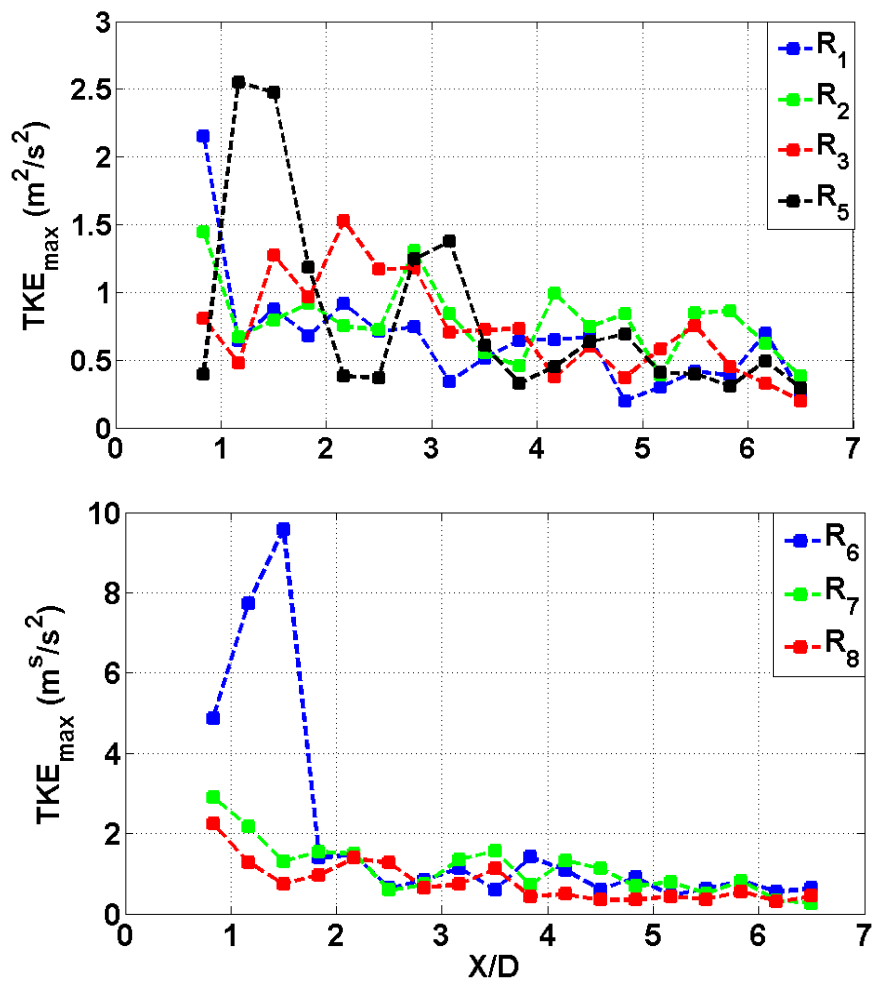
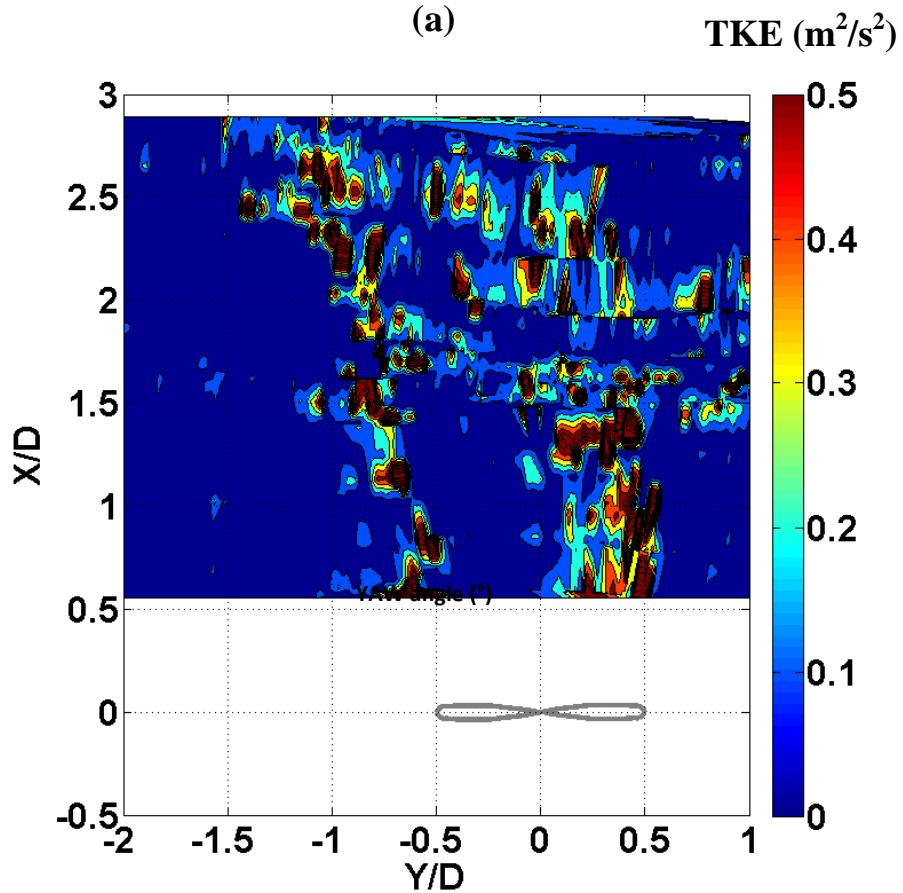
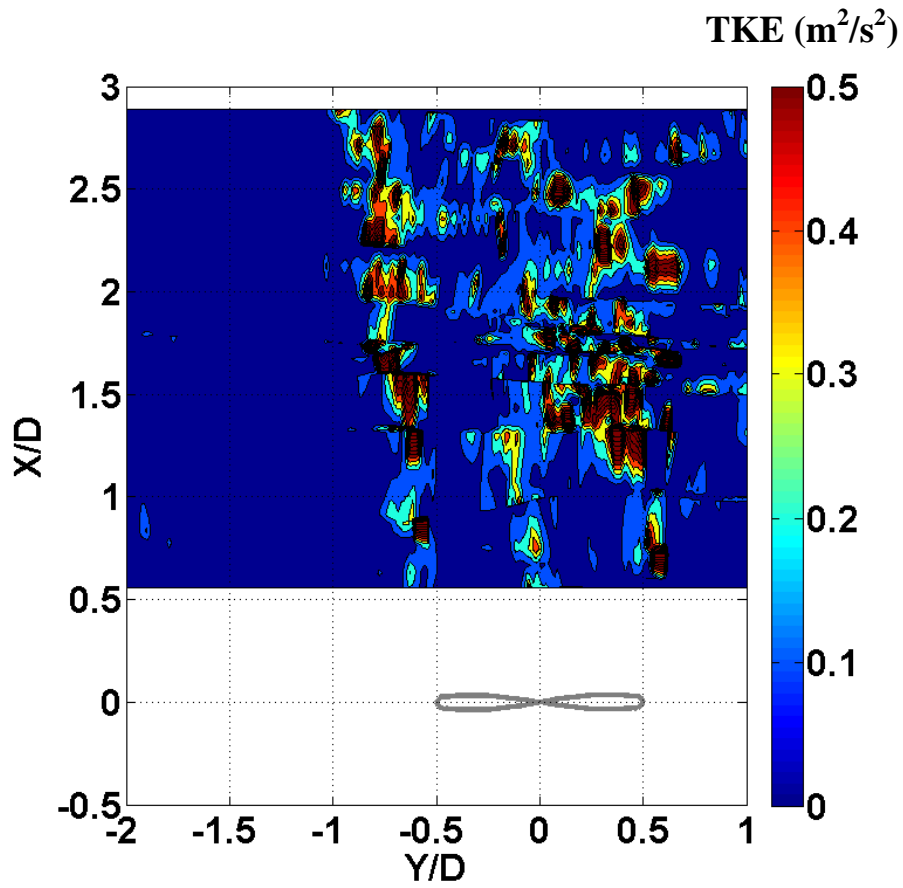
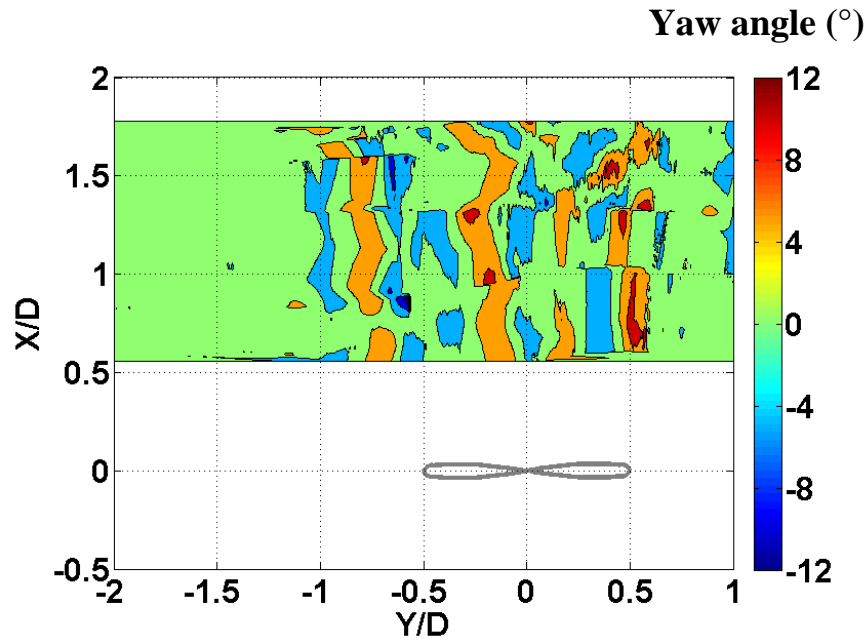


Figure 70. Streamwise evolution of maximum turbulent kinetic energy in azimuthal measurement planes R_1 - R_3 and R_5 - R_8 .

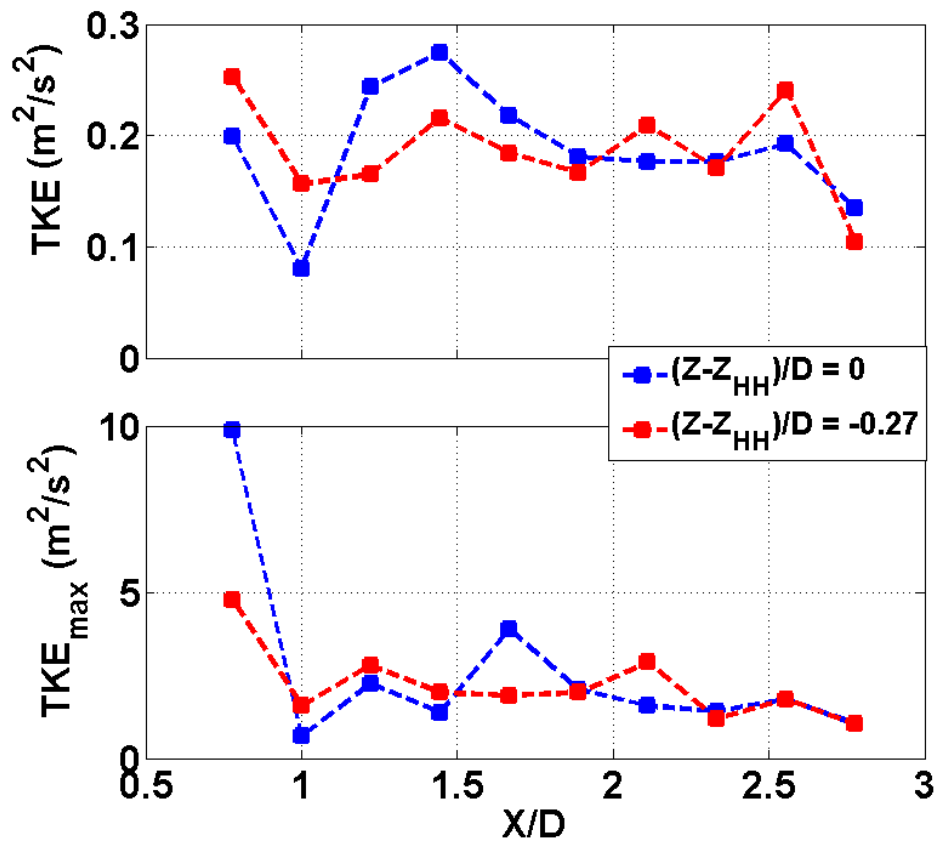
4.3.1 Turbulent Kinetic Energy in the Near-Wake

A plan view of the distribution of the turbulent kinetic energy in the near-wake, $0.5 < X/D < 2.9$, at hub height, $(Z - Z_{HH})/D = 0$, and below hub height, $(Z - Z_{HH})/D = -0.27$, are shown in Figure 71. At hub height, Figure 71a, the elevated levels of turbulent kinetic energy show the evolution of the tip vortices and the nacelle wake. The evolution follows a skewed path, and as is discussed in [104] the skewed wake is indicative of a yaw misalignment of the turbine. The tip vortices convect downstream with no significant mixing up to $X/D = 1$. At $X/D = 1$, the flow structure first appears to break down on the right side ($Y/D > 0$) of the near-wake due to an intense mixing that is indicated by the increased levels of turbulent kinetic energy ($> 0.5 \text{ m}^2/\text{s}^2$) within the wake region. The mixing is again manifested by the penetration of flow with elevated turbulent kinetic energy levels from the boundary of the wake ($X/D = 1$) into the low energy flow within the wake to reach the centre of the wake at $X/D = 1.5$; further downstream the mixing starts interacting with the nacelle wake and affects one-half of the wake evolution. The tip vortices on the other side of the wake ($Y/D < 0$) continue to be convected downstream; the spanwise extent of the region with elevated turbulent kinetic energy increases as the flow evolves and the freestream flow outside the wake is unaffected by the presence of the adjacent wake. The effect of yaw misalignment is more clearly seen in the turbulent kinetic energy distribution below hub height, $(Z - Z_{HH})/D = -0.27$, Figure 71 b. It is evident that the rotor is not aligned with the main wind direction, and that the yaw misalignment results in an earlier breakup on the right side of the flow structure that is associated with the tip vortices. For $X/D < 1.5$, the tip vortices are visible only on one side of the wake ($Y/D < 0$), and the flow mixing has already started on the other side ($Y/D > 0$) of the wake at $X/D = 0.6$. It can also be seen that the wake width below hub height, $(Z - Z_{HH})/D = -0.27$, at all downstream distances is larger than the wake width measured at hub height; this indicates that the wake width increases with yaw as also observed in the Reynolds-Averaged Navier-Stokes computations of [104] of the MEXICO rotor experiment.





(c)



(d)

Figure 71. Near-wake measurements of: (a) turbulent kinetic energy at hub height; (b) turbulent kinetic energy below hub height; (c) Yaw angle at hub height; and (d) streamwise evolution of spatially-averaged and maximum

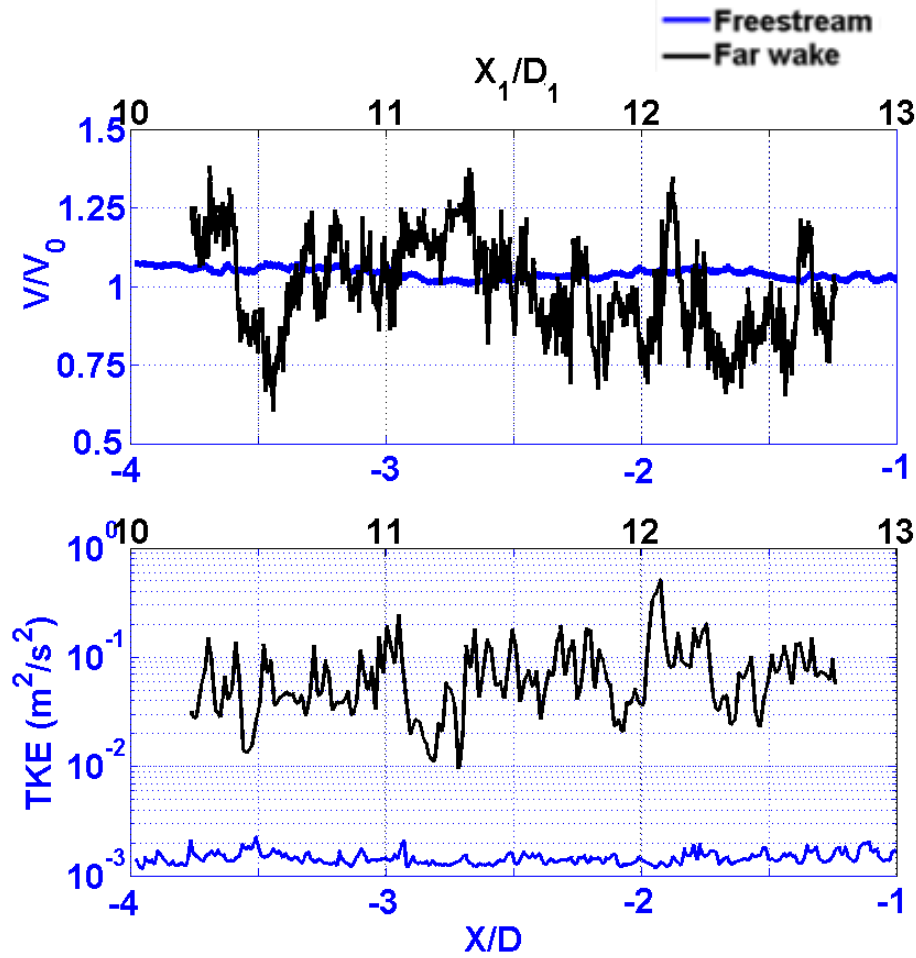
turbulent kinetic energy at and below hub height.

The distribution of the yaw angle at hub height is shown in Figure 71 c. The yaw angle is obtained from the measurements with the fast response aerodynamic probe that is discussed in Figure 14. It can be seen that regions of high turbulent kinetic energy/wake flow in Figure 71 a, are associated with vortical structures, in which there are pairs of regions with positive and negative yaw angle flow. The streamwise evolution of the spatially-averaged and maximum turbulent kinetic energy at hub height and below hub height, $(Z - Z_{HH})/D = -0.27$, are shown in Figure 71 d. At hub height, the spatially-averaged turbulent kinetic energy is maximum, $0.28 \text{ m}^2/\text{s}^2$, at $X/D = 1.45$; further downstream the turbulent kinetic energy decreases to $0.14 \text{ m}^2/\text{s}^2$ at $X/D = 2.8$. Below hub height, $(Z - Z_{HH})/D = -0.27$, the spatially-averaged turbulent kinetic energy is approximately $0.19 \text{ m}^2/\text{s}^2$ upstream of $X/D=2.7$, and decreases to $0.1 \text{ m}^2/\text{s}^2$ at $X/D = 2.8$. The highest values of maximum turbulent kinetic energy are recorded at both heights at $X/D = 0.7$, it then drops downstream to reach $1.2 \text{ m}^2/\text{s}^2$ at $X/D = 2.75$. These values are in similar range to those measured in the near wake along the eight different radial arms.

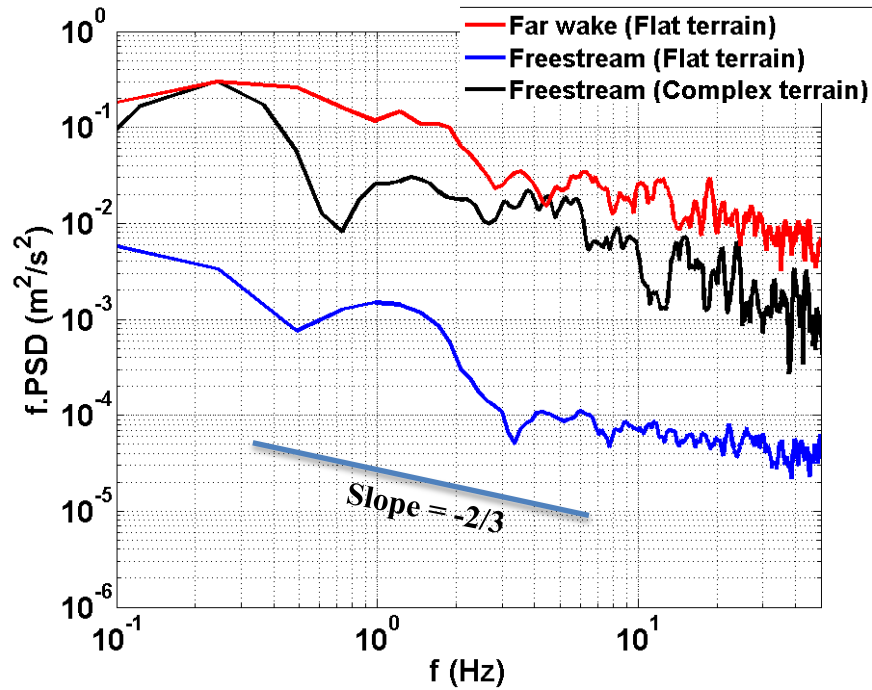
4.4 Freestream versus Far-Wake

The wind speed and turbulent kinetic energy upstream ($-4 < X/D < -1$) and in the far wake ($10 < X/D < 13$) of turbine WEA6 at 100 m AGL are compared in Figure 72 a. The mean wind speeds are $1.04V_0$ and $0.95 V_0$, respectively upstream and in the far wake. Thus, it is evident that in the far wake the wind speed has almost recovered to the freestream wind speed. However the comparison of turbulent kinetic energy, $0.078 \text{ m}^2/\text{s}^2$, in the far wake compared to $0.002 \text{ m}^2/\text{s}^2$ upstream, shows that even in the far wake the turbulence levels remain elevated. Indeed for this far-wake in flat terrain the turbulent kinetic energy is one and a half times more than the freestream turbulent kinetic energy of $0.05 \text{ m}^2/\text{s}^2$ measured in complex terrain, as made in the author's prior drone measurements [105]. Thus even in offshore wind farms, the turbines on the second and subsequent rows need to be designed for a higher turbulence class. The power spectral densities of wind speed measured at hub height upstream ($-4 < X/D < -1$) and in the far wake ($10 < X/D < 13$) are shown in Figure 72 b. Also shown for comparison is the power spectral density of the freestream wind speed measured in complex terrain. All three spectra are smoothed using the approach suggested in [99]. It can be observed that all spectra show

qualitatively similar behaviour, with a region of slope $-2/3$ that characterises the inertial sub-range. In flat terrain, over the inertial range the spectral amplitudes in the far wake are two orders of magnitude higher than the spectral amplitudes in the freestream. Similarly the spectral amplitudes in the freestream of complex terrain are nearly two orders of magnitude higher than the spectral amplitudes in the freestream in flat terrain.



(a)



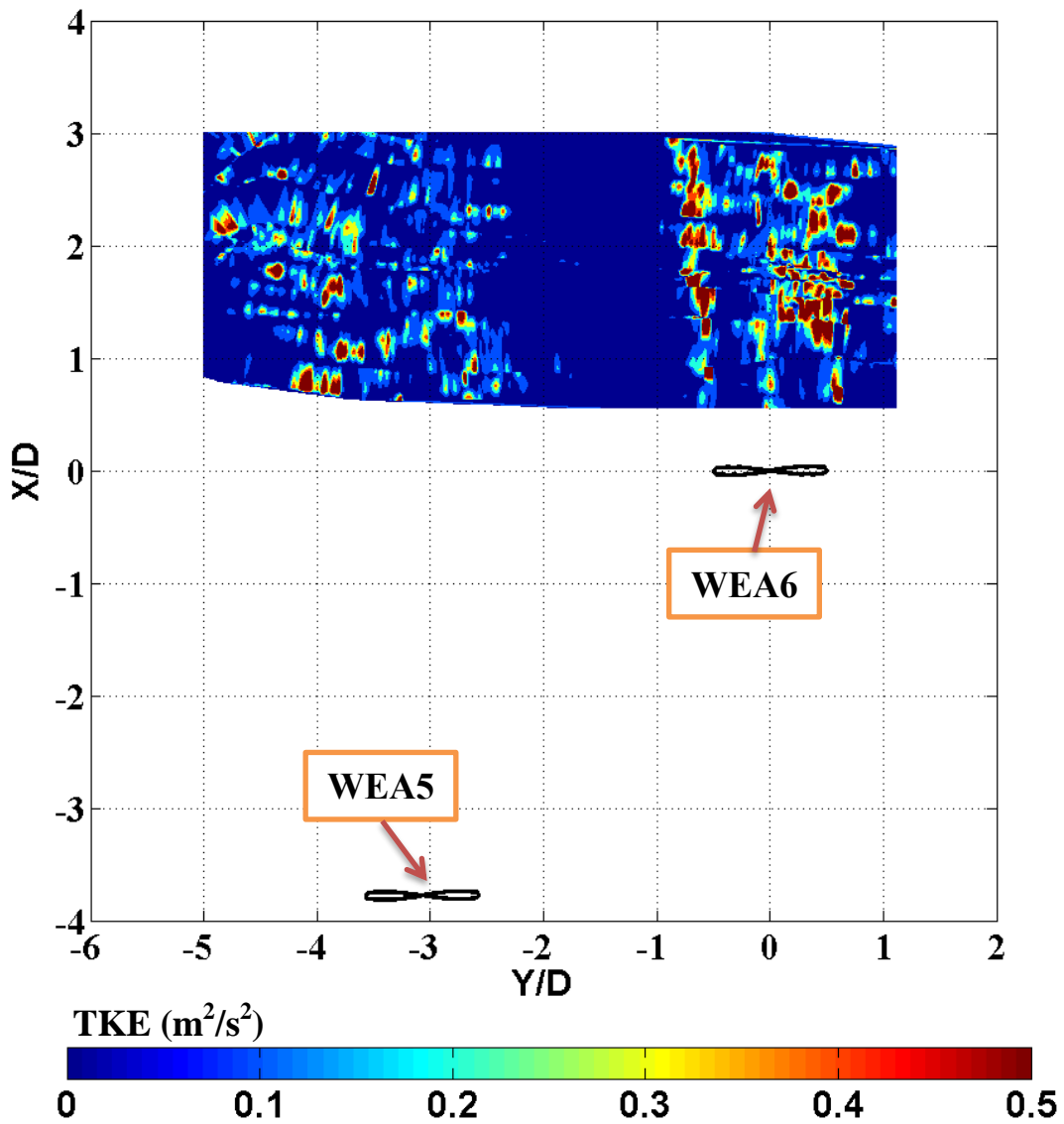
(b)

Figure 72. (a) Comparison of wind speed and turbulent kinetic energy over a streamwise distance of three diameters in freestream and wake. The measurements are made at turbine WEA6. (b) Wind speed spectra measured in freestream and far wake in flat terrain compared to the freestream spectra in complex terrain. The y-abcissa shows the product of the frequency and the power spectrum density.

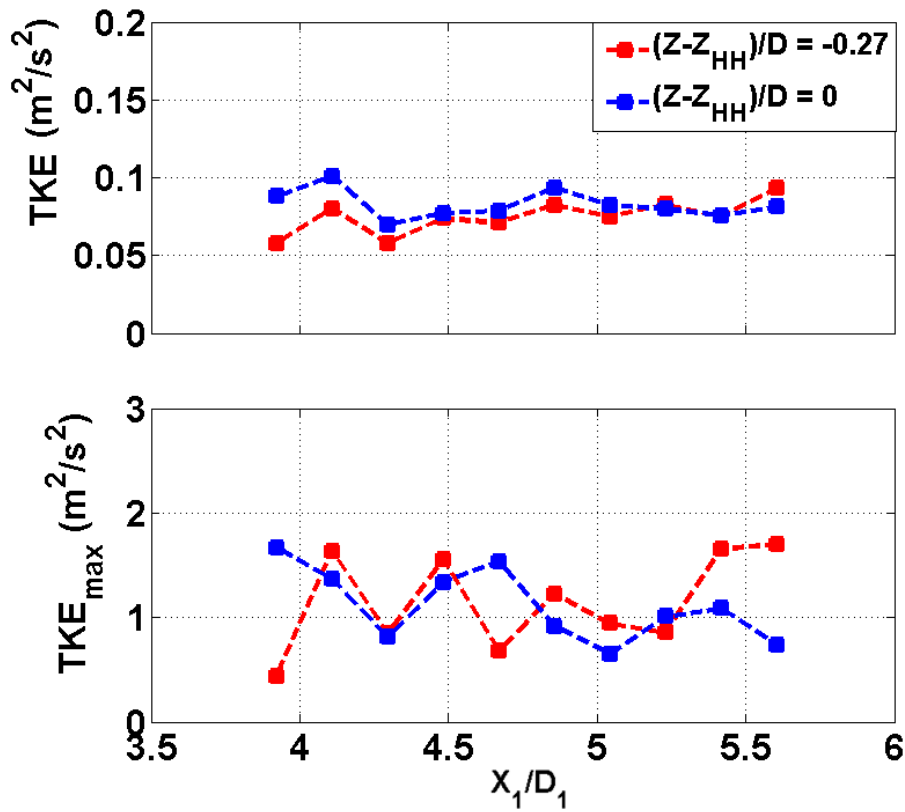
4.5 Multiple Wakes

Simultaneous measurements of multiple wakes are shown in Figure 73 in terms of the turbulent kinetic energy. The nearly parallel wakes evolve from turbines WEA5 and WEA6, and because of the wind direction, the measurements capture the near-wake, $0.5 < X/D < 3$, of turbine WEA6 and far-wake, $3.9 < X_1/D_1 < 5.6$, of turbine WEA5. The measurements are made at the hub height of turbine WEA6, which is 105 m AGL compared to the 93 m AGL hub height of turbine WEA5. The evolution of the wake from turbine WEA6 is nearly parallel to the X/D axis, however the wake from turbine WEA5 is not parallel to the X/D axis. There is a lateral shift of the latter wake towards the negative Y/D direction. At $X_1/D_1 = 4$, the width of the far wake is wider 171 m (1.6 rotor diameters of turbine WEA5) compared to the near wake at $X/D = 2.5$ that has a width of 117 m (1.3 rotor diameter of turbine WEA6); this wider wake is indicative of the

lateral spreading of a wake as it evolves from the near-wake region to the far-wake region. It can also be seen in Figure 73 that a freestream region of relatively low turbulent kinetic energy of $0.013 \text{ m}^2/\text{s}^2$ separates the wakes of the two turbines. In the far wake, the streamwise evolution of the spatially-averaged and maximum turbulent kinetic energy at hub height and at $(Z - Z_{\text{HH}})/D = -0.27$ are shown in Figure 73 b. At both heights, the spatially-averaged turbulent kinetic energy in the far wake is approximately $0.075 \text{ m}^2/\text{s}^2$, which is of the same magnitude as measured in the far wake of turbine WEA 6, Figure 72. The maximum turbulent kinetic energy plot shows the maximum values measured at both heights in the far wake. At hub height the maximum turbulent kinetic energy values show a decreasing trend downstream, but below hub height, at $(Z - Z_{\text{HH}})/D = -0.27$, they stay nearly constant.



(a)



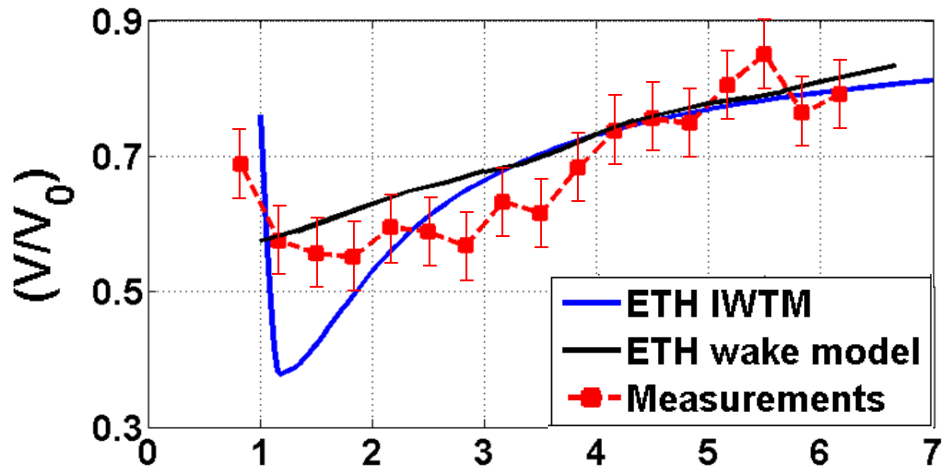
(b)

Figure 73. (a) Simultaneous measurements of turbulent kinetic energy in near-wake (of turbine WEA6) and far wake (of turbine WEA5); (b) Evolution of the spatially-averaged and maximum turbulent kinetic energy in the wake of turbine WEA5. The X_1/D_1 axis has the turbine WEA5 at its origin.

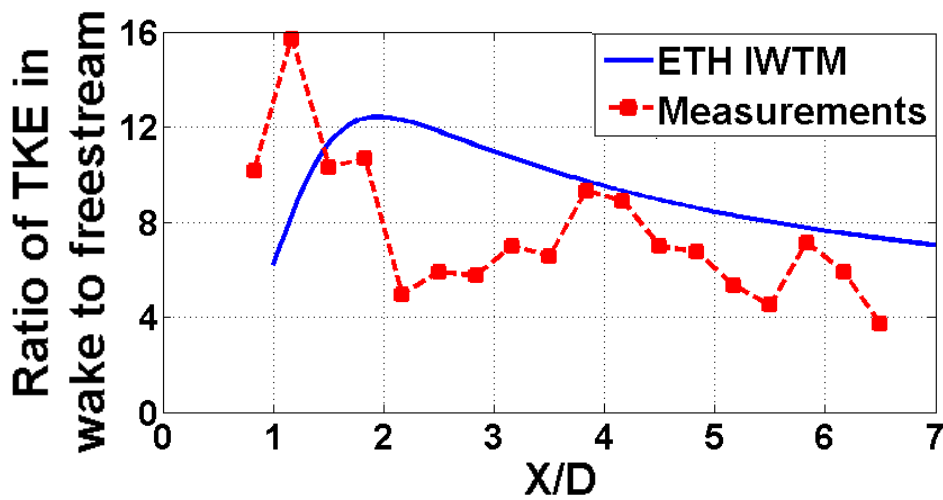
4.6 Comparison of Measurements to Predictions of Wake Flow

As discussed above the present measurements are motivated by the need to support the further development of advanced wake models and atmospheric flow simulation tools. The spatially-averaged measurements in the plane R_4 in the wake of wind turbine WEA6 are compared to the numerical predictions that are also similarly spatially-averaged in Figure 74. In the far wake, $X/D > 2.8$, the recovery of the wind speed is captured quite well by both the wake and immersed wind turbine models, Figure 74 a. In the near-wake, $X/D < 2.8$, the wake model under-predicts the deficit in wind speed, whereas the immersed wind turbine model over predicts the wind speed deficit. The evolution of the turbulent kinetic energy is compared in Figure 74 b. A good comparison of the trend is observed in the far-wake, $X/D > 3$, but the comparison is less good in the near-wake,

$X/D < 3$. This comparison between the measurements and models highlights how the observations that are made in the field experiments may be used to further develop the prediction tools.



(a)



(b)

Figure 74. Comparison of present measurements and predictions, (a) spatially-averaged wind speed, (b) spatially-averaged turbulent kinetic energy.

4.7 Summary

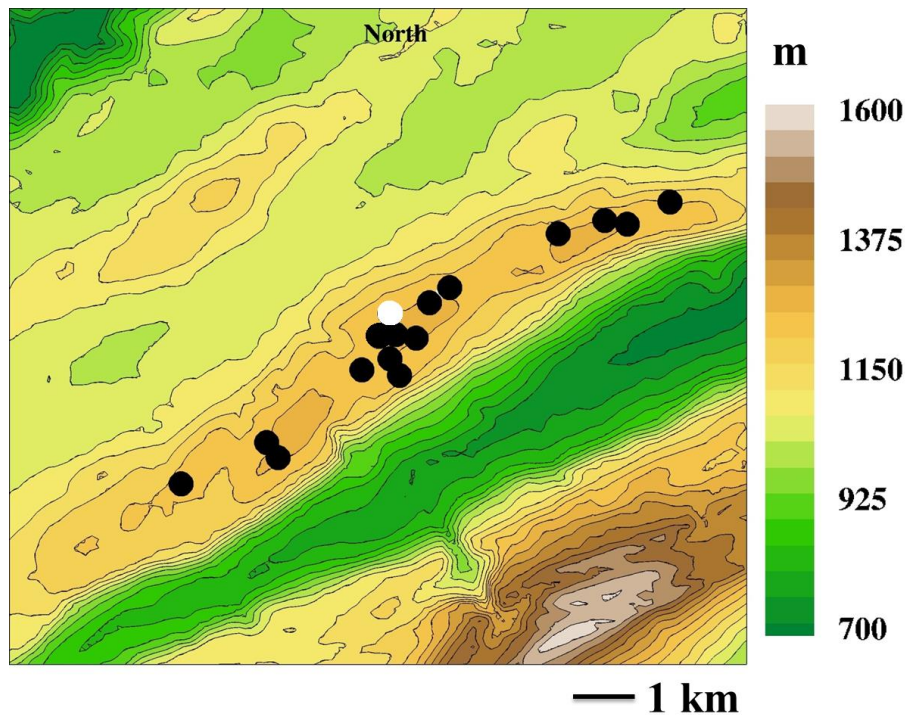
Instrumented drone measurements in a utility scale wind farm in flat terrain have been made of the near wake and far wake of the farm's multi-megawatt wind turbines. The instrumented drone allows high spatial and temporal resolution measurements of the highly three-dimensional

structure and interactions in a wind turbine's wake. The region of the near wake is measured up to 2.8 rotor diameters. In this region, tip vortices that can be distinguished from their elevated levels of turbulent kinetic energy are clearly identifiable. The tip vortices evolve just below the shear layer that separates the high speed exterior flow from the relatively low speed flow within the near wake. Further downstream of $X/D = 2.8$, the wake flow is re-energised by the penetration of the relatively large turbulent kinetic energy flow at the wake's boundary into the wake flow. By $X/D = 5-5.5$, the elevated turbulent kinetic energy flow has penetrated to the centre of the wake, and even though the upstream wind speed is recovered after $X/D = 10$, the turbulent kinetic energy is approximately two orders of magnitude larger than that upstream in flat terrain. Simultaneous measurements of the near wake (of one turbine) and the far wake (of a second turbine) confirm the distinctly different characteristics of the near wake and far wake. The measurements are compared with a recently developed semi-empirical wake model and an immersed wind turbine model that is embedded in a Navier-Stokes solver. It is shown that both models give relatively good predictions of the far wake, but need to be further improved for their near wake predictions.

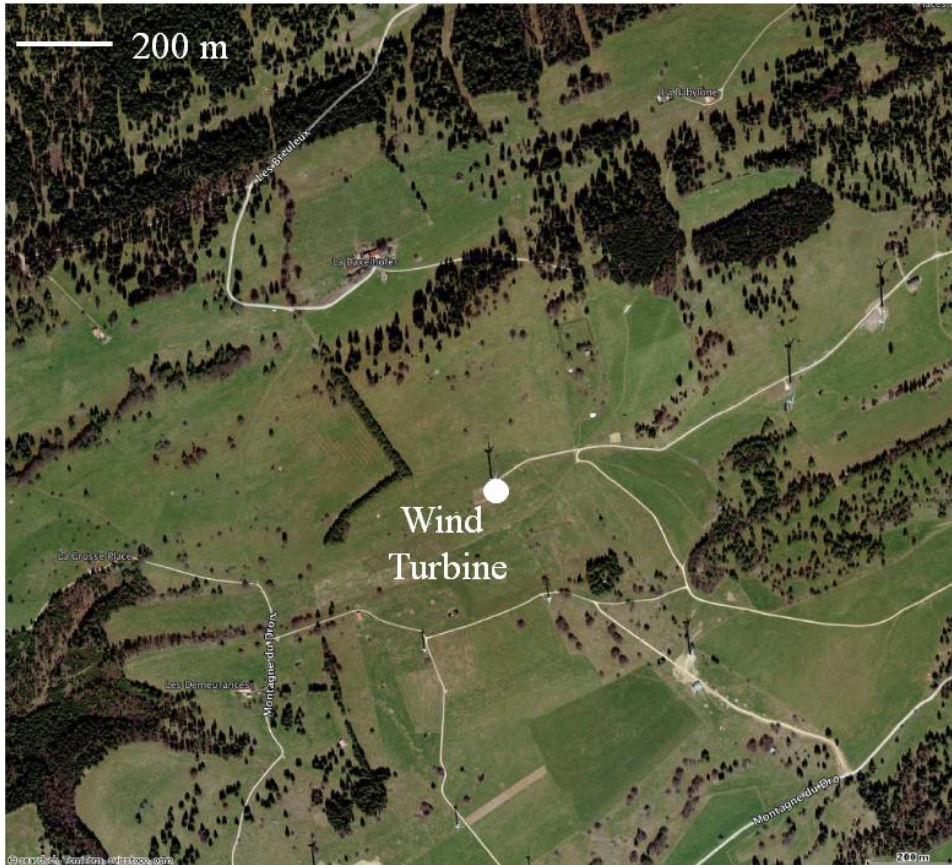
5. MEASUREMENTS IN COMPLEX TERRAIN

The aerodynamic characteristics of wakes in complex terrain have a profound impact on the energy yield of wind farms and on the fatigue loads experienced by wind turbines in a wind farm. In order to detail the spatial variations of wind speed, wind direction and turbulent kinetic energy in the near-wake, comprehensive drone-based measurements at a multi-megawatt wind turbine that is located in complex terrain have been conducted. Upstream and in the near-wake, the vertical profiles of wind speed, wind direction and turbulent kinetic energy are detailed. There is an increase in the turbulent kinetic energy across the turbine's rotor, and whereas the characteristic microscale length scales increase with increasing height above the ground upstream of the turbine, in the near-wake the microscale lengths are of constant, smaller magnitude. The first-ever measurements of the pressure field across a multi-megawatt wind turbine's rotor plane and of the tip vortices in the near-wake are also reported. The pressure rise and drop across the rotor plane is measured, and it is shown that the pitch between subsequent tip vortices that are shed from the wind turbines blades increases as the wake evolves. All measurements described in this chapter are made with the Funjet drone.

5.1 Measurement Site



(a)



(b)

Figure 75. (a) Elevation map of Mont Crosin wind farm (a complex terrain) in Switzerland. The circle symbols show the locations of the wind turbines. (b) Terrain map of the area around the wind turbine at which measurements are made.

The results presented in this chapter discuss the drone based upstream and wake measurements made on a full scale wind turbine located in a complex terrain at the Mont Crosin wind farm, Bernese Jura, Switzerland. The elevation map of the Mont Crosin wind farm is shown in Figure 75a and the terrain map of the area containing the vegetation around the wind turbine at which measurements are made is shown in Figure 75b. The locations of the wind turbines are shown by circle symbols in Figure 75a; the turbine at which measurements are made is shown as a filled white circle, whereas the other turbines are shown as filled black circles. This wind farm is located at an average elevation of 1250 m AGL in a complex terrain that is confirmed by the elevation changes around the wind turbines in Figure 75a. In addition the wind turbine at which measurements are made is also surrounded by patches of dense, tall coniferous forest, Figure 75b. During the measurements presented in this chapter, the predominant wind direction was from North-East, with wind speeds in the range of 5

m/s to 9 m/s.

The turbine chosen for the drone based wind measurements was a 2 MW Vestas V90 wind turbine. The rotor diameter is 90 m and hub height is 95 m AGL, with cut-in and cut-out wind speeds of 4 m/s and 25 m/s, respectively. The wind turbine has an automatic yaw control system, which is designed to align the rotor into the incoming wind direction. The wind farm operator provided access to the turbines' 10-minute average SCADA data, which were used for comparison to the drone based wind measurements. Table 7 summarises the characteristics of wind turbines at the Mont Crosin wind farm.

Turbines	Rated Power (MW)	Number of Turbines	Rotor Diameter (m)	Hub Height (m)
Vestas V90	2	8	90	95
Vestas V100	2	4	100	95

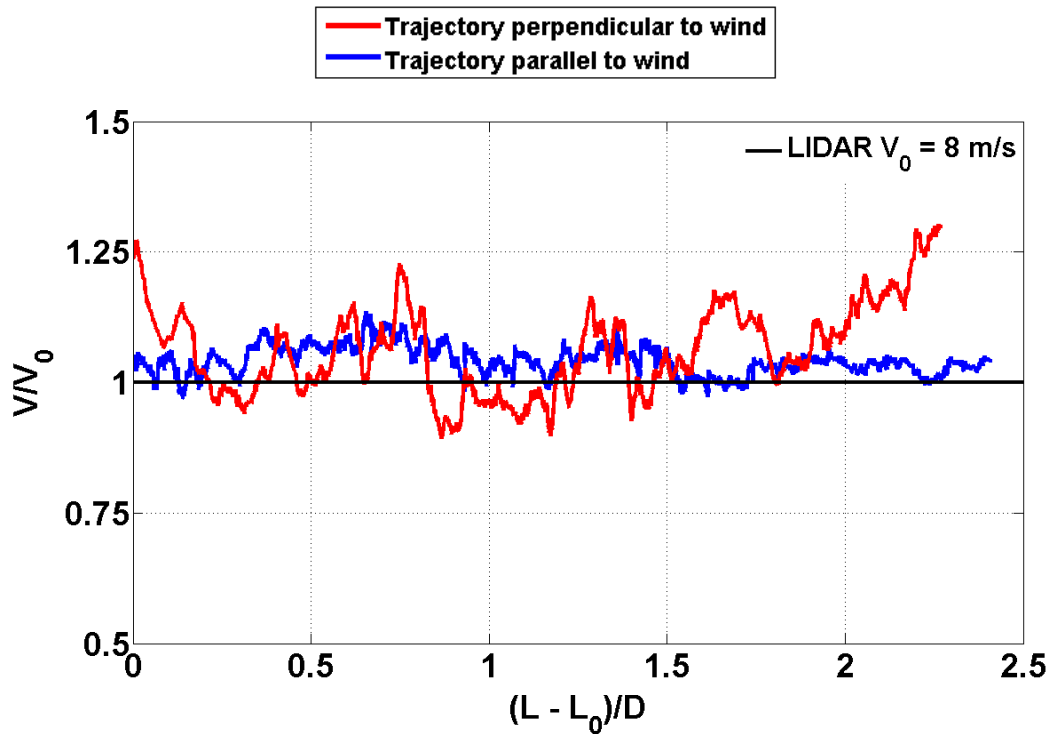
Table 7. Characteristics of wind turbines at the Mont Crosin wind farm.

5.2 Drone Measurements Versus LIDAR, SCADA and CFD

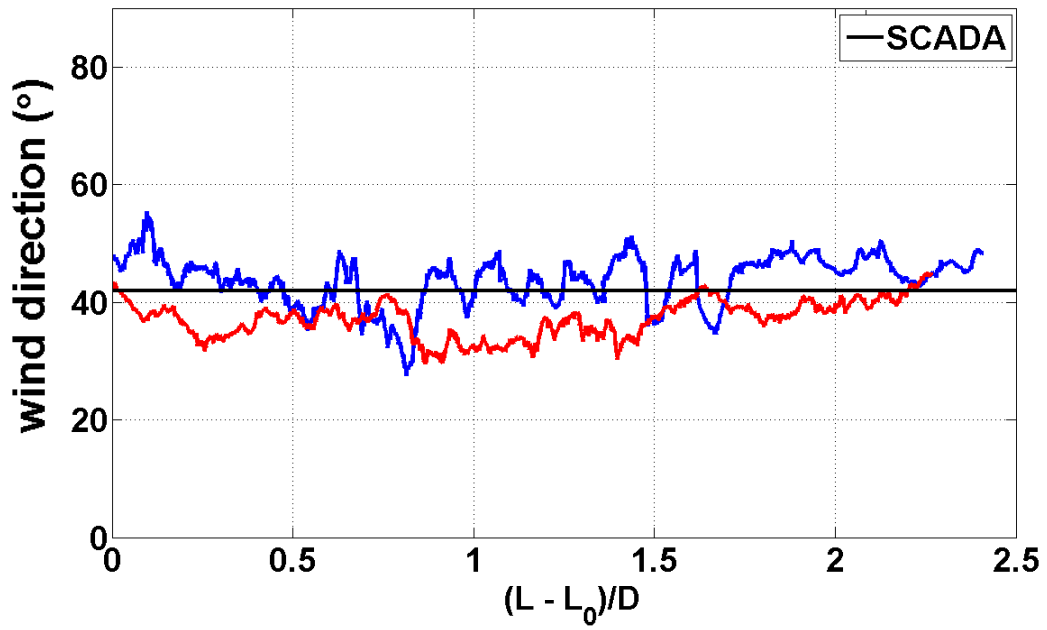
In order to assess the measurement accuracy of the drone-based system, the drone's measurements in the freestream were compared to measurements with ETH Zurich's LIDAR system and to a microscale wind CFD simulation tool, MULTI3. The LIDAR system is a Galion 3D scanning pulsed Doppler LIDAR, whose spatial resolution is 12 m and accuracy in measurement of wind speed is 0.1 m/s. The measurements described in Figure 76 are made 200 m upstream of the wind turbine, and thus the CFD simulations do not include wind turbines. The CFD spatial resolution is 20 m by 20 m in the horizontal plane. For these comparisons, two different straight-line trajectories of length 205 m and 220 m were flown at a height of 250 m AGL. In trajectory I, the drone was flown parallel to the wind and in trajectory II, the drone was flown perpendicular to the direction of the wind. The two trajectories in the freestream were flown autonomously within 3 minutes of each other, by pre-programming drone's autopilot. The drone measured wind speed, wind direction and vertical wind speed along the two drone trajectories are shown in Figure 76 a, b and c.

During these measurements, the average wind speed (V_0) was 8 m/s at a height of 250 m AGL; this measurement was made with a velocity-

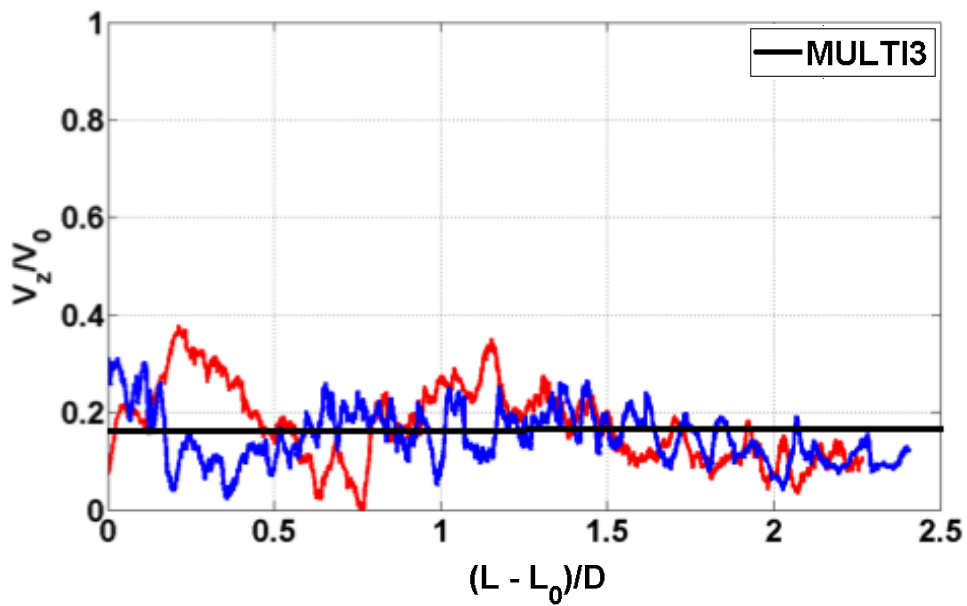
azimuth-display scan using the LIDAR. Over the same time period, the wind direction was 42° , from North-East, as measured at the hub height of the wind turbine which is downstream from the location of the drone's measurements. The mean wind speeds measured with the drone are 8.4 m/s and 8.6 m/s along the trajectories I and II, respectively. The corresponding mean wind directions are 44° and 38° respectively. As can be seen in Figure 76 a, the variations in wind speed along the two trajectories are less than ± 0.75 m/s. The variation in the wind direction, Figure 76 b, is less than $\pm 8^\circ$. Along both trajectories, positive vertical wind speeds were recorded as shown in Figure 76 c and the mean vertical wind speed is 1.5 m/s. The CFD predicted a mean vertical wind speed at the center of the drone trajectory and at a height of 250 m AGL of $V_z/V_0 = 0.17$ (1.4 m/s). Thus, the drone based measurement system is able to provide high-resolution measurements of the wind velocity.



(a)



(b)



(c)

Figure 76. (a) Wind speed, (b) Wind direction, (c) Vertical wind speed, measured along the two trajectories.

<i>Mean</i>	<i>Drone trajectory</i>			<i>% difference</i>	
	I	II		I	II
Wind speed (m/s)	8.4	8.6	8 (LIDAR)	5	7.5
Wind direction (°)	44	38	42 (SCADA)	4.8	9.5
Vertical wind speed (V_z/V_0)	0.17	0.18	0.15 (MULTI3)	13.3	20

Table 8. Comparison of drone based measurements to LIDAR and SCADA measurements and to MULTI3 (CFD) simulations

The drone measured mean wind speed, mean wind direction and mean vertical wind speed along the two trajectories are summarised in Table 8. As can be seen the difference in mean wind speed along the two trajectories is 0.2 m/s, the difference in mean wind direction is 6° and the difference in the mean vertical wind speed is 0.1 m/s. Overall, the drone-based measurements are in good agreement with the LIDAR and SCADA measurements and MULTI3 (CFD) simulations. The differences can be attributed to the different temporal and spatial resolutions of the measurement systems and simulation tool. As a further assessment, the LIDAR was programmed to track the drone along its trajectory. Whereas the drone-mounted probe measures the wind velocity vector, the LIDAR measures the line-of-sight component of wind velocity. The line-of-sight wind velocity was thus derived from the drone based measurements. The drone and LIDAR measurement of the line-of-sight velocity are compared in Figure 77. Over the range of measurements, the magnitude of the line-of-sight velocity varies monotonically from 4 m/s to -2 m/s, with an overall difference of less than 15 %.

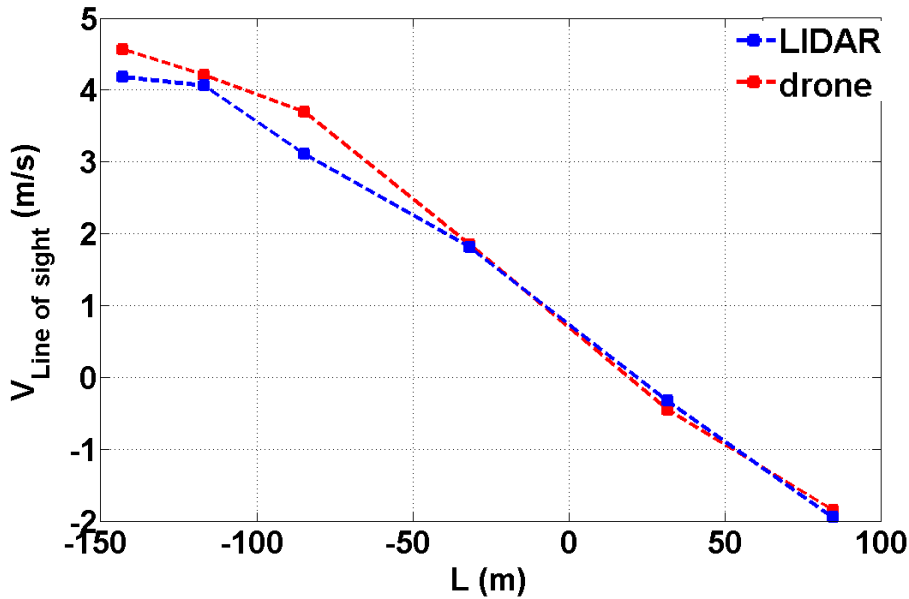


Figure 77. Comparison of LIDAR measured line of sight wind speed component to drone measurements.

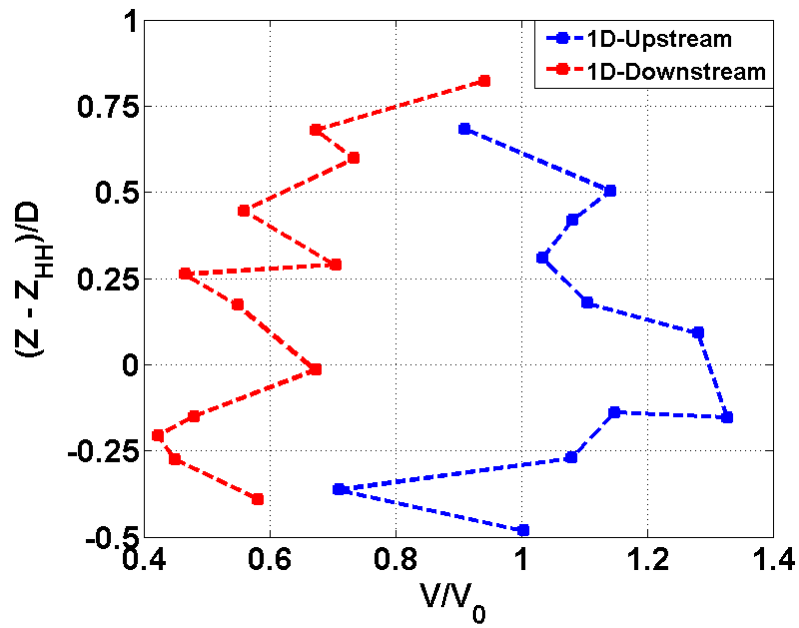
5.3 Flow Profile Around a Wind Turbine

The vertical profiles of the mean wind speed, wind direction and turbulent kinetic energy at one diameter upstream and downstream of the turbine are presented in Figure 78. As noted in Figure 4, these are the inflow and outflow boundaries of the immersed wind turbine model. The mean flow properties are evaluated over lateral distances of $Y/D = \pm 0.5$ at each height. The time taken for this complete measurement set is less than 15 minutes. During this measurement the SCADA reported wind speed, V_0 , was 6 m/s and the corresponding wind direction was 90° .

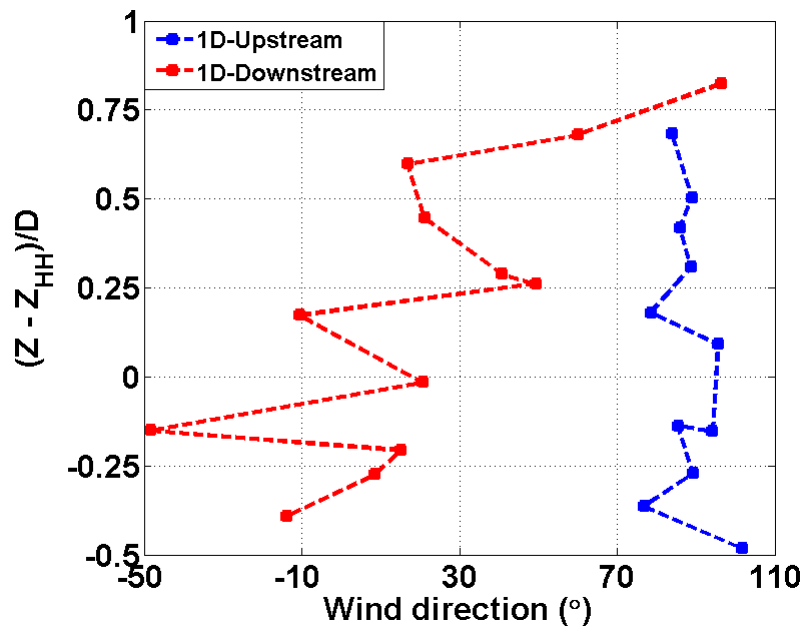
The mean wind speed profile, at 1D upstream, Figure 78 a shows a jet-like structure with a maximum wind speed of 7.8 m/s at 80 m AGL, and an area averaged wind speed of 6.4 m/s. This jet like wind profile is not seen in the wake at 1D downstream. Jet-like wind profiles in the upstream region were reported on other occasions at Mt. Crosin by Subramanian et al. [96]. The area-averaged wind speed at 1D downstream of a rotor plane is 3.9 m/s. The mean wind speed measured at 1D downstream of the turbine at $(Z-Z_{HH})/D = 0.8$ (above the rotor plane) is close to the corresponding measurement upstream of the turbine, indicating that this measurement is outside the wake. The deficit in wind speed, that is the difference between the mean wind speeds upstream and downstream of the rotor plane, is maximum between $(Z-Z_{HH})/D = -0.25$ and 0.5.

The mean wind direction profiles at 1D upstream and 1D

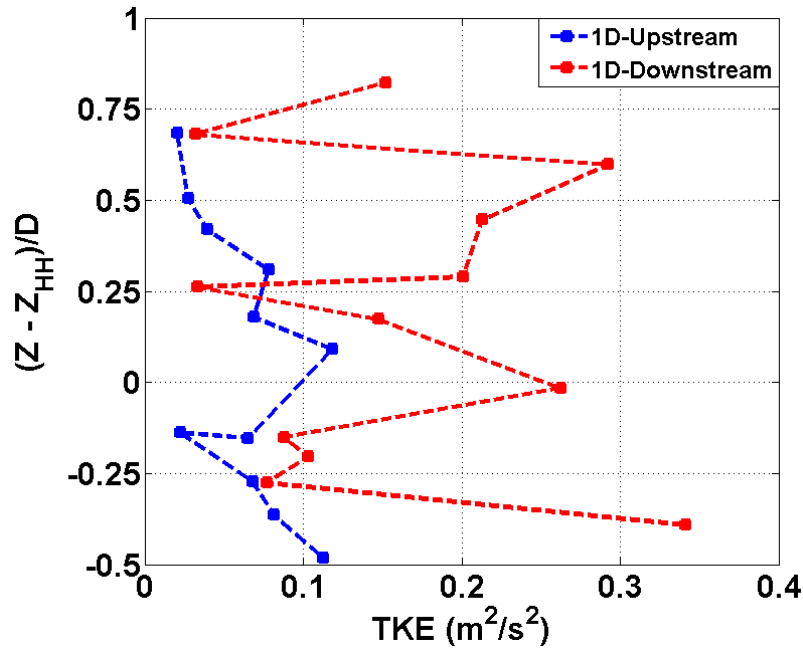
downstream are shown in Figure 78 b. The area-averaged wind direction at 1D upstream is 85° . Thus, there is a 5° difference compared to the SCADA wind direction indicating that the turbine is not aligned to the main wind direction. The upstream profile shows the wind veer upstream of the turbine with differences of $\pm 12^\circ$ relative to the area averaged wind direction. The downstream profile shows that the skewness in the wake is more pronounced in the lower half of the rotor's extent. Above the rotor plane for $(Z - Z_{HH})/D > 0.7$, the wind directions upstream and downstream are same, indicating the vertical extent of the wake.



(a)



(b)



(c)

Figure 78. Vertical profiles of mean flow properties measured upstream (blue) and downstream (red) of the turbine (a) wind speed; (b) wind direction; (c) turbulent kinetic energy.

The profile of turbulent kinetic energy is shown in Figure 78 c. The turbulent kinetic energy is calculated from the STFT with a window length of 0.25 s. At 1D upstream, the mean turbulent kinetic energy is maximum, $0.11 \text{ m}^2/\text{s}^2$ close to ground, $(Z-Z_{HH})/D < -0.35$ and decreases to $0.025 \text{ m}^2/\text{s}^2$ above the rotor plane for $(Z-Z_{HH})/D > 0.5$. The area-averaged turbulent kinetic energy at 1D upstream is $0.05 \text{ m}^2/\text{s}^2$, and the area-averaged turbulent kinetic energy at 1D downstream is $0.16 \text{ m}^2/\text{s}^2$. Thus there is a factor three increase in turbulent kinetic energy across the turbines rotor.

5.4 Pressure Variations Across a Wind Turbine Rotor

The streamwise variation of the differential static pressure at hub height is shown in Figure 79. The measurements are accomplished by making semi-automated flights of the drone across the rotor plane. An optical trigger system [97] that is linked to the autopilot is used to track in real-time the rotor blade position and speed so that flight across the rotor can be successfully accomplished. To the authors' knowledge these are the first such measurements of the pressure field at the rotor plane of an operational wind turbine. The measurements are shown at two radial

positions of $r/R = 0.4$ and 0.6 . The SCADA mean wind speed (V_0) during this measurement was 7.5 m/s. The measurements show that there is a small radial variation of the pressure change across the rotor mid-section. Furthermore, the pressure drop and recovery occur over a streamwise extent of $\Delta(X/D) = 0.06$.

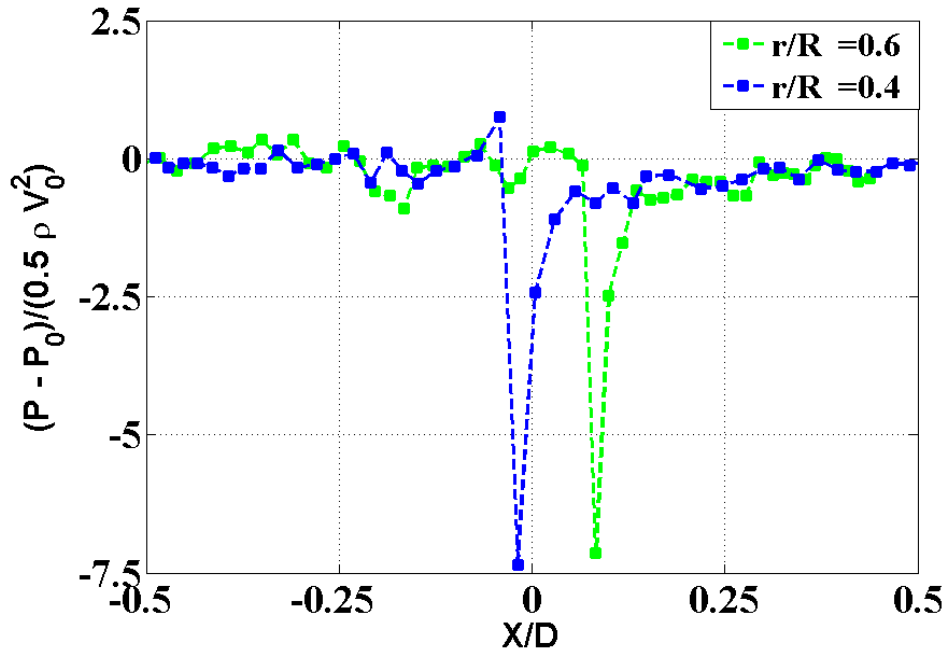


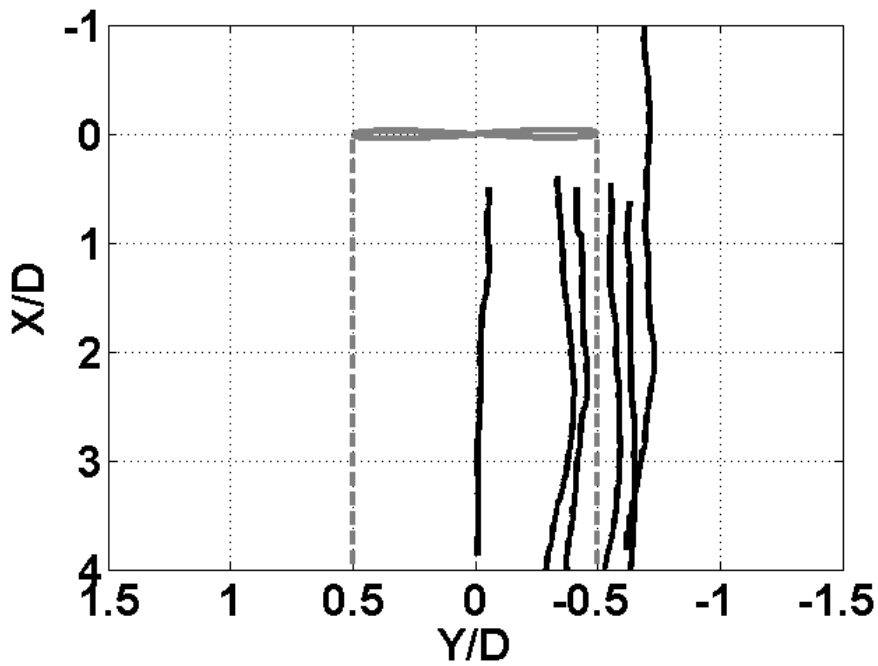
Figure 79. Streamwise variation of static pressure coefficient across wind turbine rotor. The measurements are at radial spans of $r/D = 0.4$ and 0.6 . The pressure is normalised relative to reference based on the SCADA 10-minute averages.

5.5 Wind Speed and Turbulent Kinetic Energy in Wake

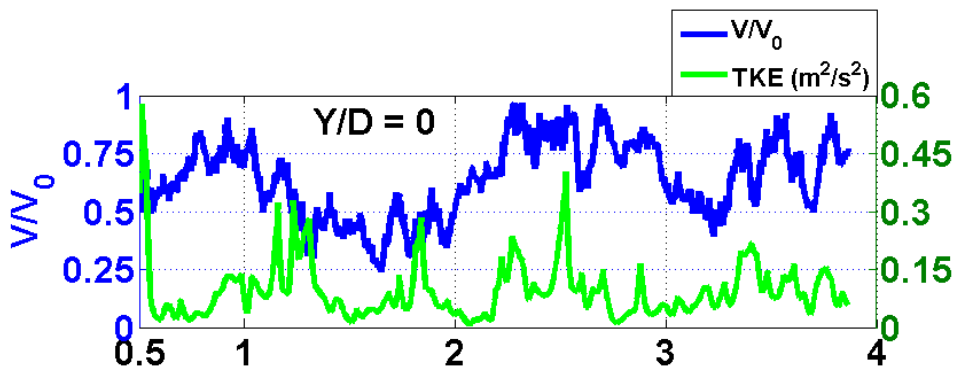
The streamwise evolution of wind speed and turbulent kinetic energy at hub height in the wake of a wind turbine is shown in Figure 80 b. This measurement is made along the drone trajectories shown in Figure 80 a. These trajectories are at six different spanwise positions between $Y/D = 0$ to -0.7 . The SCADA mean wind speed (V_0) during this measurement was 7.2 m/s and the mean wind direction was 45° (North-East).

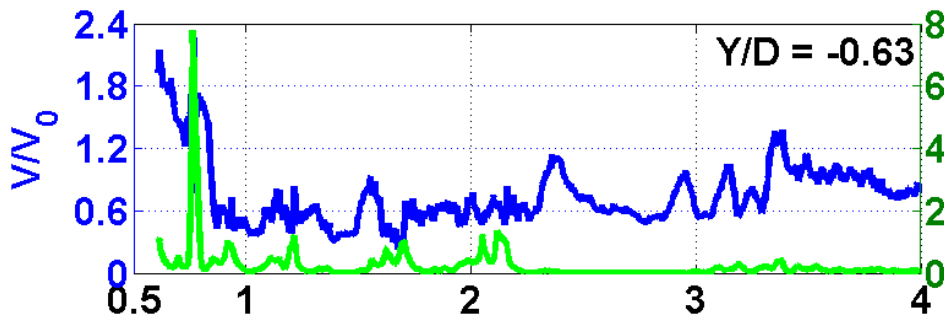
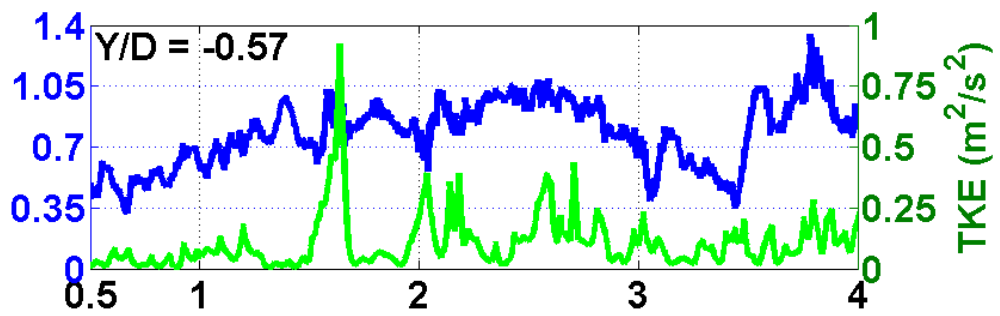
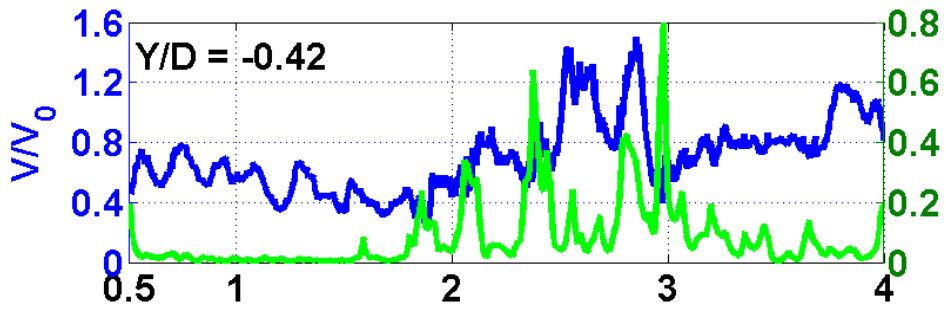
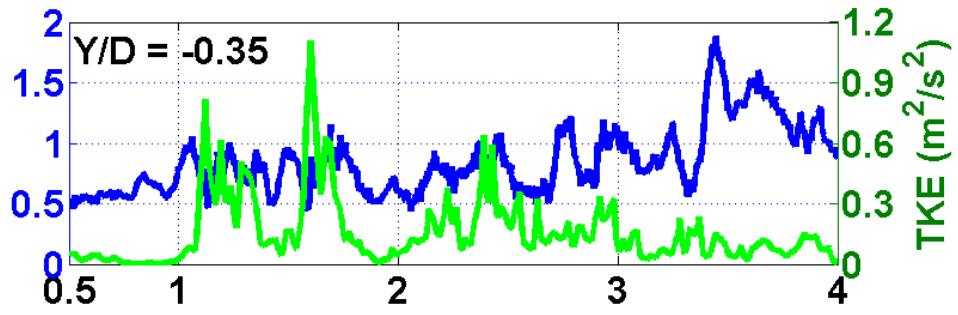
At $Y/D = 0$, the mean wind speed (V/V_0) measured is 0.68 for $X/D < 1.1$, it then drops to 0.4 at $X/D = 1.25$. This decrease in wind speed is accompanied by an increase in turbulent kinetic energy from 0.04 m^2/s^2 to 0.18 m^2/s^2 , which indicates the mixing in the near-wake. For $X/D < 4$, the wind speed varies between 0.25 and 0.75 , with a decrease in mean wind speed to 0.75 downstream of $X/D = 2.5$. The mean turbulent kinetic energy

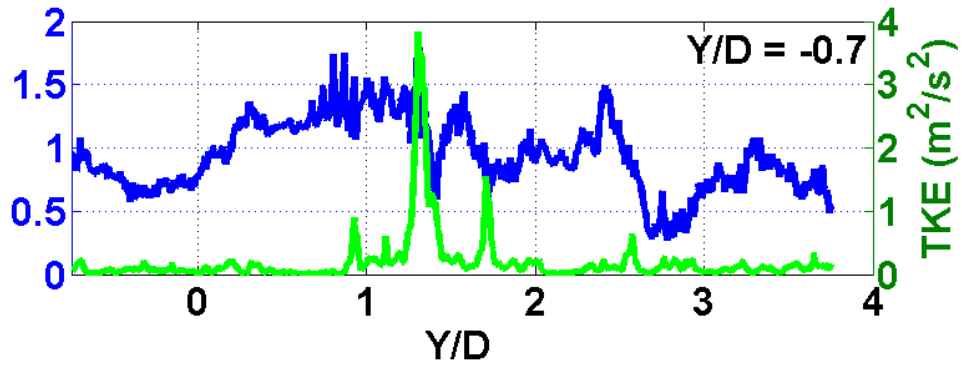
increases to $0.12 \text{ m}^2/\text{s}^2$, at $X/D = 3.5$, with peaks of $0.25 \text{ m}^2/\text{s}^2$ measured in this vicinity. For $Y/D = -0.35$, the wind speed shows a gradual recovery from 0.5 at $X/D = 0.5$ to 1 at $X/D = 4$. The mean turbulent kinetic energy shows a sudden increase from $0.05 \text{ m}^2/\text{s}^2$ for $X/D < 1$ to $0.4 \text{ m}^2/\text{s}^2$ at $X/D = 1.2$, with multiple peaks observed between $X/D = 1.2$ and $X/D = 1.8$. It then shows a gradual drop to reach $0.08 \text{ m}^2/\text{s}^2$ at $X/D = 4$. For $Y/D = -0.42$, mixing is observed between $X/D = 1.8$ and $X/D = 3$, with turbulent kinetic energies of up to $0.8 \text{ m}^2/\text{s}^2$ recorded in this trajectory. Oscillations observed in the wind speed along the $Y/D = -0.42$ and -0.57 trajectories close to the turbine - for $X/D < 1.5$ - indicate the blade passing signatures.



(a)







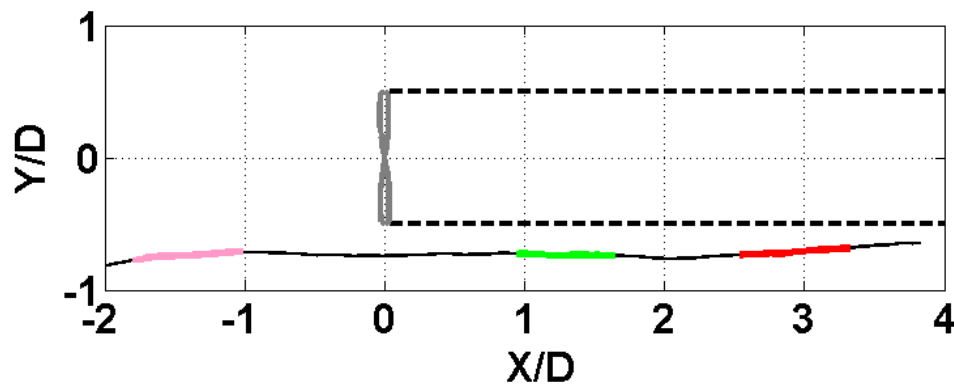
(b)

Figure 80.(a) Drone trajectory in wake scan, (b) Hub height wind speed and turbulent kinetic energy distribution in wake along different spanwise position upto $4D$.

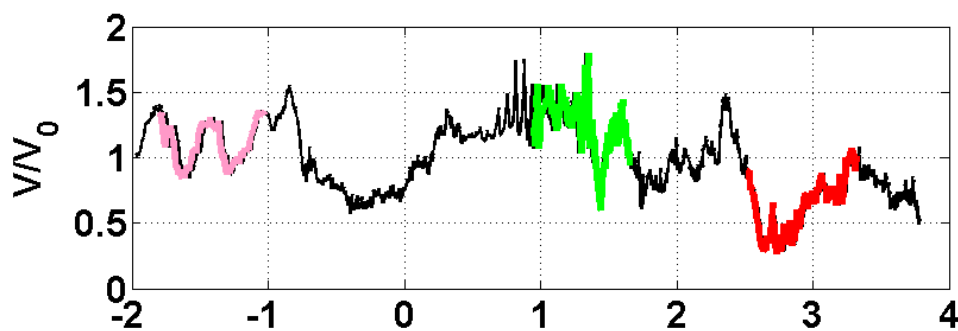
For $Y/D = -0.57$, the wind speed shows a steady recovery from 0.44 at $X/D = 0.5$ to 1.05 at $X/D = 2.5$, it then shows a gradual drop to 0.4 between $X/D = 2.8$ and $X/D = 3.5$. The mean turbulent kinetic energy along this trajectory is higher than those measured along $Y/D = -0.42$. At $Y/D = -0.63$, the wind speed shows a sudden drop from 1.5 at $X/D = 0.7$ to 0.6 at $X/D = 0.85$, then shows a gradual recovery to reach 1 at $X/D = 3.5$. The turbulent kinetic energy along this trajectory records the highest peak observed in this measurement with a value of $8 \text{ m}^2/\text{s}^2$ at $X/D = 0.75$, indicating that the drone is passing through a tip vortex. Also, this trajectory records the maximum number of turbulent kinetic energy peaks, with most of the peaks occurring at $X/D < 2.3$. A number of turbulent kinetic energy peaks along this trajectory may be an indicative of the tip vortex shedding in this region, thus resulting in higher levels of mean turbulent kinetic energy.

The streamwise evolution of the flow along a trajectory that passes through the boundary of the wake is shown in Figure 81. The measurements are at a spanwise position of $Y/D = -0.7$, and extend from upstream of the turbine at $X/D = -2$ into the far-wake at $X/D = 4$. In order to clarify different regions of the flow, 4 regions along the trajectory, Figure 81 a, are coloured blue in the segment upstream for streamwise distances $X/D = -1.8$ to -1.2 , green for $X/D = 1$ to 1.6 , red for $X/D = 2.6$ to 3.3 , and black for all other segments. It should be noted that the horizontal dashed lines in Figure 81 a indicate the spanwise extent of the rotor. Figure 81 b shows the wind speed, Figure 81 c shows the turbulent kinetic energy and Figure 81 d the wind direction along this trajectory. The mean wind

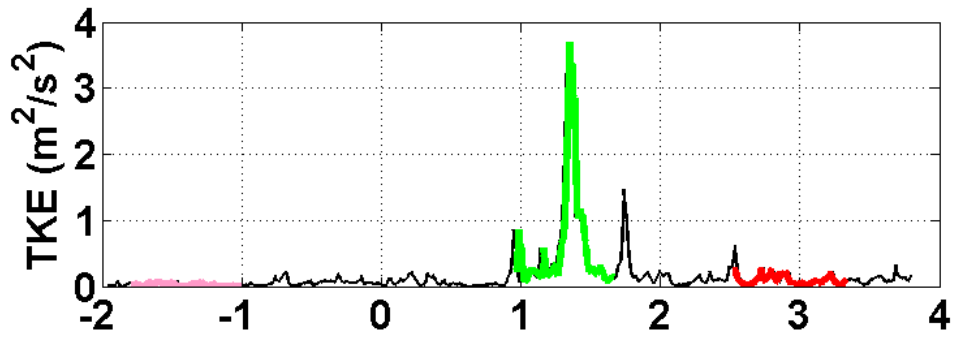
speeds upstream (blue) and downstream in the green region ($1 < X/D < 1.6$) are approximately the same. At $X/D = 1.3$, the trajectory intercepts the wake boundary and this is manifested as a spike in turbulent kinetic energy of $3.8 \text{ m}^2/\text{s}^2$ at this location. Further downstream in the red region $2.5 < X/D < 3.5$ the mean wind speed is lower than upstream. In the three regions the mean wind directions are approximately the same. The spectra of wind speeds in the three regions are compared in Figure 81 e. It can be seen that in the near-wake (green region) the amplitudes are more than 50 times higher than upstream. At $X/D = 3$, the spectral amplitudes are an order of magnitude higher than upstream but less than in the near-wake. The static pressure distribution in the near-wake position, $0.6 < X/D < 1.8$, is shown in Figure 81 f. Overall there is an increase in static pressure across the wake boundary downstream. In the immersed wind turbine model, Figure 4, as the side boundaries have a momentum exchange, these measurements may be used to formulate a specified geometry for the model's side boundaries.



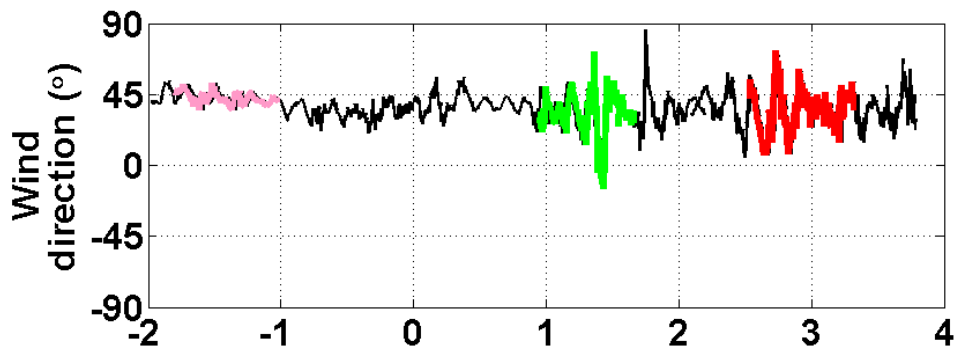
(a)



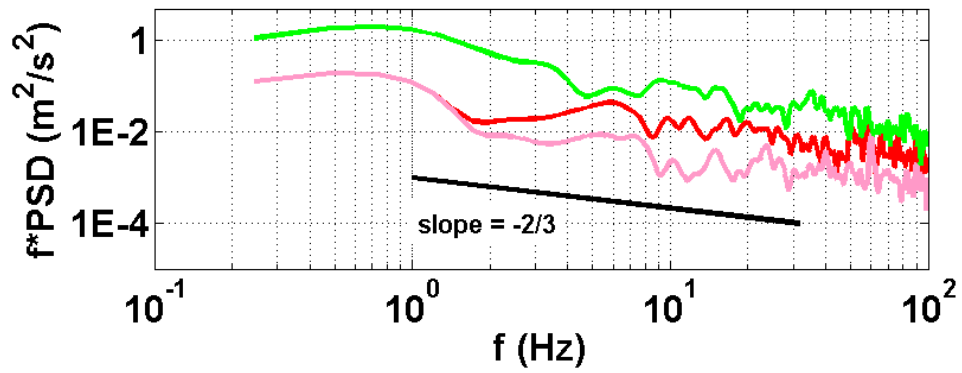
(b)



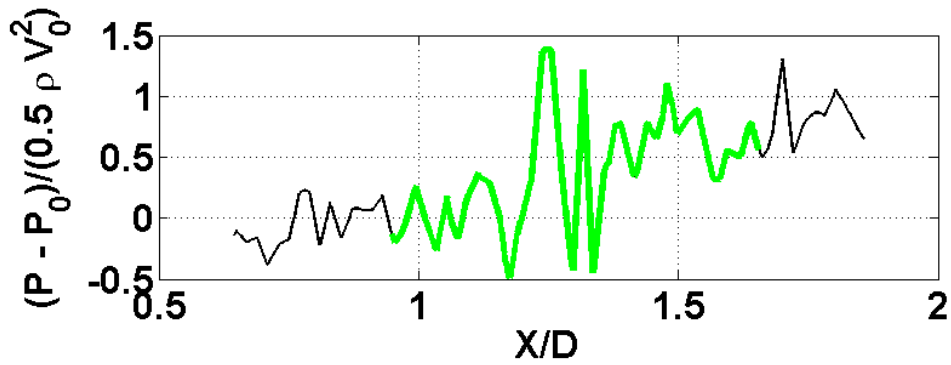
(c)



(d)



(e)



(f)

Figure 81. Drone trajectory, flow properties – wind speed, turbulent kinetic energy, wind direction, power spectra and differential static pressure - along a trajectory passing through shear layer (wake boundary).

5.6 Upstream and Wake Spectra

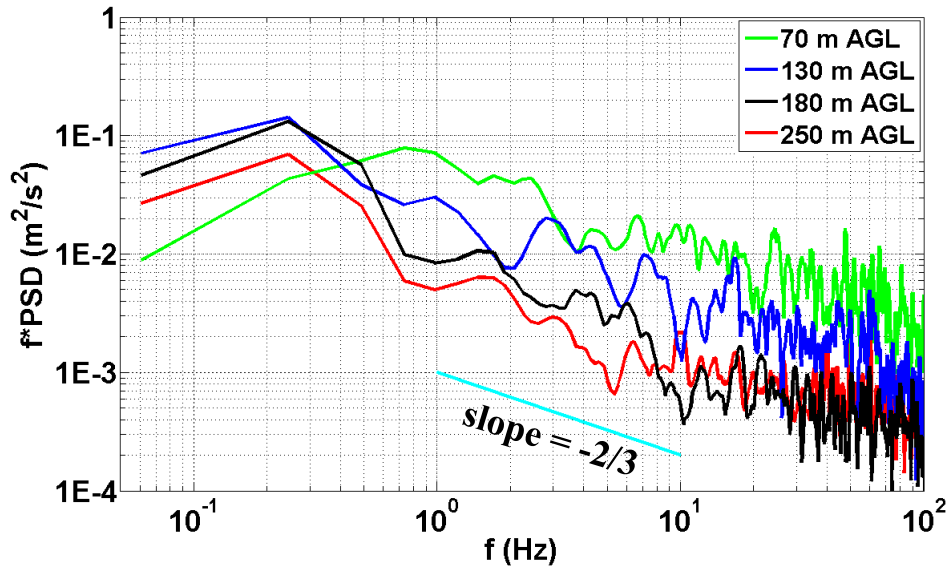
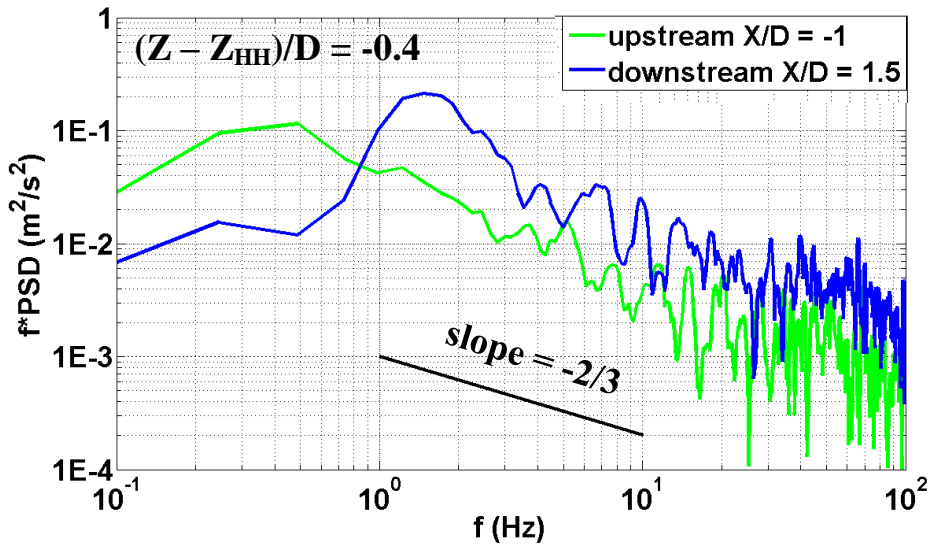


Figure 82. Power spectral density measured upstream of the turbine at heights of 70 m, 130 m, 180 m and 250 m AGL. The y-abcissa shows the product of the frequency and the power spectrum density.

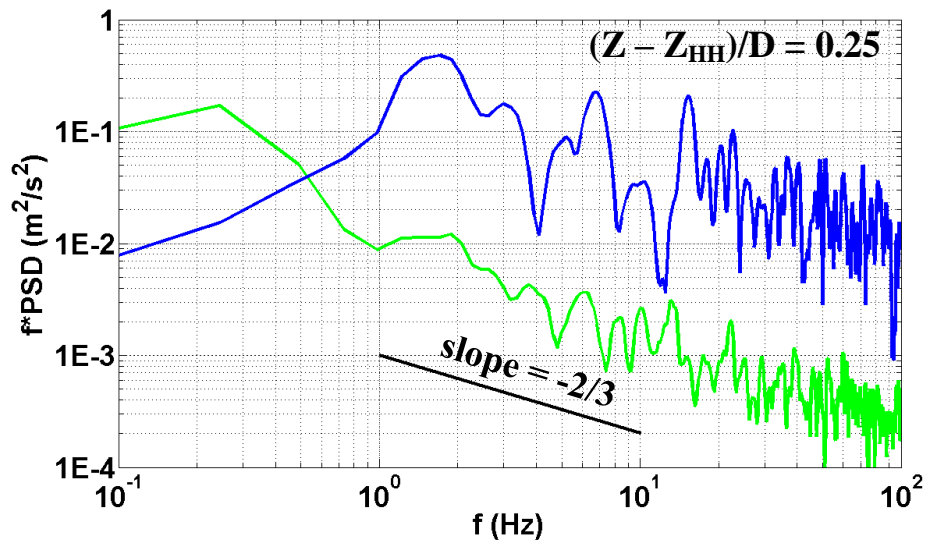
The power spectral density of the wind speed 1D upstream at four different heights of 70 m (green), 130 m (blue), 180 m (black) and 250 m (red) AGL is shown in Figure 82. It can be observed that all spectra show qualitatively similar behaviour, with a region of slope $-2/3$ that characterises the inertial sub-range. The spectral amplitudes are seen to decrease with increasing height, and the amplitude at 70 m AGL is three times the amplitude at 130 m AGL. Also for frequencies greater than 1 Hz, the spectral amplitudes at 70 m AGL are one order of magnitude larger than the amplitudes at 250 m AGL. The maximum spectral intensity at 70 m AGL is at a frequency of 0.75 Hz, but the maximum amplitude is at a lower frequency of 0.25 Hz for the other three heights.

The power spectra in the near-wake at $X/D = 1.5$ for three different heights of $(Z-Z_{\text{HH}})/D = -0.4, 0.25$ and 0.5 are shown in Figure 83. The SCADA mean wind speed (V_0) during this measurement was 6.9 m/s and the mean wind direction was 45° (North-East). At each height, the corresponding upstream spectrum measured at $X/D = -1$ is also shown for

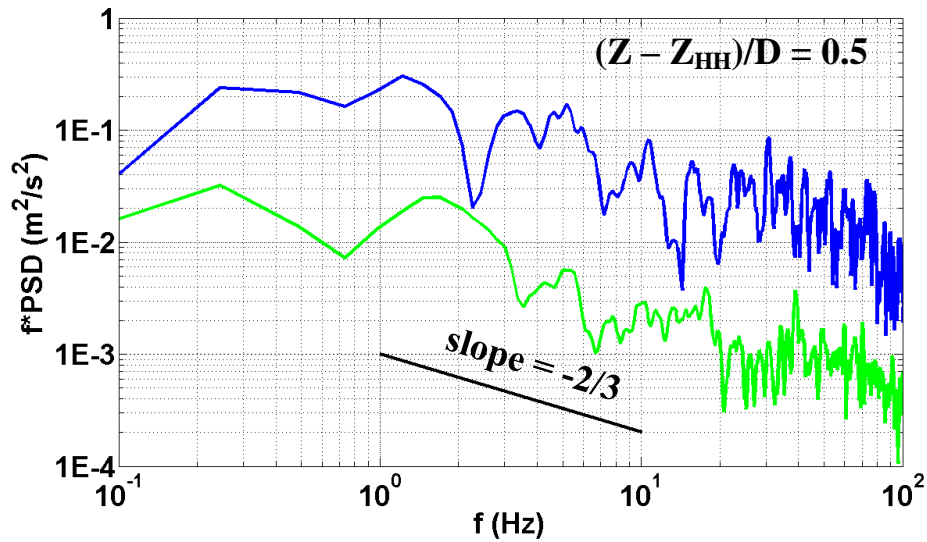
comparison. It can be observed that both the upstream and downstream spectra show the characteristic decay of $-2/3$ in the inertial range, but in the wake the spectral peaks are shifted to higher frequencies of 1 - 2 Hz compared to 0.25 - 0.75 Hz upstream. The maximum spectral amplitudes in the near-wake are at $(Z-Z_{HH})/D = 0.25$, with amplitudes that are 30 to 40 times higher than upstream.



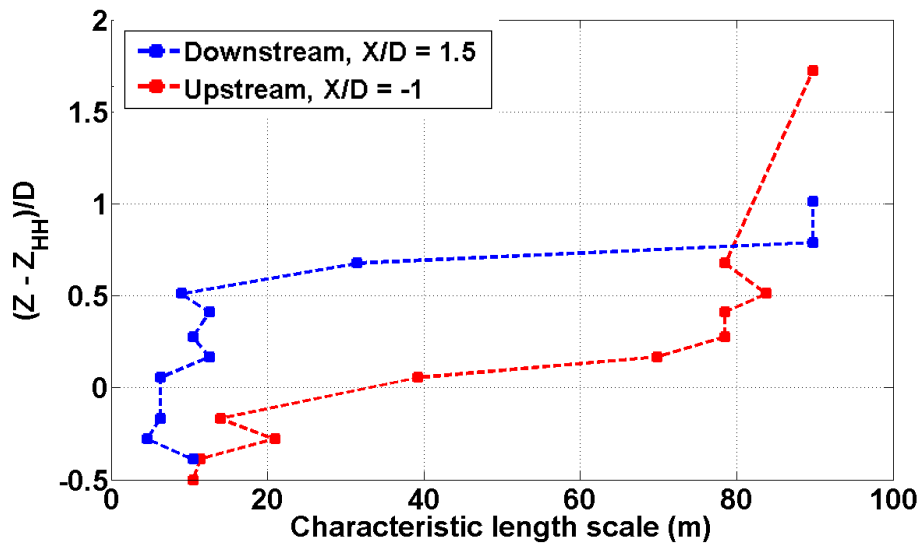
(a)



(b)



(c)



(d)

Figure 83. Power spectral density in the wake (at $X/D = 1.5$) and upstream (at $X/D = -1$) for (a) $(Z - Z_{HH})/D = 0.5$, (b) $(Z - Z_{HH})/D = 0.25$, (c) $(Z - Z_{HH})/D = -0.4$. The y-abcissa shows the product of the frequency and the power spectrum density. (d) Characteristic length scales upstream and downstream of the turbine.

The vertical profiles of the characteristic length scales upstream and downstream of the turbine are shown in Figure 83 d. The characteristic length scale is obtained by transforming the spectra from the frequency domain into the wavenumber domain to remove the effects of the drone's motion. It is observed that upstream of the turbine the length scale

increases with height, and there is a relatively large rate of increase in length up to a height of $(Z-Z_{HH})/D = 0.25$, and above this height there is a ten-fold smaller rate of increase with height. The smallest length scale upstream is 10 m and occurs at $(Z-Z_{HH})/D = -0.5$. The length scales in the wake are smaller than those upstream over heights of $(Z-Z_{HH})/D < 0.5$. Over the vertical extent of rotor, the length scales are nearly constant in the range ~ 6 to 12 m for heights $(Z-Z_{HH})/D < 0.5$. Above the rotor plane for heights $(Z-Z_{HH})/D > 0.8$ the length scales are comparable to the upstream length scales.

	<i>Kolmogorov microscale η (mm)</i>	<i>Dissipation rate of turbulent kinetic energy ε (m^2/s^3)</i>
Upstream, X/D = -1	2.5	1×10^{-4}
Wake, X/D = 1.5	2.0	2.4×10^{-4}

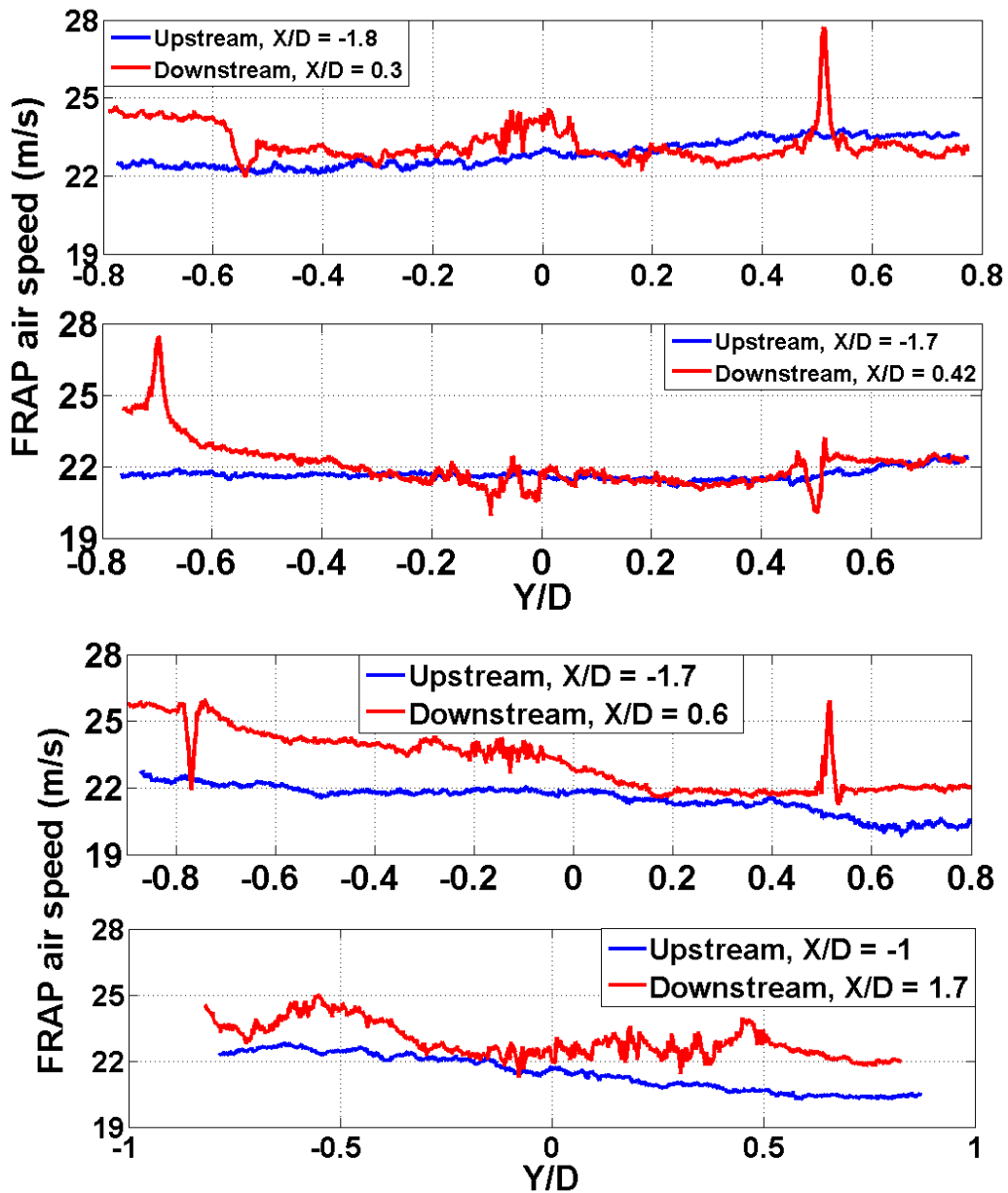
Table 9. Summary of measured Kolmogorov microscales and dissipation rates of turbulent kinetic energy upstream and in the wake.

The measured microscales and dissipation rates at hub height are summarised in Table 9. For these measurements, as the diameter of the FRAP probe is 20 mm, the Kolmogorov microscale is derived from the voltage signal of the central piezo-resistive sensing element on the FRAP probe, as the diameter of pressure port is 0.3 mm, thereby allowing flow features as small as 0.3 mm to be detected. As Reynolds-averaged Navier-Stokes solvers with two-equation turbulence closure models, for example Jafari et al. [8], are being more widely used for the simulations of the flow within wind farms, these measurements of the microscales and dissipation rates are well suited for the future development of these simulation tools.

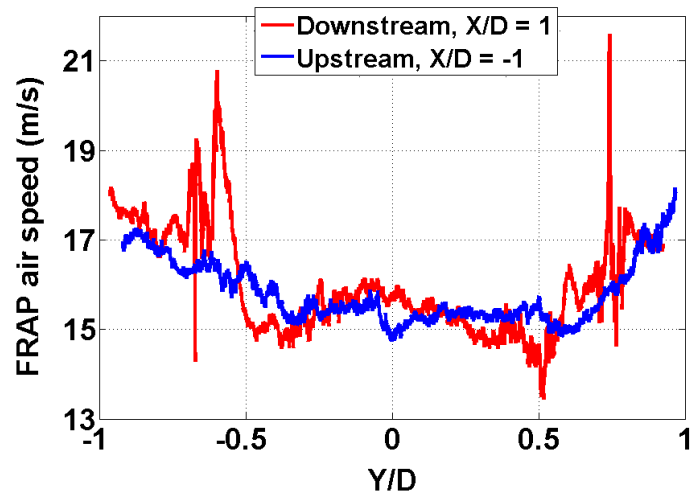
5.7 Tip Vortices

The FRAP air speed measured in the near vicinity downstream of a wind turbine shows distinct tip vortices and nacelle wake signatures. During this measurement, the drone scans the wind field in the lateral direction, parallel to the rotor plane at hub height, but at different X/D positions from -2 to 2. The spanwise profiles of the hub height FRAP air

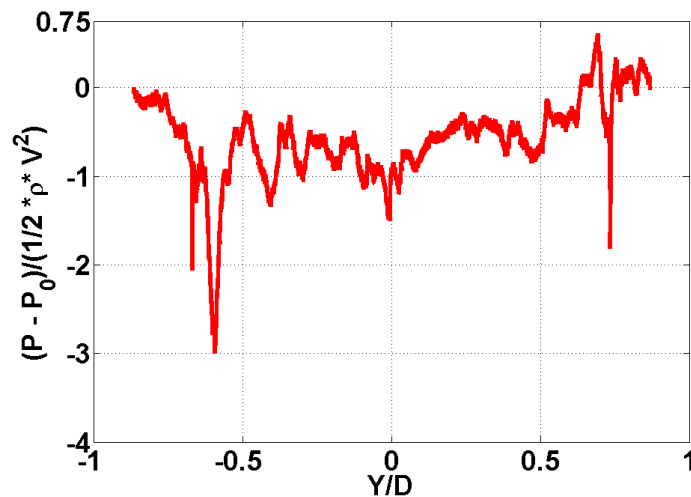
speed measured in the near-wake at $X/D = 0.3, 0.4, 0.6, 1$ and 1.7 are shown in Figure 84. Also shown with each profile is the corresponding spanwise profile that is measured upstream of the turbine. The SCADA mean wind speed during this measurement (Figure 84 a) is 5.5 m/s and the wind direction is 30° , and it is 6 m/s for the measurement reported in Figure 84 b, c with a wind direction of 90° . Within a ten minute period, alternate upstream and downstream flights parallel to the rotor are used to measure upstream (at $X/D = -1.8, -1.7, -1.7$ and -1) and downstream (at $X/D = 0.3, 0.4, 0.6$ and 1.7).



(a)



(b)



(c)

Figure 84. (a) and (b) Spanwise profiles of the hub height FRAP air speed upstream and at $X/D = 0.3, 0.4, 0.6, 1.0$ and 1.7 . The distinctive sharp peaks and elevated broadband levels are signatures, respectively, of the tip vortices and the nacelle wake. (c) Static pressure coefficient from FRAP downstream at $X/D = 1$.

The signatures of the rotor blades tip vortices and the nacelle wake are manifested as distinctive sharp peaks and/or elevated levels in the FRAP air speed. At $X/D = 0.3$, the tip vortices occur at $Y/D = 0.5$ and -0.53 , with broadband elevated levels near $Y/D = 0$ that are a signature from the nacelle wake. For $X/D > 0.3$, the spanwise position of these more elevated levels drifts towards more negative Y/D as the wake evolves. At $X/D = 0.4$ and 0.6 , the tip vortices are at a more negative Y/D compared to

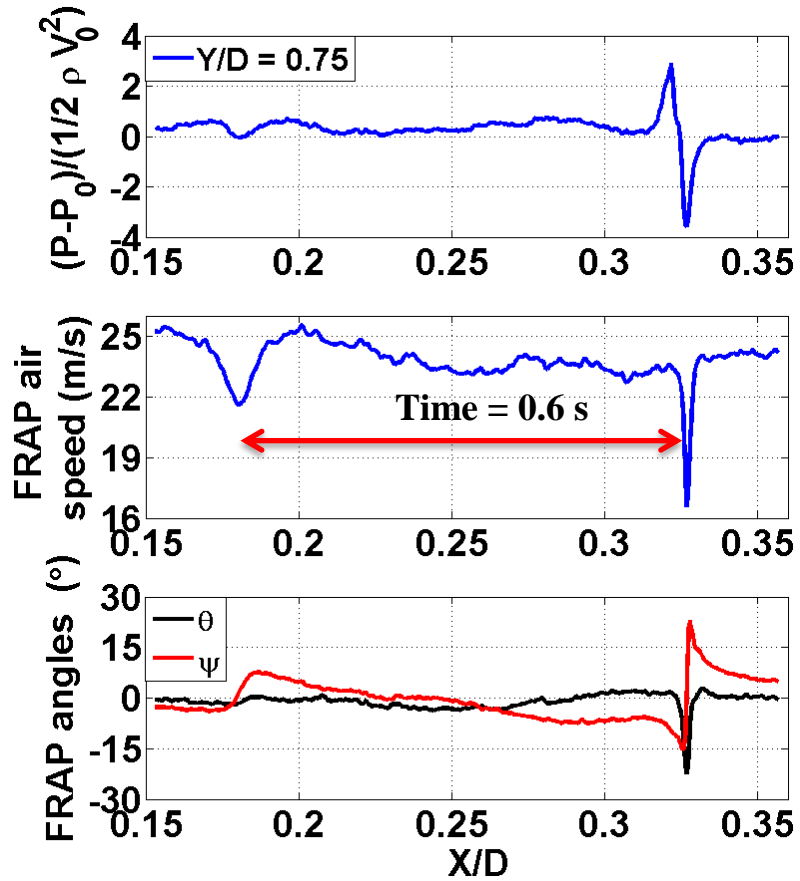
their position at $X/D = 0.3$. Furthermore, the distance between the vortices has increased to $1.25D$ compared to $1.03D$ at $X/D=0.3$. At $X/D = 1$, the tip vortices are even further apart with a separation distance of $1.4D$, but a second broad spike appears at $Y/D = -0.6$ in both the air speed and in the differential static pressure coefficient. At $X/D = 1.7$, a turbulent flow is seen with no distinct signature of tip vortices. The tip vortex signature is seen in 30-to-40 % of the measurements made close ($X/D < 1.5$) to the wind turbine. Tip vortex signature spikes appear in FRAP air speed, FRAP differential static pressure co-efficient or both, depending on where the drone trajectory crosses the tip vortex (Figure 84 b, c). The maximum amplitude peak in wind speed occurs at $X/D = 0.3$ and 1 . No distinct signatures are seen in upstream air speed measurements.

A unique advantage of using the FRAP probe is that both the velocity and pressure fields can be measured. Given the complex nature of the wind turbine wake, this utility is of benefit in order to detail the flow characteristics. This is illustrated in Figure 85 a, where the streamwise evolution of two tip vortices is shown in terms of the FRAP air speed, static pressure co-efficient and FRAP angles. The measurements are made at spanwise positions of $Y/D = 0.75$ and $Y/D = 0.63$ along the segment of a trajectory that is flown parallel to and towards the direction of the upstream wind. One set of tip vortices is located at $X/D < 0.35$ and the other set is at $0.5 < X/D < 0.8$. Both tip vortices are clearly identified in the measurement of static pressure in Figure 85 b, but only the more upstream tip vortex is seen in the FRAP air speed measurement. To the author's knowledge these are the first such measurements of the pressure field through a tip vortex.

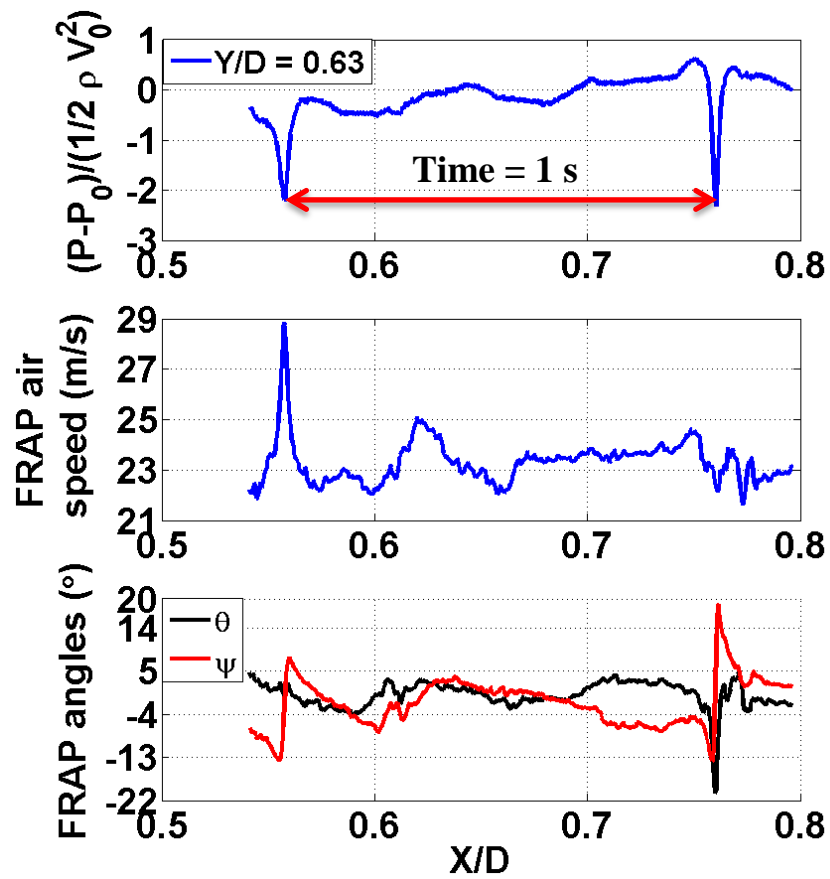
The properties of tip vortices determine the physical behavior of a wind turbine rotor like wake expansion, vortex spiral twist angle and the strength of the tip vortex spiral [22]. An attempt is made here to measure the tip vortex pitch generated from a multi-MW full-scale wind turbine. The SCADA mean wind speed (V_0) during the first measurement set (Figure 85 a) was 6.5 m/s and the mean rotor angular frequency was 12.4 rpm. The mean wind speed during the second measurement set (Figure 85 b) was 7.2 m/s and the mean rotor angular frequency was 13.6 rpm. During both measurement sets, the mean wind direction was from North-East at 46° .

Assuming that the tip vortex has a Rankine (solid body rotation) vortex core, surrounded by an irrotational swirling flow, and that the drone shoots through a pseudo-stationary vortex, the axis of rotation of vortex core can be deduced from the pitch and yaw angles plotted in Figure 85. If the axis of vortex core is perpendicular to the axis of the FRAP probe, then

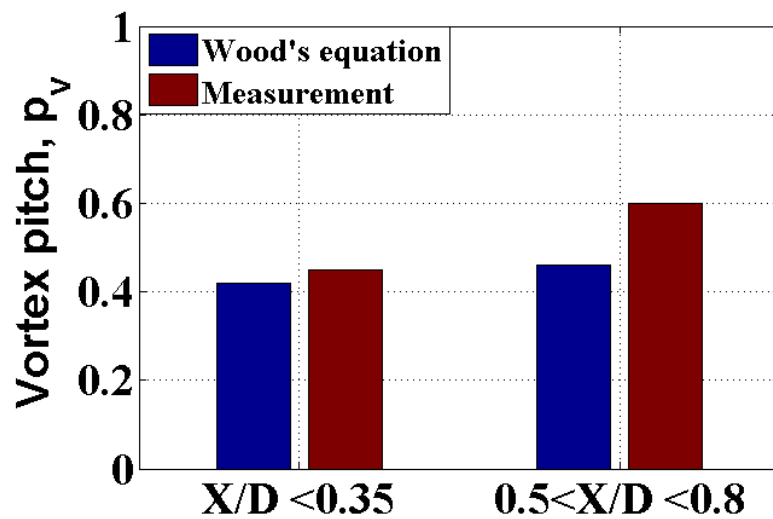
the vortex signature is captured in 2D space with no information on its thickness. In this case, the FRAP angles pitch, yaw or both show a distinct signature with a maximum and minimum. However, if the axis of rotation of the vortex core is inclined or parallel to the FRAP probe axis, then the vortex thickness is also seen in FRAP angles. In this case, the FRAP angles pitch or yaw shows distinct maximum or minimum signatures.



(a)



(b)



(c)

Figure 85. Representative streamwise profile of hub height pressure coefficient, FRAP air speed and FRAP angles at (a) $X/D < 0.5$ and $Y/D = 0.75$, (b) $0.5 < X/D < 1$ and $Y/D = 0.63$. The distinctive peaks (or troughs) identify the location of the tip vortices. (c) Comparison of measured and predicted vortex pitches.

The streamwise separation distance between the two vortices is the vortex pitch, which is the distance a tip vortex is transported during one blade revolution. The measured vortex pitch in the regions $X/D < 0.35$ and $0.5 < X/D < 0.8$ respectively are shown in Figure 85 c. Also shown in Figure 85 c are the predicted vortex pitches from Wood's [100] empirical formulation. The pitch $p_v = 0.42D$ (for the first measurement set) and $p_v = 0.46D$ (for the second measurement set) is evaluated using the SCADA mean values during these measurements. The measured pitch is three times (for 3 blades) the distance between the two consecutive tip vortices, and is $0.45D$ for $X/D < 0.35$ and $0.6D$ for $0.5 < X/D < 0.8$. The measured vortex pitch close to the turbine ($X/D < 0.35$) matches closely ($\sim 6\%$) with the value computed from Equation 34, but it appears to under predict the vortex pitch by 23 % for the second case of $0.5 < X/D < 0.8$.

5.8 Characteristics of the Wake

The streamwise evolution of the wake in complex terrain up to four diameters downstream is shown in Figure 86 in terms of the turbulent kinetic energy and wind speed. The measurements are made at hub height in a horizontal plane at the Mt. Crosin wind farm which is in complex terrain. The turbulent kinetic energy in the near-wake, $X/D < 2$, shows the evolution of the tip vortex that is identified in the high turbulent kinetic energy regions that are shed from the wind turbine blade tip. For $X/D < 1$, the tip vortices are convected downstream close to a span of $Y/D = -0.68$ parallel to the direction of the upstream wind. At $X/D = 1$, the tip vortices migrate spanwise, that is along the direction of the negative Y/D axis, due to the wake's expansion and reach $Y/D = -0.75$ at $X/D = 1.5$. The streamwise extent of the near-wake in complex terrain is approximately $X/D = 2$. This extent is one-diameter shorter than the extent of the near-wake observed in flat terrain in Figure 65, where the near wake extends to $X/D = 3$. In the near wake, the wind speed, shown in Figure 86, shows the presence of a thin shear layer that separates the low energy flow within the wake boundary and the high energy flow outside the wake. Downstream of $X/D=2$, mixing starts within the wake and is manifested by the penetration of high energy flow at the wake's boundary into the relatively low energy flow within the wake. This mixing is also seen in the measured wind speeds, as a relatively high speed flow from outside the wake penetrates into the low speed wake downstream of $X/D = 2$. The mixing of the flow affects the entire wake region downstream of $X/D = 3.7$.

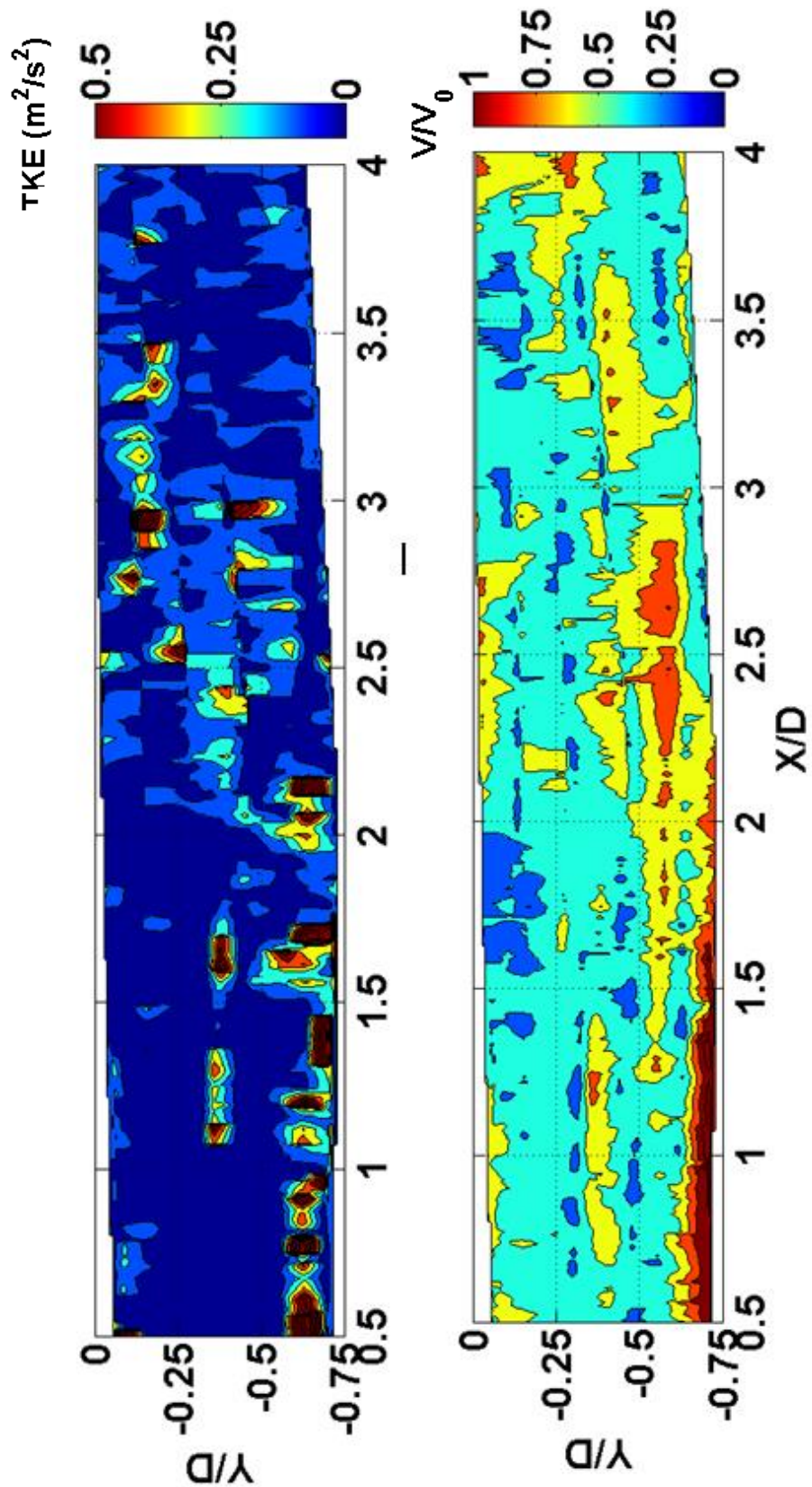
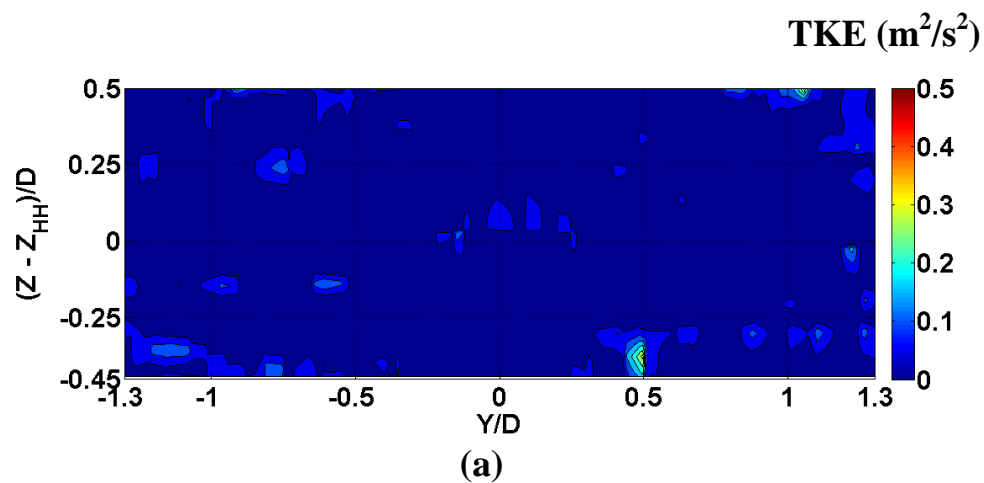
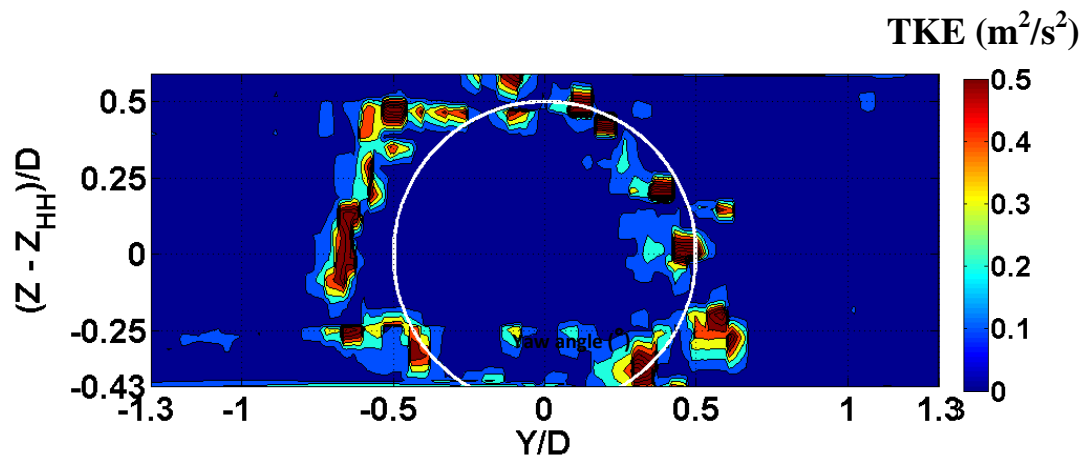


Figure 86. Measurements of turbulent kinetic energy and wind speed at hub height in a horizontal plane downstream of a wind turbine at Mt. Crosin wind farm.

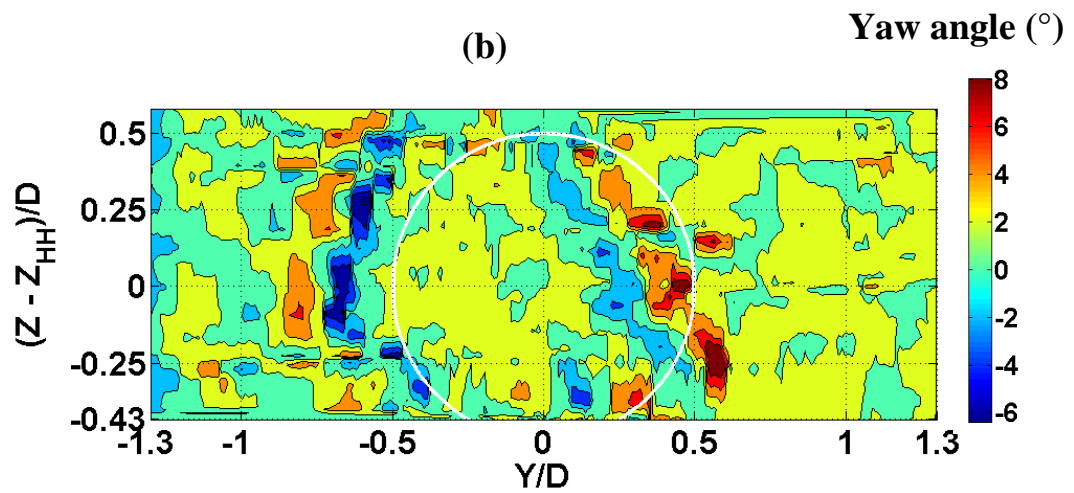
5.8.1 Turbulent Kinetic Energy in Vertical Plane

The distribution of turbulent kinetic energy in two vertical planes in complex terrain is shown in Figure 87. The first plane is upstream at $X/D = -1.5$ and the second plane is downstream at $X/D = 0.5$. The measurements are accomplished by flying the drone alternatively upstream and downstream at altitudes ranging from $-0.45 < (Z - Z_{HH})/D < 0.5$. During this measurement, the SCADA 10-minute average wind speed was 6.5 m/s with wind from East to West. The turbulent kinetic energy upstream at $X/D = -1.5$ (Figure 87 a) shows the characteristics of turbulent flow upstream of the wind turbine in complex terrain. The area-averaged turbulent kinetic energy in the upstream plane is $0.03 \text{ m}^2/\text{s}^2$. Downstream at $X/D = 0.5$ (Figure 87 b) high turbulent kinetic energy regions that are associated with the tip vortices are seen. The perimeter of the rotor tip is shown as a white circle. These vortical structures originate from the blade tips and convected downstream. The variation in the turbulent kinetic energy in wake is nearly symmetrical about a vertical axis located at $Y/D = -0.1$ indicating that there is a yaw misalignment between the wind turbine and the main wind direction. The annular-shaped region of high turbulent kinetic energy in Figure 87 b indicates the radial extent of the wake at $X/D = 0.5$. In the near wake, regions of low turbulent kinetic energy characterize the freestream outside the wake and within the wake. The distribution of the yaw angle downstream at $X/D = 0.5$ is shown in Figure 87 c. The yaw angle shows that the high turbulent kinetic energy regions identified in Figure 87 b are surrounded by pairs of positive and negative yaw angle zones; these pairs confirm that the previously identified regions of high turbulent kinetic energy are vortical structures. The mirror image of diametrically opposite yaw angle pairs indicates that the vortical structures are rotating in opposite directions.

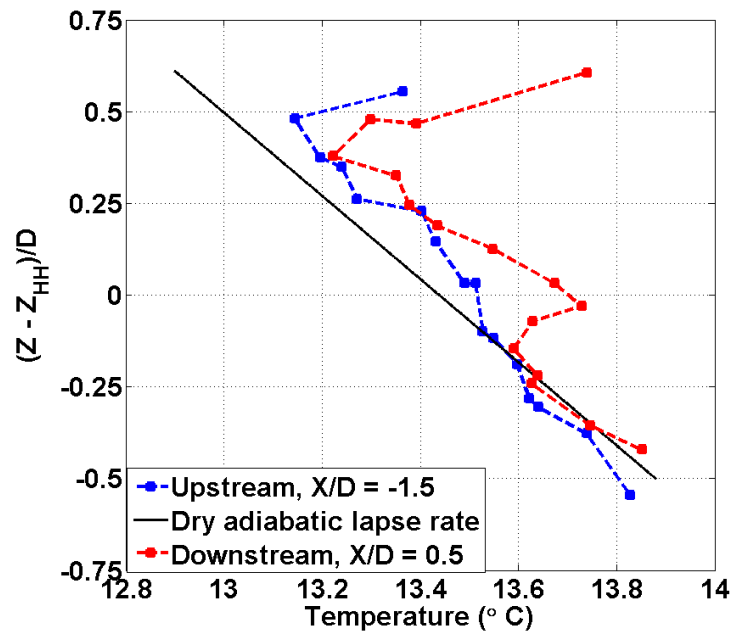




(b)



(c)



(d)

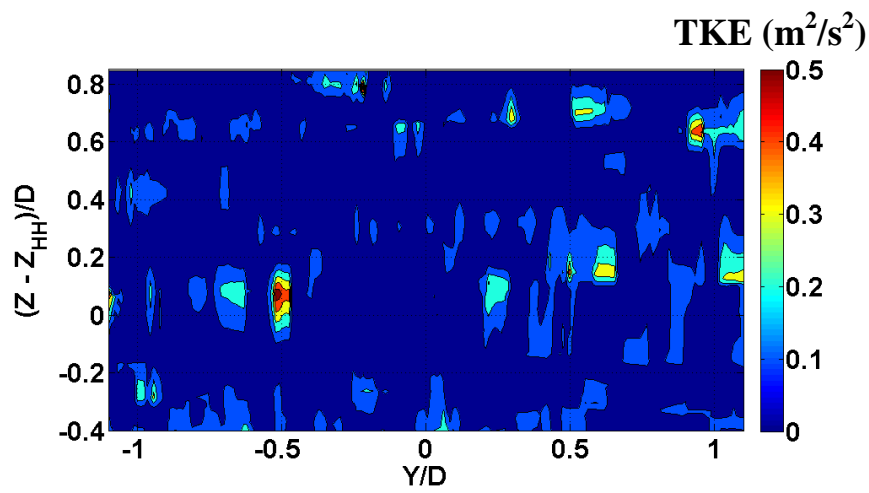
Figure 87. Measurements in complex terrain of (a) Turbulent kinetic energy upstream of turbine at $X/D = -1.5$, (b) Turbulent kinetic energy in

near-wake at $X/D = 0.5$, (c) Yaw angle in near-wake at $X/D = 0.5$, (d) Atmospheric temperature profile.

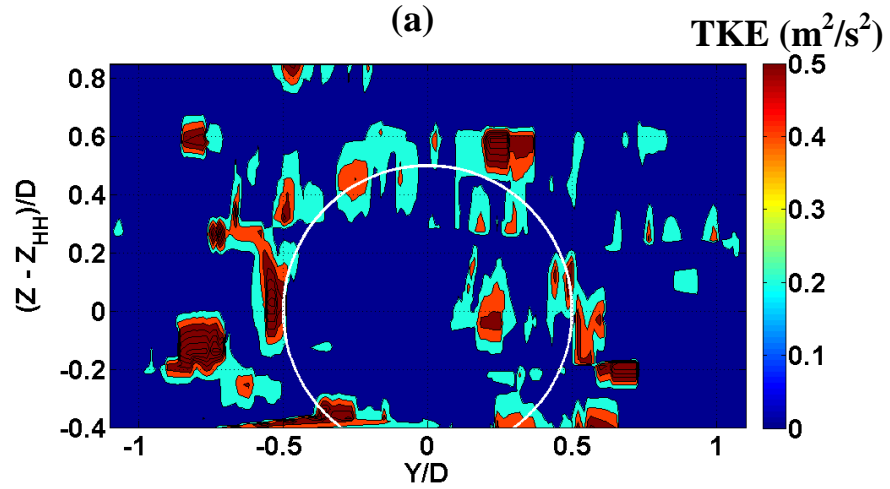
The windFlyer drone measures the atmospheric temperature along its trajectory with a resolution of $0.01\text{ }^{\circ}\text{C}$ (humidity sensor from Sensiron SHT75). The variation of atmospheric temperature with height will be an indicator of the atmospheric stability during measurements. Accordingly, the mean temperature profile measured upstream at $X/D = -1.5$ and downstream at $X/D = 0.5$ are shown in Figure 87 d. Also shown for comparison is the profile of dry adiabatic lapse rate of the atmosphere ($9.8\text{ }^{\circ}\text{C}/\text{km}$) as a black line. The plots show that the measured lapse rate $7.7\text{ }^{\circ}\text{C}/\text{km}$, upstream at $X/D = -1.5$, is less than the standard adiabatic lapse rate of dry atmosphere, thus indicating a stable atmospheric condition during this measurement. Downstream at $X/D = 0.5$, the temperature profile is affected probably due to swirl and mixing, the resulting temperature profile downstream has shifted towards the right indicating an increase in temperature at each altitude.

5.8.2 Double Wake

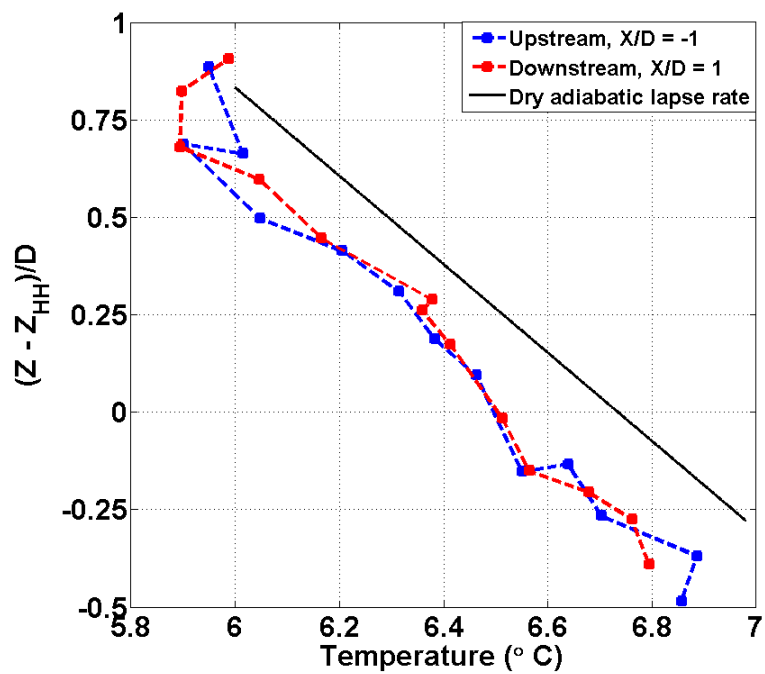
The distribution of turbulent kinetic energy in two vertical planes in complex terrain, one located upstream at $X/D = -1$ and the other located in downstream at $X/D = 1$, is shown in Figure 88. The SCADA 10-minute average wind speed during this measurement was 7 m/s and the wind direction was 80° . For this wind direction, there is another Vestas V90 wind turbine located seven diameters upstream, at $X/D = -7$, of the turbine located at $X/D = 0$. Thus, the upstream measurement plane located at $X/D = -1$ is six diameters downstream of the wind turbine located at $X/D = -7$. Figure 88 a shows the turbulent nature of wake flow seen by a wind turbine rotor located six diameters downstream of another wind turbine in complex terrain. At $X/D = -1$, the wake flow is completely mixed out with no distinct signatures of the upstream wind turbine. The area average turbulent kinetic energy at $X/D = -1$ is $0.07\text{ m}^2/\text{s}^2$, which is more than two times greater than the area averaged upstream turbulent kinetic energy discussed in Figure 87 a. Downstream at $X/D = 1$ (Figure 88 b) high turbulent kinetic energy regions that are associated with vortical structures are seen. The perimeter of the rotor tip is shown as a white circle. This distribution of turbulent kinetic energy also confirms that mixing has already started within the wake on one side (for $Y/D > 0$) and there is no symmetry in the distribution of turbulent kinetic energy at $X/D = 1$. It can also be seen in Figure 88 b that some tip vortices have strayed out of the wake shear layer into the freestream.



(a)



(b)



(c)

Figure 88. Measurements in complex terrain of (a) Turbulent kinetic energy contour upstream at $X/D = -1$, (b) Turbulent kinetic energy in near-wake at $X/D = 1$, (c) Atmospheric temperature profile.

The mean temperature profile measured upstream at $X/D = -1$ and downstream at $X/D = 1$ are shown in Figure 88 c. The plots indicate a nearly neutral atmospheric condition during this measurement as the measured lapse rate, upstream at $X/D = -1$ and downstream at $X/D = 1$, are nearly equal to the standard adiabatic lapse rate of dry atmosphere.

5.9 Summary

The measurements presented in this chapter detail the spatial variations of the wind speed, wind direction and turbulent kinetic energy in the flow field around a multi-megawatt wind turbine that is located in complex terrain. The measurement accuracy of the drone-based system is verified with comparisons against measurements with a three-dimensional scanning LIDAR system, the wind turbine's SCADA system, and microscale simulations of the wind field. The vertical profiles of the mean wind speed, wind direction and turbulent kinetic energy upstream of the turbine show non-uniformities that are associated with the wind flow in complex terrain. In the wind speed profile, there is a jet-like structure with a maximum wind speed near hub height. The wind veer differs $\pm 12^\circ$ relative to the area-averaged wind direction, and the wind turbine has a misalignment of 5° relative to the main wind direction. The magnitude of turbulent kinetic energy decreases monotonically with increasing height above ground. In the near-wake, at one diameter downstream of the turbine, the jet-like structure is absent in the wind speed profile and the wind direction varies little over the vertical extent of the rotor. Furthermore there is a factor three increase of the area-averaged turbulent kinetic energy across the turbine's rotor, and the vertical profile of the turbulent kinetic energy shows maxima at the locations of the blade tips. The drone's fast-response aerodynamic probe allows for simultaneous measurements of wind speed and static pressure. Thus the first-ever measurements of the pressure field across a wind turbine rotor plane are reported. Additionally, the distinctive signatures of the blade tip vortices are measured in terms of the air speed and static pressure. The pitch between subsequent tip vortices that are shed from the wind turbines blades increases as the near-wake evolves. The Kolmogorov inertial sub-range is identified in the measured power spectra, and it is seen that in the near-wake, the spectral amplitudes are 30 to 40 times higher than upstream, and the spectral peaks are shifted from frequencies of 0.5-0.75Hz to higher frequencies of 1-2 Hz. Whereas

the characteristic microscale length scales, that are derived from the spectra, increase with height upstream of the turbine, in the near-wake the microscale lengths are of constant and smaller magnitude.

6. FLAT TERRAIN VERSUS COMPLEX TERRAIN

A comparison of the wake evolution measured downstream of a multi-megawatt wind turbine located in flat and complex terrains is presented in this chapter. The spatially-averaged wind speed and the spatially-averaged turbulent kinetic energy plots in the near and far wake help to compare the wake evolution downstream of a wind turbine located in flat and complex terrains. Reynolds decomposition yields the nature of turbulent fluctuations in the surface layer in flat and complex terrains, and its detailed analysis reveals the turbulence statistics, degree of anisotropy and friction velocity.

6.1 Measurement Sites

The measurement sites at the Mont Crosin wind farm (complex terrain) and at the Altenbruch wind farm (flat terrain) were presented in the previous two chapters. In addition to these two wind farms, the freestream measurements at two other wind farms will be discussed in this chapter. The first of these is the Freudenberg-Beiersdorf windfarm in Brandenburg, Germany that is in flat terrain and surrounded by patches of dense tall coniferous trees. A detailed description of this wind farm is presented in chapter 7. The second of these wind farms is at Collonges, Switzerland [92]. This wind farm is in a valley that extends approximately northwest-southwest, and has hills on its sides rising up to 2500 m AGL. Thus this second site is in complex terrain. Table 10 summarises the characteristics of these two wind farms.

Wind farm	Wind turbine	Diameter (m)	Hub Height (m)	Terrain	Ground Elevation (m)
Freudenberg-Beiersdorf	V80	80	100	Flat	95
Collonges	E70	70	100	Complex	448

Table 10. Summary characteristics of the Freudenberg-Beiersdorf wind farm, Germany and Collonges wind farm, Switzerland.

6.2 Wake Evolution: Complex Terrain versus Flat Terrain

The streamwise evolution of the wake is quantified in terms of the area-averaged wind speed and turbulent kinetic energy as shown in Figure 89. The area averages are derived from the flow properties in the planes that are shown in Figure 86 and Figure 65. In the near wake, the area-averaged wind speed is 50-60% of the reference wind speed in both flat and complex terrains. In both terrains, the area-averaged wind speed initially decreases in the near-wake, but then increases in the far wake. In complex terrain the wind speed increases at the rate of 10% per diameter in the near-wake to reach 64% at $X/D = 3.75$. In flat terrain, the area-averaged wind speed is nearly constant in the near-wake and is 60% of the reference wind speed up to $X/D = 3$, and then starts to recover at a rate of 10 % per diameter distance downstream up to $X/D = 5.5$ where the wind speed is 80% of the reference wind speed. As seen earlier, the streamwise extent of the near wake is shorter in complex terrain than in flat terrain by one diameter. The area-averaged turbulent kinetic energy also decreases as the wake evolves in both terrains; in complex terrain the area-averaged turbulent kinetic energy is $0.075 \text{ m}^2/\text{s}^2$ in the near-wake ($X/D < 2$). The area-averaged turbulent kinetic energy increases from $0.07 \text{ m}^2/\text{s}^2$ at $X/D = 2$ to $0.18 \text{ m}^2/\text{s}^2$ at $X/D = 2.7$; over this range, $2 < X/D < 2.7$, a recovery in wind speed is also seen. The area-averaged turbulent kinetic energy then increases to reach $0.1 \text{ m}^2/\text{s}^2$ at $X/D = 3.7$. In the complex terrain of the Mont Crosin wind farm, the ensemble-averaged freestream turbulent kinetic energy measured at hub height is $0.04 \text{ m}^2/\text{s}^2$. Thus, at the end of near wake, the turbulent kinetic energy is about two times higher than in the freestream. The area-averaged turbulent kinetic energy at $X/D = 3.75$ in the far wake is still two and a half times larger than the turbulent kinetic energy measured in the freestream. In flat terrain the area-averaged turbulent kinetic energy also decreases as the wake evolves. There is initially a decrease in the near-wake to $0.075 \text{ m}^2/\text{s}^2$ at $2.8D$, followed by an increase to $0.12 \text{ m}^2/\text{s}^2$ at $X/D = 3.7$. The region between $X/D = 3$ and $X/D = 5.5$ is where enhanced flow mixing occurs and this is the reason for the increase in wind speed, and the (increase and) decrease that is observed in the area-averaged turbulent kinetic energy. Further downstream at $X/D = 6$, the area-averaged turbulent kinetic energy is again $0.075 \text{ m}^2/\text{s}^2$. The same evolution was also seen in the area-averaged wind speed and area-averaged turbulent kinetic energy in the wake at the Collonges wind farm, a complex terrain, but the mean turbulent kinetic energy values in the wake at this wind farm are two to three times larger than the values measured at the other two wind farms.

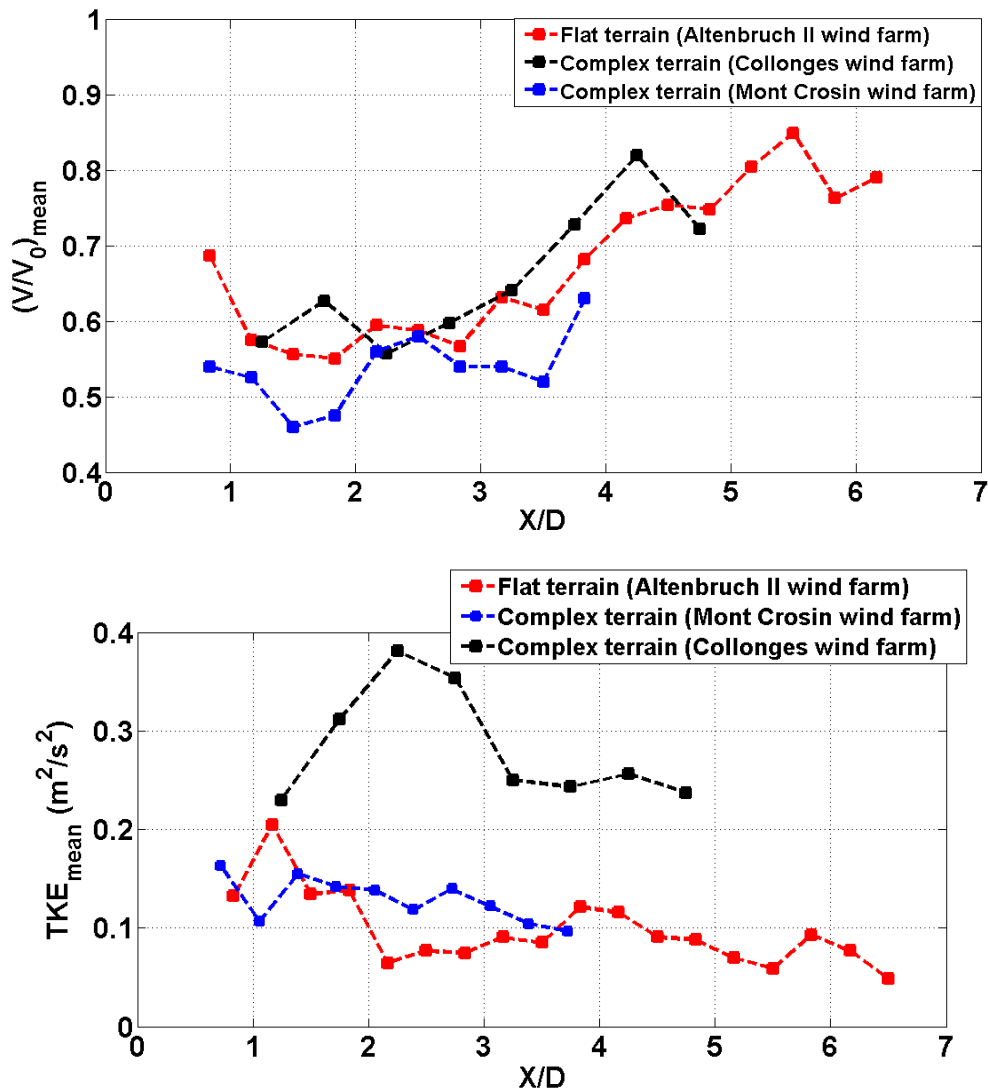
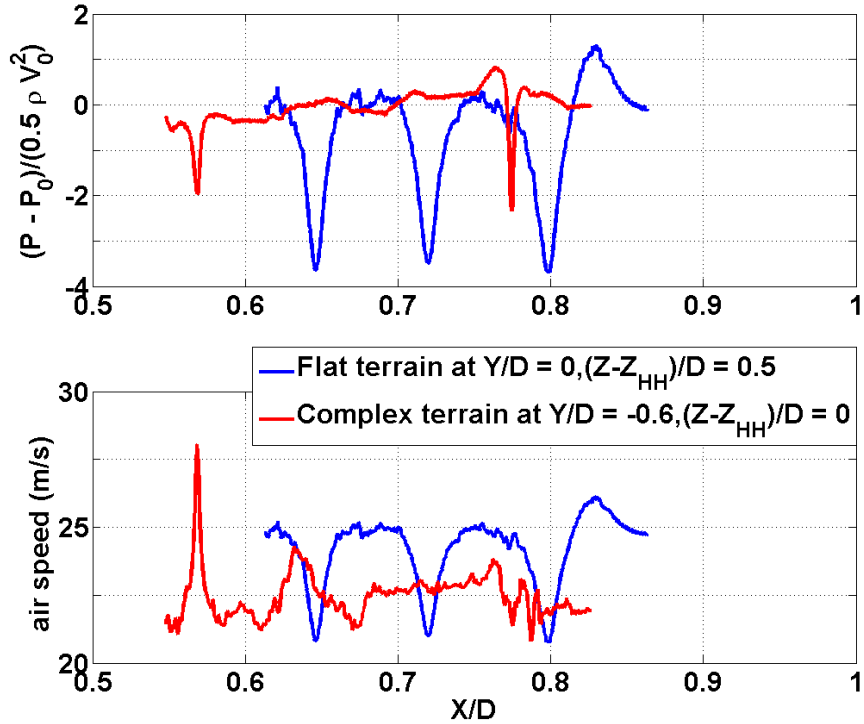


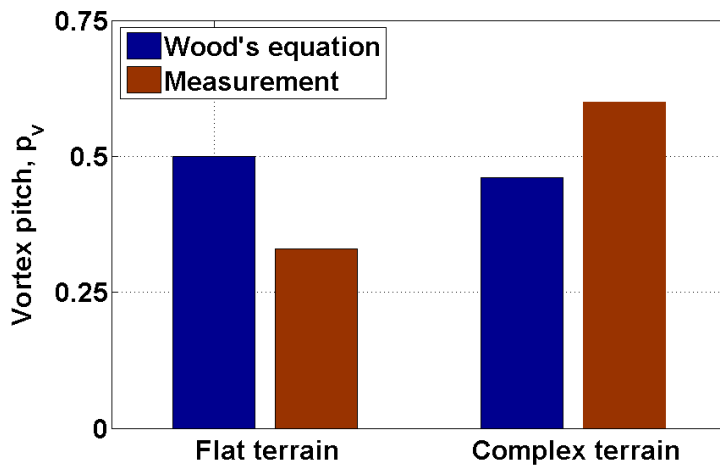
Figure 89. Streamwise evolution of spatially-averaged wind speed and spatially-averaged turbulent kinetic energy in the wake in flat and complex terrains.

As the velocity and pressure fields can be measured with high resolution using the FRAP probe, Figure 90 a, the streamwise evolution of consecutive tip vortices in the flat terrain of the Altenbruch wind farm and the complex terrain of the Mt. Crosin wind farm are compared in terms of the air speed and static pressure. The measurements in flat terrain are made at a spanwise position of $Y/D = 0$ and at a height of $(Z - Z_{\text{HH}})/D = 0.5$, and the measurements in complex terrain are made at a spanwise position of $Y/D = -0.6$ and at a height of $(Z - Z_{\text{HH}})/D = 0$. The tip vortices can be identified from the sharp drops in air speed and/or pressure. In the flat terrain case, three consecutive tip vortices are captured; whereas in the complex terrain two consecutive tip vortices are captured. As the vortex pitch per blade is three times the separation distance of consecutive vortices in Figure 90 a, the measurements can be used to validate Wood's

empirical formulation (Equation 34). As seen in Figure 90 b, Wood's formulation over predicts the vortex pitch by 33% in flat terrain, and under predicts the vortex pitch by 23% in complex terrains. Thus the formulation cannot be considered to have universal applicability.



(a)

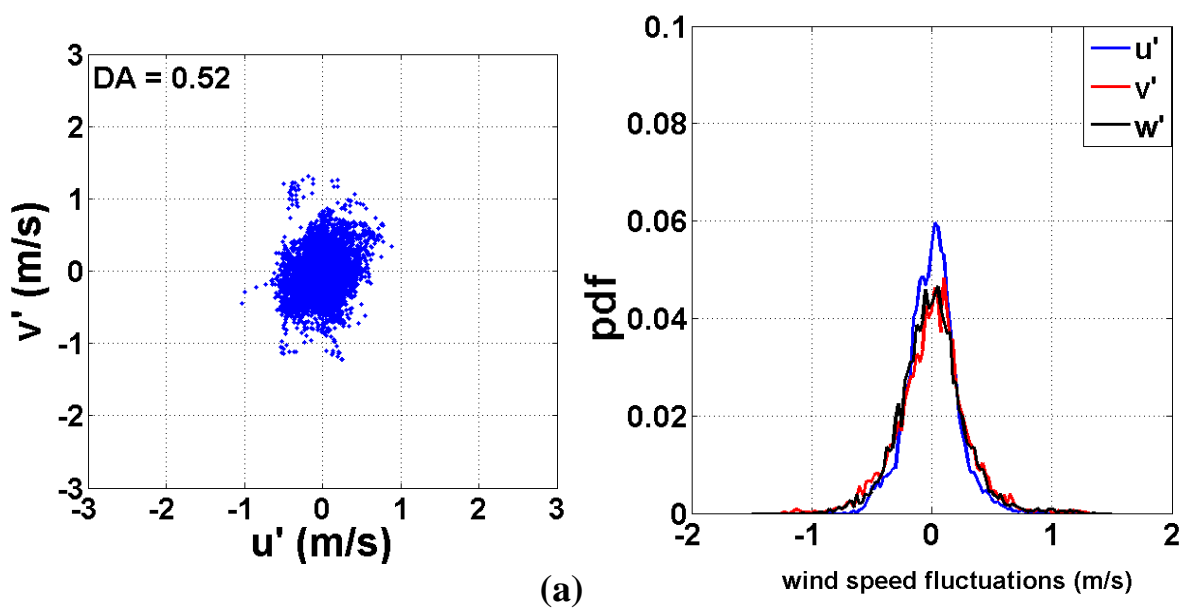


(b)

Figure 90. (a) Streamwise profiles of static pressure and air speed in flat terrain at $Y/D = 0, (Z - Z_{HH})/D = 0.5$ and in complex terrain at $Y/D = -0.6, (Z - Z_{HH})/D = 0$. (b) Comparison of measured and predicted vortex pitches in flat and complex terrains.

6.3 Comparison of Turbulence Structure in Flat and Complex Terrains

Figure 91 compares the turbulence structure at hub height upstream and in the wake of a turbine in complex terrain. In the wake the measurements are made at hub height from $X/D = 1.5$ to $X/D = 4.5$. On the left side of Figure 91 are scatter plots of spanwise velocity fluctuations versus the streamwise velocity fluctuations. On the right side are shown the probability distribution functions of the three fluctuating velocity components. For these measurements, the SCADA 10-minute average wind speed was 7 m/s from the North-East direction. As seen in Figure 91, the distribution of turbulence in the freestream and in the wake is anisotropic, with a degree of anisotropy of 0.5 that indicates the presence of secondary flow structures in the freestream and in the wake. The scatter plots in Figure 91 show that in complex terrain, in the wake the turbulence structure is more isotropic than in the freestream. The vortical structures manifest themselves as the relatively large magnitude spanwise and streamwise fluctuations that are seen outside the cores in the scatter plot of the wake. However sizes of the core are similar in the freestream and wake. The probability distribution functions in the freestream and wake have normal distributions. The maximum probability density function of the streamwise fluctuating velocity, u' , in the freestream is 0.06 and reduces in the wake to 0.055. However in contrast the maximum probability density function of the spanwise fluctuating velocity, v' , increases from 0.045 in the freestream to 0.055 in the wake. The probability density function of vertical fluctuating velocity, w' , is quite similar in the freestream and wake. The statistical parameters derived from probability density functions are summarized in Table 11.



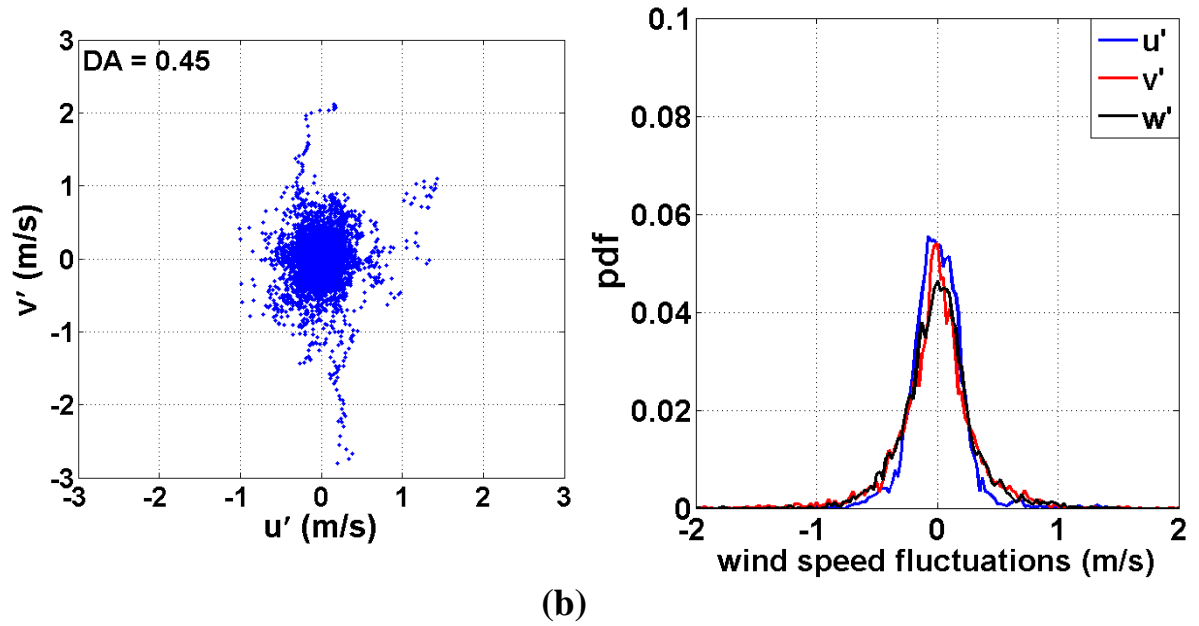


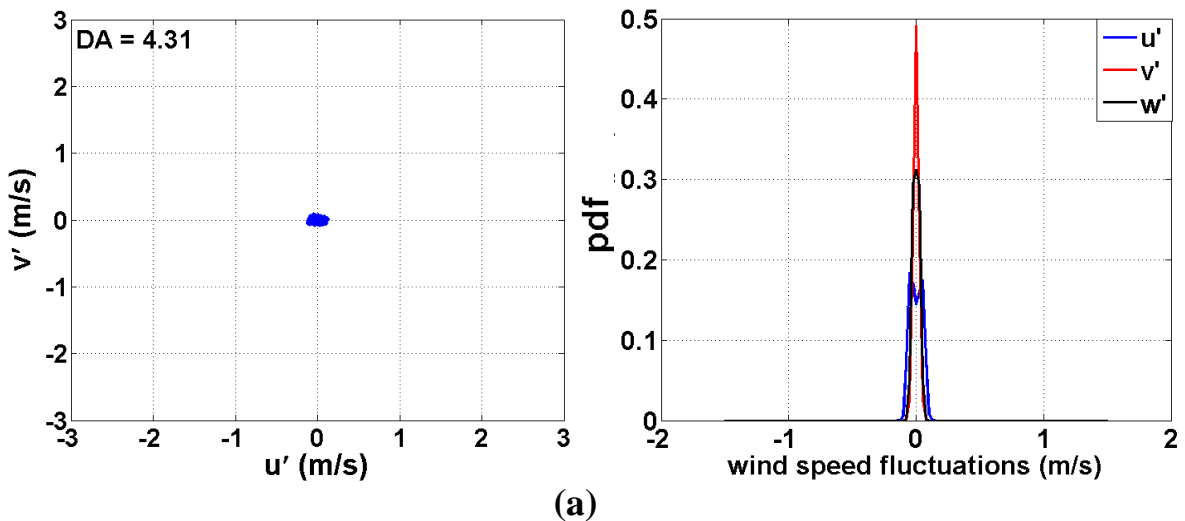
Figure 91. Scatter plot (left) and probability density function, pdf, (right) of hub height velocity fluctuations in complex terrain, (a) Freestream, (b) Wake.

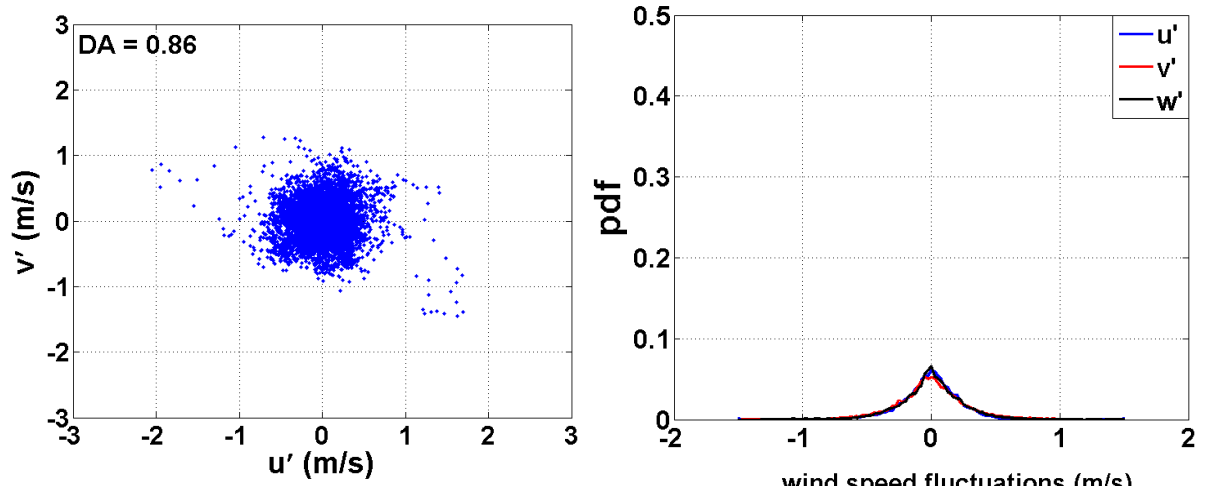
	Freestream	Wake
	(m/s)	
$\overline{u'}$	-1.6×10^{-4}	1.6×10^{-3}
$\overline{v'}$	2×10^{-3}	-6×10^{-3}
$\overline{w'}$	-5×10^{-4}	1.5×10^{-3}
$\overline{u'v'}$	0.01	0.007
$\sigma_{u'}$	0.2	0.22
$\sigma_{v'}$	0.29	0.35
$\sigma_{w'}$	0.27	0.29

Table 11. Statistical parameters derived from the probability density functions measured in complex terrain. In the wake measurements are obtained over $X/D = 1.5-4.5$.

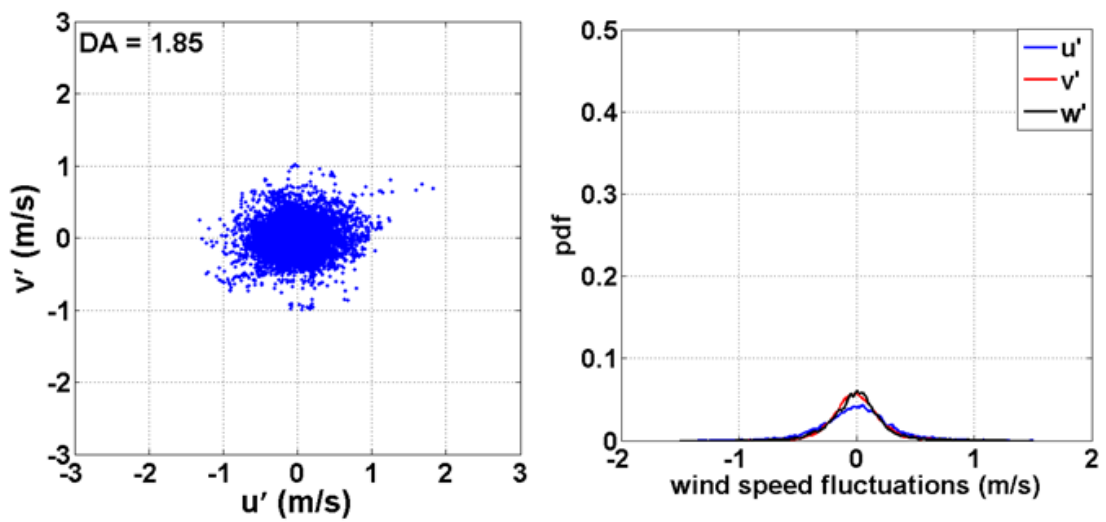
The turbulence structures at hub height in flat terrain are shown in Figure 92. The measurements at the Altenbruch wind farm are made in the freestream, in the wake ($X/D = 2.0 - 5.0$) and in the far-wake ($X/D = 11 -$

14), and are presented in terms of scatter plots (on the left side) and probability density functions (on the right side). For these measurements, the SCADA 10-minute average wind speed was 8 m/s from the South-West direction. In the freestream the degree of anisotropy is 4.3 that indicates an absence of secondary flow structures. In comparison, in complex terrain (Figure 91 a) the degree of anisotropy is 0.5 in the freestream. In the wake in flat terrain, Figure 92 b, the degree of anisotropy is 0.9, indicating that the turbulence structure is more isotropic in the wake compared to the freestream. The presence of strong vortical structures in the wake is indicated by the presence of large magnitude fluctuations in both the streamwise, u' , and spanwise, v' , velocity fluctuations outside the core distribution. It can also be seen that the core of the scatter plot is ten times larger in the wake (Figure 92 b) compared to the freestream (Figure 92 a). In the freestream, the probability density functions of the spanwise fluctuating velocity, v' , and the vertical fluctuating velocity, w' , are uni-modal normal distributions with maxima of 0.5 for the spanwise fluctuations and 0.3 for the vertical velocity fluctuations centered on a zero wind speed. However, the probability density function of the streamwise velocity, u' , has a bi-modal normal distribution with a maximum of 0.18 that is centered on a wind speed fluctuation of -0.1 m/s. The probability density functions have a normal distribution in the wake and far-wake, Figure 92 b, and are quite similar to the probability density functions that are measured in complex terrain, Figure 91 b. The statistical parameters derived from Figure 8 are summarised in Table 12.





(b)



(c)

Figure 92. Scatter plot (left) and probability density function, pdf, (right) of hub height velocity fluctuations in flat terrain, (a) Freestream, (b) Wake, (c) Far-wake.

	Freestream	Wake (m/s)	Far-Wake
$\overline{u'}$	5.8×10^{-6}	-2.32×10^{-4}	-2.6×10^{-5}
$\overline{v'}$	5.3×10^{-6}	-2.61×10^{-4}	-2×10^{-6}
$\overline{w'}$	-4.6×10^{-5}	-3×10^{-5}	-9×10^{-5}
$\overline{u'v'}$	-2×10^{-4}	-9×10^{-4}	6.3×10^{-3}
$\sigma_{u'}$	0.05	0.23	0.29
$\sigma_{v'}$	0.02	0.26	0.21
$\sigma_{w'}$	0.03	0.25	0.22

Table 12. Statistical parameters derived from probability density functions measured in flat terrain. In the wake measurements are made over $X/D = 2-5$ and in far-wake the measurements were made over $X/D = 11-14$.

6.4 Degree of Anisotropy

The streamwise variations of the degree of anisotropy (Equation 31) in complex and flat terrains are compared in Figure 93. The measurements are made along the wake center line at hub height at the Mt. Crosin and Altenbruch wind farms respectively. In both complex and flat terrains, the degree of anisotropy increases in the near wake regions and decreases in the far wake. In flat terrain, the degree of anisotropy increases from 1 at $X/D = 1.25$ to reach a maximum of 1.7 at $X/D = 3.2$. As discussed earlier, in flat terrain, $X/D = 3$ indicates the streamwise extent of the near wake region, thus the degree of anisotropy can be a useful parameter to identify the extent of near wake region. Further downstream for $X/D > 3.2$, the degree of anisotropy decreases due to mixing and flow re-energisation, and the degree of anisotropy is 0.75 at $X/D = 5.75$. In complex terrain, the degree of anisotropy in the near wake at $X/D = 1.25$ is 0.5. The degree of anisotropy increases to 1.15 at $X/D = 2.2$. Again as discussed earlier, the streamwise extent of the near wake in complex terrain is $X/D = 2$. Downstream of $X/D = 2.2$, the degree of anisotropy decreases to 0.3 at $X/D = 4.75$. Overall it is observed that in the near- and far-wake regions the degree of anisotropy in flat terrain is higher than in complex terrain.

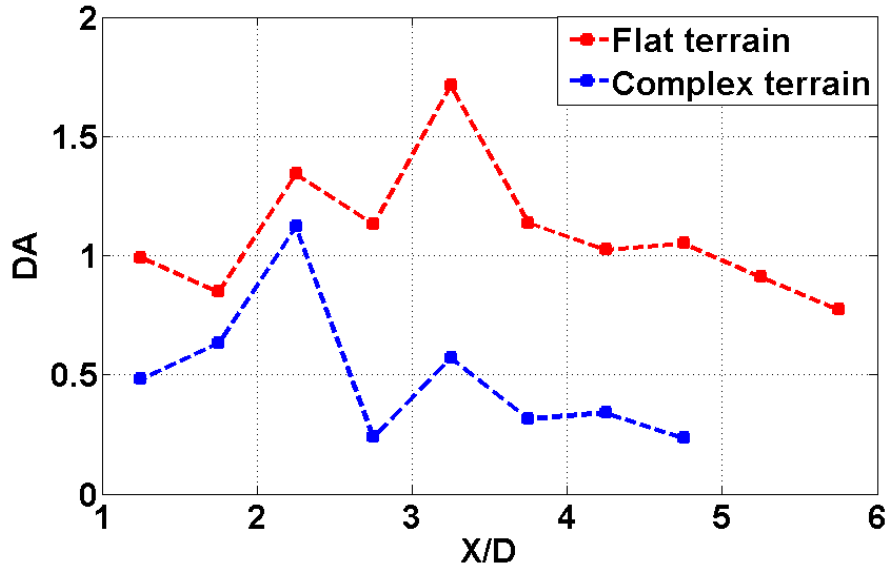


Figure 93. Degree of anisotropy (DA) along wake center line at hub height as a function of downstream distance in flat and complex terrains.

6.5 Friction Velocity

Terrain, atmospheric condition (Wind farm)	Friction velocity, u_* (m/s)
Complex terrain, neutral (Mt. Crosin)	0.23
Complex terrain, neutral (Collonges)	0.4
Flat terrain, neutral (Altenbruch II)	0.03
Flat terrain, neutral (Freudenberg-Beiersdorf)	0.11
Flat terrain, unstable (Freudenberg-Beiersdorf)	0.15

Table 13. Measured friction velocity derived from drone landings upstream of wind turbines in complex and flat terrains.

As the temperature and relative humidity sensors on the drone enable the atmospheric conditions to be determined, the friction velocity (Equation 32) derived from landings in neutral and unstable atmospheric conditions are summarised in Table 13. Under neutral atmospheric condition, the friction velocity ranges from 0.23-0.4 in complex terrain and from 0.03-0.11 in flat terrain. A 35% increase in friction velocity is observed under unstable atmospheric condition at the Freudenberg-Beiersdorf wind farm. The streamwise variations of the friction velocity measured in horizontal flight at a height of 70 m AGL in the freestream of complex and flat terrain are shown in Figure 94. In complex terrain, the mean friction velocity is 0.23 m/s and in flat terrain the mean friction velocity is 0.03 m/s.

Components of turbulence in surface layer	Freestream		Open literature [90, 107]
	Flat terrain	Complex terrain	
$\overline{u'^2}/u_*^2$	5.1	1	6
$\overline{v'^2}/u_*^2$	1.1	2	2
$\overline{w'^2}/u_*^2$	1.6	1.8	1.7

Table 14. Measured turbulent fluctuations in the surface layer under neutral atmospheric conditions in flat and complex terrains. The measurements are compared to literature [90, 107].

The measured turbulent fluctuations normalised by the friction velocity in the surface layer are summarised in Table 14. Also shown in Table 14 are the commonly used values that are presented in the open literature for the streamwise fluctuations [90] and the spanwise and vertical fluctuations [107]. In flat terrain, the streamwise turbulence is dominant and in complex terrain the turbulence is more isotropic.

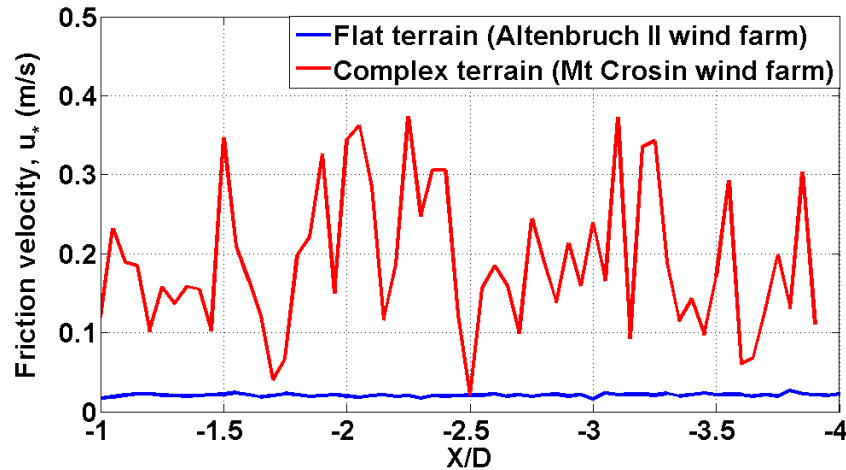
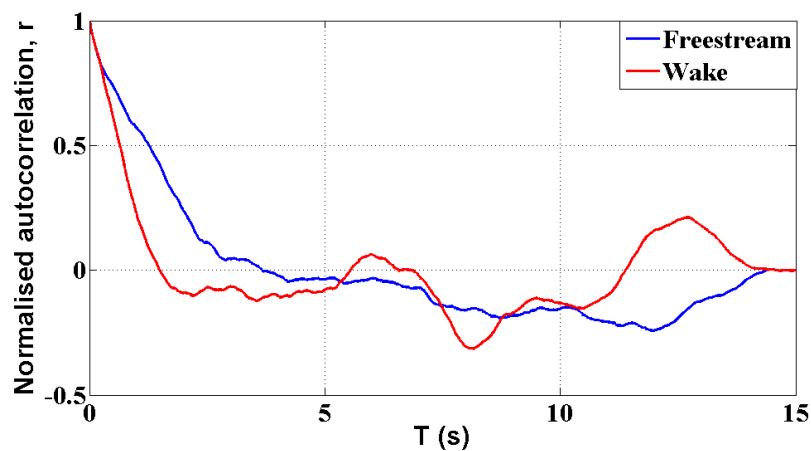


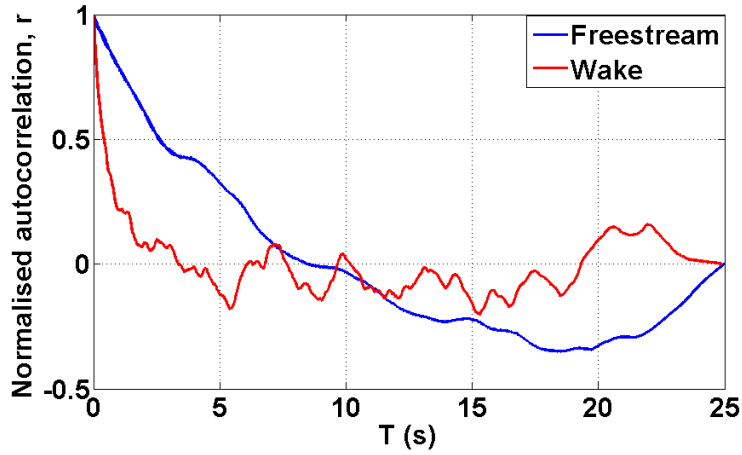
Figure 94. Friction velocity variation along the drone trajectory in flat and complex terrains at 70 m AGL.

6.6 Integral Length and Time Scales

The integral length and time scales (Equation 33) measured at hub height in flat and complex terrains are summarised in Table 15. In the complex terrain of the Mt. Crosin wind farm, the integral length and time scales in the freestream are 43 m and 6 s respectively. While the integral time scale in the complex terrain is unchanged, the length scale in the wake, 19 m, is half that in the freestream. In the flat terrain at the Altenbruch wind farm, the integral time scale measured in the freestream is 15 s and the corresponding integral length scale is 119 m. In the wake, the integral time scale is 6 s and the corresponding integral length scale is 20 m.



(a)



(b)

Figure 95. Normalised autocorrelation along a straight line drone trajectory in free stream and wake at hub height, (a) complex terrain, (b) flat terrain.

	Integral time scale, τ (s)	Integral length scale, \mathcal{L} (m)
Complex terrain, freestream	6.1	43
Complex terrain, wake	5.4	18.8
Flat terrain, freestream	15 – 16.5	113 - 124
Flat terrain, wake	2.3 – 9.1	8 - 32

Table 15. Integral time scale and integral length scale measured in complex and flat terrains.

6.7 Summary

A detailed comparison of wake evolution in flat and complex terrains was discussed in this chapter in terms of spatially-averaged wind speed and spatially-averaged turbulent kinetic energy. Reynolds decomposition of the measured wind speed yields the components of turbulence in the surface layer. In complex and flat terrains, detailed

analysis of the measured fluctuating parts in freestream and wake reveals the turbulence statistics. In both terrains, the variation of the degree of anisotropy along the wake centreline was presented as a function of downstream distance. Friction velocity computed from measurements made during many drone landings in four different wind farms were tabulated. Finally, the integral time scales and the integral length scales computed from the normalised autocorrelation of the FRAP measured airspeed were tabulated.

7. EFFECTS OF ATMOSPHERIC STABILITY

The measurements in the wake of a wind turbine, located in a flat terrain, under neutral and unstable atmospheric conditions are described in this chapter. These measurements detail at full-scale Reynolds number and at both unstable and neutral atmospheric conditions, the wind speed and turbulent kinetic energy evolution in the near and farwake (up to six-diameters) including their profiles at eleven different locations downstream. The dissipation rate of turbulent kinetic energy, obtained from wavenumber spectra using measurements under different atmospheric conditions, in flat and complex terrains is also tabulated. All measurements described in this chapter are made with the WindFlyer drone.

7.1 Measurement Site



Figure 96. Above: Location of Freudenberg-Beiersdorf wind farm (red

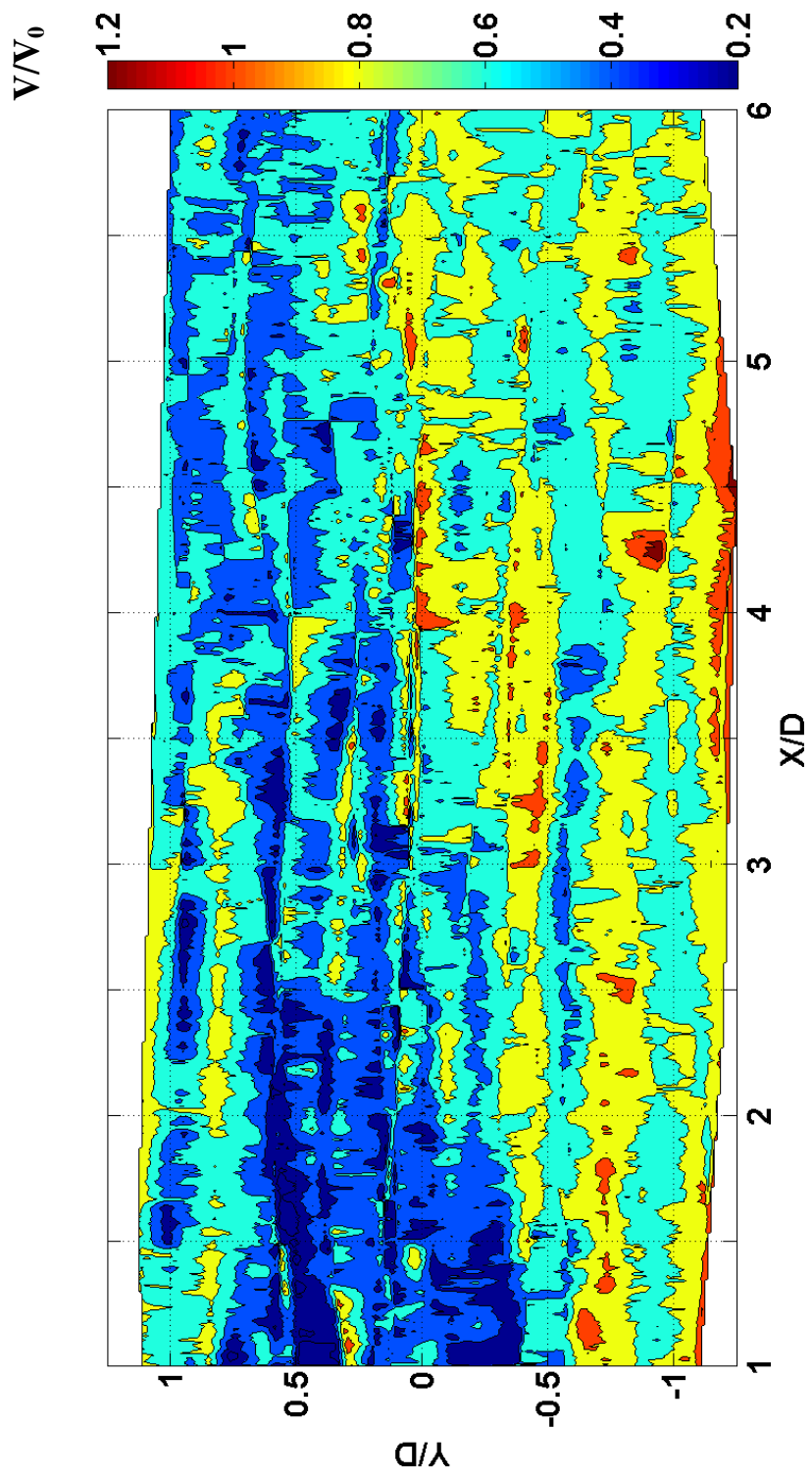
square). Below: Layout of wind turbines in the wind farm. The circle symbols show the locations of wind turbines.

The measurements under unstable atmospheric condition were made at the 28 MW Freudenberg-Beiersdorf wind farm in Brandenburg, Germany. The wind farm is located in a flat terrain at a distance of 100 km from the North Sea coast, Figure 96 (above). The locations of the wind turbines in this wind farm are shown by the circle symbols in Figure 96 (below); the turbine at which measurements are made is shown as filled white circle, whereas the other turbines are shown as filled black circles. Two small Enercon E40 wind turbines – with hub height of 65 m - belonging to a neighbouring wind farm are also shown in Figure 96 marked with filled red circles. The turbine under measurement is a Vestas V80 with a rated power 2.0 MW, diameter of 80 m and a hub height of 100 m. The predominant wind direction during wake measurements in unstable atmospheric condition was 28° , but due to an error in SCADA, the 10-minute average wind and nacelle direction were not available from the wind farm operator. However, the wind farm operator provided access to a limited set of the turbine's 10-minute average SCADA data, which were used for comparison to supplement the drone based wind measurements. The wake measurements were intentionally scheduled to scan and cover a plane at hub height – covering a streamwise distance of 600 m and a lateral distance of ± 80 m downstream of the wind turbine under measurement – in unstable atmospheric condition. It took 40 minutes to complete the wake measurements flying towards the wind turbine rotor in the wake and taking a turn to return back to start the next scan. The lateral spacing between any two adjacent measurement trajectories in wake is $0.09D$. The SCADA wind speed during this measurement was in the range of 7-8.5 m/s. The atmospheric stability measured based on the atmospheric lapse rate of $18^\circ\text{C}/\text{km}$ confirms the unstable atmospheric condition during the wake scan.

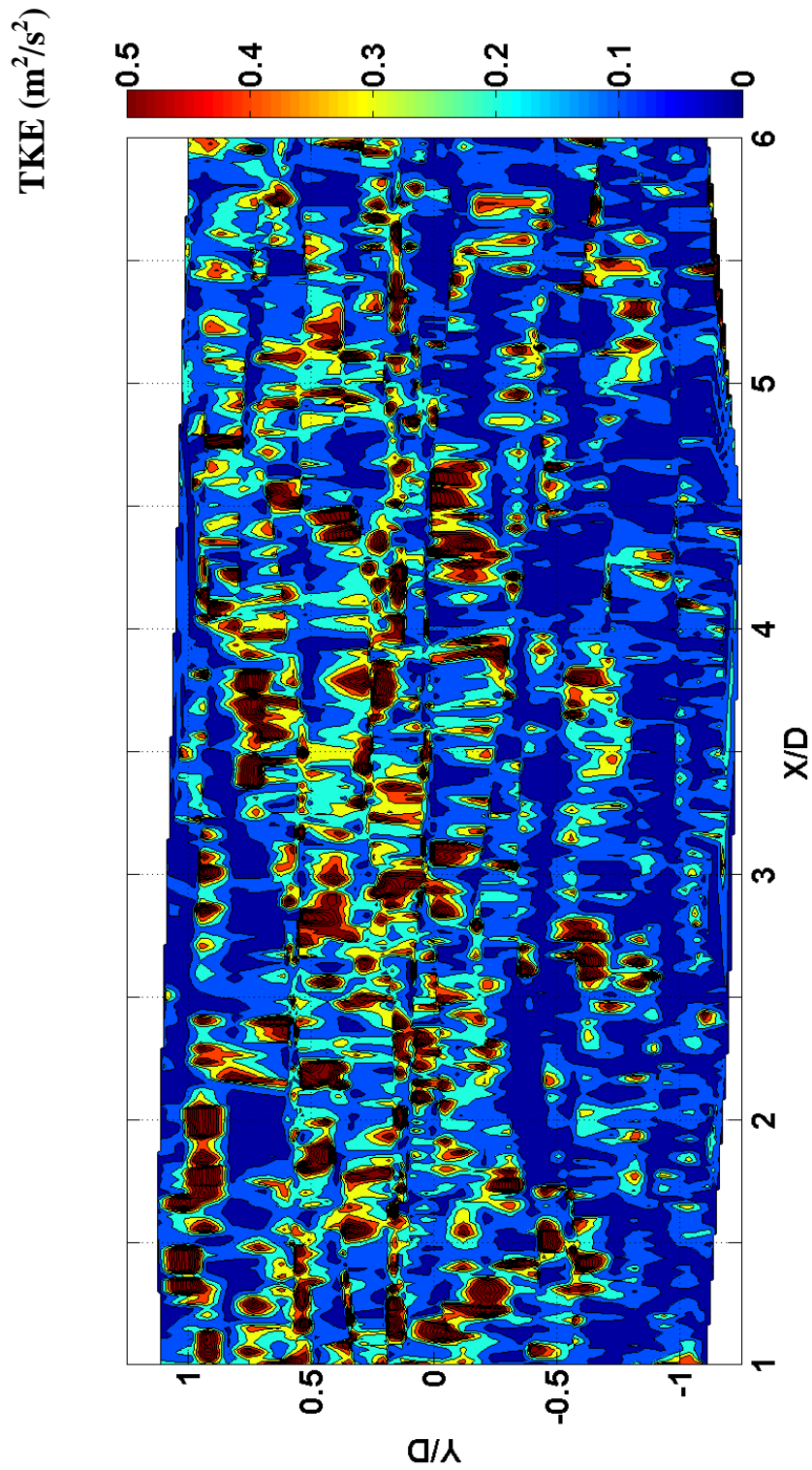
7.2 Wake Evolution

The evolution of the wake up to six diameters downstream, at hub height, in unstable atmospheric condition is shown in Figure 97 in terms of the wind speed and turbulent kinetic energy. These measurements are made in a horizontal plane downstream of the wind turbine. The energy extraction results in low wind speed in the near-wake, but the wind speeds

in the near-wake show both spatial non-uniformity and asymmetry about the rotor axis. Under unstable atmospheric conditions, the shear layer is not prominently visible in wind speed contour on either side, and the turbulent kinetic energy contour confirms the tip vortices – which were clearly visible under neutral atmospheric condition (Figure 65) - are also not clearly distinguishable. The low wind speeds observed in the near-wake continue downstream till $X/D = 2-3$ before re-energisation. The wind speed contour confirms that the wake evolution and re-energisation is asymmetrical, and the wake exhibits lateral migration (meandering) towards the positive Y/D axis as it evolves downstream. For the 28° wind direction there is a turbine located upstream with a lateral separation of 200 m between the two turbines' rotor axis. The wake lateral migration (meandering) towards the positive Y/D axis as it evolves downstream could be due to the impact of this upstream turbine's wake evolution, combined with the impact of flow around the forested area separated by a lateral separation of 500 m. The wake lateral migration (meandering) can also be observed in the turbulent kinetic energy contour plot, as the high turbulent kinetic energy regions shift along the positive Y/D axis. The near-wake region extends up to $X/D = 2-3$ in the unstable atmospheric condition. Downstream after $X/D = 3$, mixing starts within the wake and is manifested by the penetration of relatively high turbulent kinetic energy flow inside the wake. This mixing is also seen in the measured wind speeds, as relatively high speed flow from outside the wake starts to penetrate into the low wind speed wake downstream of $X/D = 3$, and subsequently re-energises the wake flow. The wake lateral migration (meandering) continues downstream till $X/D = 6$, and the wake core evolution is 9° inclined to the streamwise wind direction.



(a)



(b)

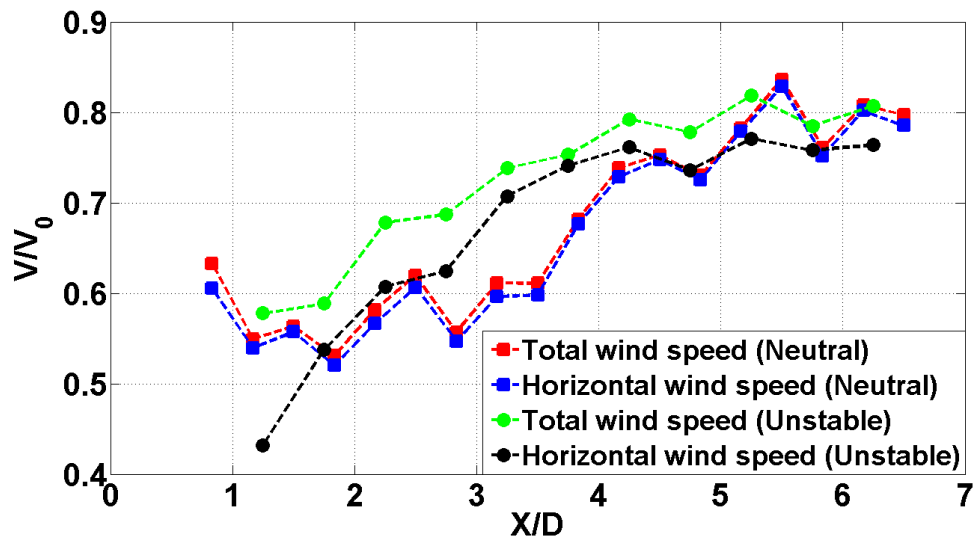
Figure 97. Under unstable atmospheric condition, measurements of (a) wind speed, (b) turbulent kinetic energy at hub height in a horizontal plane downstream of a wind turbine at the Freudenberg-Beiersdorf wind farm.

The streamwise evolution of the wake under unstable and neutral atmospheric conditions is represented in terms of the spatially-averaged horizontal and total wind speeds, and the spatially-averaged turbulent kinetic energy as shown in Figure 98. The spatially-averaged flow properties are derived from the area-averaged (within $|Y/D| < 0.5$ or $(Z - Z_{HH})/D < 0.5$) flow properties in the plane shown in Figure 97 and Figure 65. When the atmosphere is neutral, the spatially-averaged horizontal wind speed in the near-wake ($X/D < 3$) is nearly constant at 55% of the reference wind speed, and the difference between the horizontal and total wind speed is less than 2% of the reference wind speed. The horizontal and total wind speeds start to recover at a rate of 10% per diameter distance downstream between $X/D = 3$ and $X/D = 5.5$, with no observable difference between these two quantities in this region. At $X/D = 6$, the horizontal and total wind speeds are about 80% of the reference wind speed.

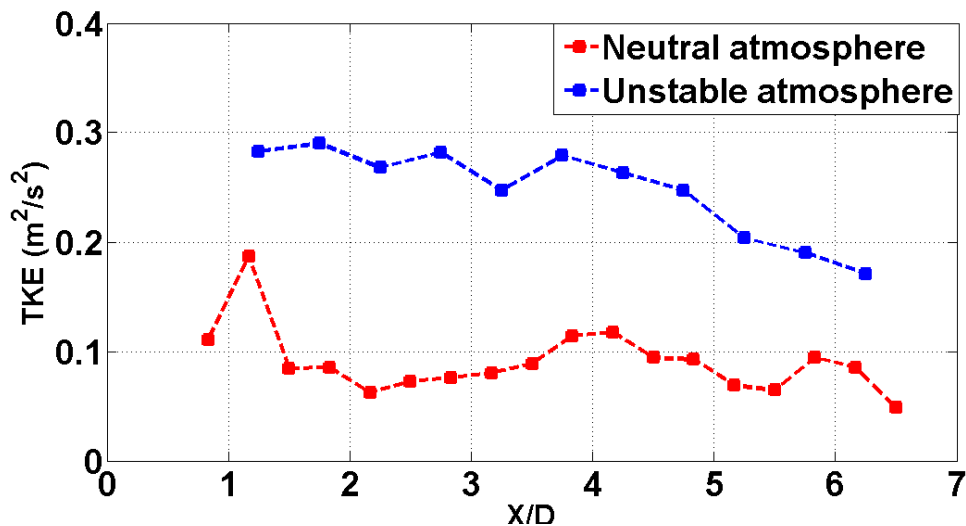
When the atmospheric condition is unstable, the spatially-averaged horizontal and total wind speeds show a slightly different trend with both increasing initially till $X/D = 3.25$ and then showing a constant trend further downstream. Initially at $X/D = 1.25$, the difference between the spatially-averaged horizontal and total wind speed is maximum at 10% of the reference wind speed, but this difference narrows down quickly further downstream. The horizontal and total wind speeds start to recover at a rate of 15% per diameter distance downstream between $X/D = 1.25$ and $X/D = 3.25$, to reach 80% of the reference wind speed at $X/D = 3.25$. The reason for the early recovery in wind speed and the subsequent constant trend under unstable atmospheric condition could be the lateral migration of the wake towards the positive Y/D axis as it evolves downstream.

The spatially-averaged turbulent kinetic energy drops downstream with distance in both neutral and unstable atmospheric conditions as shown in Figure 98 b. For neutral atmospheric condition, the turbulent kinetic energy decreases in the near-wake to $0.075 \text{ m}^2/\text{s}^2$ at $X/D = 3$, followed by an increase to $0.12 \text{ m}^2/\text{s}^2$ at $X/D = 4$. The region between $X/D = 3$ and $X/D = 5.5$ is where enhanced flow mixing occurs and this is the reason for the increase in wind speed, and the increase/decrease that is observed in the spatially-averaged turbulent kinetic energy. Further downstream at $X/D = 6.5$, the spatially-averaged turbulent kinetic energy again reaches $0.075 \text{ m}^2/\text{s}^2$. In the wake, the spatially-averaged turbulent kinetic energy under unstable atmospheric condition is more than twice the spatially-averaged turbulent kinetic energy measured under neutral atmospheric condition for all downstream locations. For unstable atmospheric condition, the turbulent

kinetic energy is nearly constant (or falls slowly) at $0.28 \text{ m}^2/\text{s}^2$ till $X/D = 3$, followed by a drop to rate of $0.045 \text{ m}^2/\text{s}^2$ per diameter till $X/D = 6$. As in neutral atmospheric condition, the wake re-energisation under unstable atmospheric condition is observed when turbulent kinetic energy is maximum. At $X/D = 6$, the spatially-averaged turbulent kinetic energy in the wake is $0.18 \text{ m}^2/\text{s}^2$, which is still two times larger than the turbulent kinetic energy measured upstream at hub height under unstable atmospheric condition (Table 16).



(a)



(b)

Figure 98. In flat terrain, streamwise evolution of (a) total and horizontal wind speed, (b) turbulent kinetic energy in wake under neutral and unstable

atmospheric condition.

7.3 Wake Profile

The spanwise profile of spatially-averaged wind speed and turbulent kinetic energy in the wake at different downstream distances under unstable and neutral atmospheric condition is shown in Figure 100 and Figure 101. The spatially-averaged flow properties are derived from the area-averaged flow properties in the plane shown in Figure 99 and Figure 97. The near- and far-wake deficit induced due to energy extraction by the wind turbine is visible in both neutral and unstable atmospheric condition. This energy extraction results in low wind speed inside near-wake core ($r/D < \pm 0.5$) and high wind speed outside the near-wake shear layer, with a wind speed gradient bridging the gap between these two locations. For neutral atmospheric condition, the mean wind speed inside the near-wake core is $V/V_0 = 0.5-0.6$ and is nearly uniform. At $X/D = 1$, the shear layer results in a spatial wind speed gradient with a slope of $(V/V_0)/(r/D) = 2-2.5$, suggesting that the wind speed doubles radially with distance in the shear layer. Downstream of $X/D = 1$, the shear layer (and hence the wake) grows in size by decelerating the wind speed outside the wake core. The re-energisation, starting at $X/D = 3$, results in non-uniformity (spatial gradient) inside wake thus generating a gradient with a slope of $(V/V_0)/(r/D) = 2/3$. As the wake starts re-energising, the wind speed starts increasing in the wake core and the spatial gradient observed at $X/D = 3$ starts to diminish.

When the atmospheric condition is unstable, the wake deficit is again clearly noticeable in the near-wake (say, at $X/D = 1.5$) with the mean wind speed inside the near-wake core around $V/V_0 = 0.5$. The wind speed profile at $X/D = 1$ is not symmetric about the axis at $r/D = 0$ suggesting asymmetry in energy extraction on either side of the axis by the wind turbine rotor (This is also visible in the contour plots in Figure 97). At $X/D = 1$, the shear layer at both ends results in a spatial wind speed gradient in the wind speed profile with a slope of $(V/V_0)/(r/D) = 2$, similar to those observed in the near-wake under neutral atmospheric condition. For unstable atmospheric condition, both the wind speed profile and the turbulent kinetic energy profile exhibit higher non-uniformity for $X/D < 4$ compared to the profiles measured in the far-wake after $X/D > 4$. Downstream as the wake evolves, it is inclined to the main wind direction and moving laterally towards the positive r/D axis, resulting in a more uniform wind speed

profile along the negative r/D axis with wind speeds in this region reaching ambient wind speeds of $V/V_0 = 1$ (say, at $X/D = 5.5$). In both neutral and unstable atmospheric condition, the wake deficit and thus wind turbine signature are observed even at $X/D = 6$.

The turbulent kinetic energy profile in neutral atmospheric condition shows high radial non-uniformity in the near-wake (say, at $X/D = 1$) compared to the far-wake (the more uniform profile at $X/D = 5$). For neutral atmospheric condition at $X/D = 1$, the signature of tip vortices and nacelle vortices are manifested as high turbulent kinetic energy regions at $r/D = 0.5$ and $r/D = 0$. As the wake evolves downstream, the high turbulent kinetic energy regions diffuse their energy radially to other locations, due to mixing, resulting in increases in turbulent kinetic energy both inside and outside the wake vortex zones. For unstable atmospheric condition in the near-wake, the tip vortex signature is not clearly visible at $X/D = 1$ and the turbulent kinetic energy inside the wake core is uniformly high at $0.25 \text{ m}^2/\text{s}^2$, which is three times the upstream turbulent kinetic energy (Table 16). As the wake evolves downstream, more non-uniformity is observed across the turbulent kinetic energy profile and the signature of the wake lateral migration is manifested as high turbulent kinetic energy regions shifting radially out towards the positive r/D axis till $X/D = 4$. As observed in neutral atmospheric condition, the turbulent kinetic energy profile becomes more uniform in the far-wake after $X/D = 4.5$. In the far wake, the turbulent kinetic energy at all radial locations under unstable atmospheric condition are higher than the turbulent kinetic energy measured under neutral atmospheric condition. It can also be observed that the non-uniformity in the turbulent kinetic energy profile initially increases downstream under unstable atmospheric condition before starting to decrease in the far-wake after $X/D = 4$.

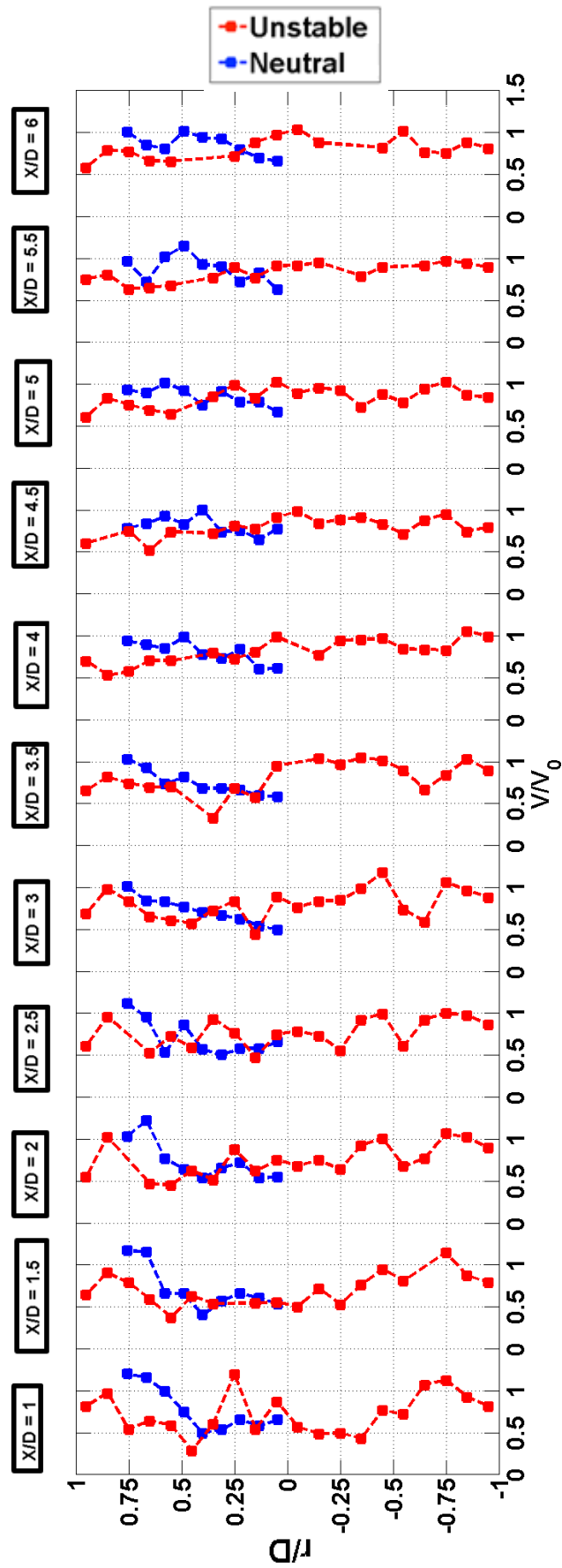


Figure 100. Spatially averaged spanwise wind speed profile at eleven downstream locations under unstable and neutral atmospheric condition.

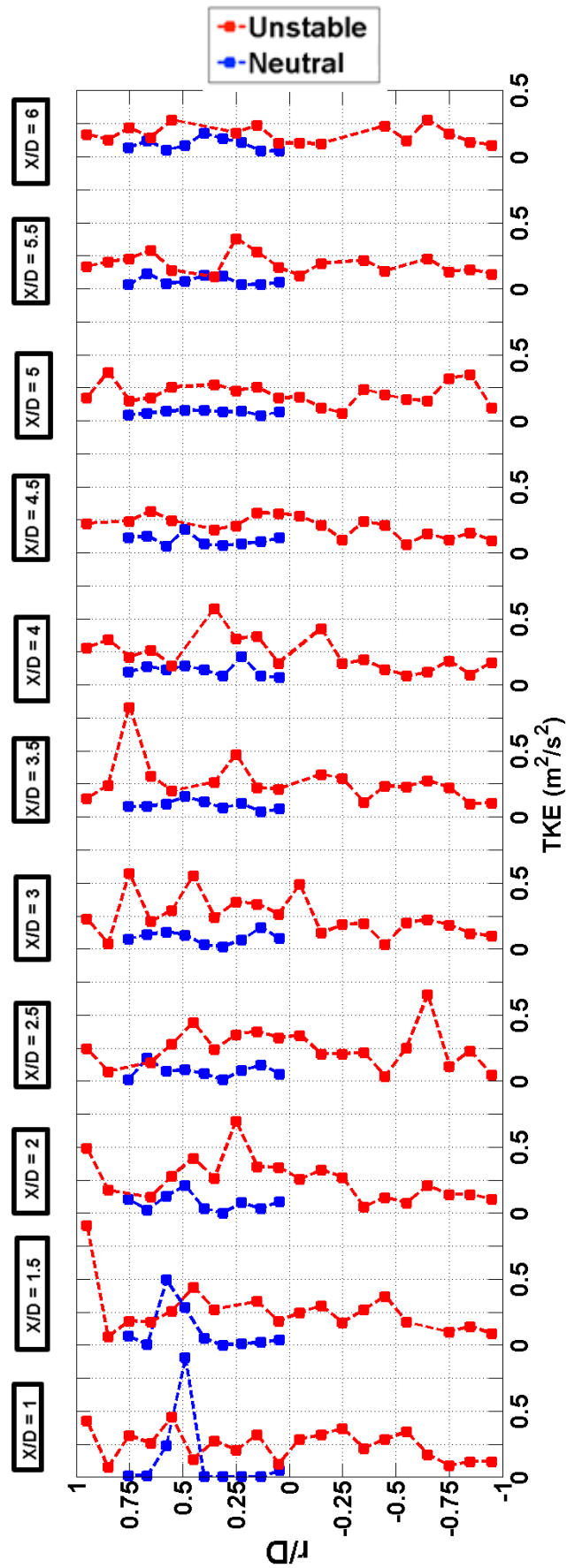


Figure 101. Spatially averaged spanwise turbulent kinetic energy profile at eleven downstream locations under unstable and neutral atmospheric

condition.

7.4 Dissipation Rate of Turbulent Kinetic Energy

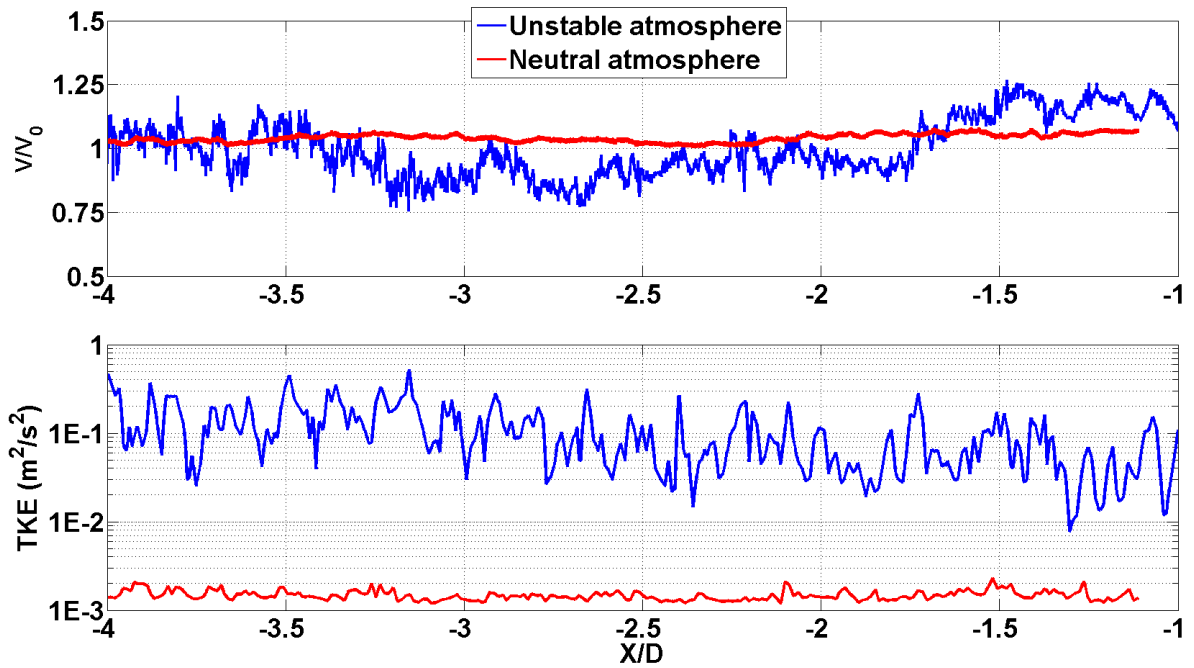
In flat terrain, the wind speed, turbulent kinetic energy and spectra measured upstream ($-4 < X/D < -1$) at hub height in neutral and unstable atmospheric condition are compared in Figure 102. The upstream wind speed is relatively constant in neutral atmospheric condition with fluctuations smaller than $\pm 5\%$, but large fluctuations - as high as $\pm 25\%$ - are observed in the upstream wind speed measured under unstable atmospheric condition. The mean wind speeds are $1.04V_0$ and $1.01V_0$, respectively in neutral and unstable atmospheric condition. The large fluctuations in wind speed result in higher turbulent kinetic energy upstream in unstable atmospheric condition compared to neutral atmospheric condition. The turbulent kinetic energy upstream under unstable atmospheric condition is 50 times larger than the turbulent kinetic energy upstream measured in neutral atmospheric condition (Figure 102 a). The mean turbulent kinetic energy measured upstream at hub height, under unstable and neutral atmospheric condition, for flat and complex terrains are tabulated in Table 16. The mean turbulent kinetic energy under unstable atmospheric condition in flat terrain is twice larger than the mean turbulent kinetic energy measured under neutral atmospheric condition in complex terrain. In complex terrain, the turbulent kinetic energy in unstable atmospheric condition is three times larger than in neutral atmospheric condition.

The power spectral densities of wind speed measured at hub height upstream ($-4 < X/D < -1$) for neutral and unstable atmospheric conditions are shown in Figure 102 b. It can be observed that both spectra show qualitatively similar behaviour in a region of slope $-2/3$ that characterises the inertial subrange. In flat terrain, over the inertial range the spectral amplitudes in unstable atmospheric condition are two orders of magnitude higher than the spectral amplitudes in neutral atmospheric condition. The dissipation rate of turbulent kinetic energy thus obtained – from the spectra by curve fitting in the inertial subrange (Equation 28) - in freestream and wake, for different terrain conditions, under unstable and neutral atmospheric condition is tabulated in Table 17. In both flat and complex terrains, the dissipation rate of turbulent kinetic energy is larger in the wake compared to the freestream. Similarly in both flat and complex terrains, the dissipation rate of turbulent kinetic energy is also larger under unstable

atmospheric condition compared to the dissipation rate measured under neutral atmospheric condition. The highest dissipation rates are observed in the wake under unstable atmospheric condition in both flat and complex terrains.

Terrain	Atmospheric condition	Mean TKE (m^2/s^2)
Flat	Neutral	0.002
Complex	Neutral	0.04
Flat	Unstable	0.09
Complex	Unstable	0.13

Table 16. Hub height turbulent kinetic energy measured upstream at an ambient wind speed of $V_0 = 8$ m/s.



(a)

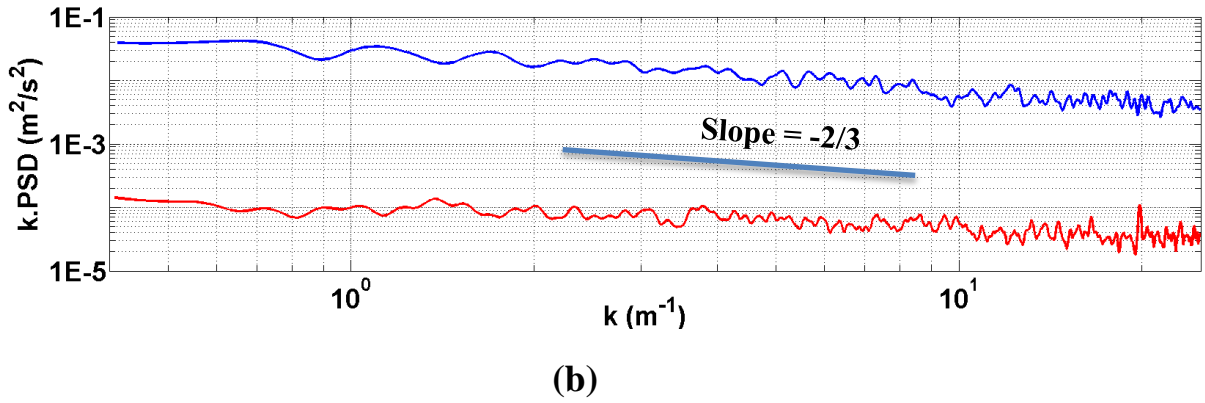


Figure 102. (a) In flat terrain, comparison of wind speed and turbulent kinetic energy measured at hub height over a streamwise distance of three diameters in unstable and neutral atmospheric condition, (b) In flat terrain, inertial range wind speed spectra measured at hub height in unstable and neutral atmospheric condition. The y-abcissa shows the product of the wave number and the power spectrum density.

Terrain	Atmospheric condition	Dissipation rate of TKE (m²/s³)	Wake/Freestream at Hub Height
Complex	Unstable	0.004	Freestream
Complex	Neutral	0.0002-0.002	Freestream
Complex	Unstable	0.015	Wake
Complex	Neutral	0.002-0.005	Wake
Flat	Unstable	0.002	Freestream
Flat	Neutral	6E-06	Freestream
Flat	Unstable	0.005-0.015	Wake
Flat	Neutral	0.0022	Wake

Table 17. Dissipation rates of turbulent kinetic energy measured under unstable and neutral atmospheric condition in freestream and wake.

7.5 Phase Locking

As discussed earlier, phase-locking is needed to understand the relative contributions of the periodic and stochastic parts of the fluctuating components in the Reynolds decomposition. During these measurements, the drone was flown repeatedly along a chosen trajectory (15 times) at hub

height of a V80 wind turbine located at Freudenberg-Beiersdorf wind farm, Brandenburg (Germany). The SCADA wind speed during this measurement was 6.5 m/s. The periodic turbulent kinetic energy as a function of blade position at four different positions in the wake at $X/D = 1$ and freestream at $X/D = -1$ are shown in Figure 103. The upstream turbulent kinetic energy does not vary significantly in each of the four cases and is independent of the blade position. The downstream turbulent kinetic energy contains one peak in the 120° sector with maximum values one order of magnitude larger than the upstream turbulent kinetic energy. The turbulent kinetic energy downstream for all other blade positions is the same as the value measured in upstream. The process of extracting data from phase locking is explained in Figure 58 with a flow chart.

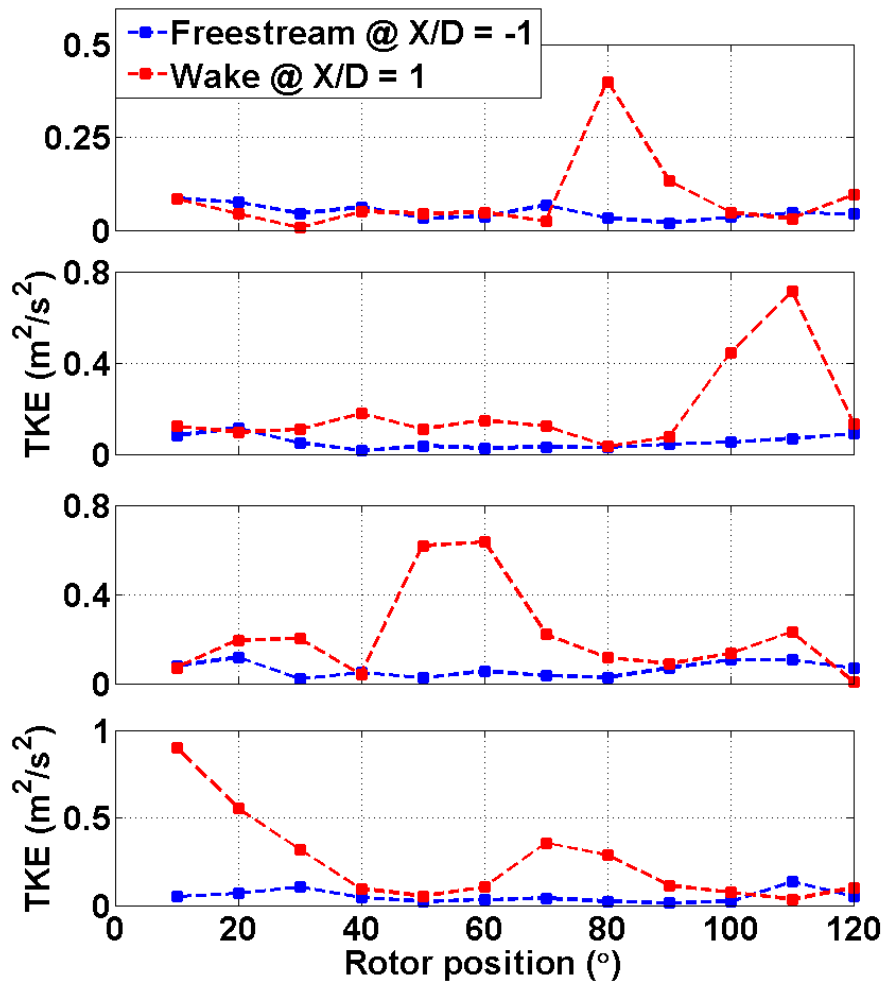


Figure 103. Periodic turbulent kinetic energy as a function of rotor blade position in the wake and freestream.

7.6 Wake Profile: Measurements versus ETH Wake Model

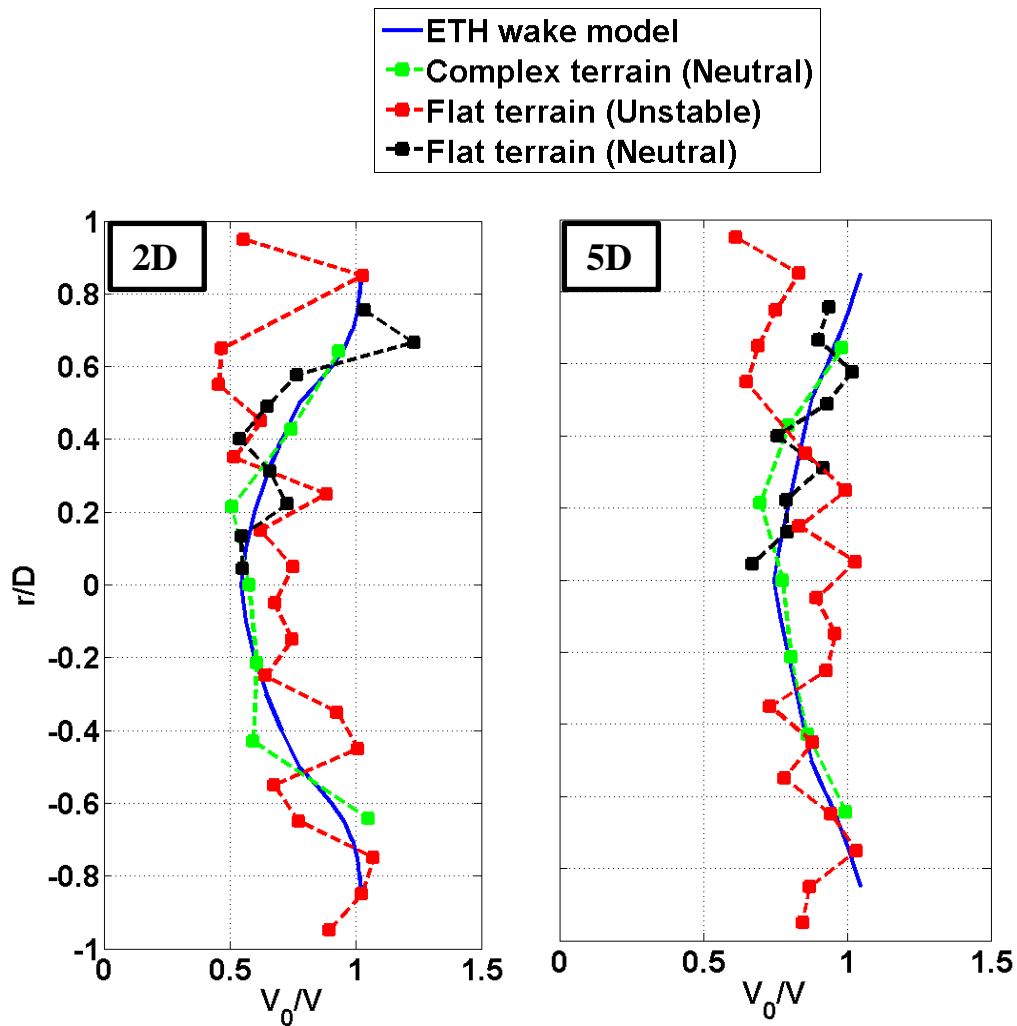


Figure 104. Comparison between the spatially-averaged spanwise profiles of wind speed measured under different atmospheric conditions and the predictions from the ETH wake model at two-diameter and five-diameter downstream.

As the measurements are under-taken to support the further development of advanced wake models and atmospheric flow simulation tools, comparing them with measurements may reveal the extent of deviation under unstable atmospheric condition. The spatially-averaged spanwise profiles of wind speed in the wake of a wind turbine are compared to the predictions from the ETH wake model, at two different downstream locations, in Figure 104. The measurements in complex terrain under neutral atmospheric condition were carried out - at hub height of a 2 MW Enercon E70 wind turbine - in the Collonges wind farm, Switzerland. More details of the complex terrain and the wind power generator at the

Collonges wind farm can be found here [92]. At two diameters and five diameters downstream, a good comparison is observed between the spanwise wake profiles measured in flat and complex terrains under neutral atmospheric condition and the ETH wake model. As mentioned above the ETH wake model assumes a symmetrical wake profile across the wake centerline, but this symmetry is clearly not observed under unstable atmospheric condition. For unstable atmospheric condition, the ETH wake model under-predicts the wind profile inside wake core. The comparison between the spatially-averaged streamwise evolution of wind speed measured in the wake of a wind turbine and the predictions from ETH wake model can be found in Figure 74.

7.7 Summary

Instrumented drone measurements in a utility scale wind farm, located in a flat terrain, have been made to detail the near-wake and far-wake under neutral and unstable atmospheric conditions. Under unstable atmospheric condition, the distinct near-wake signatures like tip vortices and shear layer are not explicitly noticeable from the contour plots. The near and farwake deficits in both cases are measured and reported through wind speed profiles; to the authors' knowledge these wake profiles from full-scale experiments have been presented for the first time at eleven different locations downstream in both neutral and unstable atmospheric conditions. For unstable atmospheric condition, the wake evolution and wake core centre line were not aligned to the main wind direction but were inclined at an angle of 9° as seen in the wind speed contour plot. The wake re-energisation can be seen in both the contour and profile plots of wind speed and turbulent kinetic energy under unstable and neutral atmospheric conditions. The wind speed spectral amplitudes upstream at hub height under unstable atmospheric condition are two orders of magnitude higher than the spectral amplitudes under neutral atmospheric condition, and the dissipation rates of turbulent kinetic energy obtained from wind speed spectra are tabulated for different conditions. Finally, the measurements are compared with a recently developed semi-empirical wake model at two different downstream locations – one in the near-wake at two diameters and the other in the farwake at five diameters.

8. SUMMARY AND CONCLUSION

The capabilities and potential of an innovative measurement approach to characterize the flow field around a wind turbine – that comprises of miniature Fast Response Aerodynamic Probe (FRAP) mounted on a drone - is now well proven. The instrumented drone allows high spatial and temporal resolution measurements of the highly three-dimensional structure and interactions in a wind turbine's wake; to the authors' knowledge these are the first such measurements in full-scale experiments. The measurement accuracy of the drone-based system is verified with comparisons against measurements with a three-dimensional scanning LIDAR system, the wind turbines' SCADA system, and microscale simulations of the wind field. A STFT based approach was successfully employed to compute the turbulent kinetic energy along the drone trajectory. The key accomplishments of the FRAP-on-drone wind measurement system can be summed up as follows.

- The first ever measurements of wake evolution, at full-scale Reynolds number conditions in complex and flat terrains, that show the evolution and breakdown of tip vortices (that are characteristic of the near wake) and the turbulent mixing and entrainment of more energized flow (that is distinctive in the far wake).
- The first-ever measurements of the pressure field through a tip vortex. This includes the ability of the FRAP probe to resolve the distinctive signatures of both the blade tip vortices and nacelle wake as the wake evolves.
- The first-ever measurements of the pressure field across a wind turbines rotor plane.
- Spatially-averaged wake profiles from full-scale experiments have been presented for the first time at eleven different locations downstream in both neutral and unstable atmospheric condition.
- Finally, a comparison of these measurements to a recently developed semi-empirical wake model and an immersed wind turbine model that highlights how these measurements can support further model development.

The region of the near wake is measured to extend up to three-rotor diameters in flat terrain and two-rotor diameters in complex terrain. In this region, tip vortices that can be distinguished from their elevated levels of

turbulent kinetic energy are clearly identifiable. The tip vortices evolve just below the shear layer that separates the high speed exterior flow from the relatively low speed flow within the near wake. Further downstream of the near-wake, the wake flow is re-energised by the penetration of the relatively high energy flow from the wake's boundary into the wake core. In flat terrain by $X/D = 5-5.5$ and in complex terrain by $X/D = 3.5-4$, the elevated turbulent kinetic energy flow has penetrated to the centre of the wake. In flat terrain, even though the upstream wind speed is recovered after $X/D = 10$, the turbulent kinetic energy in the far-wake is approximately two orders of magnitude larger than the value measured upstream in flat terrain and is of similar magnitude to the turbulent kinetic energy measured upstream in complex terrain. Simultaneous measurements of the near wake (of one turbine) and the far wake (of a second turbine) confirm the distinctly different characteristics of the near wake and far wake. Instrumented drone measurements in a utility scale wind farm, located in a flat terrain, under unstable atmospheric condition are also detailed.

These measurements are accomplished using flight trajectories that are tailored to provide the level of detail that is required to advance the development of three-dimensional field wake models that are embedded within computational fluid dynamics codes. The vertical profiles of the mean wind speed, wind direction and turbulent kinetic energy upstream of the turbine show non-uniformities that are associated with the wind flow in complex terrain. In the wind speed profile, there is a jet-like structure with a maximum wind speed near hub height. The wind veer differs $\pm 12^\circ$ relative to the area-averaged wind direction, and the wind turbine has a yaw misalignment of 5° relative to the main wind direction. The magnitude of the turbulent kinetic energy decreases monotonically with increasing height above ground. In the near-wake, at one diameter downstream of the turbine, the jet-like structure is absent in the wind speed profile and the wind direction varies little over the vertical extent of the rotor. Furthermore there is a factor three increase of the area-averaged turbulent kinetic energy across the turbine's rotor, and the vertical profile of the turbulent kinetic energy shows maxima at the locations of the blade tips.

In complex terrain, the pitch between subsequent tip vortices that are shed from the wind turbine's blades increases as the near-wake evolves. The Kolmogorov inertial sub-range is identified in the measured power spectra, and it is seen that in the near-wake, the spectral amplitudes are 30 to 40 times higher than upstream, and that the spectral peaks are shifted from frequencies of 0.5-0.75Hz to higher frequencies of 1-2 Hz. Whereas the characteristic microscale length scales, that are derived from the

spectra, increase with height upstream of the turbine, in the near-wake the microscale lengths are of constant and smaller magnitude. In flat terrain, over the inertial range the spectral amplitudes in the far wake are two orders of magnitude higher than the spectral amplitudes in the freestream. Similarly the spectral amplitudes in the freestream of complex terrain are nearly two orders of magnitude higher than the spectral amplitudes in flat terrain. Also, the wind speed spectral amplitudes upstream at hub height under unstable atmospheric condition are two orders of magnitude higher than the spectral amplitudes under neutral atmospheric condition, and the dissipation rate of turbulent kinetic energy obtained from wind speed spectra is tabulated for different atmospheric conditions.

A Reynolds decomposition of measured wind speed yields the components of turbulence in the surface layer. In complex and flat terrains, detailed analysis of the measured fluctuating parts in the freestream and wake reveals the turbulence statistics. In both terrains, the variation of the degree of anisotropy along the wake centreline was presented as a function of downstream distance. The friction velocity computed from measurements made during many drone landings in four different wind farms were tabulated.

As the aerodynamic characteristics of wakes (especially in complex terrains) have a profound impact on the energy yield of wind farms and on the fatigue loads of wind turbines in the wind farm, these field measurements at a multi-megawatt wind turbine that is located in flat and complex terrains both improve our knowledge of flows in wind farms, and are well suited to advance the development of three-dimensional wake models that are integrated into a Reynolds-Averaged Navier-Stokes solver. These advanced wake models shall allow the wind flow and turbine wake to be simulated simultaneously, and thus allow for the optimised micro-siting and the improved operation of wind turbines.

The impact of this work on the wind industry can be summed up as follows.

- Wake models should be tuned based on experimental data to better predict the wind speed recovery downstream of a wind turbine. This reduces the uncertainty involved in AEY predictions.
- When a turbine operates with yaw error: Near-wake mixing is initiated earlier on one side of the wake, resulting in a shorter near wake region on one side and is triggered on the side of the wake facing the mainstream wind. This effect has to be included in wake models.

- Wind speed recovery reaches 80% of the SCADA wind speed upstream of the wind turbine at a streamwise distance of 5.5D in a coastal flat terrain. So, this minimum distance has to be maintained between 2 turbines to reduce loads and to increase the amount of energy extracted from the downstream wind turbine.
- The first-ever measurements of the pressure field across a wind turbine's rotor plane will help in tuning the actuator disk model. The streamwise extent of pressure drop and recovery gives the thickness of the actuator disk.
- The far-wake in offshore could be treated similar to the freestream in a complex terrain as the levels of turbulent kinetic energy measured are comparable in the two cases. Thus, the turbines in 2nd and subsequent rows could be chosen for a higher turbulence class and they can be regarded as operating in complex terrain.
- In complex terrain, the wake recovery is faster and the streamwise extent of the wake is at least one-diameter shorter than in flat (offshore) terrain. The reason for the faster streamwise evolution of wind speed in the wake in complex terrain is due to the shorter near-wake region and the higher turbulent kinetic energy (that is increasing the rate of wake re-energisation). Thus, more wind turbines can be packed in a given area in complex terrain than in offshore flat terrain.
- Turbulent kinetic energy and eddy dissipation rates measured upstream and downstream should be used for fatigue life calculations.

8.1 Future Work

The drone based wind measurement system has a potential to empower wind farm research and atmospheric flow research by providing direct insights into real world phenomena. Research groups working in these areas should start using it as a complementary tool.

As the FRAP-on-drone wind measurement system's capabilities in providing the wind flow field and in resolving turbulent features around a wind turbine is now well proven, in future it can be used to investigate the impact of forests and terrain features (like ridges, small hills etc.) on the wind flow field in the atmospheric boundary layer. The measurement system should be used on a regular basis in wind farms to systematically assess the upstream and downstream flow behaviours at different ambient

wind speeds and wind directions. In addition, the measurement system should also be improved by providing it with night operational capabilities (i.e. the safety pilot should be able to keep an eye on the drone during measurements at night and to land it safely) as this increases the probability of getting measurement data during measurement campaigns. The data collected from a systematic study will help in reducing the uncertainties in Annual Energy Yield (AEY) calculations.

The drone based wind measurement system can also be employed in offshore wind farms - especially at high wind speeds that seldom occur on land - to understand the wake evolution and interactions in the absence of terrain features. For this to occur, the drone mounted with the FRAP probe should be flight tested for safe landing on-board a ship.

As the FRAP probe is sampled at 500 Hz and the other on-board sensors at much lower sampling rates (Table 2), there is a mismatch that is presently fixed by interpolation during post-processing. The rapid improvements in sensor technology have resulted in increased availability of new sensors in the market that offer higher sampling rates and improved accuracy [85]. Thus, a careful analysis needs to be done to upgrade the on-board sensors. The FRAP software should be made compatible with the new and improved version of Paparazzi. Finally, the GPS accuracy could be improved by two orders of magnitude using Real-Time Kinematic (RTK) navigation techniques [109, 110]. All these advancements will help in reducing the overall measurement uncertainty.

REFERENCES

- [1]. Global Wind Energy Council report, 2013, <http://www.gwec.net/global-figures/wind-energy-global-status/>.
- [2]. IEA Technology Roadmap: Wind Energy - 2013 edition, 2013, <http://www.iea.org/publications/freepublications/publication/technology-roadmap-wind-energy---2013-edition.html>
- [3]. Sanderse B., 2009, “ Aerodynamics of Wind Turbine Wakes,” *Energy Research Center of the Netherlands*, ECN-E-09-016.
- [4]. Wegley H. L., Ramsdell J. V., Orgill M. M., Drake R. L., 1980, “A Siting Handbook for Small Wind Energy Conversion Systems,” *Batelle Pacific Northwest Laboratories*. Richland, WA(USA), PNL-2521 (Rev. 1).
- [5]. Krohn S., Morthorst P. E., Awerbuch S., 2009, “The Economics of Wind Energy: A report by the European Wind Energy Association,” *European Wind Energy Association*, Brussels.
- [6]. Bingol F., 2009, “Complex Terrain and Wind Lidars,” *Doctoral Thesis*, Riso-PhD-52 (EN).
- [7]. Singh A., Willi D., Chokani N., Abhari R. S., 2015, “Increasing On-Shore Wind Generated Electricity In Germany’s Transmission Grid,” *Journal of Engineering for Gas Turbines and Power*, v. 137, No. 2, p. 021801 1-8.
- [8]. Jafari S., Chokani N., Abhari R. S., 2014, “Simulation of Wake Interactions in Wind Farms Using an Immersed Wind Turbine Model,” *ASME Journal of Turbomachinery*, v. 136, p. 061018 1-7.
- [9]. Ainslie J. F., 1988, “Calculating the Flowfield in the Wake of Wind Turbines,” *Journal of Wind Engineering and Industrial Aerodynamics*. v. 27, p. 213–224.
- [10]. Crespo A., Hernández J., Frandsen S., 1999, “Survey of Modelling Methods for Wind Turbine Wakes and Wind Farms,” *Wind Energy*, v. 2, p. 1–24.
- [11]. Kress C., Barber S., Chokani N., Abhari R. S., 2012, “A New Kinematic Model for Improved Modeling of Wakes,” *German Wind Energy Conference (DEWEK)*, Bremen, Germany
- [12]. Jafari S., Chokani N., Abhari R. S., 2014, “Simulation of Wake Interactions in Wind Farms Using an Immersed Wind Turbine Model,” *ASME Journal of Turbomachinery*, v. 136, p. 061018 1-7.
- [13]. Sorensen J. N., Myken A., 1992, “Unsteady Actuator Disc Model for Horizontal Axis Wind Turbines,” *Journal of Wind Engineering and Industrial Aerodynamics*. v. 39, p. 139–149.
- [14]. Politis E. S., Prospathopoulos J., Cabezon D., Hansen K. S., Chaviaropoulos P. K., Barthelmie R. J., 2012, “Modelling Wake Effects in Large Wind Farms in Complex Terrain: the Pro the Methods and the

Issues,” *Wind Energy*, v. 15, p. 161–182.

[15] Lissaman P. B. S., 1979, “Energy Effectiveness of Arbitrary Arrays of Wind Turbines,” *Journal of Energy*, v. 3, p. 323–328.

[16]. Larsen G. C., Højstrup J., Madsen H. A., 1996, “Wind Field in Wakes,” *Proceedings of the 1996 European Union Wind Energy Conference*, Gothenburg, Sweden, p. 764–768.

[17]. Larsen G. C., Carlen I., Schepers G., 1999, “Fatigue Life Consumption in Wake Operation,” *Proceedings of European Wind Energy Conference and Exhibition*, Dublin, Ireland, Irish Wind Energy Association, p. 605–610.

[18]. Larsen, G. C., Madsen H. A., Sørensen N. N., 2003, “Mean Wake Deficit in the Near Field,” *Proceedings of European Wind Energy Conference*, Madrid, Spain, CD-ROM.

[19]. Mortensen, N. G., Landberg L., Troen I., Petersen E. L., 1998, “Wind Atlas Analysis and Application Program (WASP): Getting Started (volume 1),” *Risø-I-666 (EN)*, Risø National Laboratory, Roskilde, Denmark.

[20]. Frandsen S., Barthelmie R., Pryor S., Rathmann O., Larsen S., Højstrup J., Thøgersen M., 2006, “Analytical Modelling of Wind Speed Deficit in Large Offshore Wind Farms,” *Wind Energy*, v. 9, p. 39–53.

[21]. Schepers J. G., 2003, “ENDOW: Validation and Improvement of ECN’s Wake Model,” *ECN-C-03-034 (March 2003)*, p. 1–113.

[22]. Vermeer L. J., Sørensen J. N., Crespo A., 2003, “Wind Turbine Wake Aerodynamics,” *Progress in Aerospace Sciences*, v. 39, p. 467–510.

[23]. Simms D., Schreck S., Hand M., Fingersh L. J., 2001, “NREL Unsteady Aerodynamics Experiment in the NASA-Ames Wind Tunnel: a Comparison of Predictions to Measurements,” *Technical Report NREL/TP-500-29494*, NREL, National Renewable Energy Laboratory.

[24]. Schepers J. G., Snel H., 2007, “Model Experiments in Controlled Conditions,” *Final report ECN-E-07-042*, Energy Research Center of the Netherlands.

[25]. Boorsma K., Schepers J. G., 2009, “Model Experiments in Controlled Conditions,” *Technical report*, Energy Research Center of the Netherlands.

[26]. Höglström U., Asimakopoulos D. N., Kambezidis H., Helmis C. G., Smedman A., 1988, “A Field Study of the Wake Behind a 2 MW Wind Turbine,” *Atmospheric Environment*, v. 22, p. 803-820.

[27]. Crespo A., Hernández J., 1996, “Turbulence Characteristics in Wind Turbine Wakes,” *Journal of Wind Engineering and Industrial Aerodynamics*, v.61, p. 71-85.

[28]. Zambrano T. G., Gyatt G. W., 1983, “Wake Structure Measurements at the MOD-2 Cluster Test Facility at Goodnoe Hills, Washington,” *IEE Proceedings*, v. 130, p. 562-565.

[29]. Baker R. W., Walker S. N., 1984, “Wake Measurements Behind a

- Large Horizontal Axis Wind Turbine Generator,” *Solar Energy*, v. 33, p. 5-12.
- [30]. Elliott D. L., Barnard J. C., 1990, “Observations of Wind Turbine Wakes and Surface Roughness Effects on Wind Flow Variability,” *Solar Energy*, v. 45, p. 265-283.
- [31]. Milborrow D. J., 1983, “Wake and Cluster Research: Past, Present and Future,” *IEE Proceedings*, v. 130, p. 566-573.
- [32]. Hassan U., Taylor G. J., Garrad A. D., 1988, “The Dynamic Response of Wind Turbines Operating in a Wake Flow,” *Journal of Wind Engineering and Industrial Aerodynamics*, v. 27, p. 113-126.
- [33]. Papadopoulos K. H., Helmis C. G., Soilemes A. T., Papageorgas P. G., Asimakopoulos D. N., 1995, “Study of the Turbulent Characteristics of the Near-Wake field of a Medium-Sized Wind Turbine Operating in High Wind Conditions,” *Solar Energy*, v. 55, p. 61-72.
- [34]. Helmis C. G., Papadopoulos K.H., Asimakopoulos D. N., Papageorgas P. G., Soilemes A. T., 1995, “An Experimental Study of the Near-Wake Structure of a Wind Turbine Operating over Complex Terrain,” *Journal of Solar Energy*,” v. 54, p. 413-428.
- [35]. Taylor G. J., 1983, “Wake and Performance Measurements on the Lawson-Tancred 17 m Horizontal-Axis Windmill,” *IEE Proceedings*, v. 130, p. 604-612.
- [36]. Kambezidis H. D., Asimakopoulos D. N., Helmis C. G., 1990, “Wake Measurements Behind a Horizontal-Axis 50 kW Wind Turbine,” *Solar & Wind Technology*, v. 7, p. 177-184.
- [37]. Barthelmie R. J., Hansen K., Frandsen S. T., Rathmann O., Schepers J. G., Schlez W., Phillips J., Rados K., Zervos A., Politis E. S., Chaviaropoulos P. K., 2009, “Modelling and Measuring Flow and Wind Turbine Wakes in Large Wind Farms Offshore,” *Wind Energy*, v. 12, p. 431–444
- [38]. Barthelmie R. J., Rathmann O., Frandsen S. T., Hansen K., Politis E. S., Prospathopoulos J., Rados K., Cabezón D., Schlez W., Phillips J., Neubert A., Schepers J. G., van der Pijl S. P., 2007, “Modelling and Measurements of Wakes in Large Wind Farms,” *Journal of Physics: Conference Series*, v. 75 (012049), p. 1–9.
- [39]. Alfredsson P. H., Dahlberg J. A., 1979, “A Preliminary Wind Tunnel Study of Windmill Wake Dispersion in Various Flow Conditions,” *Technical Note AU-1499, Part 7, FFA*, Stockholm, Sweden.
- [40]. Alfredsson P. H., Dahlberg J. A., 1981, “Measurements of Wake Interaction Effects on Power Output from Small Wind Turbine Models,” *NASA STI/Recon Technical Report N 82: 18720*.
- [41]. Hand M. M., Simms D. A., Fingersh L. J., Jager D. W., Cotrell J. R., Schreck S., Larwood S. M., 2001, “Unsteady Aerodynamics Experiment

Phase VI: Wind Tunnel Test Configurations and Available Data Campaigns,” *Technical report NREL/TP- 500-29955*, National Renewable Energy Laboratory.

[42]. Clive P. J. M., 2008, “LIDAR and Resource Assessment for Wind Power Applications: The State of the Art,” *SPIE Remote Sensing*, v. 7111, p. 1-10.

[43]. Käsler Y., Rahm S., Simmet R., Kühn M., 2010, “Wake Measurements of a Multi-MW Wind Turbine with Coherent Long-Range Pulsed Doppler Wind Lidar,” *Journal of Atmospheric and Oceanic Technology*, v. 27, p. 1529–1532.

[44]. Bingöl F., Mann J., Larsen G. C., 2010, “Light Detection and Ranging Measurements of Wake Dynamics Part 1: One Dimensional Scanning,” *Wind Energy*, v. 13, p. 51–61.

[45]. Trujillo J. J., Bingöl F., Larsen G. C., Mann J., Kühn M., 2011, “Light-Detection and Ranging Measurements of Wake Dynamics. part II: Two-Dimensional Scanning,” *Wind Energy*, v. 14, p. 61–75.

[46]. Massouh F., Dobrev I., 2007, “Exploration of the Vortex Wake Behind of Wind Turbine Rotor,” *Journal of Physics: Conference Series*, v. 75 (012036), p. 1-9.

[47]. Pascheke, F., Hancock P. E., 2007, "Wake Development and Interaction within an Array of Large Wind Turbines," *The International Workshop on Physical Modelling of Flow and Dispersion Phenomena (PHYSMOD 2007)*, University of Orleans, France.

[48] Whale J., Anderson C. G., Bareiss R., Wagner S., 2000, “An Experimental and Numerical Study of the Vortex Structure in the Wake of a Wind Turbine,” *Journal of Engineering and Industrial Aerodynamics*, v. 84, p. 1–21.

[49]. Medici D., 2005, “Experimental Studies of Wind Turbine Wakes - Power Optimisation and Meandering,” *PhD thesis*, KTH Mechanics, Royal Institute of Technology.

[50]. Rhyne R. H., Steiner R., 1964. “Power Spectral Measurement of Atmospheric Turbulence in Severe Storms and Cumulus Clouds,” *NASA Technical Note, NASA TN D-2469*.

[51]. Burns A., 1964. “Power Spectra of Low Level Atmospheric Turbulence Measured from an Aircraft,” *Aeronautical Research Council*, C. P. No. 733.

[52]. Lenschow D. H., Sun J., 2007, “The Spectral Composition of Fluxes and Variances Over Land and Sea Out to the Mesoscale,” *Boundary Layer Meteorology*, v. 125, p. 63-84.

[53]. Lovejoy S., Tuck A. F., Schertzer D., Hovde S. J., 2009, “Reinterpreting Aircraft Measurement in Anisotropic Scaling Turbulence,” *Atmospheric Chemistry and Physics*, v. 9, p. 5007-5025.

- [54]. Schlipf D., Trabucchi D., Bischoff O., Hofsäss M., Mann J., Mikkelsen T., Rettenmeier A., Trujillo J. J., Kühn M., 2010, "Testing of Frozen Turbulence Hypothesis for Wind Turbine Applications with a Scanning LIDAR System, " *International Symposium for the Advancement of Boundary Layer Remote Sensing*, Paris, France.
- [55]. Kocer G., Mansour M., Chokani N., Abhari R. S., Müller M., 2011, "Full-Scale Wind Turbine Near-Wake Measurements Using an Instrumented Uninhabited Aerial Vehicle," *ASME Journal of Solar Energy Engineering*, v.133, p. 041011 1-8.
- [56]. Mansour M., Kocer G., Lenherr C., Chokani N., Abhari R. S., 2011, "Seven-Sensor Fast-Response Probe for Full-Scale Wind Turbine Flowfield Measurements," *ASME Journal of Engineering for Gas Turbines and Power*, v.133, p. 081601 1-8.
- [57]. Giebel G., Paulsen U. S., Bange J., Cour-Harbo A. la, Reuder J., Mayer S., van der Kroonenberg A., Mølgaard J., 2012, "Autonomous Aerial Sensors for Wind Power Meteorology - A Pre-Project," *Risø-R-1798(EN)*, National Laboratory for Sustainable Energy, Risø DTU.
- [58]. Wildmann N., Hofsäss M., Weimer F., Joos A., Bange J., 2014, "MASC – A Small Remotely Piloted Aircraft (RPA) for Wind Energy Research," *Advances in Science and Research*, v. 11, p. 55-61.
- [59]. Kupferschmied K., Köppel P., Roduner C., Gyarmathy G., 2000, "On the Development and Application of the FRAP (Fast-response Aerodynamic Probe) System for Turbomachines- Part 1: The Measurement System," *Journal of Turbomachinery*, v. 122, p. 505-516.
- [60]. Pfau A., Schlienger J., Kalfas A. I., Abhari R. S., 2002, "Virtual Four Sensor Fast Response Aerodynamic Probe (FRAP)," *16th Symposium on Measuring Techniques in Transonic and Supersonic Flows in Cascades and Turbomachines*, Cambridge, UK.
- [61]. Porecca L., Hollenstein M., Kalfas A. I., Abhari R. S., 2007, "Turbulence Measurements and Analysis in a Multistage Axial Turbine," *Journal of Propulsion and Power*, v. 23, p. 227-234.
- [62]. Mansour M., Chokani N., Kalfas A. I., Abhari R. S., 2008, "Time-Resolved Entropy Measurements Using a Fast Response Entropy Probe " *Measurement Science and Technology*, v. 19, p. 115401 1-14.
- [63]. Bryer D. W., Pankhurst R. C., 1971, "Pressure-Probe Methods for Determining Wind Speed and Flow Direction," *Her Majesty's Stationary Office*, London.
- [64]. Zilliac G. G., 1993, "Modelling, Calibration, and Error Analysis of Seven-Hole Pressure Probes," *Experiments in Fluids*, v. 14, p. 104-120.
- [65]. Gallington R. W., 1981, "Measurement of Very Large Flow Angles with Non-Nulling Seven-Hole Probe," *International Instrumentation Symposium; 27th; April 27-30, Indianapolis, IN*.

- [66]. Brücker D., 2010, "Assessment and Improvement of UAV Measurement System," *Master's Thesis*, Laboratory for Energy Conversion, ETH Zurich.
- [67]. Gossweiler C., Humm H. J., Kupefrschmied P., 1989, "The Use of Piezo-Resistive Semi-Conductor Pressure Transducers for Fast-Response Probe Measurements in Turbomachinery," Proceedings 10th Symposium on Measuring Techniques for Transonic and Supersonic Flows in Cascades and Turbomachines, Brussel.
- [68]. Ublox. *LEA-6x-Data Sheet* (2012).
- [69]. Guerer M. L., 2014, "Performance Optimisation of WindFlyer," *Master's thesis*, Laboratory for Energy Conversion, ETH Zurich.
- [70]. Pressure Sensor – MS5611-01BA03 (data sheet), 2012, <http://www.meas-spec.com/product/pressure/MS5611-01BA03.aspx>.
- [71]. Humidity & Temperature Sensor – SHT7x (data sheet), 2011, http://www.sensirion.com/fileadmin/user_upload/customers/sensirion/Dokumentation/Humidity/Sensirion_Humidity_SHT7x_Datasheet_V5.pdf.
- [72]. Caruso M. J., "Applications of Magnetic Sensors for Low Cost Compass Systems", Honeywell, SSEC.
- [73]. Jacobi S., 2012, "Structural and Modal Analysis of windFlyer," *Semester project report*, LEC, ETH Zurich.
- [74]. Compoengineering Inc. ESAComp., <http://www.esacomp.com/index.php>.
- [75]. Karl M. Prewo, 1982, "A Compliant, High Failure Strain, Fibre-Reinforced Glass-Matrix Composite," *Journal of Materials Science*, 17:3549-3563, 1982.10.1007/BF00752199.
- [76]. Bezazi A., El Mahi A., Berthelot J., 2003, "Investigation of Cross-Ply Laminates Behaviour in Three Point Bending Tests. Part II: Cyclic Fatigue Tests," *Journal of Materials Science*, v. 9, p. 128-133.
- [77]. Baron Ch., Schulte K., 1987, "Influence of Fibre and Matrix Failure Strain on Static and Fatigue Properties of Carbon Fibre-Reinforced Plastics," *Composites Science and Technology*, v. 29, p. 257-272.
- [78]. Barlow J. B., Rae W. H., Pope A., 1999, "Low-Speed Wind Tunnel Testing," *John Wiley and Sons*, New York.
- [79]. Ruesch T., 2011, "An aerodynamic Probe for upstream Wind Measurements on a Wind Turbine," *Masters thesis*, Laboratory for Energy Conversion, ETH Zurich.
- [80]. Ettlin K., 2012, "A Kite-Based Fast-Response Aerodynamic Probe System for Wind Measurements," *Masters thesis*, Laboratory for Energy Conversion, ETH Zurich.
- [81]. Vogel K., 2011, "Integrated Optimized Flight Trajectory and Autopilot for Wind Measurements using a UAV," *Semester project report*, Laboratory for Energy Conversion, ETH Zurich.

- [82]. <http://aerospace.illinois.edu/m-selig/props/propDB.html>.
- [83]. Silvagni M., *AXI 2814-16 test*. 2009.
- [84]. Selig M., Brandt J., 2011, "Propeller Performance Data at Low Reynolds Numbers," *49th AIAA Aerospace Sciences Meeting*.
- [85]. Paparazzi autopilot, https://wiki.paparazziuav.org/wiki/Main_Page.
- [86]. Beswick K. M., Gallagher M. W., Webb A. R., Norton E. G., Perry F., 2008, "Application of the Aventech AIMMS20AQ Airborne Probe for Turbulence Measurements during the Convective Storm Initiation Project," *Atmospheric Chemistry and Physics*, v. 8, p. 5449-5463.
- [87]. Norris J. D., Chokani N., 2001, "Identifical of Nonlinear Interactions in Hypersonic Boundary Layers Using STFT," *AIAA 2001-0207*.
- [88]. Taylor, G., 1938, "The Spectrum of Turbulence," *Proceedings of the Royal Society of London*.
- [89]. Kaimal J. C., Finnigan J. J., 1994, "Atmospheric Boundary Layer Flows – Their Structure and Measurement," *Oxford University Press*.
- [90] Stull R., 1989, "An Introduction to Boundary Layer Meteorology," V. 13 *Springer Science & Business Media*.
- [91]. Behr T., Kalfas A. I., Abhari R. S., 2006, "A Probabilistic Uncertainty Evaluation Method for Turbomachinery Probe Measurements " *XVIII Symposium on Measuring Techniques in Transonic and Supersonic Flows in Cascades and Turbomachines*, Thessaloniki, Greece.
- [92]. Kocer G., 2012, "Full-Scale Wind Turbine Flow Field Measurements Using an Instrumented Uninhabited Aerial Vehicle," PhD thesis, LEC, ETH Zurich.
- [93]<http://www.bazl.admin.ch/dienstleistungen/02658/index.html?lang=de>.
- [94]. <http://www.gnu.org/copyleft/gpl.html>.
- [95]. Jafari S., Chokani N., Abhari R. S., 2011, "An Immersed Boundary Method for Simulation of Wind Flow over Complex Terrain," *ASME Journal of Solar Energy Engineering*, v. 134, p. 011006 1-12.
- [96]. Subramanian B., Chokani N., Abhari R. S., 2012, "Full-Scale HAWT: Structure of Near-Wake Turbulence Measured with Instrumented UAV," *Euromech Colloquium 528*.
- [97]. Kocer G., Chokani N., Abhari R. S., 2012, "Wake Structure of a 2 MW Wind Turbine Measured Using an Instrumented UAV," *AIAA 2012-0231, 50th AIAA Aerospace Sciences Meeting*.
- [98]. Dubovikov M. M., Tatarskii V. I., 1987, "The Calculation of the Asymptotics of the Spectrum of Locally Isotropic Turbulence in the Viscous Range," *Zhurnal Eksperimental'noi i Teoreticheskoi Fiziki*. 93, 1992-2001. (English translation by American Institute of Physics, 1988).
- [99]. Kaimal J. C., Finnigan J. J., 1994, "Atmospheric Boundary Layer Flows – Their Structure and Measurement," *Oxford University Press*.
- [100]. Wood D. H., 1994, "Simple Equations for Helical Vortex Wakes,"

Journal of Aircraft, v. 31, p. 994–995.

[101]. Barthelmie R. J., Frandsen S. T., Nielsen M. N., Pryor S. C., Rethore P. E., Jorgensen H. E., 2007, “Modelling and Measurements of Power Losses and Turbulence Intensity in Wind Turbine Wakes at Middelgrunden Offshore Wind Farm,” *Wind Energy*, v. 10, p. 517-528.

[102]. Chokani N., Ettl K., Mansour M., Subramanian B., Costa D., Abhari R. S., 2013, "Near-Wake Measurements in an Offshore Reference Field Using a Kite-Based Aerodynamic- Probe System", *European Wind Energy Conference (EWEA)*, Vienna, Austria.

[103]. Dahlberg J., 2009 “Assessment of the Lillgrund Wind Farm: Power Performance Wake Effects,” *Vattenfall Vindkraft AB, 6_1 LG Pilot Report*.

[104]. Tsalicoglou C., Jafari S., Chokani N., Abhari R. S., 2014 “RANS Computations of MEXICO Rotor in Uniform and Yawed Inflow,” *Journal of Engineering for Gas Turbines and Power*, v. 136, No. 1, 011202.

[105]. Subramanian B., Chokani N., Abhari R. S., 2014, "Experimental Investigation of Three-Dimensional Flow Structure of a Multi-MW Wind Turbine in Complex Terrain," submitted to *ASME Journal of Solar Energy Engineering*.

[106]. Shao Y., Hacker H. M., 1990, “Local Similarity Relationships in a Horizontally Inhomogeneous Boundary layer,” *Boundary layer Metrology*, v. 52, p. 17-40.

[107]. Gryning S. E., Holtslag A. A. M., Irwin S. J., Sivertsen B., 1987, “Applied Dispersion Modelling Based on Meteorological Scaling Parameters,” *Atmospheric Environment*, v. 21, p. 79-89.

[108]. Kundu P. K., Cohen I. M., 2002, “Fluid Mechanics,” *2nd Edition Academic Press*, New York.

[109]. Takasu T., Yasuda A., 2009, "Development of the low-cost RTK-GPS receiver with an open source program package RTKLIB," *International Symposium on GPS/GNSS*, Jeju, Korea: International Convention Centre.

[110]. Takasu T., Yasuda A., 2008, "Evaluation of RTK-GPS performance with low-cost single-frequency GPS receivers," *International symposium on GPS/GNSS*.

[111]. Sommer D., 2011, “Wind Resource Assessment using WRF Mesoscale Solver,” *Master’s Thesis*, Laboratory for Energy Conversion, ETH Zurich.

[112]. Durand W. F., Lesley E. P., 1923, “Experimental Research on Air Propellers,” *NACA Report 141*.

[113]. Schenk H., 2002, “Die Propellersteigung,”

[114]. Philipps W. F., 2009, “Mechanics of Flight,” John Wiley and Sons, Hoboken, New Jersey.

[115]. Wildi J., 2012, “Grundlagen der Flugtechnik,” ETH Zürich.

[116]. Smedma AS., Tjernström M., Högström U., 1994, "The Near-Neutral Marine Atmospheric Boundary Layer with no Surface Shearing Stress: A Case Study," *Journal of the Atmospheric Sciences*, v. 51 (23), p. 3399-3411.

[117]. Elston J, Argrow B., Stachura M., Weibel D., Lawrence D., Pope D., 2015, "Overview of Small Fixed-Wing Unmanned Aircraft for Meteorological Sampling." *Journal of Atmospheric and Oceanic Technology*, v.32, p. 97-115.

APPENDIX A: STFT, WT and MEM

The STFT, WT and MEM codes developed at LEC were tested using a virtual test signal generated in Matlab to evaluate and compare its performance. The test signal (characterized in Table 18) is divided into four equal time periods and is 20 s long as shown in Figure 105, with a 4 Hz sine wave located between 5-10 s and a 17 Hz sine wave present in the interval 15-20 s. Random noise is also added along the entire length of this signal to simulate turbulence effects.

Time period (s)	RMS	Variance	Peak	Frequencies (Hz)	Signal characteristics
0-5	-	-	0.1	-	Random noise ONLY (mean = 0)
5-10	0.71	0.5	1	4	4 Hz sine signal + random noise
10-15	-	-	0.1	-	Random noise ONLY (mean = 0)
15-20	1.41	2	2	17	17 Hz sine signal + random noise

Table 18. Virtual test signal characteristics.

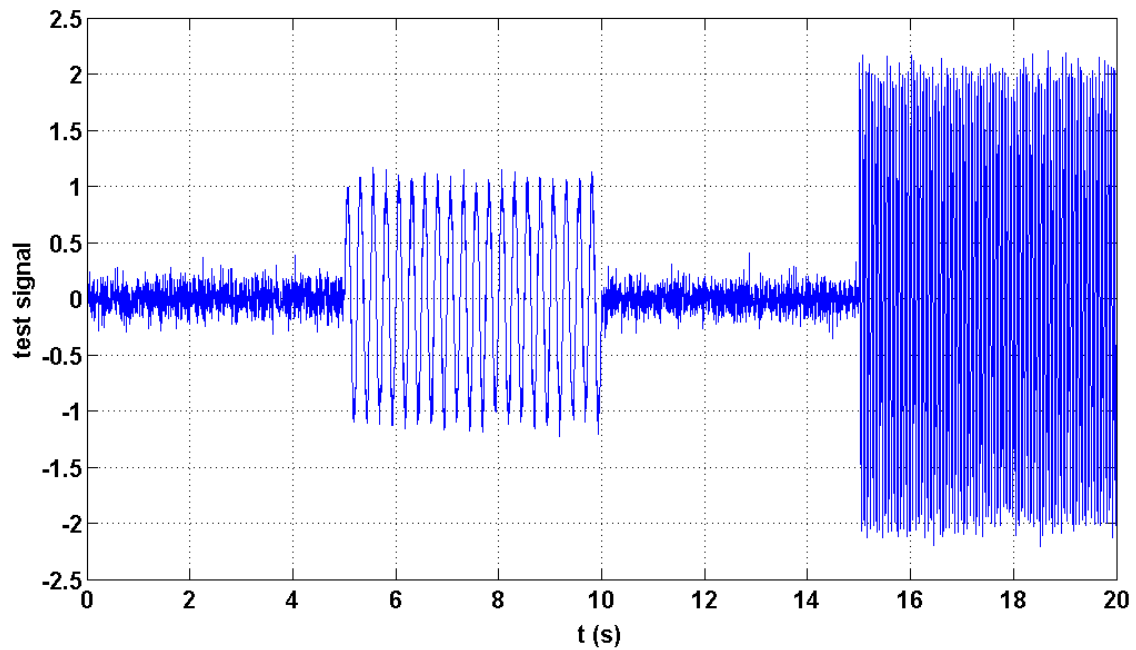
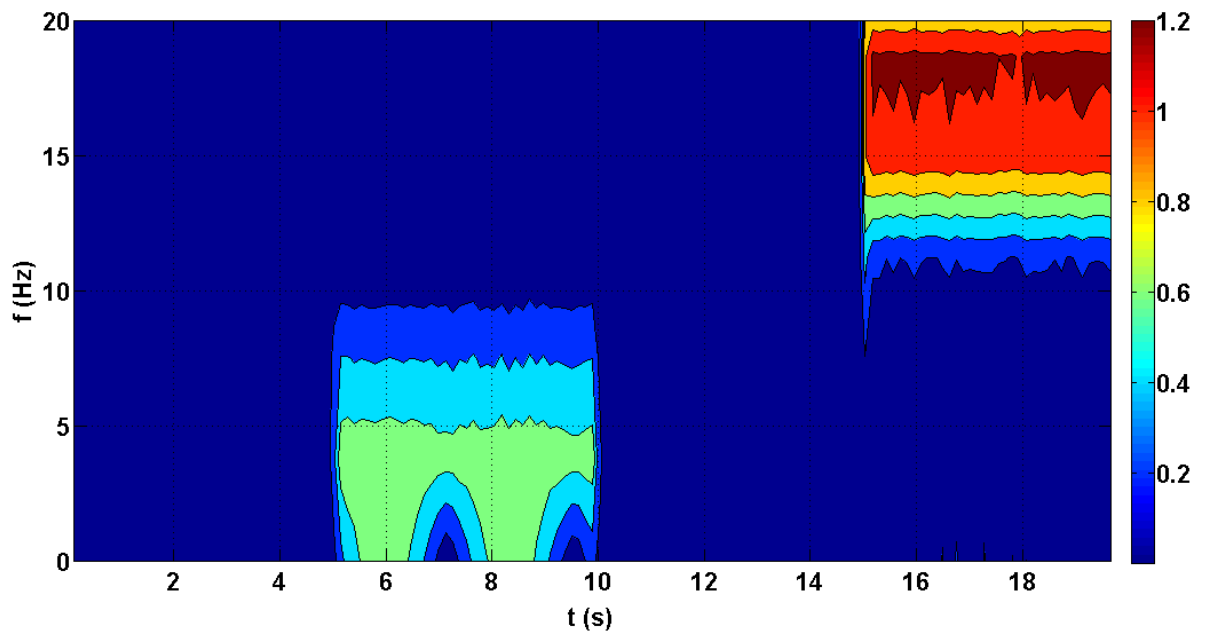
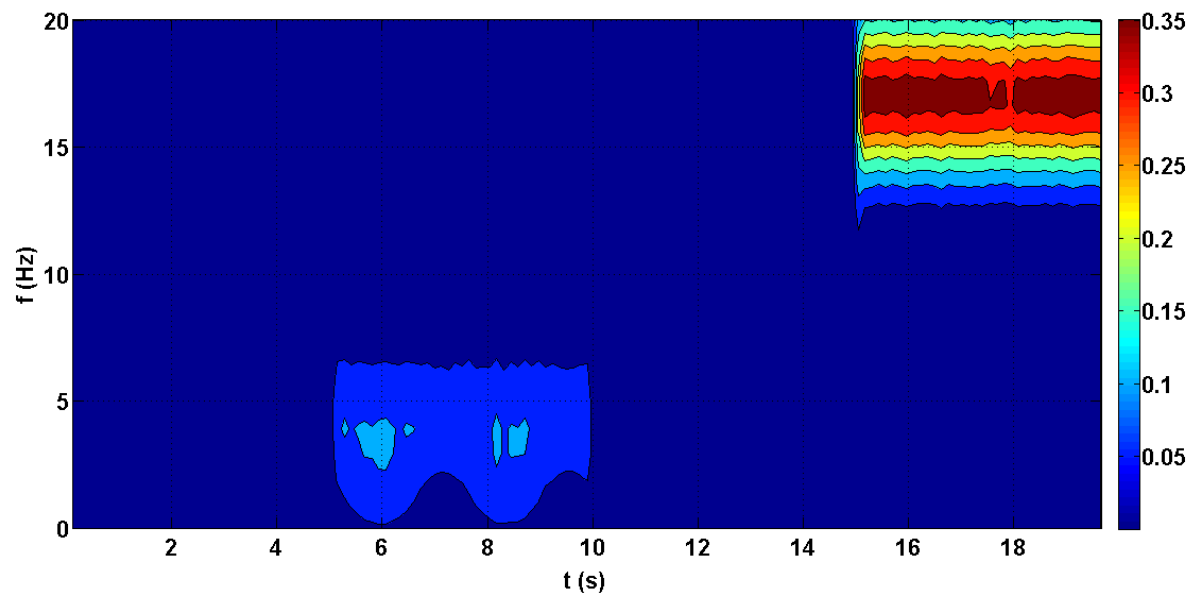


Figure 105. Virtual test signal.

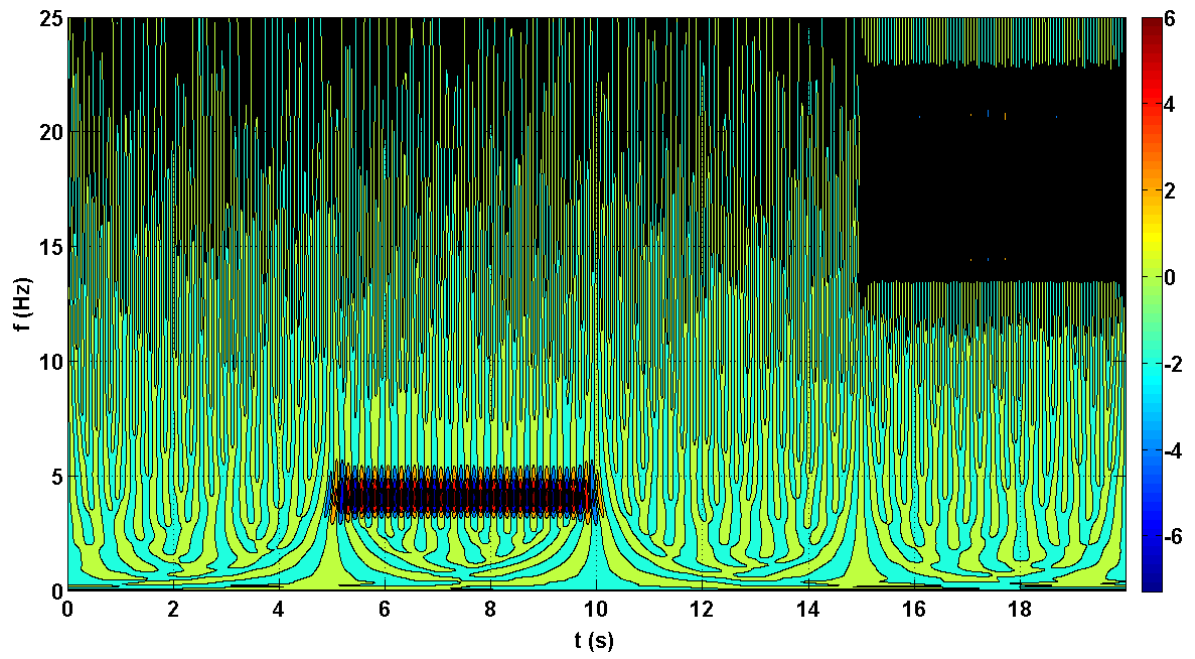
The virtual test signal is then sampled at 250 Hz for analysis and testing with STFT (with FFT OR using Matlab pwelch command), WT and MEM to reveal its time-frequency representation, Figure 106. Although STFT (FFT and using Matlab pwelch command), WT and MEM correctly predicts the 4 Hz signal between 5-10 s and 17 Hz signal between 15-20 s, but WT and MEM are not considered for further analysis as the process for obtaining the signal variance is not explicit. The variance of virtual test signal as a function of time computed from STFT (computed with Matlab ‘pwelch’ command) with a Hamming window size of 0.2 s and a 50% overlap is shown in Figure 107. The variance of 4 Hz signal in the interval 5-10 s is 0.5 and the variance of 17 Hz signal between 15-20 s is 2 (Table 18), and they are correctly predicted with STFT (with Matlab ‘pwelch’ command). Thus, it is still possible to get the correct variance from small parts of a signal.



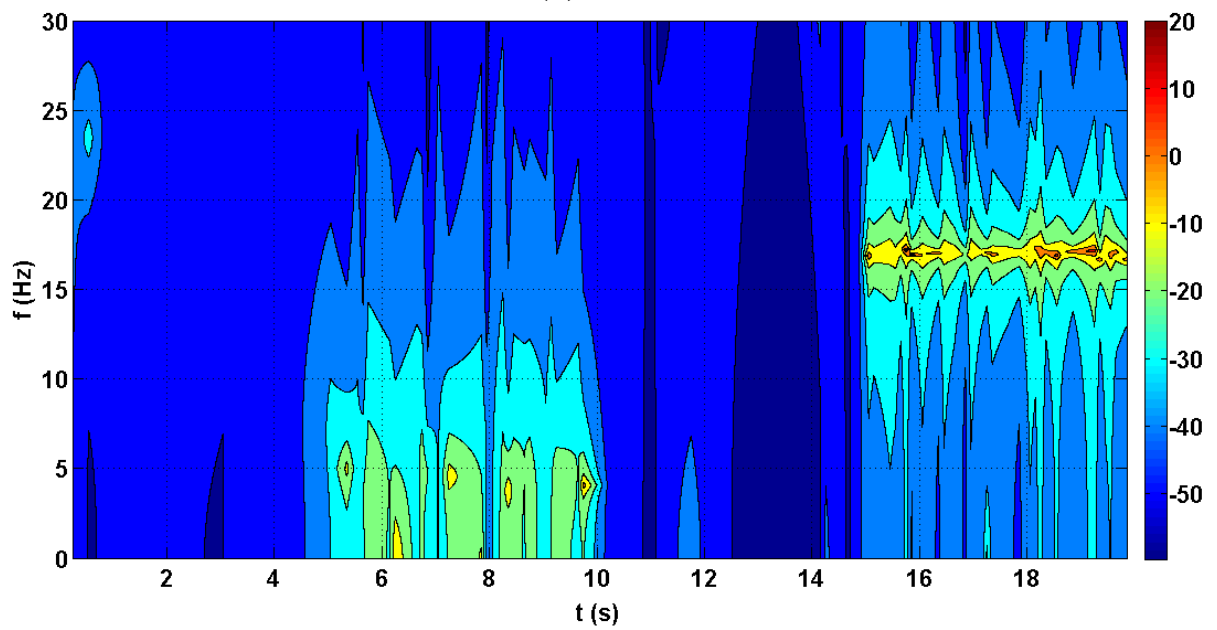
(a)



(b)



(c)



(d)

Figure 106. Time-frequency representation of test signal using (a) STFT (FFT), (b) STFT (with Matlab pwelch command), (c) Wavelet Transform (WT), (d) Maximum Entropy Method (MEM).

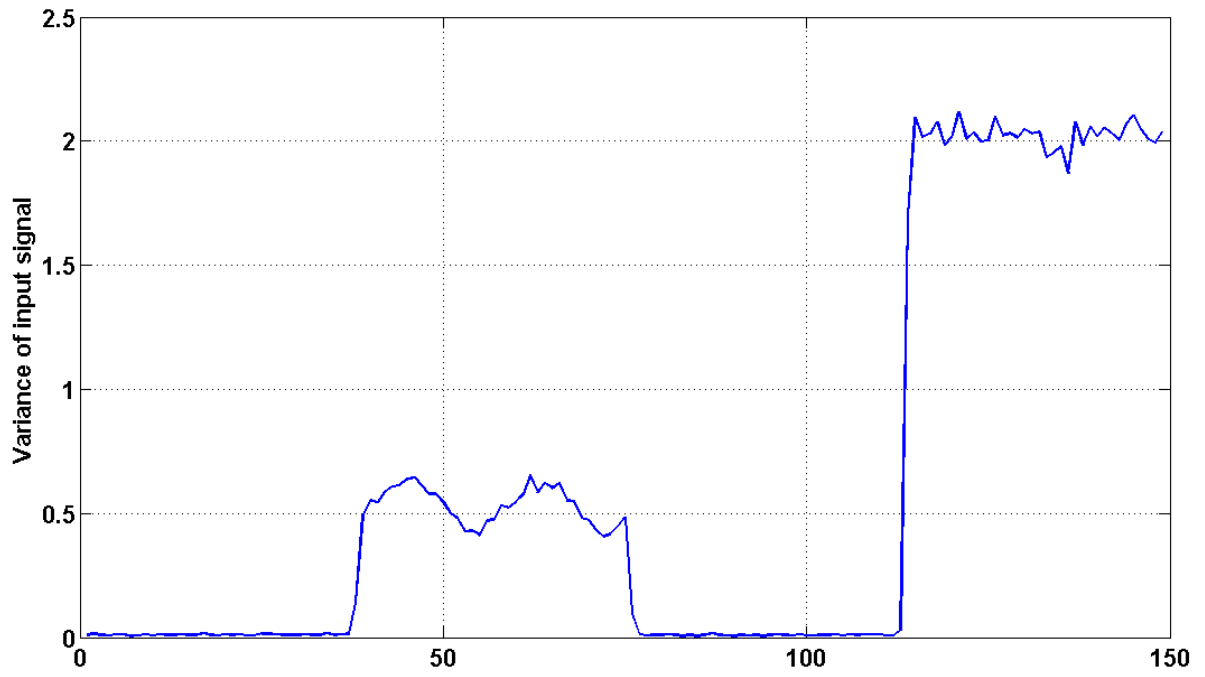


Figure 107. Variance of test signal predicted using STFT. X-axis represents the number of data points.

APPENDIX B: PROPELLER THEORY [73]

The propellers used in RC-aircraft applications follow the same physical principles as the bigger propellers used in manned aircrafts. The aerodynamic theory of propellers was first assessed in the 1920s and documented in the NACA report Nr.141 [112]. The same definitions and physical models are used until today.

B.1 Propeller Types and Geometrical Definitions

The two different types of propellers are used in RC aircrafts were fixed propellers and folding-propellers, Figure 108. The folding-propellers are generally used in models with low ground clearance to prevent damage during landing, but their efficiency is slightly smaller than the fixed ones.

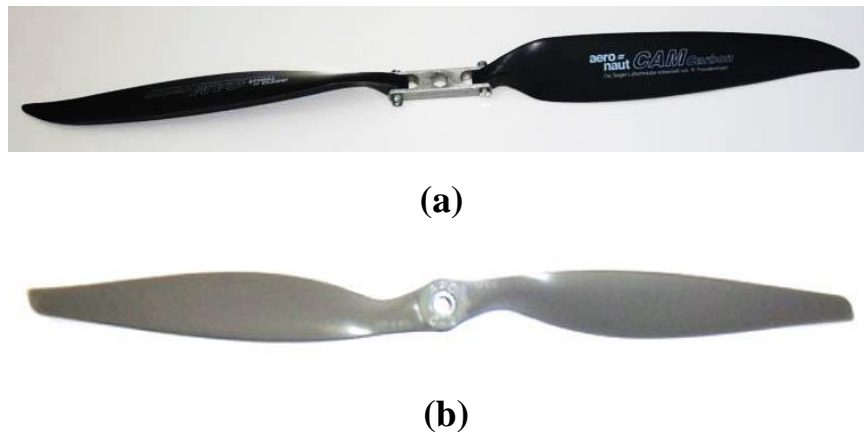


Figure 108. (a) Aeronaut CAM Carbon folding propeller, (b) APC fixed propeller.

A variety of propellers from different brands are available in the RC market, and their efficiency was systematically assessed in [84]. The most popular brands - APC, Graupner and Aeronaut - turned out to manufacture the most efficient blade geometries. The characteristic geometrical parameters of a propeller are the diameter D and pitch H . The diameter is simply the distance from one tip to the other, whereas the pitch is defined as function of the diameter and blade angle β at 75% of the blade radius.

$$H = 2\pi \cdot 0.75 \cdot D/2 \cdot \tan \beta \quad (35)$$

Figure 109 illustrates the relationship between blade angle and propeller pitch. Propellers for RC-model are generally labeled using the

nomenclature $D \times H$, where D and H are measured in inches. For example, an 11x8 propeller has a diameter of 11'' and a pitch of 8''.

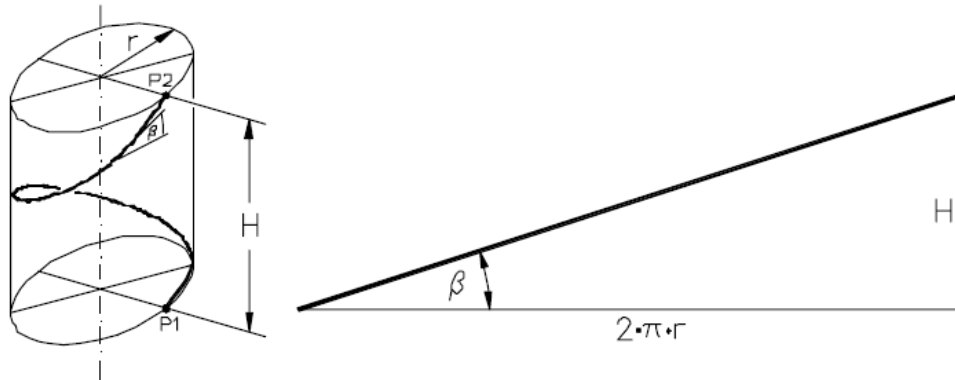


Figure 109. Definition of propeller pitch and blade angle [113].

B.2 Propeller Efficiency

The efficiency of a propeller is highly dependent on the incidence angle between the relative wind and the blade chord. Figure 110 shows the velocity triangle composed out of the axial velocity (the relative wind of the aircraft) and the tangential velocity (resulting from the rotation of the propeller blade).

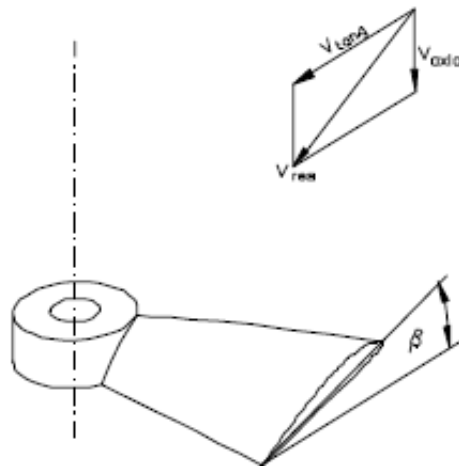


Figure 110. Velocity triangle of the airfoil section of a propeller blade [113].

The advance ratio J , which is an indicator for the incidence angle, is defined as

$$J = \frac{V_{air}}{N \cdot D} \quad (36)$$

where N is the rotational speed of the propeller and V_{air} is the relative airspeed of the aircraft. The efficiency of the propeller can be written as the ratio of the propulsive power and the shaft power.

$$\eta_{propeller} = \frac{P_{propulsive}}{P_{shaft}} = \frac{Th \cdot V_{air}}{T_{shaft} \cdot 2\pi N} = f(J) \quad (37)$$

where T_{shaft} is the shaft torque and Th is the thrust produced by the propeller. As mentioned above, it turns out that the propeller efficiency is strongly correlated to the advance ratio, which becomes obvious when looking at a propeller diagram, Figure 111. The following figure shows the performance data of a typical RC propeller, resulting of the experimental investigations of [84].

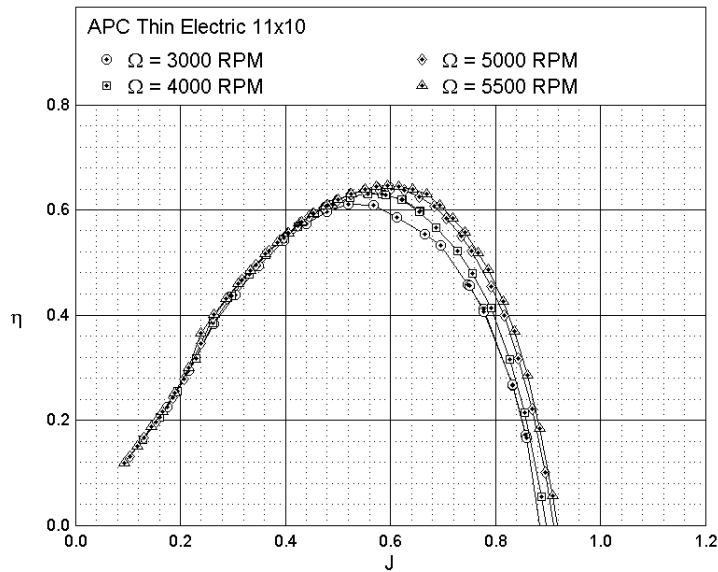


Figure 111. Propeller diagram [82].

The qualitative shape of the above curve is common for all propellers: at a certain advance ratio, the propeller efficiency is maximized. If the airspeed is further increased (or the rotational speed decreased), the incidence angle becomes negative. The efficiency decreases rapidly with the advance ratio due to negative stall. Finally the propeller enters the so-called “wind-milling state” and the efficiency becomes zero. Therefore, an

operating point at the optimal advance ratio (around 0.6 in the diagram above) is desired. It turns out that the magnitude of this J_{opt} mainly depends on the pitch to diameter ratio of the propeller [114].

B.3 Parameters Affecting the Peak-efficiency

The impulse theory (see e.g. [115]) yields that the (ideal) efficiency of a propeller increases with the diameter. However, the blade Reynolds number and the pitch to diameter ratio also have a high impact on the magnitude of the peak efficiency η_{max} . According to [114], quadratic propellers (i.e. $H/D = 1$) yield the highest η_{max} (if Re , H/D remain constant). Furthermore, an increase in the blade Reynolds number shifts the curves in propeller diagrams towards higher efficiency. This trade-off is illustrated in Figure 112 and has to be considered when choosing the optimal propeller for a particular application (cruise speed, thrust requirement...).

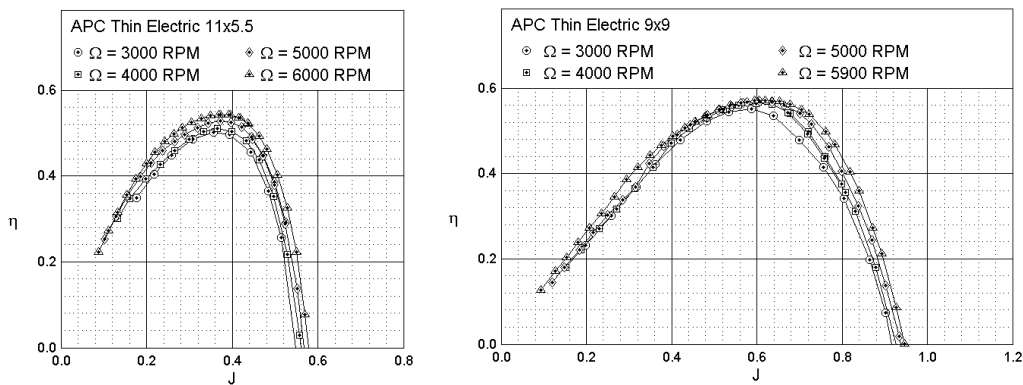


Figure 112. Trade-off between diameter and pitch to diameter ratio [82].

B.4 Power Considerations for the windFlyer Propulsion System

The propulsion system of windFlyer consists of a propeller powered by a brushless electric motor. Since energetic losses occur on both components, the required electric power for horizontal flight can be rewritten as

$$P_{elec} = \frac{P_{propulsive}}{\eta_{propeller} \cdot \eta_{motor}} = \frac{D(V) \cdot V}{\eta_{propeller} \cdot \eta_{motor}} \quad (38)$$

where D denotes the drag and V the airspeed of the drone. It has to be noted that the physical limit for the overall efficiency of windFlyer is around 50% since:

- the maximum efficiency of the electric motors, that can be mounted into windFlyer is 82%
- the maximum efficiency of propellers with diameters smaller than 14'' is 65% (bigger propellers would require a gear-box)

B.5 Static Thrust Limitation

To characterize the static thrust of a propeller, the dimensionless parameter c_{T0} (static thrust coefficient) is introduced [84] and defined as

$$c_{T0} = \frac{Th}{\rho \cdot N^2 \cdot D^4} \quad (39)$$

where Th denotes the thrust, ρ the air density, N the rotational speed of the shaft and D the diameter of the propeller. The static thrust coefficient is a specific property of each propeller and virtually independent of the blade Reynolds number. This implies that the static thrust of a given propeller scales with the maximum rotational speed of the electric motor.

Three different motors with different maximum rotational speeds were used within the flight tests:

- AXI 2814/16 with a kV of 1035 rpm/V (the original motor)
- AXI 2814/20 with a kV of 840 rpm/V
- AXI 2814/32 with a kV of 520 rpm/V

This implies that if the original propeller (11x8) is used with the AXI 2814/20 respectively the 2814/32 instead of the original motor, the static thrust decreases by 35% respectively 75 %. Therefore, a propeller with a higher diameter has to be used with those motors to ensure a safe launching of the drone.

APPENDIX C: FRAP AERO-CALIBRATION

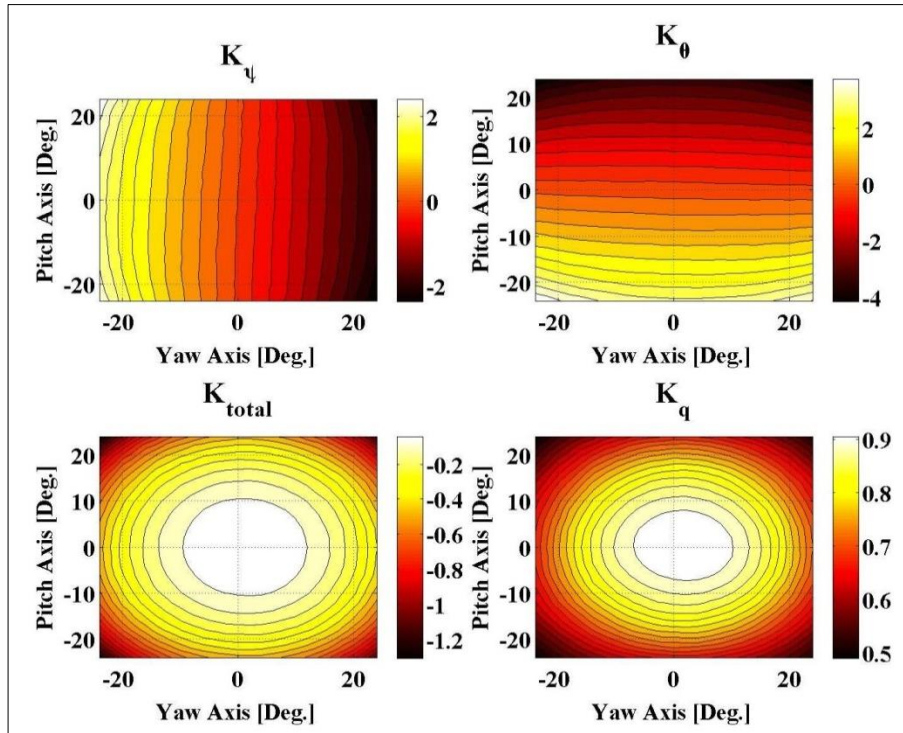


Figure 113. FRAP1 Aero calibration

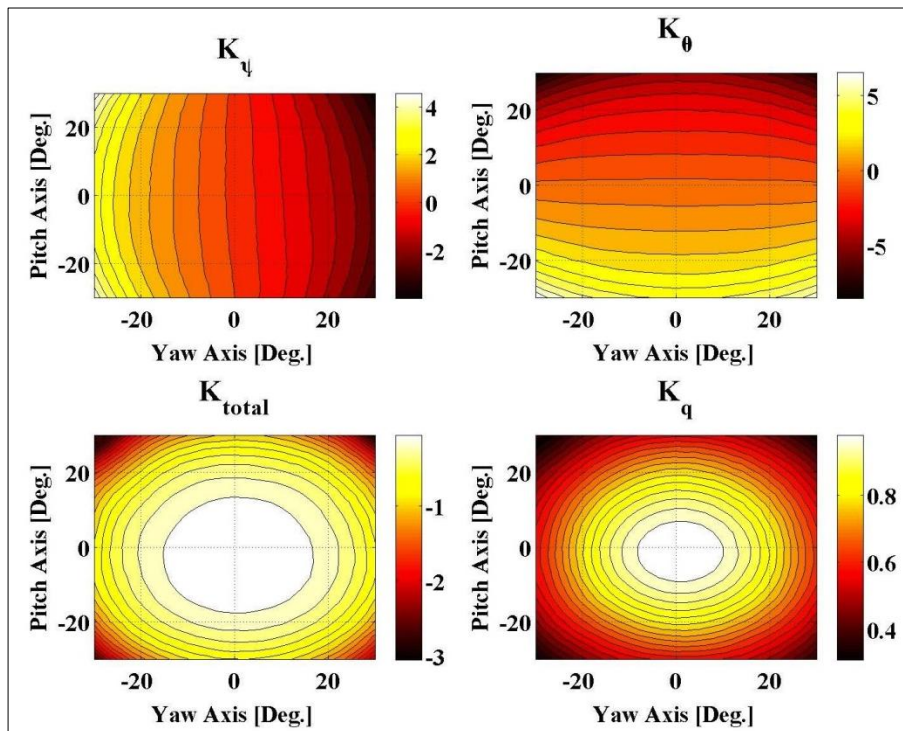


Figure 114. FRAP2 Aero calibration

APPENDIX D: FIELD OPERATING PROCEDURE

D.1 Before Take-Off Instructions

1. Mount the porous FRAP probe cap.
2. Check if SD card is in FRAQ board.
3. Check if the CG of drone is balanced from levelling points.
4. Precisely level the drone in pitch and roll axis with spirit level
5. Power ON and wait for 45 seconds.
6. Check if green LED in FRAQ board is ON.
7. Mount top and battery cover, and wait for 15 s at zero wind speed.
8. Remove FRAP probe cap and clean FRAP head with isopropanol.
9. Check if drone telemetry messages has all sensor outputs and if
 Logfile is created

LAUNCH THE DRONE

D.2 After Landing Instructions

1. Place drone on the mechanical jig.
2. Clean FRAP head with isopropanol and mount FRAP probe cap.
3. Wait for 30 seconds
4. Push button in FRAQ to stop logging. (causes green LED to blink)
5. Power OFF drone.
6. Paparazzi GCS OFF.

Curriculum Vitae

Personal data

- **Name:** Balaji Subramanian
- **Birth:** 6th March 1982, Chennai, India

Education

- Ph.D., Laboratory for Energy Conversion, Institut für Energietechnik, Swiss Federal Institute of Technology (ETH), Zürich, Switzerland.
July 2010 – September 2015
- M.Tech, Aerospace Engineering (Flight dynamics and Aerodynamics), Indian Institute of Technology (IIT), Kanpur, India.
August 2004 – June 2006
- B.E, Mechanical Engineering, S.R.M Engineering College, University of Madras, Chennai, India
July 1999 – May 2003

Professional experience

- Teaching assistant for Wind Energy, Experimental Methods for Engineers, and Energy Systems and Power Engineering courses, ETH Zürich, 2010 – 2014.
- Supervision of master and bachelor student projects, ETH Zürich, 2010 – 2014.
- Engineer/Technologist in Wind CFD Team (Renewable energy CoE), John F. Welch Technology Center (JFWTC), General Electric (GE) India, 2007 – 2010.
- Engineer/Technologist: Systems, KLA Tencor, India, 2006 – 2007.

List of Publications

- **B. Subramanian**, N. Chokani and R. S. Abhari, 2015, "Experimental Analysis of Wakes in a Utility Scale Wind Farm," *Journal of Wind Engineering and Industrial Aerodynamics*, v.138, p. 61-68.
- **B. Subramanian**, N. Chokani and R. S. Abhari, 2015, "Experimental Investigation of Three-Dimensional Flow Structure of a Multi-MW Wind Turbine in Complex Terrain," *ASME Journal of Solar Energy Engineering including wind energy*, v.137, p. 051007 1-10.
- **B. Subramanian**, N. Chokani and R. S. Abhari, 2016, "Aerodynamics of Wind Turbine Wakes in Flat and Complex Terrains," *Renewables Energy Journal*, v.85, p. 454-463.
- **B. Subramanian**, N. Chokani and R. S. Abhari, 2015, "Impact of Atmospheric Stability on Wind Turbine Wake Evolution," *manuscript nearing completion*.
- N. Chokani, **B. Subramanian** and R. S. Abhari, 2014, "Instrumented Drone Measurements of 3D Flow Structure of Multi-MW Wind Turbines," *Invited Paper at European Wind Energy Conference (EWEA 2014)*.
- N. Chokani, K. Ettlin, M. Mansour, **B. Subramanian**, D. Costa and R. S. Abhari, 2013, "Near-Wake Measurements in an Offshore Reference Field Using a Kite-Based Aerodynamic- Probe System", *European Wind Energy Conference EWEA Vienna, Austria*.
- **B. Subramanian**, N. Chokani and R. S. Abhari, 2012, "Full-Scale HAWT: Structure of Near-Wake Turbulence Measured with Instrumented UAV," *Euromech Colloquium 528 conference series*.